Direct reduction of copper-cobalt sulphide mineral concentrates for metal/alloy production

Yotamu Stephen Rainford Hara

Submitted in accordance with the requirements for the degree of
Doctor of Philosophy

The University of Leeds

School of Process, Environmental and Materials Engineering

June, 2014

The candidate confirms that the work submitted is his own, except where work which has formed part of jointly-authored publications has been included. The contribution of the candidate and the other authors to this work has been explicitly indicated below. The candidate confirms that appropriate credit has been given within the thesis where reference has been made to the work of others.

All the results that are presented in the papers were obtained and analysed by the author of the thesis. The author of this thesis wrote the draft of the papers. The supervisor (Animesh Jha) revised the papers before sending them for publication.

Acknowledgements

This work would have not been possible without the guidance, knowledge and support from my supervisor, Professor Animesh Jha. It was a very good experience to study under the supervision of Professor Animesh Jha and I have learnt different skills and techniques. I am indebted to the Institute of Materials, Minerals and Mining (IOM^3) and the Copperbelt University in Zambia for the financial support. I am so thankful to M. Javed for the technical support throughout my study. The trainings on X-ray diffraction and scanning electron microscope analysis given by Dr. T. Comyn and Mr J. Harrington, respectively, are gratefully acknowledged.

I am thankful to the Nchanga, Nkana and Baluba concentrators in Zambia, for supplying the mineral sulphide concentrates. Special thanks to Mr. K. Tompwe and Mr. B. Chulu for assisting me in acquiring the mineralogical data of the mineral sulphide concentrates.

I am very grateful to the following colleagues: Terry Makanyire, Lidia Escudero Castejo, Steven Parirenyatwa, Steven Mudenda and Felix Kalaba for their friendship. Special thanks to Dr. Sergio Sanchez Segado for providing some meaningful suggestions to this report.

Heartfelt thanks to all members of the family for the constant encouragements, love and spiritual support during my study. Special thanks to my wife Faith Mbwembwembwe Hara, Titus Hara, Nason Hara, Nelson Hara, Auntie Grace Mwale, Auntie Marjorie Daka Ndhlovu, Benny Daka, Dean Chola, deacon Mpasi and Nathan Siminika.

Finally, I am very grateful to the almight God for enabling me reach this far.

Dedication

I dedicate this thesis to my late mum, Anness Soko Hara who died during final stages of my study. Your love, patience and hardwork will forever be remembered.

Abstract

The investigation focuses on an alternative route to metallic phase extraction from complex Cu-Co-Fe mineral sulphide concentrates, from the Copperbelt region in Zambia. In the context of developing a novel process route for metal extraction without SO_2 gas emission and slag waste generation, the reduction of Cu-Co-Fe mineral sulphide concentrates via carbothermic reduction in the presence of lime (CaO) by following the equilibrium: MS + CaO + C = M + CaS + CO(g), where M represents the metallic Cu, Co and Fe, was studied. The reduction experiments were carried out in a temperature range of 1073 K - 1573 K, under argon atmosphere. The extent of metallization was analyzed by plotting the percentage reduction (%R) for each reaction against time (t). The reacted and partially reacted samples were characterised by X-ray powder diffraction (XRD), scanning electron microscopy (SEM) and energy dispersive X-ray (EDX) techniques. SEM-EDX analysis of the reduced samples showed that the purity of the metallic/alloy phases were over 97 wt.%. The reduced samples were subjected to magnetic separation for separating out the metallic/alloy phases from CaS, excess CaO and gangue minerals. The regeneration of CaO from CaS and utilisation of CaS were investigated.

The effects of reduction temperature, type of carbon and mole ratios of CaO and C were investigated. Complete reduction/metallisation occurred within 2 hours above 1173 K and 1273 K with carbon black and graphite, respectively. Carbon black was found to be a better reductant as there was excessive sintering between the metallic and CaS phases, in the reduction with graphite. However, the mole ratio of carbon black should be slightly higher than that of CaO, because of; (i) consumption of part of CaO by the gangue minerals (SiO_2 and Al_2O_3) at lower mole ratio of C than CaO (e.g. MS:CaO:C = 1:2:1) and (ii) incomplete reduction at very high mole ratio of C than CaO CaO (e.g. MS:CaO:C = 1:2:4), at T ≤ 1323 K. The reaction mechanisms were studied by stopping the reduction experiments at different times and characterising the partially reacted samples. The metallisation of Fe occured via reduction of the intermediate phase of Fe-O (FeO and Fe_3O_4) at C(carbon black) ≥ CaO (mole ratio). There was broad agreement between the experimental results and the thermodynamic predictions.

The low temperature (≤ 1123 K) metallisation of Cu, Co and Fe was achieved via lime roast – reduction process. The mineral sulphide concentrates were roasted in air (21 % O_2), in the presence of CaO by following the equilibrium: MS + CaO + $2O_2$ = MO + $CaSO_4$, in the temperature range of 773 K – 923 K. The lime roast calcine was

reduced at 1073 K and 1123 K with; (i) carbon black for the selective metallisation of Cu and for retaining the $CaSO_4$ phase and (ii) activated charcoal for the complete metallisation of Cu, Co and Fe by following the equilibrium: $MO + CaSO_4 + 4C = M + CaS + 4CO$ (g).

Because copper smelting slag is the major source of Cu and Co, the low temperature recovery of Cu and Co from a 40wt.%SiO_2-(30wt.%Fe,6wt.%Al)$_2O_3$-10wt%CaO-7wt%CuO-7wt%CoO slag over a temperature range of 1173 K to 1323 K, was investigated via; (i) carbothermic reduction of metal oxides according to $MO + C = M + CO$(g) reaction and (ii) sulphidisation in the presence of $CaSO_4$ and C according to $MO + CaSO_4 + SiO_2 + 4C = MS + CaSiO_3 + 4CO$ reaction. In the direct reduction of oxides, the recovery of metallic phase was below 90 % at 1323 K. Nearly all Cu, Co and Fe converted to metal sulphides or matte phase during sulphidisation of the slag. The reaction kinetics for the sulphidisation of slag in the presence of $CaSO_4$ and C were determined. The sulphidised slag was reduced in the presence of CaO and C to obtain metallic/alloy, CaS and CaO rich slag phases. The metallic particles produced via sulphidisation – carbothermic reduction route were larger than those produced by direct reduction of the slag. The sulphidisation of slag in the presence of CaS via $MO + CaS + SiO_2 = MS + CaSiO_3$ reaction, was also investigated.

Table of contents

List of Figures

List of Tables

Notations and abbreviation

atm	atmosphere
At.	atomic
Conc.	concentrates
BSE	backscattered electron
Cu-S	copper sulphide (Cu_2S, $Cu_{1.8}S$)
EDX	energy dispersive X-ray
Fe-O	iron oxide (FeO or Fe_3O_4)
K	rate constant
M	metallic phase
MO	metal oxide
MS	metal sulphide
PAD	predomince area diagram
Q	activation energy
TGA	thermogravimetric analysis
SE	scanning electron
SEM	scanning electron microscopy
t	time
T	temperature
XRD	X-ray powder diffraction
XRF	X-ray florescence
Wt.	weight
Wt. %	weight percentage

1.0 Introduction

Copper is widely used in construction and electric cables [1]. Cobalt and its alloys have important applications in the areas of energy storage in lithium cobalt oxide batteries, high temperature alloys [2] and cobalt alloy based magnetic materials [3, 4] for transduction devices [5, 6]. The detailed applications of copper and cobalt and their respective alloys are discussed in references [7] and [5, 6], respectively.

A majority of copper and cobalt are not found in the pure or metallic state but in the form of complex sulphide and/or oxide minerals [6, 8]. The copper and cobalt mineral sulphides are associated with iron in the form of chalcopyrite ($CuFeS_2$), bornite (Cu_5FeS_4) and cobaltian pyrite $(Fe,Co)S_2$ [9] minerals. The concentration of the Cu-Co-Fe mineral sulphides is very low in the ore bodies, due to the presence of impurities or gangue minerals. The total amount of copper in the ore bodies rarely exceeds 5 wt. % [8]. The extraction of Cu and Co from the ores containing high gangue content is uneconomical because of; (i) handling costs and (ii) high energy requirement as more heat is spent in melting of the gangue minerals, in the case of the high temperature extraction process [8, 10]. As a result, the Cu and Co mineral ores from the mine are beneficiated prior to the extraction process [8, 10-12]. Beneficiation is aimed at separating the mineral sulphides (Cu and Co mineral sulphides) from the gangue minerals.

Even though there are many beneficiation techniques through which mineral sulphides may be concentrated, the copper and cobalt mineral sulphides are normally concentrated via froth flotation process [11]. The iron mineral sulphides (FeS_2 and FeS) float with the copper and cobalt mineral sulphides during the froth flotation process. Consequently, the Cu-Co mineral sulphide concentrates may contain more iron than copper and cobalt. The froth flotation mineral sulphide concentrates also contain gangue minerals as the separation of mineral sulphides from the gangue minerals is never 100 % efficient [13]. The major consitituents of the froth flotation concentrates from the Copperbelt province in Zambia are presented in table 1.1.

Table 1.1 – Major constituents of the froth flotation concentrates from the Copperbelt province in Zambia

Mineral	Chemical formula
Chalcocite	Cu_2S
Chalcopyrite	$CuFeS_2$
Bornite	Cu_5FeS_4
Carrolite	$CuCo_2S_4$
Cobaltian pyrite	$(Fe,Co)S_2$
Pyrite	FeS_2
Quartz	SiO_2
Dolomite	$CaMg(CO_3)_2$
K-feldspar	$KAlSi_3O_8$

1.1 Conventional treatment of Cu-Co mineral sulphide concentrates

The common methods of recovering Cu and Co from their respective mineral sulphides are pyrometallurgical, hydrometallurgical or a combination of pyrometallurgical and hydrometallurgical processes [11]. By comparison, nearly 90 % of the copper originating from the sulphide minerals is recovered via pyrometallurgical or smelting process [8, 11].

1.1.1 Pyrometallurgical or smelting process

In the pyrometallurgical recovery of copper from the mineral sulphides, the mineral sulphide concentrates are smelted in a temperature range of 1473 K – 1673 K [14, 15]. Iron and sulphur are removed from the mineral sulphides (Cu_2S, $CuFeS_2$ and Cu_5FeS_4 etc.) via selective oxidation. In the conventional copper smelting process, the production of copper or removal of iron and sulphur takes place via copper matte smelting [16] and converting processes [11, 12]. In the copper matte smelting process, iron and sulphur are partially oxidised according to equation 1.1a and, a copper rich sulphide or matte phase ($Cu_2S.FeS$) is produced. The partial pressure of the O_2 gas is carefully controlled during copper smelting process, to avoid oxidation of FeO to Fe_3O_4. The Fe_3O_4 phase is undesirable because it is solid at the copper smelting temperature as it has a melting temperature of 1871 K. A fluxing agent (SiO_2) may be added for

lowering the activity of FeO via formation of $FeSiO_3$ liquid phase (equation 1.1b), depending on the composition of the feed concentrates. The gangue minerals from the mineral sulphide concentrates dissolve in the $FeSiO_3$ liquid phase to form the molten slag phase. The molten matte and slag phases separate out during smelting, due to phase immiscibility. The matte phase being heavier than the slag phase sinks to the bottom of the furnace. The basic principle of the copper matte smelting process is that; (i) the oxidised metallic phases (CoO, Cu_2O, CuO) dissolve into the molten slag phase as they are less denser and soluble into the silicate slag phase and (ii) metallic and metal sulphide phase which might include the precious metals dissolve into the molten matte phase.

$$2CuFeS_2(l) + 2.5O_2(g) = Cu_2S \cdot FeS(l) + FeO(l) + 2SO_2(g) \quad 1.1a$$

$$FeO(l,s) + SiO_2(s) = FeSiO_3(l) \quad 1.1b$$

$$Cu_2S \cdot FeS(l) + O_2(g) = Cu_2S(l) + FeO(l) + SO_2(g) \quad 1.1c$$

$$Cu_2S(l) + O_2(g) = 2Cu(l) + SO_2(g) \quad 1.1d$$

The matte phase from the smelting process has 10 wt.% - 79 wt. % Cu and maybe classified as low, medium and high grade copper matte as shown in table 1.2 [15]. The high grade copper matte is also known as white metal as its composition is close to Cu_2S [11, 15].

Table 1.2 - Typical analysis of copper smelting matte in weight percent (wt. %)

	Range of composition for Cu, Fe and S		
	Cu	*Fe*	*S*
High grade matte	45 - 79	1 - 15	20 - 22
Medium grade matte	30 - 45	25 - 37	24 - 27
Low grade matte	10 - 30	37 - 50	22 - 24

Iron and sulphur in the mate phase are removed in the converting process [11]. The converting of copper matte occurs in two stages:

(i) Slag forming stage in which iron and part of sulphur are removed via equation 1.1c. Silica (SiO_2) is added as a fluxing agent during the slag forming stage to react with, FeO and form the molten $FeSiO_3$ phase as shown in equation 1.1b. The slag forming stage is completed when the iron content in the copper matte is below 1wt. % [11]. The converting process is generally more oxidizing than the copper matte smelting process such that any cobalt in the matte phase and part of copper are oxidized and subsequently lost into the slag phase.

(ii) Copper making stage, involves the oxidation of the remaining sulphur to produce blister copper and the main reaction is shown in equation 1.1d.

The production of Cu via copper matte smelting - converting route has some environmental issues due to the release of SO_2 gas (see equations 1.1a, 1.1c and 1.1d). The SO_2 gas released in reactions 1.1a, 1.1c and 1.1d, which is generic to both the smelting and converting processes, is only available in dilute form and is, therefore, uneconomical for sulphuric acid manufacture. Lack of control over SO_2 gas emission may seriously endanger the lives of people, animals, and the eco-system through acid rain.

1.1.1.1 Direct-to-blister copper smelting

The direct-to-blister copper smelting process combines the copper smelting and converting processes, i.e. the copper sulphide concentrates are reacted with enriched air or oxygen gas to give blister copper and slag phases, in a single process. The major reactions that occur in the direct-to-blister copper smelting process are shown in equations 1.2a – 1.2c. The off-gas can be as high as 30% SO_2 and hence sulphur can be fixed as sulphuric acid or elemental sulphur. In other words, the direct-to-blister copper smelting process is environmentally friendly, because nearly all sulphur can be converted to sulphuric acid or elemental sulphur.

$$Cu_2S\ (l) + O_2\ (g) = 2Cu(l) + SO_2(g) \qquad 1.2a$$

$$CuFeS_2(l) + 2.5O_2\ (l) = Cu(l) + FeO(s,l) + 2SO_2(g) \qquad 1.2b$$

$$Cu_2S.FeS.CoS(l) + 4O_2(g) = Cu(l) + FeO(s,l) + CoO(l) + 3SO_2(g) \qquad 1.2c$$

However, the direct-to-blister copper smelting process is economically viable only with feed concentrates having high ratios of Cu/S and Cu/Fe, because of oxidation of copper at lower ratios of Cu/S and Cu/Fe. As state above, most copper sulphide concentrates have low ratios of Cu/S and Cu/Fe, due to the presence of $CuFeS_2$ and FeS_2 minerals and hence different types of feed concentrates are blended prior to the direct-to-blister copper smelting process. For example, the $CuFeS_2$ and FeS_2 mineral rich concentrates may be blended with the Cu_2S mineral rich concentrates, for increasing the ratios of Cu/Fe and Cu/S.

At Nchanga smelter in Zambia, the copper concentrates containing about 0.4 wt. % Co, 35 wt. % Cu, 25 wt. % Fe and 15 wt.% S, are smelted to blister copper. However, all cobalt and nearly 20 wt. % of the copper [17, 18] from the mineral sulphide concentrates, are lost out into the slag phase via oxidation, owing to the strong oxidising conditions. The molten slag is reduced with coke for reduction of Cu and Co oxide phase. The reduction of the slag phase is carried out in two separate electric furnaces. The first furnace is known as the slag cleaning furnace (SCF) and is operated under mildly reducing condition to allow for the selective reduction or recovery of copper. Therefore, blister copper and slag phases are produced from the slag cleaning furnace. The slag from the slag cleaning furnace contains up to 5 wt.% Cu and 0.8 wt. % Co and, it is treated under more reducing conditions, in the cobalt recovery furnace (CRF) to produce the Cu-Co-Fe alloy. The Cu-Co-Fe alloy has a high liquidus temperature, due to the high content of Fe and hence, fresh sulphide concentrates are injected into the molten bath to produce sulphur containing Cu-Co-Fe alloy phase. The sulphur containing Cu-Co-Fe alloy phase has up to 15 wt. % sulphur and is processed hydrometallurgically, for the recovery of copper and cobalt metals. The simplified flow sheet for the Nchanga smelter in Zambia is shown in figure 1.1.

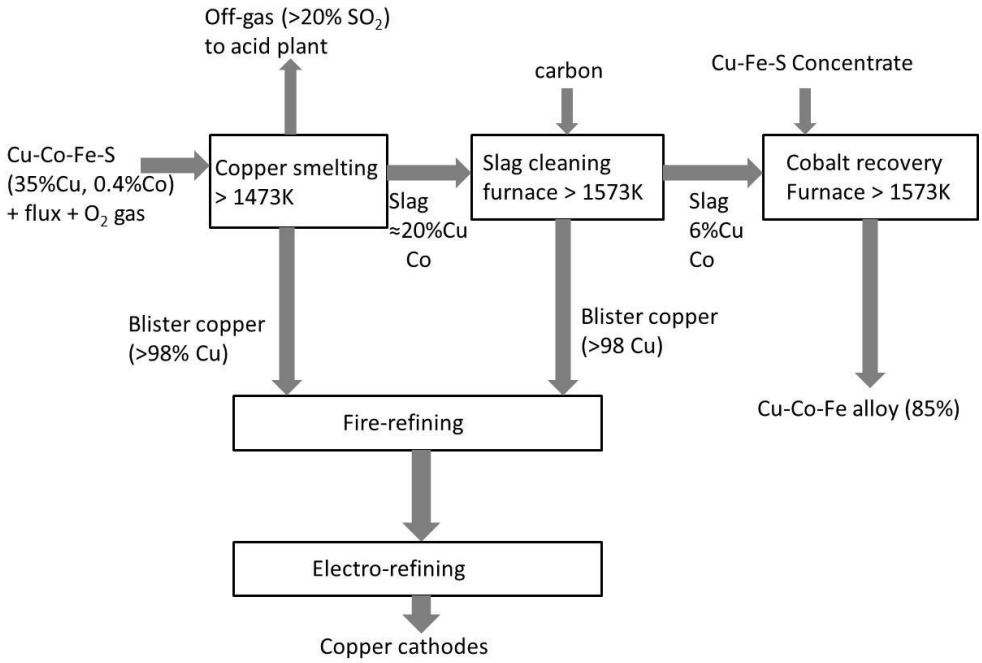

Figure 1.1 - Simplified process flow sheet at the Nchanga smelter plant in Zambia

Although the direct-to-blister copper smelting process is environmentally friendly, there are a number of drawbacks for treating the Cu-Co-Fe mineral sulphide concentrates, as:

i. Cobalt and part of copper are lost into the slag phase, thereby requiring two additional electric furnaces (slag cleaning and cobalt recovery furnaces), and both operating above 1573 K (see figure 1.1).
ii. The Cu-Co-Fe alloy phase from the second electric furnace has low purity as it contains up to 15 wt. % sulphur.
iii. There is need for strict control of the ratios of Cu/S and Cu/Fe in the feed concentrates and hence the process is not possible for certain type of mineral sulphide concentrates.

1.1.1.2 Loss of Cu and Co into the slag

Even though various studies have revealed that the copper and cobalt from the copper smelting and converting slag, exists in the metallic, metal sulphide (matte) and metal oxide forms, a majority are in the oxide form [19, 20]. This shows that oxidation is the main cause for the loss of copper and cobalt, during the conventional smelting and converting processes. By comparison, only part of copper is oxidised but nearly all cobalt is oxidised during the conventional copper smelting and converting processes

[21]. The high loss of cobalt into the slag phase is because of the higher stability of the cobalt oxide phase. The higher stability of the Co-O phase and the acidic nature of the copper smelting slag, mean that the Co-O reacts with SiO_2 to form cobalt silicate (figure 1.2) and dissolves in the slag phase. The thermodynamic prediction in figure 1.2 shows that Cu and Co can be recovered during smelting process at $\log_{10}PO_2(atm) < -10.8$. However, conventional copper smelting processes are carried out at $-5 > \log_{10}PO_2(atm) < -6.5$ such that Co is oxidised and lost into the slag phase.

The Cu and Co content in the Nkana slag dump in Zambia can be as high as 3.9 wt. % [20] and 2.6 wt. % [22], respectively, which makes the metal extraction uneconomical as metallic cobalt has to be recovered from the slag phase. By comparing the spot metal price for cobalt and copper from London Metal Exchange in June 2014 (>$30,000 per tonne for cobalt compared with the $6700 per tonne for copper), the 2.6 wt. % cobalt in slag is equivalent to 11.7 wt. % copper in the slag. In fact, the 2.6 wt. % cobalt in slag is actually more than the physical value found in natural minerals. The price differential compels that the cobalt recovery from slag is essential, which is an energy inefficient process because it requires temperatures higher than 1773 K to re-melt the Cu-Co slag, [22, 23].

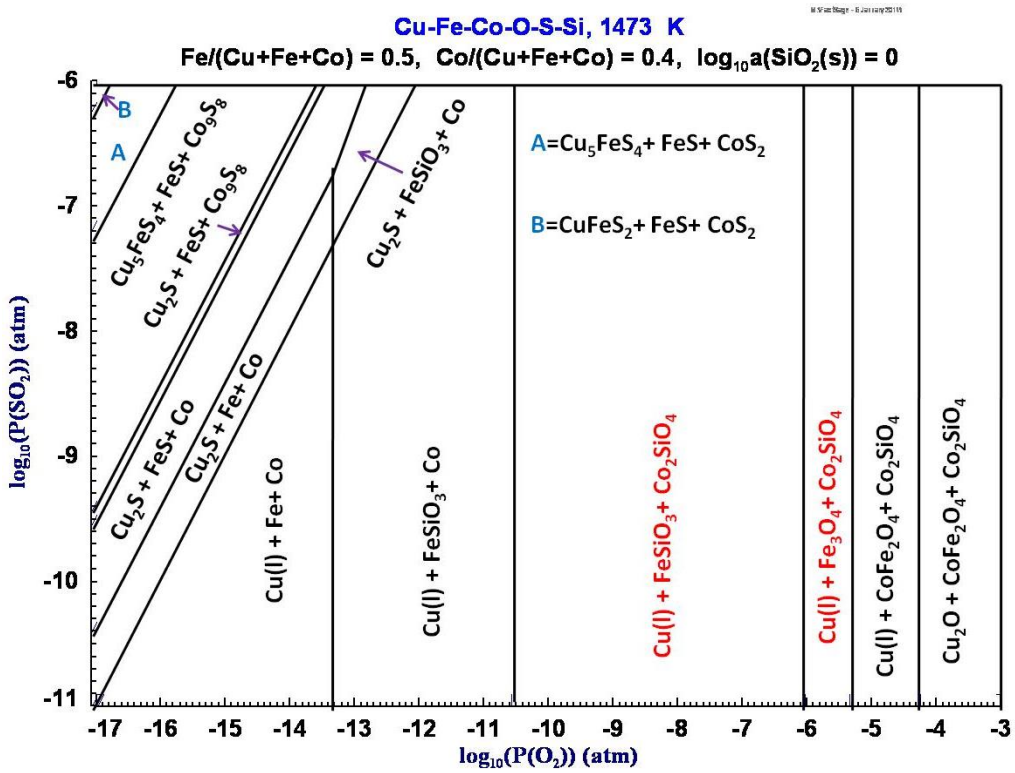

Figure 1.2 –The Co-Cu-S-O predominance area diagram at 1473 K, computed from the FactSage software 6.1 [24]

1.1.1.3 Recovery of Cu and Co from slag

Leaching – electro-winning process is the method by which metallic cobalt and copper may be recovered from there oxides [11]. However, the cobalt and copper oxides in the slag, are mainly dissolved in the silicate and ferrite phases [15, 25]. The dissolved copper and cobalt oxides cannot be selectively leached out, irrespective of the lixiviant employed, unless the silicates and ferrites structures are destroyed or leached out as well. Furthermore, iron is more abundant and is present in much higher concentration than copper and cobalt. The worst problem is that the partially leached silica significantly interferes with filtration [25, 26]. The two problems are the major challenges to the hydrometallurgical extraction of copper and cobalt from slag, which could otherwise be the easiest.

Chambishi Metals PLC in Zambia treats the Nkana slag dump. The slag is initially crushed, ground to fine particles (< 100 μm). The ground slag is mixed with malachite ($Cu_2CO_3(OH)_2$), pyrite (FeS_2) and carbon and, smelted at about 1823 K to produce the molten Cu-Co-Fe alloy and slag phases. The temperature of the molten Cu-Fe-Co alloy is raised to 1873 K and the alloy is atomized by subjecting it to the high pressure water stream to produce fine particles [22]. Normal leaching of this alloy is a problem because iron is equally leached out. As a result, the atomized alloy particulates are leached under high temperature and pressure in an autoclave, to form copper and cobalt sulphates and, iron oxide / hydroxide precipitates. The summary of the process flow sheet at Chambishi Metals plant is given in figure 1.3. The energy and operation costs for smelting the slag at 1823 K and autoclave leaching of the Cu-Fe-Co alloy are generally high. The cost of energy consumption is continuously rising which can have an unfavourable effect on the recovery of cobalt by making it economically unviable.

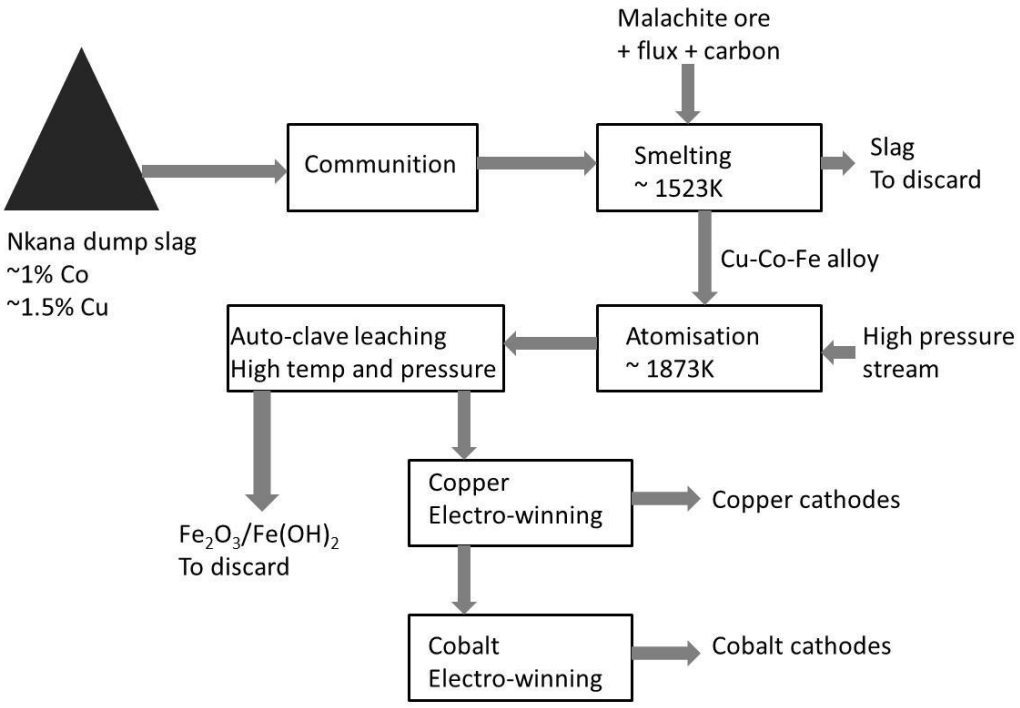

Figure 1.3 – Simplified process flow sheet for treating Nkana dump slag at the Chambishi Metals PLC, modified from Barnes and Jones [27]

1.1.1 Pyro-hydrometallurgical processes

The copper-cobalt sulphide concentrates are sometimes treated through pyro-hydrometallurical (roast - leach) route, because of the high losses of cobalt that occurs during the conventional copper smelting and converting processes [21]. Roasting is carried out prior to hydrometallurgical processing, to convert the mineral sulphides into acid soluble compounds (i.e. metal oxides and/or sulphates). In essence, oxygen gas is blown into the feed material and the overall reactions that occur between the mineral sulphides and oxygen gas are shown in reactions 1.3a - 1.3d. There is a great need for controlling reaction temperature and time so as to avoid the formation of copper and cobalt ferrites. Copper and cobalt ferrites are undesirable in the roast calcine as they can only be leached out in very strong sulphuric acid. Therefore, a good roast calcine should have metal oxides and sulphates and, this is favoured by low roasting temperature (below 973 K) [28]. However, the reactions are very slow at low roasting temperature such that dilute SO_2 off-gas is generated. The production of dilute SO_2 off-gas is unattractive because SO_2 gas cannot be economically converted into sulphuric acid or

elemental sulphur, which are the common methods of preventing the emission of SO_2 gas into the environment [10, 11].

$$CuCo_2S_4 + 5O_2 = CuO + CoO + 4SO_2 \quad 1.3a$$

$$CuCo_2S_4 + 7O_2 = CuSO_4 + 2CoSO_4 + SO_2 \quad 1.3b$$

$$CuFeS_2 + 3.25O_2(g) = CuO + 0.5Fe_2O_3 + 2SO_2(g) \quad 1.3c$$

$$CuFeS_2 + 3.75O_2(g) = CuSO_4 + 0.5Fe_2O_3 + SO_2(g) \quad 1.3d$$

The Cu-Co ores from the Nkana mine in Zambia are treated by bulk and segregation flotation processes to produce streams of Cu and Cu-Co concentrates as shown in figure 1.4. The Cu-Co concentrates have a typical assay grade of 10 wt. % Cu and 2 wt. % Co and 20 wt. % S and are known as the Cu-Co sulphide concentrate because of the value of cobalt compared to copper, in the concentrates. Conventional smelting of such concentrates (low grade concentrates) generates high tonnage of slag per ton of the metallic phase and hence metal loss via entrainment tends to be high [11]. The worst problem is that nearly all cobalt in the mineral sulphide concentrates is oxidised and dissolve in the slag phase during the smelting process. As a result, the Nkana Cu-Co concentrates are treated via roast – leach – electro-winning process. The mineral concentrates are roasted at temperatures below 973 K, to produce copper and cobalt oxides / sulphates. The roast calcine is leached with sulphuric acid to dissolve Cu and Co. The leach solution is separated from the leach residue and copper is recovered from the purified leach solution via electro-winning process. Cobalt is precipitated as $Co(OH)_2$ from the copper tank house spent electrolyte at a pH of 6.5 – 7 [29] and then dissolved in sulphuric acid. Cobalt is then recovered from the solution via electro-winning process. The simplified process flow sheet is shown in figure 1.4. The disadvantages of the roast - leach - electro-winning process are:

i. A dilute SO_2 off-gas is generated from the roaster plant and hence the fixation of sulphur via sulphuric acid or elemental sulphur production, is uneconomical. The dilute SO_2 gas is commonly vented into the atmosphere at Nkana Cu-Co roaster, resulting into serious environmental pollution.

ii. A significant amount of lime (CaO) is consumed in the prepitation of $Co(OH)_2$. CaO converts to $CaSO_4$ but the later is not utilised at the moment [29].

iii. High loss of Co during the precipitation process [29].

iv. Silver and precious metals that are normally present in the mineral sulphide concentrates [10] cannot be recovered because they are not soluble in sulphuric acid.

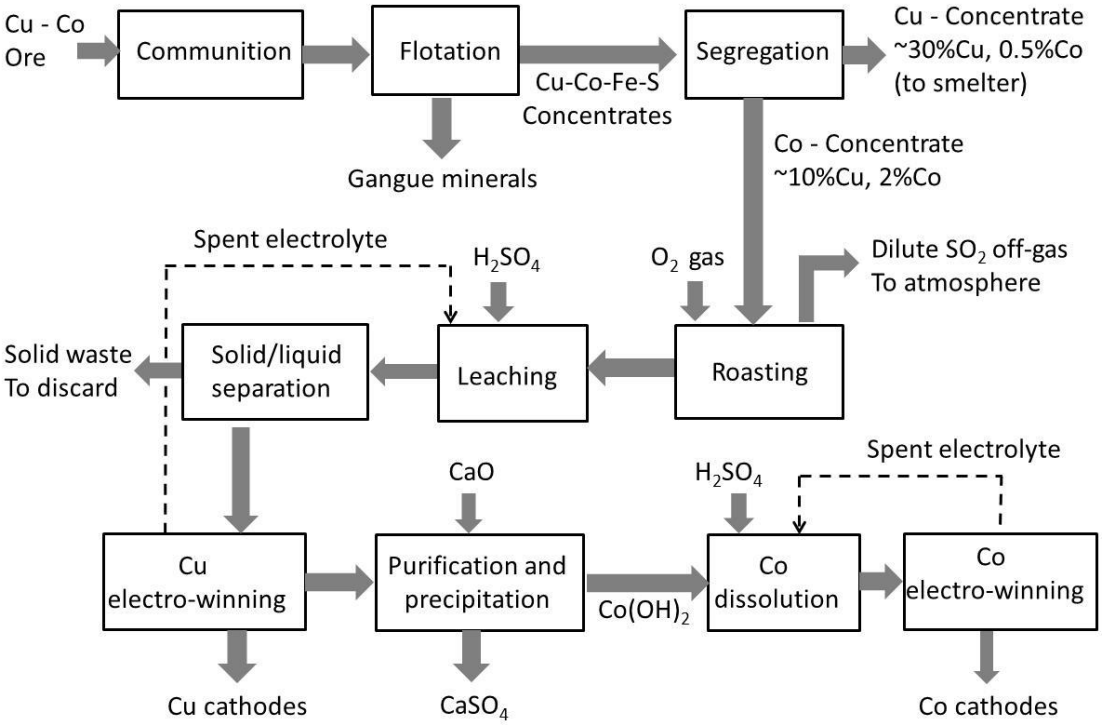

Figure 1.4 - Simplified process flow sheet for treating Cu-Co ore at Nkana plant, modified from Mututubanya [29]

1.2 Carbothermic reduction of mineral sulphides in the presence of CaO

Calcium forms one of the stable sulphides and is readily available in the form of calcium oxide (CaO) [10]. However, calcium oxide is more stable than calcium sulphide [10], and hence the Gibbs energy change for reaction 1.4a is positive at all temperatures. On the other hand, reaction 1.4a can be driven in the forward direction in the presence of carbon (equation 1.4b), because of the entropy increase, since 2 moles of CO gas are produced per mole of sulphur gas.

$$2CaO + S_2 = 2CaS + O_2 \qquad 1.4a$$

$$2CaO + S_2 + 2C = 2CaS + 2CO \quad \text{1.4b}$$

Based on reaction 1.4b, sulphur can be removed from the metal sulphides in the presence of CaO to yield metallic, CaS and CO gas phases , as shown in equation 1.5a [10, 30, 31]. The carbothermic reduction of the mineral sulphides in the presence of lime has been carried out by a number of authors [30, 32-38]. The mechanism leading to the reduction of mineral sulphides has been proposed by Jha et al., [30, 35, 38]. It occurs via two stages; (i) ion exchange reaction between the mineral or metal sulphides (MS) and CaO as shown in equation 1.5b, (ii) reduction of the metal oxide (MO) phase by carbon and intermediate gas (CO) as shown in reactions 1.5c and 1.5d. The CO_2 gas from equation 1.5d can react with C to generate CO gas according to equation 1.5e.

$$MS(s,l) + CaO(s) + C = MO(s,l) + CaS(s) + CO(g) \quad \text{1.5a}$$

$$MS(s,l) + CaO(s) = MO(s,l) + CaS(s) \quad \text{1.5b}$$

$$MO(s,l) + C(s) = M(s,l) + CO(g) \quad \text{1.5c}$$

$$MO(s,l) + CO(s) = M(s,l) + CO_2(g) \quad \text{1.5d}$$

$$CO_2(g) + C(s) = 2\,CO(g) \quad \text{1.5e}$$

Where MS is the metal sulphide phase, MO is the metal oxide phase and M is the metallic phase

For the sulphides of copper (CuS, Cu_2S), cobalt (CoS) and iron (FeS), the computed values of equilibrium constant are plotted as a function of temperature in figure 1.5 from which it is apparent that the logarithmic values of equilibrium constants ($\log_{10}K$) are greater than zero above 825 K for CoS, Cu_2S, and FeS. Since covellite (CuS) decomposes to Cu_2S above 773 K, the significant conclusion from the equilibrium calculations is that thermodynamically, the reduction reactions defined by equation 1.5a, for CoS, FeS, and Cu_2S are feasible above 825 K.

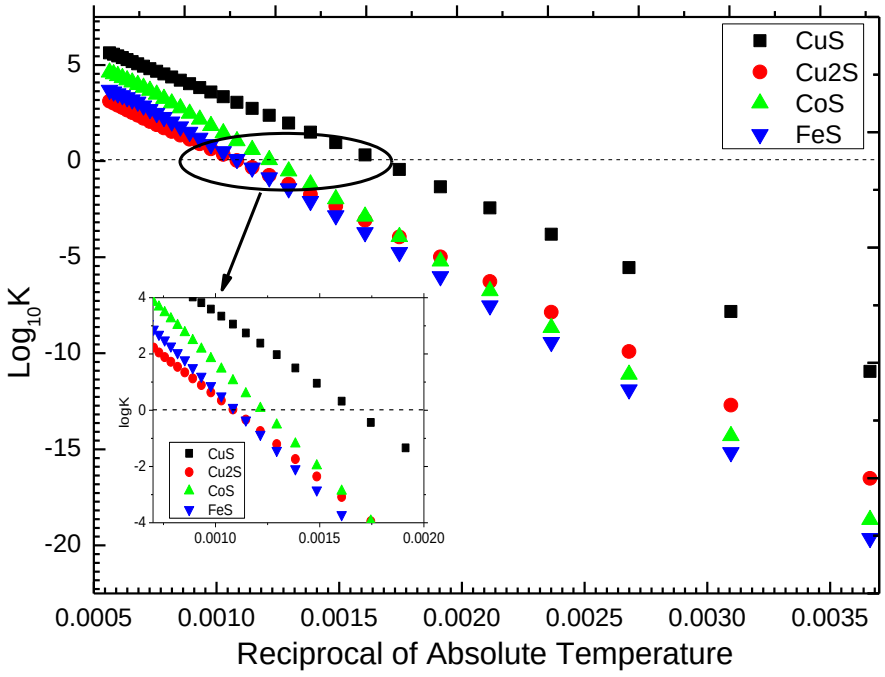

Figure 1.5 - A plot of logarithmic equilibrium constant ($log_{10}K$) against the reciprocal of absolute temperature (T, K) for FeS, Cu_2S, CuS, and CoS, per mole of CO gas [39] via MS + CaO + C = M + CaS + CO(g) reaction

It is clear from figure 1.5 that metallization of copper, cobalt and iron will occur below the melting points of pure metallic phases by reducing the mineral sulphide concentrates in the presence of lime and carbon. In naturally occurring complex sulphide minerals consisting of Cu_2S, Co_xS_y and FeS_x, the MS - CaO exchange reaction via equation 1.5b may occur and lead to reduction of metal oxides to metals, which may then form one or more alloy phases, due to extensive solid solubility of the constituent metallic elements [5, 6, 8]. The thermodynamic condition for alloy formation will further force the equilibrium in equation 1.5a in the forward direction, by lowering the chemical potential of the constituent metallic elements. Consequently, the equilibrium partial pressure of CO gas will increase, with respect to the equilibrium condition for the pure metal as a standard state. The carbothermic reduction of copper and cobalt from the mineral sulphide concentrates in the presence of lime and carbon offers several advantages:

i. Lime is cheap and readily available [10, 31, 40].

ii. It is possible to completely fix sulphur as calcium sulphide during metal production (see equation 1.5a) and hence there is no environmental pollution with the sulphurous gas.

iii. The process can be carried out below the melting points of pure metallic phase e.g. 1273 K, without the need of melting the gangue minerals in the mineral sulphide concentrates which requires additional energy.

iv. Metallization is independent of the ratios of Cu/Fe and Cu/S in the mineral sulphide concentrates whereas these ratios should be high in the direct-to-blister copper smelting process.

v. It is possible to achieve zero waste process because:
   a. There is no oxidation of the metallic values as reactions occur under reducing conditions.
   b. CaO can be regenerated from CaS.
   c. Carbon monoxide rich gas can be re-used to supply part of the energy into the process.

1.3 Hypothesis of the study

Although several studies have been carried out on carbothermic reduction of copper sulphides, iron sulphide and Cu-Fe sulphide, the carbothermic reduction Cu-Co-Fe mineral sulphides concentrates, particularly with more than 30 wt. % gangue minerals, have never been carried out. The pyrometallurgical treatment of Cu-Co-Fe mineral sulphide concentrates is a major problem in the extractive metallurgical industry because of oxidation of cobalt and iron. The oxidation of cobalt and iron increases the amount of waste generation per tonne of copper produced. Furthermore, the separation of metallic values from the carbothermic reduction of the mineral sulphides has been least studied. The carbothermic reduction of Cu-Co-Fe mineral sulphides in the presence of lime was therefore carried out, with a view of producing the metallic/alloy phases of Cu, Co and Fe.

1.4 Objectives of the study

- To obtain metallic / alloy phases of Cu, Co and Fe via carbothermic reduction of the mineral sulphide concentrates in the presence of CaO, under argon atmosphere.
- To determine the optimal operating conditions of the carbothermic reduction of the mineral sulphide concentrates in the presence of CaO, in terms of temperature and mole ratios of CaO and C.

- To investigate the separation of metallic /alloy phases of Cu, Co and Fe from the reduced samples.
- Investigate the low temperature preferential reduction of copper via lime-roast carbothermic reduction process.
- To utilise CaS or regenerate CaO from CaS.
- To investigate the low temperature recovery of copper and cobalt from Cu-Co silicate slag.

1.5 Structure of the Thesis

The thesis has 9 chapters:

- Chaper 2: presents the basic principles of metal extraction from the mineral sulphides. The previous studies on reduction of mineral sulphides in the presence of CaO are discussed. The thermal decomposition of mineral sulphides under inert atmosphere, equilibrium phase diagrams and solution thermodynamics are also discussed.
- Chapter 3: provides details of the as-received samples, experimental details and characterization techniques.
- Chapter 4: looks at the characterization (XRD, XRF and SEM analyses) of the as-received mineral sulphide concentrates.
- Chapter 5: The heat treatment of the mineral sulphide concentrates in the presence and absence of CaO, under argon atmosphere are analysed. The results are compared with the predominance area diagrams.
- Chapter 6: Covers the carbothermic reduction of the mineral sulphide concentrates in the presence of CaO. The reaction mechanism and kinetics of the carbothernic reduction of mineral sulphide concentrates in the presence of CaO, are discussed. The separation of the metallic/alloy phases from the reduced samples and the regeneration of CaO from CaS are also discussed. The energy analysis for the carbothermic reduction of the mineral sulphides in the presence of CaO is analyzed using HSC software 5.1 [39] and compared with the conventional processes.
- Chapter 7: roasting of the mineral sulphides concentrates in the presence of CaO as a way of fixing sulphur as $CaSO_4$. The roast calcine is reduced at $T \leq 1123$ K with; (i) carbon black for the selective metallization of Cu and (ii) activated charcoal for the complete metallization of Cu, Co and Fe. The overall energy

requirement for the lime roast – reduction processes is estimated with HSC software 5.1 [39].

- Chapter 8: the Cu-Co slag is reduced in the presence of carbon black and activated charcoal and, the reaction kinetics are determined. The Cu-Co slag is sulphidised in the presence of $CaSO_4$ and C. The sulphidised slag is reduced in the presence of CaO and carbon to obtain metallic, CaS and slag phases. The Cu-Co slag is also sulphidised in the presence of CaS
- Chapter 9: Gives the conclusions drawn from the experimental work, future work and major achievements of the project.

2.0 Literature review

2.1 Principles of metal sulphide reduction

Mineral sulphides only lose part of sulphur when heated at elevated temperatures, under inert atmosphere as shown in equations 2.1a - 2.1c. Therefore, the extraction of metallic phase via thermal decomposition of minerals sulphides is not practically possible.

$$2CuS \Leftrightarrow Cu_2S + 0.5S_2 \quad \text{2.1a}$$

$$5CuFeS_2 \Leftrightarrow Cu_5FeS_4 + 4FeS + S_2 \quad \text{2.1b}$$

$$FeS_2 \Leftrightarrow FeS + 0.5S_2 \quad \text{2.1c}$$

However, all sulphur can be removed as SO_2 gas, when the mineral sulphides are heated in the O_2 gas atmosphere. As a result, metals can be extracted from the mineral sulphides via oxidation of sulphur, provided that the oxidation of the metallic phase does not occur. The oxidation of the metallic phase cannot occur, when the SO_2 gas is more stable than the metal oxide phase. The Gibbs energy changes for the oxidation of Cu, Co, Fe, and S_2 gas are compared in figure 2.1, per mole of O_2 gas. It is evident from figure 2.1 that CoO and FeO are more stable than the SO_2 gas but, Cu_2O is less stable than the SO_2 gas. The thermodynamic prediction in figure 2.1 explains as to why; (i) Cu is extracted from the mineral sulphides via smelting process (see equations 1.1a – 1.1d) and (ii) Co and Fe are oxidised during conventional smelting of Cu-Co-Fe-S concentrates.

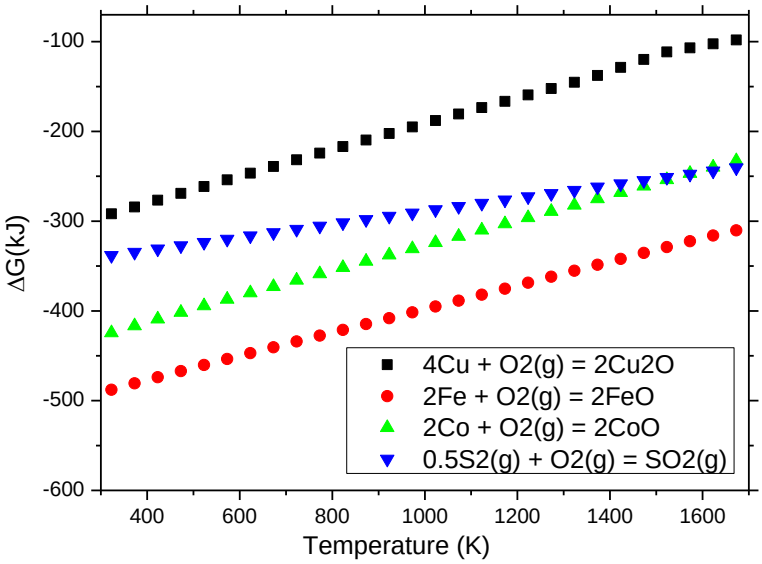

Figure 2.1 – The Gibbs energy change versus absolute temperature plots for the oxidation of Cu, Co, Fe and S_2 gas per mole of O_2 gas

Based on the thermodynamic prediction in figures 1.2 and 2.1, the simultaneous recovery of Cu, Co and Fe from the sulphide minerals requires: (i) reducing condition so as to avoid oxidation of the metallic/alloy phases and (ii) sulphur absorber for removing sulphur from the mineral sulphides, as the metal sulphides cannot be reduced to metallic state by any of the reductants such as C, CO gas and H gas. The equilibrium constant in equations 2.2a – 2.2c is very small, for all metal sulphides.

$$2MS + C = 2M + CS_2 \qquad 2.2a$$

$$MS + H_2(g) = M + H_2S(g) \qquad 2.2b$$

$$MS + CO(g) = M + COS(g) \qquad 2.2c$$

2.2 Carbothermic reduction of mineral sulphides in the presence of basic oxide

Even though the direct carbothermic reduction of the metal sulphides (equation 2.2a) is not practically possible, the reduction can be achieved in the presence of sulphur absorber [41]. By comparison, the sulphides of Ca, Na and Mg are more stable than the metal sulphides (Cu_2S, FeS and CoS) as shown in figure 2.2. Although CaS, MgS and Na_2S are more stable than metal sulphides, CaS is the most stable. Based on the

thermodynamic prediction in figure 2.2, Ca may be employed as a sulphur absorber. However, it would be uneconomical to use Ca because, Ca is mainly available in the form of CaO [10]. The formation of CaS or reduction of metal sulphides in the presence of CaO can proceed via two mechanisms:

i. Carbothermic reduction of CaO to form Ca and CO(g) (equation 2.3a), followed by the reaction between Ca and metal sulphide (MS) (equation 2.3b). Nonetheless, this mechanism may not occur because the Gibbs energy change for reaction 2.3a is highly positive even at 2000 K [39].

$$CaO(s) + C(s) = Ca(s,l) + CO(g) \qquad 2.3a$$

$$MS(s,l) + Ca(s,l) = 2M(s,l) + CaS(s) \qquad 2.3b$$

ii. Ion exchange reaction between MS and CaO to form MO and CaS (see equation 1.5b). Several authors [38, 42-45] have reported the presence of MOs in the partially reduced samples which implies that metallisation proceed via formation of metal oxide as an intermediate phase.

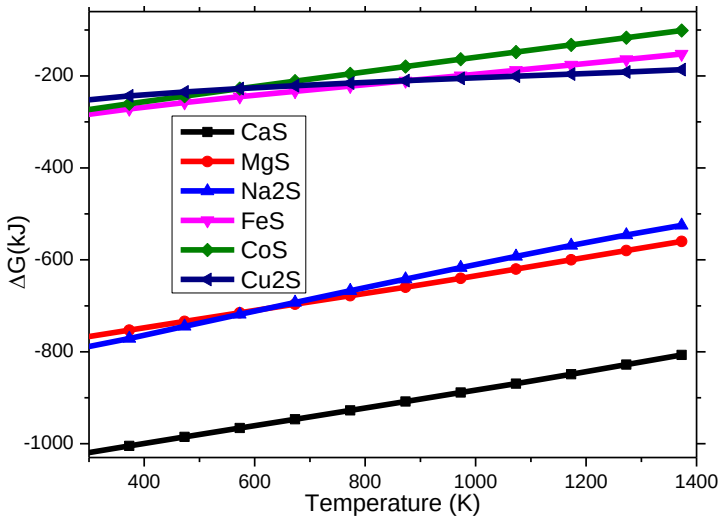

Figure 2.2 – Computed Gibbs energy change against temperature for the formation of metal sulphides via 2M + S_2(g) = 2MS equation, data obtained from HSC 5.1 software database [39]

2.2.1 Thermodynamic consideration

The ability of the mineral sulphide to undergo the ion exchange reaction depends on the relative stability of the metal oxide compared to its sulphide. The ionic radius of O^{2-} (1.4Å) [46] is smaller than the S^{2-} (1.84 Å) ionic radius [46] and hence, there is an increase in the force of attraction when the oxide ion replaces the sulphide ion as shown in equation 2.4 [14].

$$E_{lattice} = \frac{-AZ_m Z_O e^2}{r_d} + \frac{B}{r_d} \qquad 2.4$$

Where A is the Madelung constant, r_d is the interionic distance, Z_m and Z_o are the cationic and anionic charges and e is the electric charge (1.6022×10^{-19} C). The second term is the repulsive interactions between cation and anion cores.

The effect of replacement is more noticeable as the cation radius decreases [14]. As such, the mineral sulphide with the smaller cationic radius may easily undergo exchange reaction compared to the mineral sulphide with a larger ionic radius. The ionic radius for Cu^{1+}, Co^{2+} and Fe^{2+} are 0.96 Å [46], 0.79 Å (octahedral) and 0.74 Å [46] respectively so that the stability decreases in the order of FeO, CoO and Cu_2O.

The plots of the Gibbs energy change against temperature for the ion exchange reaction between CaO and Cu_2S, CoS and FeS are shown in figure 2.3. The Gibbs energy change is more negative for the reaction between FeS and CaO because, FeO is more stable than FeS [14, 19]. On the other hand, the Gibbs energy change for the exchange reaction between Cu_2S and CaO becomes more positive with temperature as the stability of Cu_2S increases with temperature [19]. The Gibbs energy change for the exchange reaction between CoS and CaO is positive and negative, below and above 1303 K, respectively. In a system having a mixture of Cu_2S, FeS, CoS and CaO, the exchange reactions may readily take place because of formation of more stable compounds from the reactions involving metal oxides (MOs) and CaO/CaS.

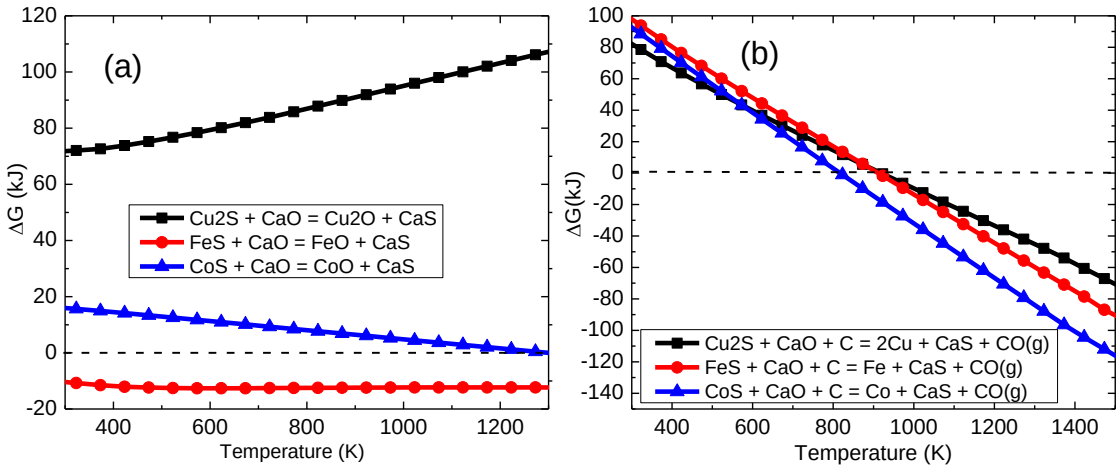

Figure 2.3 – Gibbs energy change against temperature for; (a) ion exchange reaction between metal sulphides with CaO and (b) carbothermic reduction of metal sulphides in the presence of CaO, computed from HSC software 5.1 database [39]

Even though the Gibbs energy change is positive for the reaction between Cu_2S and CaO, it becomes negative in the presence of carbon because of the production of the CO gas as shown in figure 2.3b. By comparison, the Gibbs energy change is more negative for the carbothermic reduction of CoS, although the Gibbs energy change is more negative for the exchange reaction between FeS and CaO, due to the higher stability of FeO. Based on the thermodynamic predictions in figures 2.3a and 2.3b, it can be summarised that; (i) metallisation of copper may be limited by the exchange reaction as the Gibbs energy change for the Cu_2S - CaO exchange reaction is more positive in figure 2.3a (ii) metallisation of iron may be limited by the reduction reaction.

2.2.2 Previous studies on reduction of mineral sulphides

The reduction of synthetic chalcopyrite ($CuFeS_2$) in the presence of lime, with coal, graphite and CO gas, has been studied by Jha and Grieveson [32] in the temperature range of 1123 K - 1273 K. Three oxysulphide liquid phases namely 3CaS•4FeO, CaS•FeO and CuFeCaSO were analysed in the partially reacted samples when coal and graphite were used as reductants. A number of observations were made when CO gas was used as a reductant:

i. The rates of reductions were independent of temperature.
ii. The experimental weight losses were higher than the theoretical weight losses, due to the evolution of SO_2 gas.

iii. Segregation of metallic iron to the periphery of the pellet and copper to the core of the pellet, due to diffusion of the Fe^{2+} and O^{2-} ions towards the periphery and, Cu^{+1} ions towards the core, caused by the difference in oxygen potential [32].

The carbothermic reduction of chalcopyrite ($CuFeS_2$) concentrates containing 12 wt. % gangue minerals (SiO_2 and Al_2O_3), in the presence of lime, has been studied by Payne [47]. The reduction experiments were carried out at mole ratio of MS:CaO:C = 1:2:2 and, the rate of metallisation was dependent on reduction temperature. Nonetheless, the effects of changing the mole ratios of lime and carbon, were not analysed by Payne. A quinary phase with a general formula of CuFeCaOS was identified when the mixture of $CuFeS_2$ concentrates and CaO were heated in the absence of carbon [47]. The mechanism leading to the formation of the CuFeCaOS phase was not explained but it was considered that the phase was formed as result of reaction 2.5a [47]. However, there is no thermodynamic data for the CuFeCaOS phase and hence the possibility of reaction 2.5a is uncertain. Payne also reported the presence of metallic copper after heating the mixture of $CuFeS_2$ and CaO, in the absence of reducing agent and it was explained that the formation of metallic copper was due to equation 2.5b [47].

$$CuFeS_2 + 2CaO(s) = CuFeCaOS(s) + CaS(s) + 1/2O_2(g) \qquad 2.5a$$

$$CuFeS_2 + 2CaO(s) = Cu + FeO \bullet CaS(s) + CaS(s) + 1/2\,O_2(g) \qquad 2.5b$$

The carbothermic reduction of chalcopyrite ($CuFeS_2$) concentrates containing about 6.4 wt. % SiO_2, in the presence of CaO with graphite, has been studied by Khaki et al. [48] in the temperature range of 1073 K - 1273 K. The extent of metallisation increased as the mole ratios of CaO and C were increased. Khaki et al. [48] reported that metallisation was complete at 1173 K and mole ratio of MS:CaO:C = 1:2:2 but several peaks were unidentified in the XRD pattern, which appear to belong to the Ca_2CuFeO_3S phase [49].

The carbothermic reduction of covellite (CuS) and chalcocite (Cu_2S) in the presence of lime, with coal and graphite has been investigated by Jha et al. [35]. The extent of metallisation increased with increase in reduction temperature. The carbothermic reduction of covellite (CuS) and chalcocite (Cu_2S) were completed in 25 minutes and 60 minutes respectively, at 1273 K, for a mole ratio of MS:CaO:C = 1:1:2, with coal. However, Jha et al. [35] found that the % reduction reached 82 % reduction

and about 100 % for chalcocite (Cu_2S) and covellite (CuS) respectively, when graphite was used as a reductant at 1273 K. The reduction of chalcocite (Cu_2S) in the presence of CaO, with CO gas, has also been carried out by Mohan et al. [50] in the temperature range of 1123 K – 1273 K. The reactions were completed in 30 minutes at 1273 K.

The reduction of pyrrhotite ($Fe_{1-x}S$) [51, 52] in the presence of lime, with coal, graphite and carbon monoxide gas has been studied by Jha and Grieveson [34]. The reduction with graphite was ineffective at 1073 K [34]. The extent of metallisation reached 30 % reduction in 20 hours at 1073 K and, 100 % reduction in 10 minutes at 1273 K, in the reduction with coal. The C_1(3CaS•4FeO) and C_{11}(CaS•FeO) oxysulphide phases were identified in the partially reacted samples, in the reduction with coal, below 1173 K. The mechanism leading to the formation of oxysulphide phases were explained as follows; (i) ion exchange reaction between FeS and CaO as shown in equation 2.6a and (ii) reaction between FeO and CaS as shown in equation 2.6b. It was discussed that metallisation of Fe occurred via reduction of the oxysulphide phases.

$$FeS(s) + CaO(s) = FeO(s) + CaS(s) \qquad 2.6a$$

$$aFeO(s) + bCaS(s) = (CaS)b \bullet (FeO)a \qquad 2.6b$$

The carbothermic reduction of pyrrhotite ($Fe_{1-x}S$) in the presence of CaO, with activated carbon, has also been studied by Kutsovskaya et al. [53]. The reductions reached 95 % reduction in 20 minutes and 40 minutes at 1323 K and 1273 K, respectively, whereas the % reduction only reached 70 % after 2 hours at 1223 K, for a molar ratio MS:CaO:C = 1:1.1:1.1.

The carbothermic reduction of synthetic cobalt sulphide (Co_9S_8) has been studied by Ford and Fahim [36] in the presence of CaO and hydrogen gas. The rate of reduction did not improve as the mole ratio of CaO was increased above 300 % of the stoichiometric mole ratio. The reduced cobalt particles had needle-like whiskers after reduction at 1073 K [36]. The reduction of bornite (Cu_5FeS_4) in the presence of lime and hydrogen gas has been investigated by Habashi and Dugdale [54]. The reactions were complete in about an hour at 1073 K. The carbothermic reduction of molybdenum sulphide (MoS_2) in the presence of lime, with activated carbon, has been carried out by Padilla et al. [55] in the temperature range of 1173 K - 1473 K. Complete metallisation was achieved in 30 minutes at 1473 K. The rate and extent of metallisation did not

increase as the mole ratio of CaO was increased above 300 % of the stoichiometric mole ratio [55].

The carbothermic reduction of lead sulphide (PbS) in the presence of lime, with graphite has been carried out by Rao and El-Rahaiby [56] in the temperature range of 1068 K - 1263 K. The off-gas from the carbothermic reactions were analysed by gas chromatograph [56] and there was no evidence of any sulphurous gas, confirming that sulphur was tied up as CaS, during metal production. Several catalysts such as lithium, potassium and sodium carbonates and, sodium sulphate, were used. The uncatalysed reactions were about four times slower than the catalysed reactions. Lithium carbonate was found to be more effective because of lack of volatilisation of the oxide or metal. The role of catalysts in speeding up the reactions is shown in equations 2.7a - 2.7c.

$$M_2CO_3(s,1) + C(s) = M_2O(s,l) + 2CO(g) \quad \text{2.7a}$$

$$MO(s,1) + CO(g) = M(s,l) + CO_2(g) \quad \text{2.7b}$$

$$M_2O(s,1) + CO_2(s) = M_2CO_3(s,l) \quad \text{2.7c}$$

The carbothermic reduction of lead sulphide (PbS) in the presence of CaO, has also been studied by Igiehon et al. [45]. Metallisation of Pb occured in the absence of carbon via reaction 2.8a. It was also proposed that the metallisation of lead in the absence of carbon occurs via reaction 2.8b [45]. Igiehon et al. [45] further suggested that the carbothermic reduction of PbS in the presence of carbon can proceed via reduction of the $PbSO_4 \cdot 2PbO$ phase.

$$3PbS(s,1) + 2CaO(s) = 3Pb(l) + 2CaS + SO_2(g) \quad \text{2.8a}$$

$$6PbO(1) + PbS(s) = PbSO_4 \cdot 2PbO(s) + 4Pb(l) \quad \text{2.8b}$$

The carbothermic reduction of antimony sulphide has been investigated by Igiehon et al. [44] in the presence of CaO and MgO, with coal or graphite. CaO was more effective than MgO, which can be due to the higher stability of CaS than MgS (see figure 2.2). The metallisation of antimony was controlled by the reduction reaction, in the reduction with graphite as the $Ca_2Sb_2O_5$ phase was found in the partially reacted samples [44].

However, the metallisation of antimony was not limited by the reduction reaction, in the reduction with coal as the $Ca_2Sb_2O_5$ compound [44] was not observed in the partially reacted samples. Igiehon et al. [44] also studied the exchange reaction between antimony sulphide and CaO in a temperature range of 973 K - 1173 K. The exchange reactions were incomplete at all temperatures but CaS and $Ca_2Sb_2O_5$ phases were produced. The exchange reactions were more favourable at excess CaO and, the CaO rich antimony oxide ($Ca_3Sb_2O_6$) phase was produced.

The carbothermic reduction of nickel sulphide in the presence of calcium hydroxide ($Ca(OH)_2$) has been studied by Bronson and Sohn [33] in the temperature range of 1073 K - 1397 K [33]. The off-gas was analysed by gas chromatograph and, CO_2 and CO were the only gases. Machingawuta et al. [38] have also studied the carbothermic reduction of nickel sulphide in the presence of lime, with coal and graphite as the reductants. The reductions were slower with graphite than with coal.

The reduction of molybdenite (MoS_2) in the presence of CaO, with carbon, H_2 gas and CO gas has been investigated by Prasad et al. [43]. The reduction of MoS_2 with hydrogen yielded Mo and CaS phases, whereas the reduction with C and CO gas yielded Mo, Mo_2C and CaS phases [43]. Furthermore, $CaMoO_4$ was detected in the partially reacted samples, in the reduction with C or CO gas [43], suggesting that metallisation proceeds via reduction of the metal oxide. The carbothermic reduction of molybdenite (MoS_2) has also studied by Padila et al. [55] in the temperature range of 1173 K - 1473 K. Padila et al. [55] also reported about the presence of the metal oxide (MoO_2 and $CaMoO_4$) in the partially reacted samples and, Mo and Mo_2C in the fully reacted samples. Therefore, it was suggested the MOs phases are the intermediate phases formed by the ion exchange reaction, which then reduce to Mo and Mo_2C, in the presence of carbon.

2.2.3 Factors affecting the carbothermic reduction of mineral sulphides

Previous studies [32, 35, 57, 58] on carbothermic reduction of the mineral sulphides in the presence of lime have showed that the carbothermic reduction of mineral sulphide in the presence of lime is affected by reaction temperature, stoichiometric ratio of the reactants (lime and carbon), type of carbon and particle size of the mineral sulphides. All previous studies have showed that the rate of reaction increases with increase in the reduction temperature [31-34, 42, 44, 45, 57, 58].

The effect of increasing the stoichiometric ratio of CaO, in the carbothermic reduction of mineral sulphides has been studied by Kutsovskaya et al. [53] and Bronson and Sohn [33]. Kutsovskaya et al. [53] studied the effect of increasing the stoichiometric ratio of lime in the reduction of pyrrhotite ($Fe_{1-x}S$) at a ratio of MS:C = 1:1.1 and 1:2. The rate of reduction was higher for MS:CaO = 1:2 than for MS:CaO = 1:1.1. The effect of increasing the stoichiometric ratio of CaO in the carbothermic reduction of nickel sulphide (Ni_3S_2) with coconut charcoal has been studied by Bronson and Sohn [33] for MS:C = 1:4, between 1073 K and 1397 K. The rate of reaction and the extent of metallisation was higher at MS:CaO = 1:4 than at MS:CaO = 1:2. However, the rate of reaction was lowest at MS:CaO = 1:6, probably, due to formation of intermediate compounds between CaO and Ni-O.

The effect of increasing the stoichiometric ratio of carbon has been studied by Kutsovskaya et al. [53], Jha et al.[35] and, Bronson and Sohn [33]. The results by Kutsovskaya et al. [53] showed an increase in the rate of reduction with increase in the stoichiometric ratio of C, from MS:C = 1:1.1 to 1:2 for MS:CaO = 1:1.1 or 1:2, at 1273 K. On the other hand, Jha et al.[35], observed that the extent of metallisation was slightly slower at MS:CaO:C = 1:2:4 than at MS:CaO:C = 1:2:3, in the carbothermic reduction of Cu_2S with coal. The rate of reactions was slower at MS:CaO:C = 1:2:4 than at MS:CaO:C = 1:2:3, due to the decrease in the rate of the exchange reaction when the stoichiometric ratio of carbon is increased. The experimental results by Bronson and Sohn [33] in the carbothermic reduction of nickel sulphide shows that the rate of reactions increases with increase in the stoichiometric ratio of coconut charcoal.

There are several types of carbon namely coal, carbon black, coke, graphite etc. The effect of using coal and graphite in the reduction of Cu_2S has been studied by Jha et al. [35]. The reductions at 1123 K reached; (i) 100 % reduction in 6 hours with coal and (ii) 30 % reduction in 8 hours with graphite. The effect of coal and graphite in the reduction of chalcopyrite ($CuFeS_2$) has been studied by Jha and Grieveson [32]. The evolution of SO_2 gas occurred below 30 % reduction, in the reduction with graphite, between 1123 K and 1273 K. The SO_2 gas was evolved in the initial stages of the reactions because of the reactions between MO and MS/CaS. However, SO_2 gas was not evolved in the reduction with coal, since the metal oxide phase is reduced to metallic state, as coal is a very reactive reductant. In short, the reduction reaction was able to cope with the ion exchange reaction when coal was used and hence eliminating the reaction between metal oxides and metal sulphides/CaS.

The effect of mineral concentrates particle sizes has been studied by Bronson and Sohn [33] at 1193 K and 1293 K. The rate of reactions increased with decrease in the mineral concentrates particle sizes, due to the increase in the reaction surface area.

2.3 Reduction with solid carbon

As the carbothermic reduction of mineral sulphides in the presence of lime may proceed via reduction of the metal oxide phases, it is necessary to discuss the reduction of the metal oxides with solid carbon. The reduction of metal oxides with carbon may yield CO or CO_2 gases, depending on the reduction temperature. The CO_2 gas is more stable than the CO gas below about 990 K but the CO gas is more stable above this temperature (figure 2.4). CO_2 gas is more stable than Cu_2O and CoO (figure 2.4) such that the carbothermic reduction of these oxides (Cu_2O and CoO) may proceed with CO_2 gas as the product gas. On the other hand, the carbothermic reduction of Fe_xO is only possible above 990 K as Fe_xO is less stable than both CO and CO_2 gas. It is evident from figure 2.4 that the stability of CO gas increases with temperature compared to that of CO_2 gas and hence there is a higher possibility of generating CO gas at higher temperature during reduction of metal oxides.

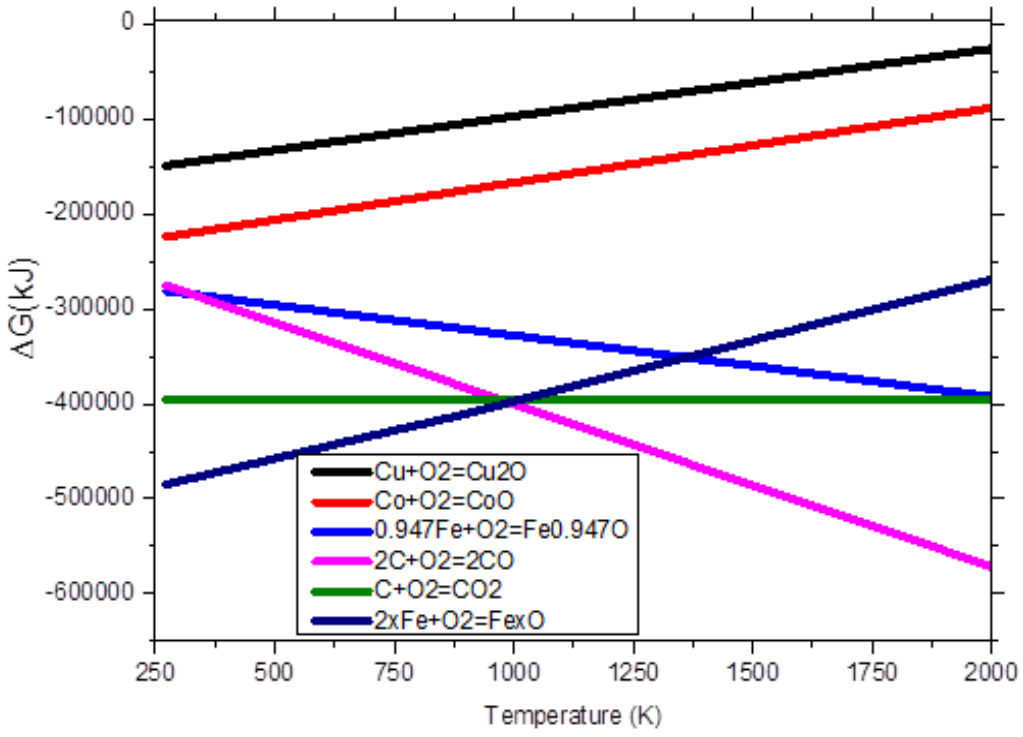

Figure 2.4 – The Gibbs energy change for the oxidation of Cu, Co, Fe and C per mole of O_2 gas

2.3.1 Mechanism

The carbothermic reduction between solid metal oxide and solid carbon takes place via two mechanisms: (i) direct reduction of the solid metal oxide with solid carbon at the contact surface as shown by reaction 2.9a and (ii) indirect reduction of the metal oxide with CO gas (intermediate gas) (equation 2.9b). The CO_2 gas from equation 2.9a can react with carbon to regenerate CO gas according to equation 2.9c. Equation 2.9c is known as the Boudouard reaction [59-63].

The rate of reduction increases with increase in the C/MO mole ratio because of increase in the reacting surface area. Similarly, the rate of reduction increases with decrease in the particle sizes as the contact surface area increases. The rate of reduction slows down when a rim of metallic phase surrounds the un-reacted core of metal oxide as the reduction might occur, either by diffusion of carbon or CO gas through the solid metal layer.

$$MO(s) + C(s) = M(s) + CO(g) \qquad 2.9a$$

$$MO + CO = M + CO_2(g) \qquad 2.9b$$

$$C + CO_2 = 2CO(g) \qquad 2.9c$$

2.4 Reaction models

Different kinetic models have been established for examining the solid state reactions. The solid state reactions maybe controlled by: (i) the reaction at the interface, (ii) diffusion of the reacting and product species through the product layer and (iii) diffusion and chemical reaction, also known as mixed reaction. In the case of a porous reaction product, where the diffusion of species is faster than the chemical reaction at the interface, the process is controlled by the chemical reaction [64]. The diffusion controlled process is where the diffusion of the reacting and product species are faster than the interface reaction. The model for chemically controlled reaction was developed by Spencer and Topley and is given in equation 2.10a [65]. Such processes are temperature dependent as the rate of chemical reaction increases with temperature [64]. Jander proposed the product layer diffusion controlled reaction based on the parabolic

law where it was assumed that the growth of the reaction product is inversely proportional to its thickness and is given in equation 2.10b. However, the Jander model cannot be applied when the surface area changes with time due to the change in the rate of reaction [64, 66]. The model is just valid to one dimensional diffusion or can only be useful during the early stages of a three dimensional reaction. Ginstling and Bronstein proposed a new model for a diffusion controlled reaction (equation 2.10c) [66, 67].

$$1-(1-X)^{\frac{1}{3}} = kt \qquad 2.10a$$

$$(1-(1-X)^{\frac{1}{3}})^2 = kt \qquad 2.10b$$

$$1-\frac{2}{3}X-(1-X)^{\frac{2}{3}} = kt \qquad 2.10c$$

Where X is the fraction reacted at time t and K is the rate constant

The shrinking core model has been broadly applied in the field of metallurgy. According to this model, the reaction starts from the outer surface of the particle and the reaction zone advances inwards, leaving behind the reaction product [68]. The unreacted core shrinks in size during the reaction [68]. The schematic illustration of the shrinkng core model is shown in figure 2.5.

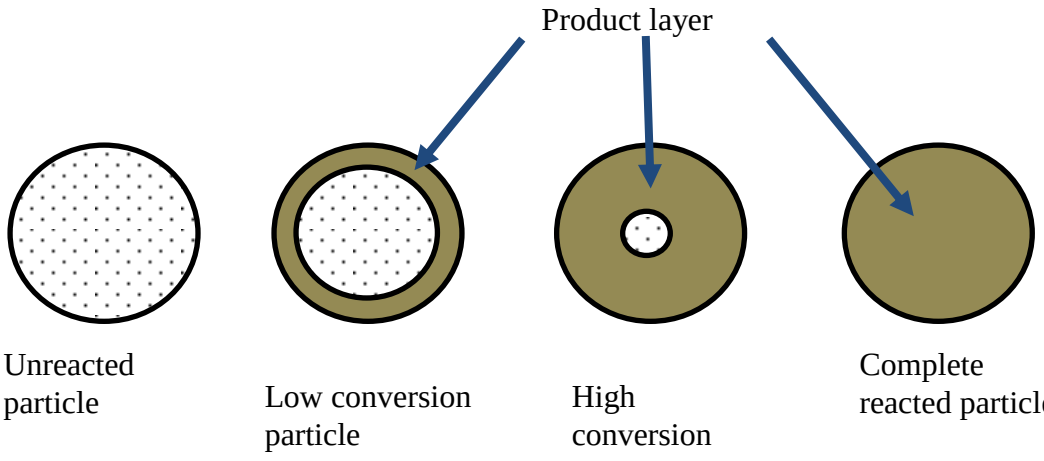

Figure 2.5 – Illustration of shrinking core model

The rate determining step in the shrinking core model can be diffusion through the reaction product or chemical reaction at the interface [69]. The chemically and diffusion controlled reactions in the shrinking core model are represented by equation 2.10a and 2.11a [69, 70], respectively, for spherical particles.

$$1-3(1-X)^{\frac{2}{3}}+2(1-X)=kt \qquad 2.11a$$

$$X+(1-X)\ln(1-X)=kt \qquad 2.11b$$

For cylindrical particles, it is assumed that the particles are considerably long and that the reactions and diffusion take place in the radial direction [71]. The chemically controlled and diffusion controlled reaction are given in equations 2.10a and 2.11b, respectively.

The relationship between temperature and the rate constant (K) is given by the Arrhenius (equation 2.12) [72, 73].

$$k=A\exp\left[\frac{Q}{RT}\right] \qquad 2.12$$

Where Q is the activation energy, T is the absolute temperature in kelvin, R is universal gas constant = 8.314 J/mol/K and A is constant.

There is no published data for the activation energy of carbothermic reduction of Cu-Co-Fe mineral sulphide concentrates in the presence of lime. The activation energy for the reduction of Cu_2S with CO gas has been determined by Mohan et al.[50] as 170 kJ/mole, in temperature range of 1123 K - 1273 K. The activation energy for the carbothermic reduction of pyrrhotite ($Fe_{1-x}S$) in the presence of lime has been determined by Jha and Grieveson [34]. The activation energies were 308 ± 45 kJ and 270 ± 14 kJ/mol, for reduction with graphite and coal [53], respectively. The activation energy for the carbothermic reduction of pyrrhotite with activated carbon has also been determined by Kutsovskaya et al. [53] as 299 kJ/mole, between 1223 K and 1323 K.

2.5 Separation of metallic phases from the carbothermically reduced samples

The reaction products from the carbothermic reduction of mineral sulphide concentrates will consist of metallic phases (Cu, Co, Fe), CaS, excess CaO and impurity phases (SiO_2, Al_2O_3 etc.). The metallic phases must be separated from the unwanted reaction products. The separation of metallic phases from the reaction products of carbothermic reduction can be achieved in a number of ways.

2.5.1 Magnetic separation

Magnetic separation is a separation technique that is used for separating out the magnetically susceptible products from the non-magnetic products to produce streams of magnetic and non-magnetic compounds. The magnetic fractions can further be separated into weakly magnetic (paramagnetic) and strong magnetic (ferromagnetic) fractions depending on the difference in the magnetic susceptibility [28]. The magnetic separation of iron and cobalt from the reaction products of the carbothermic reduction of Cu-Fe-Co mineral sulphide concentrates is possible because Co and Fe metallic/alloys phases are ferromagnetic [74]. The dissolution of iron and cobalt in the copper matrix may enable the magnetic separation of copper due to precipitation of magnetic phases of iron and cobalt during cooling of the samples. Nonetheless, the copper rich phase containing iron and cobalt precipitates may be weakly magnetic compared to the metallic/alloy phases of iron and cobalt phase. It is therefore possible to produce a strongly magnetic (ferromagnetic) fraction consisting of Co and Fe metallic/alloy phases and a weakly magnetic (paramagnetic) Cu rich alloy phase.

The magnetic separation of the metallic phases from the reaction products of the carbothermic reduction of mineral sulphides in the presence of CaO has been carried out by a few authors [48, 53, 75]. The magnetic separation of Ni-Fe alloy(s) from the reaction products of the carbothermic reduction of synthetic pentlandite $\mathbf{(Fe,Ni)_9S_8}$ in the presence of $Ca(OH)_2$, has been carried out by Shah and Ruzzi [75]. Iron and nickel were separated out from the reaction products as they are both ferromagnetic. However, Shah and Ruzzi [75] did not report the effects of the reduction temperature, type of carbon and the stoichiometric ratios of CaO and C, on the magnetic separation of the metallic phases. Magnetic separation of iron from the carbothermic reduction of $Fe_{1-x}S$ in the presence of CaO, has been investigated by Kutsovskaya [53]. The separation of Fe was sensitive to the reduction temperature. The magnetic fraction of the samples

reduced at high temperature (1458 K) had about 12 wt. % S in the form of CaS due to sintering in the sample. Nevertheless, Kutsovskaya et al. [53] did not explain the cause of sintering in the sample at high reduction temperature. Kutsovskaya [53] further observed that, even though sintering of the sample was less at low reduction temperature, the magnetic fraction contained about 4 wt. % S sulphur but in the form of FeS as a result of incomplete reduction. The magnetic separation of Cu and Fe from the carbothermic reduction of chalcopyrite ($CuFeS_2$) concentrates in the presence of CaO (MS:CaO:C = 1:2:2), with graphite, has been carried out by Khaki et at.[48]. The magnetic fractions had high XRD peak intensities for CaS, meaning that the separation process was extremely poor. Moreover, Khaki et al. did not analyse the effects of the reduction temperature, type of carbon and the stoichiometric ratios of CaO and C.

The magnetic separation of the metallic values (Cu, Fe and Zn) from the reduction of chalcopyrite ($CuFeS_2$) concentrates in the presence of H_2 gas and CaO has been carried out by Habashi and Yostos [76]. The mineral sulphide concentrates were formed into pellets and reduced in a bed of CaO, to achieve good separation. The reduced pellets were separated from CaS and excess CaO by the magnet. However, this method may not be used for the reduction of the mineral sulphide concentrates in the presence of CaO with carbon. This is because, the exchange reaction between MS and CaO is limited to the surface of the pellets, when the mineral sulphide concentrates are pressed into the pellets and reduced in the bed of CaO. Good contact between MS and CaO is necessary for the complete carbothermic reduction of the mineral sulphides in the presence of CaO. However, the contact between MS and CaO may not be necessary for the reduction of mineral sulphides in the presence of CaO and H_2 gas because, metallisation can occur via reactions 2.13a and 2.13b. Based on reaction 2.13a, CaS may be formed in the bed of CaO, for the reduction with H_2 gas.

$$MS + H_2(g) \Rightarrow M + H_2S(g) \qquad 2.13a$$

$$CaO + H_2S(g) \Rightarrow CaS + H_2O(g) \qquad 2.13b$$

Magnetic separation of the metallic phases from the reaction products is quite advantageous as CaS can be reprocessed to regenerate CaO or converted into a stable $CaSO_4$ phase [15, 28, 41]. The only drawback of magnetic separation is that the non-magnetic metallic phases cannot be separated out.

2.5.2 Selective leaching of the unwanted reaction products

The separation of metallic phases from the reduction of mineral sulphides in the presence of CaO, has been achieved via selective leaching (dissolution) of CaS and excess CaO in weak acid (less than 5% HCl or acetic acid) [54, 55, 75, 77, 78]. However, the separation or recovery of metallic values via selective dissolution of CaS and excess CaO in acid, is ineffective in the presence of acid insoluble compounds (SiO_2, Al_2O_3, etc.), because the acid insoluble compounds remain with the metallic phases [76]. In practice, most mineral sulphide concentrates contain significant quantities of acid insoluble gangue minerals [11] which cannot be dissolved in acid. Therefore, the separation of metallic values via selective leaching of CaS and excess CaO, has very limited practical application.

2.5.3 Gravity method

Gravity method is a separation technique that is widely used for separating out materials of different densities. It is a sink-float process in which the heavier particles sink to the bottom. The gravity separation method is very effective in the presence of liquid media whose density is between the lighter and denser particles. The liquid density can be controlled via addition of fine particles [79]. The gravity method has never been applied for separating out the heavier metallic phases from the reduced mineral samples. The presence of carbon and fine gangue mineral particles may enhanced flotation of lighter CaS and gangue mineral particles.

2.5.4 Carbonyl process

The carbonyl process is based on the principle that some metals react with the CO gas to produce carbonyls according to equation 2.14 [15]. In the later stage, the metal carbonyl is decomposed to give the metal phase and CO gas. The decomposed CO gas can be recycled back into the process. The carbonyl process can be used to obtain high grade Fe and Co phases [80] because of the difference in the decomposition temperatures of their respective carbonyls. For example, cobalt carbonyl ($Co_2(CO)_8$) decomposes below 363 K [81] under inert atmosphere whereas $Fe(CO)_5$ decomposes at 413 K. The carbonyl process has been used for obtaining Fe and Ni from the reduced laterite ores [80]. The process has also been used for producing high grade (> 99.8 %)

powders of Co, Fe and Ni, from the reduced samples [82]. The major advantage of carbonyl process for separating iron and cobalt is that high purity Co and Fe may be produced, while utilizing CO gas from the carbothermic reduction process.

$$M + xCO \Rightarrow M(CO)x \qquad 2.14$$

2.6 Treatment of CaS

It has been shown in equation 1.5a, that no SO_2 gas emission arises as a result of simultaneous exchange and reduction reactions as sulphur is fixed as CaS. However, for such a metal sulphide reduction process to occur efficiently, the CaS formed must be reprocessed for the regeneration of lime.

Calcium sulphide can be converted into $CaCO_3$ via hydrolysis and carbonation process [83]. The hydrolysis and carbonation reaction, leading to the regeneration of $CaCO_3$ from CaS are shown in equations 2.15a – 2.15c. The CO_2 gas used in reactions 2.15a – 2.15c can be obtained by burning off (oxidising) the CO gas from the carbothermic reduction, in air (equation 2.15d). The heat from reactions 2.15d can be used in heating up the mineral sulphide concentrates. The proposed method in equations 2.15a – 2.15c is summarised in figure 2.6. The summary in figure 2.6 does not include the gangue minerals but this may not affect the hydrolysis and carbonation reactions. Furthermore, the recycled $CaCO_3$ does not really need to be pure, may be used for the reduction of mineral sulphides even with impurity gangue minerals.

$$CaS(s) + H_2O(l) + CO_2(g) = H_2S(g) + CaCO_3(s) \qquad 2.15a$$

$$CaS(s) + 2H_2O(l) = H_2S(g) + Ca(OH)_2(s) \qquad 2.15b$$

$$Ca(OH)_2(s) + CO_2(g) = H_2O(g) + CaCO_3(s) \qquad 2.15c$$

$$CO(g) + 0.5O_2(g) = CO_2(g) \qquad 2.15d$$

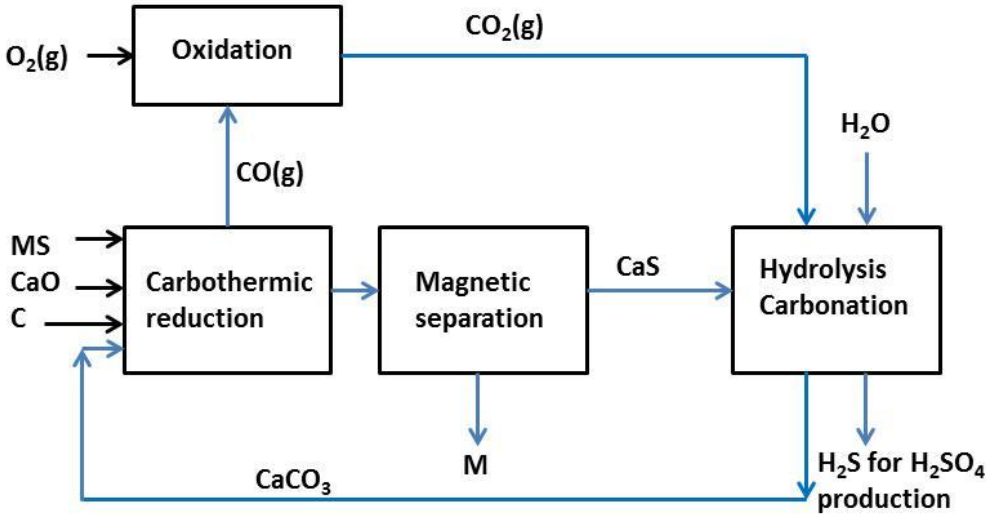

Figure 2.6 – Simplified flow sheet for the carbothermic reduction, magnetic separation and regeneration of $CaCO_3$ from CaS

The regeneration of lime from CaS can also be achieved by heating CaS with $CaSO_4$, according to equation 2.16 [84, 85]. As shown in equation 2.16, no air is required for the regeneration of CaS in the presence of $CaSO_4$ such that the off-gas will be nearly 100% SO_2 gas and can be converted to sulphuric acid or elemental sulphur. The production of CaO from CaS via equation 2.16 has been studied by Jha and Grieveson [84] and, Kutsovskaya et al. [53]. The rates of reactions increased with increase in the reaction temperature, completing in about 2 hours at 1323 K, under argon atmosphere.

$$CaS + 3CaSO_4 = 4CaO + 4SO_2 \qquad 2.16$$

Alternately, the regeneration of CaO from CaS can be achieved by heating CaS in an atmosphere of H_2O, CO_2 and 1 - 3 % O_2 gas [35, 85]. The overall reaction is given in equation 2.17. According to Turkdogan [85], there is no formation of $CaSO_4$ if the reaction is carried out above 1273 K although the complete conversion is achieved in 7 – 10 cycles [85]. However, the presence of CO_2 dilutes the concentration of SO_2 in the off-gas.

$$CaS + 1.5O_2 = CaO + SO_2 \qquad 2.17$$

Rosenqvist [41] and Habashi [15, 78] have proposed that CaS can be roasted in a rich O_2 gas atmosphere to form a stable $CaSO_4$ compound (equation 2.18). This method may be necessary in countries where there is no market for sulphuric acid or where the emission of sulphurous gas is completely prohibited. The sulphation of CaS in the O_2 gas atmosphere has been studied by Dong et al. [86] in a temperature range of 923 K - 1123 K. It was found that sulphation was dependent on the CaS particle sizes. Sulphation of CaS to $CaSO_4$ was complete at -50 µm particle size but incomplete at +50 µm particle size. The sulphation of CaS to $CaSO_4$ has also been studied by Dong et al. [87] in the temperature range of 973 K – 1573 K. The complete sulphation was achieved for smaller CaS particles (< 50 µm) and at temperatures below 1273 K.

$$CaS + O_2(g) = CaSO_4 \qquad 2.18$$

2.7 Thermal decomposition of the mineral sulphides under inert atmosphere

Most mineral sulphides are unstable at high temperature, they decompose by losing part of sulphur to form low sulphur, stable phase(s) [15, 78]. The thermal decomposition of the mineral sulphides may result in colour, magnetic properties and density changes. Chalcopyrite ($CuFeS_2$) is a copper sulphide mineral ($CuFeS_2$) with a brass yellow appearance [78]. It has a tetragonal structure with c = 5.25Å and a = 10.32Å [78]. Each sulphur atom is coordinated by 2 atoms of iron and 2 atoms of copper as shown in figure 2.7 [78]. The room temperature α-tetragonal phase transforms to cubic β-phase at 673 K. The β–phase also transforms to the tetragonal γ-phase above 823 K [78, 88]. The α → β → γ phase changes are due to volatilization of sulphur, according to equation 2.19a [89]. The deficiency of sulphur in γ-chalcopyrite may be up to 15 wt. % [89] but bornite and pyrrhotite ($Fe_{1-x}S$) are formed as sulphur deficiency reaches 20 wt. % (equation 2.19b [89]).

$$CuFeS_2 = CuFeS_{2-x} + xS_2 \; ; x \leq 0.4 \qquad 2.19a$$

$$5CuFeS_{2-x}(s) = Cu_5FeS_4(s) + 4FeS(s) + (1-5x/2S_2(g) \qquad 2.19b$$

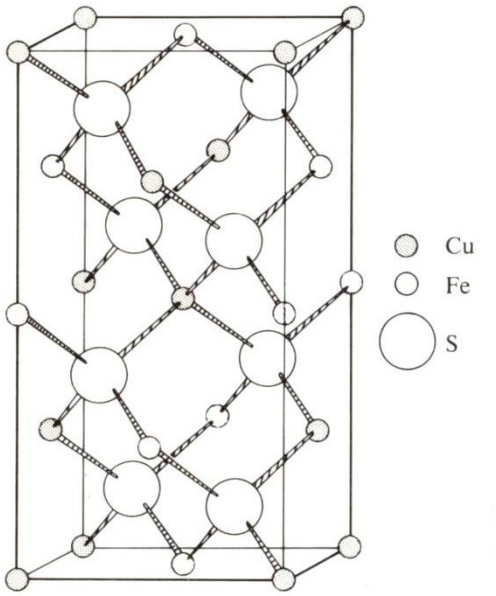

Figure 2.7 – Crystal structure of chalcopyrite [78]

The thermal decomposition of chalcopyrite ($CuFeS_2$) and chalcocite (Cu_2S) have been studied by Winkel et al. [89, 90] under inert (nitrogen) atmosphere. Metallic copper in the form of fibres was found with Cu_5FeS_4 and FeS phases, after heating the $CuFeS_2$ mineral at 1773 K. Winkel et al. also reported the presence of metallic copper after heating Cu_2S at 1773 K, under nitrogen atmosphere. It was explained that the formation of copper during heating of the mineral sulphides, was due to excessive loss of sulphur. However, the explanation does not agree with the thermodynamic prediction in equations 2.20a – 2.20c, as the Gibbs energy changes are positive.

$$Cu_5FeS_4(l) = 3Cu(l) + Cu_2S + FeS(l) + S_2(g),\ \Delta G_{1773K} = +105.2\ kJ \qquad 2.20a$$

$$2Cu_2S(l) = 4Cu(l) + S_2(g),\ \Delta G_{1773K} = +140\ kJ \qquad 2.20b$$

$$Cu_5FeS_4(l) = 3Cu(l) + Cu_2S + FeS(l) + S_2(g),\ \Delta G_{1773K} = +105.2\ kJ \qquad 2.20c$$

Nonetheless, metallic copper can be formed in the presence of small concentration of oxygen gas and this happens when the reaction vessel is not completely air tight. The metallisation of Cu due to the presence of O_2 gas can occur via equations 2.21a and 2.21b. Note that the Gibbs energy changes for reactions 2.21a and 2.21b are negative. Based on equations 2.20a – 2.20c and, 2.21a and 2.21b, the formation of metallic

copper in the work by Winkel et al. might have occurred due to the presence of O_2 gas in the reaction vessel.

$$Cu_5FeS_4(l) + O_2g) = Cu(l) + 2Cu_2S(l) + FeS(l) + SO_2(g), \quad \Delta G_{1773K} = -207\ kJ \tag{2.21a}$$

$$Cu_2S(l) + O_2(g) = 2Cu(l) + SO_2(g), \quad \Delta G_{1773K} = -154.5\ kJ \tag{2.21b}$$

Pyrite (FeS_2) is unstable above 1016 K, decomposes to troilite (FeS) or pyrrhotite ($Fe_{1-x}S$) [91] according to equation 2.22. The thermal decomposition of pyrite (FeS_2) under inert atmosphere starts between 683 K and 789 K [92].

$$(1-x)FeS_2(s) = Fe_{1-x}S(s) + (\frac{1}{2} - x)S_2(g) \tag{2.22}$$

The thermal decomposition of FeS_2 under nitrogen atmosphere has been studied by Boyabat et al. in a temperature of 673 K and 1023 K [93]. The thermal decomposition of FeS_2 to FeS, completed within 3 minutes at 1023 K. The rate of thermal decomposition of FeS_2 increased with the decrease in the particle size.

Covellite (CuS) is also unstable at higher temperature. The thermal decomposition of CuS can occur according to equations 2.23a and 2.23b [94, 95].

$$3.6CuS = 2Cu_{1.8}S + 0.9S_2(g) \tag{2.23a}$$

$$4CuS = 2Cu_2S + S_2(g) \tag{2.23b}$$

2.8 Thermodynamics of solution

The metallic phases and/or gangue minerals may form liquid and solid solutions during the carbothermic reduction of mineral sulphides in the presence of lime. The thermodynamics of metallic solutions is therefore briefly discussed in this section.

2.8.1 Thermodynamic properties of solutions

There are three important thermodynamic properties for all mixtures and they are, the entropies, heats and free energies of mixing [96, 97]. The relationship between the Gibbs energy change of mixing (ΔG^m) and, the entropy change (ΔS^m) and the enthalpy or heat change of mixing (ΔH^m), at constant temperature are given in equation 2.24.

$$\Delta G^m = \Delta H^m - T\Delta S^m \qquad 2.24$$

The partial molar free energies, entropies and enthalpies are the important properties that can be derived from three thermodynamic properties [96]. The partial molar free energy, partial molar entropy and partial molar heat are given in equations 2.25a, 2.25b, and 2.25c, respectively [96, 98]. The partial free energy ($\overline{G}_A$) is simply the change in the total energy due to the addition of component A by ∂nA [99] and is also known as the chemical potential (μ_A) [10, 100].

$$\overline{G}_A = \left(\frac{\partial G}{\partial nA}\right) n_B, n_C, ..., T, P \qquad 2.25a$$

$$\overline{H}_A = \left(\frac{\partial \Delta H_m}{\partial nA}\right) n_B, n_C, ..., T, P \qquad 2.25b$$

$$\overline{S}_A = \left(\frac{\partial \Delta S_m}{\partial nA}\right) n_B, n_C, ..., T, P \qquad 2.25c$$

Where G is the free energy, N_A is the number of moles of A, at constant moles of B (N_B), C (N_C), temperature (T) and pressure (P) [10, 96].

The relationship between the chemical potential and the composition of the alloy or mole fraction is given by the Gibbs-Duhem equation (equation 2.26) [10, 96, 101-103].

$$N_A d\overline{G}_A + N_B d\overline{G}_A + ... + N_i d\overline{G}_i = 0 \qquad 2.26$$

2.8.2 Activity

The activity of the solution may be defined as its effective concentration [104, 105]. The activity of the component i in the solution is therefore directly related to its concentration [104]. If the activity of the component in a solution is equal to its concentration or mole fraction X_i, the solution is known as ideal solution and is said to obey the Raoult's law (equation 2.27a) [10, 99, 100, 104, 105]. However, most solutions are non-ideal, they deviate from the ideal behaviour [28] and hence they do not obey equation 2.27a. The deviation from the ideal behaviour is represented by the activity coefficient (γ_i) (equation 2.27b). The relationship between the activity and the mole fraction in a binary system is shown in figures 2.8a and 2.8b. A straight line is obtained at very concentrations in a non-ideal solution and, the solution is said to obey Henry's law [10, 100, 104, 105].

$$\alpha_i = X_i \qquad 2.27a$$

$$\alpha_i = \gamma_i X_i \qquad 2.27b$$

Where γ_i is known as the activity coefficient of component i.

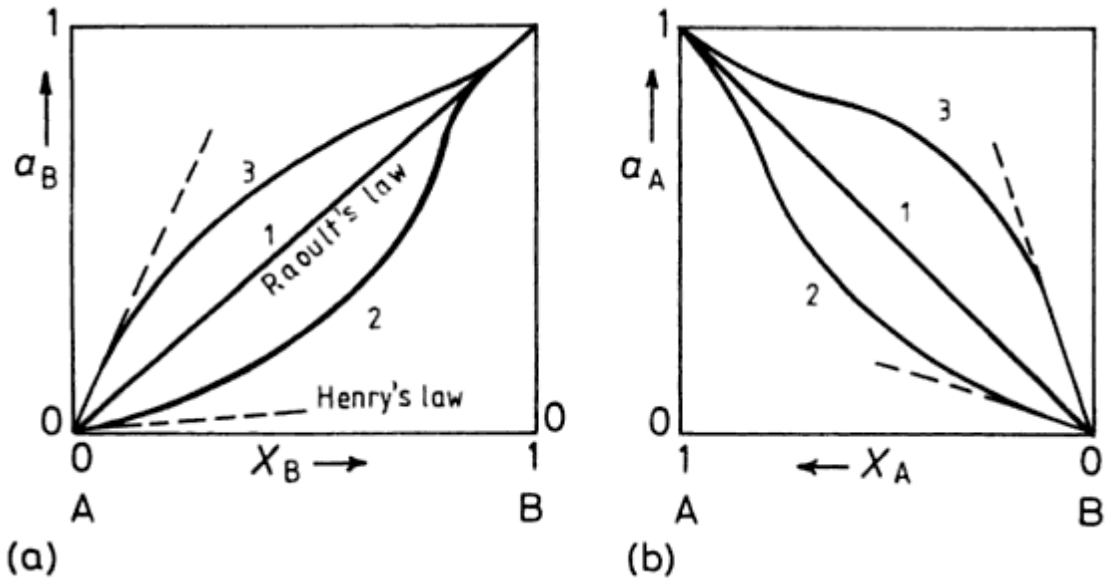

Figure 2.8- Variation of the activity against mole concentration (a) for component B and (b) for component A , line 1 Raoult's law (ideal solution) line 2 negative enthalpy of mixing ($\Delta H_m < 0$) and line 3 positive enthalpy of mixing ($\Delta H_m > 0$), [100]

The activity coefficient can be greater or less than one unity, positive deviation in the former case and negative deviation in the latter case [28]. The deviation from the Raoult's law may determine the mixing or de-mixing tendency of the solution [105]. The positive deviation from the ideal behaviour represents the de-mixing tendency whereas the negative deviation from the ideal behaviour represents compound formation [10, 105]. The Fe-Mn solution is ideal but the Fe-Cu [106] and Fe-Si show positive and negative deviation, respectively, from the Raoult's law.

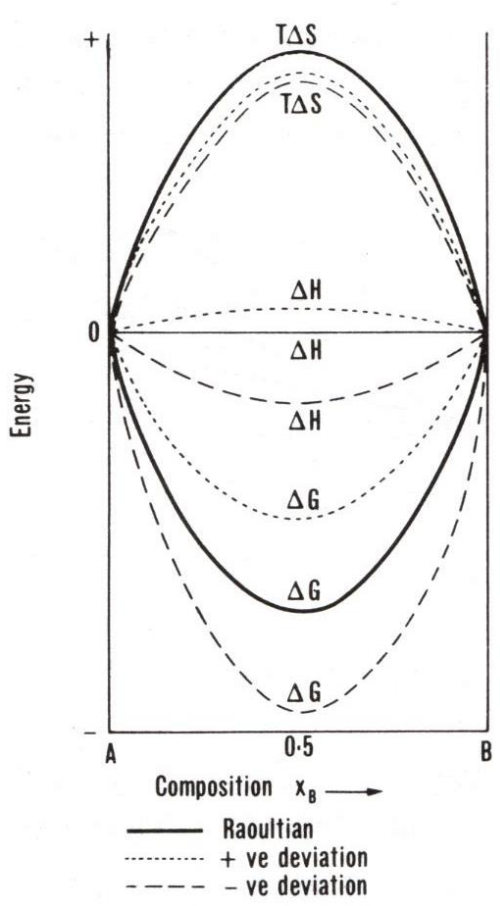

Figure 2.9 – Free energy of mixing for ideal solution and for the solutions exhibiting positive and negative departure from the ideal behaviour

2.8.3 Ideal solution model

The ideal solution model assumes that the activity of each component or species is equal to the mole fraction of the component or species in the solution [10] (equation 2.27a). The enthalpy of mixing is zero ($\Delta H_{mix} = 0$) in an ideal solution because the energy change for breaking up the bonds between the unlike atoms is zero [100, 107]. In

short, there is no interaction between the unlike atoms [108]. However, the entropy change is never zero for the ideal solution as entropy is driven by the natural tendency for mixing of atoms so as to reach the state of complete randomness [108]. Since ΔH_{mix} = 0 for ideal solutions, then from equation 2.24, the Gibbs free energy change for mixing is given by equation 2.28.

$$G^m = -T\Delta S^m \qquad 2.28$$

Where G^m and ΔS^m are the free energy change and entropy change of mixing, respectively.

The partial molar free energy change for component A in a solution is given by equation 2.29a [10]. Since the enthalpy change is zero for the ideal solution, the partial molar entropy of mixing for component A will be given by equation 2.29b.

$$\overline{G}_A^m = RT \ln N_A \qquad 2.29a$$

$$\overline{S}_A^m = -\frac{\overline{G}_A^m}{T} = -R \ln N_A \qquad 2.29b$$

The integral molar entropy of mixing (S^m) is given by equations 2.30a and 2.30b.

$$S^m = (N_A \overline{S}_A^m + N_B \overline{S}_B^m + ...N_i \overline{S}_i^m) \qquad 2.30a$$

$$S^m = -R(N_A \ln N_A + N_B \ln N_B + ...N_i \ln N_i) \qquad 2.30b$$

The integral molar free energy change (S^m) can be derived from equations 2.28 and 2.30b and is given by equation 2.31. As shown in equation 2.8, the Gibbs energy of mixing will depend on temperature (T) and composition (N_x) for the ideal solution.

$$G^m = RT(N_A \ln N_A + N_B \ln N_B + ...N_i \ln N_i) \qquad 2.31$$

2.8.4 Regular solution model

The regular solution model assumes that the enthalpy change for mixing is not zero due to the interactions between the unlike atoms. However, the entropy of mixing in the regular solution is the same as that of the ideal solution [10]. The enthalpy of mixing is therefore given by equations 2.32a – 2.32d. Equation 2.32c can be written items of activity coefficient (equation 2.32d), because of the relationship between the activity, the activity coefficient and the mole fraction (see equation 2.27b).

$$H^m = G^m + TS^m \qquad 2.32a$$

$$H^m = RT(N_A \ln a_A + N_B \ln a_B + ...N_i \ln a_i) - RT(N_A \ln Na + N_B \ln B.... + Ni \ln N_i) \qquad 2.32b$$

$$H^m = RT(N_A \ln \frac{a_A}{N_A} + N_B \ln \frac{a_B}{N_B} + ...N_i \ln \frac{a_i}{N_i}) \qquad 2.32c$$

$$H^m = RT(N_A \ln \gamma_A + N_B \ln \gamma_B + ...N_i \ln \gamma_i) \qquad 2.32d$$

The partial molar enthalpy of mixing is given by equation 2.33 [10, 96].

$$\overline{H}^m_A = RT \ln \gamma_A, \overline{H}^m_B = RT \ln \gamma_B, \quad \overline{H}^m_C = RT \ln \gamma_C \qquad 2.33$$

2.8.5 Derivation of binary phase diagram from free energy curves

A phase diagram has been defined by Bodsworth [10] as a map or chart that shows how at equilibrium, the coexisting phase boundaries are moved by the change in temperature (T) and compositions [10]. The locations of the phase boundaries or the stability regions are determined by the thermodynamic properties of the system and hence knowledge of the phase diagram can be used to evaluate or estimate the thermodynamic data [10]. The phase diagrams can be constructed from the free energy composition curves at isothermal temperature [105].

Complete solid and liquid solubility (miscible) - This is found in systems that conform completely or nearly to ideal behaviour [10], such as the Cu-Ni binary phase diagram.

The major phases at any temperature and composition (at X_A = O to X_A = 1), are the liquid (L), solid (S) and S + L phases. In practice, there will be solid A (G_A^S), liquid A (G_A^l), solid B (G_B^S) and liquid B (G_B^L). The liquid phase is the most stable phase above the melting temperatures of both A and B ($T_1 > T_m(A) > T_m(B)$) and hence it has lower free energy than the solid phase (figure 2.10a). The free energy curves for the solid and liquid phases move upwards or increase as the temperature decreases based on equation 2.28 but the increase is more rapidly for the liquid phase (figure 2.10b), because it has higher entropy than the solid phase. The free energy for the liquid phase continues to decrease more rapidly than the solid phase and hence $G_A^L = G_A^S$, between b and c (figure 2.10c). Since the free energies are the same for the solid and liquid phases, between b and c, a two phase field (s + l) co-exists. The solid is more stable at composition between A and b whereas the liquid phase is more stable at composition between c and B, at T_2. The solid phase becomes the only stable phase at temperatures below $T_m(B)$.

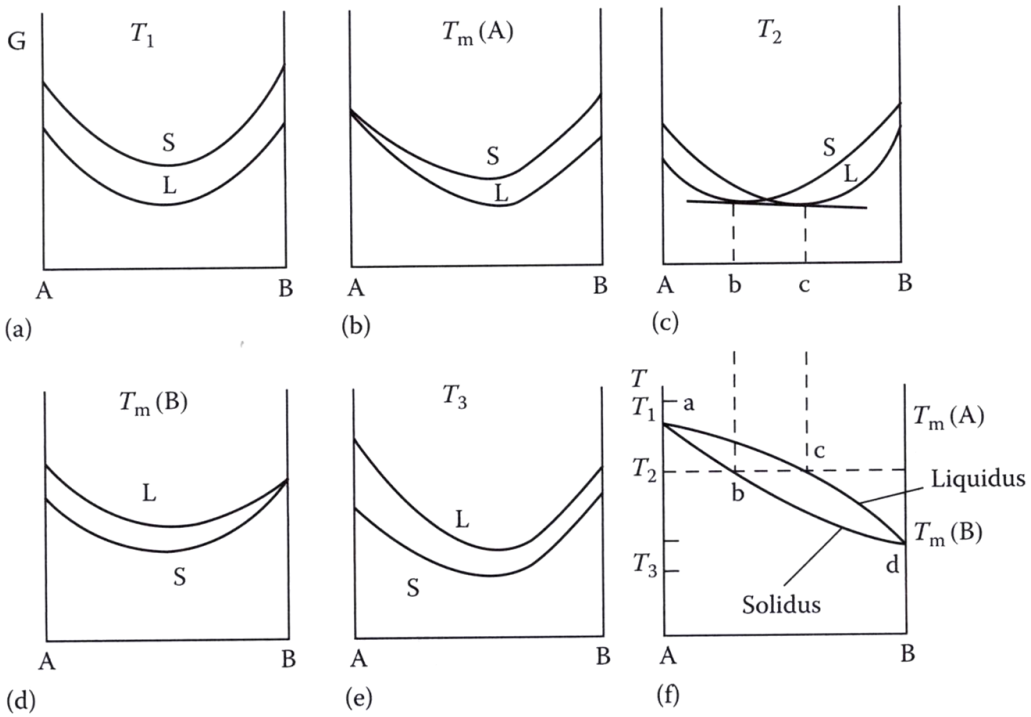

Figure 2.10 - Derivation of the binary phases diagram (f) with a complete solid and liquid solubility, from the Gibbs energy change from the solid and liquid curves (a), (b), (c), (d) and (e) [100]

Where S and L are the solid and liquid phases, respectively.

The line separating the S + L phase field from the L phase field is known as the liquidus line and it gives the composition of the liquid phase. Similarly, the line separating the S + L phase field from the S phase field is known as the solidus line and it gives the composition of the solid phase. The width between the solidus and liquidus lines or width of the two phase region is proportional to the difference in the melting points of the two components and the entropy of fusion (equation 2.34).

$$b^s - c^l = \frac{\Delta S_f^\circ \Delta T_f}{4RT_o} \qquad 2.34$$

Where ΔS_f^o is the standard entropy change, T_o is the temperature, ΔT_f is the difference in the melting temperatures of the pure components A and B.

Complete liquid solubility with a solid miscibility gap – This is found in systems in which the liquid phase is nearly ideal (complete liquid solubility) but $\Delta H_{mix} > 0$, for the solid phase, i.e. the different types of atoms dislike each other [100]. As a result, the free energy curve for the solid assumes a negative curvature at the centre [10, 100] and a common tangent can be drawn as shown in figure 2.11c to give a two phase region, consisting of α' and α" phases. However, e and f approach each other at higher temperatures since $-T\Delta S_{mix}$ becomes more negative and, the two phase field disappears [100]. The α' + α" phase field is known as the miscibility gap [100]. The Co-Fe system belongs to this type of the system.

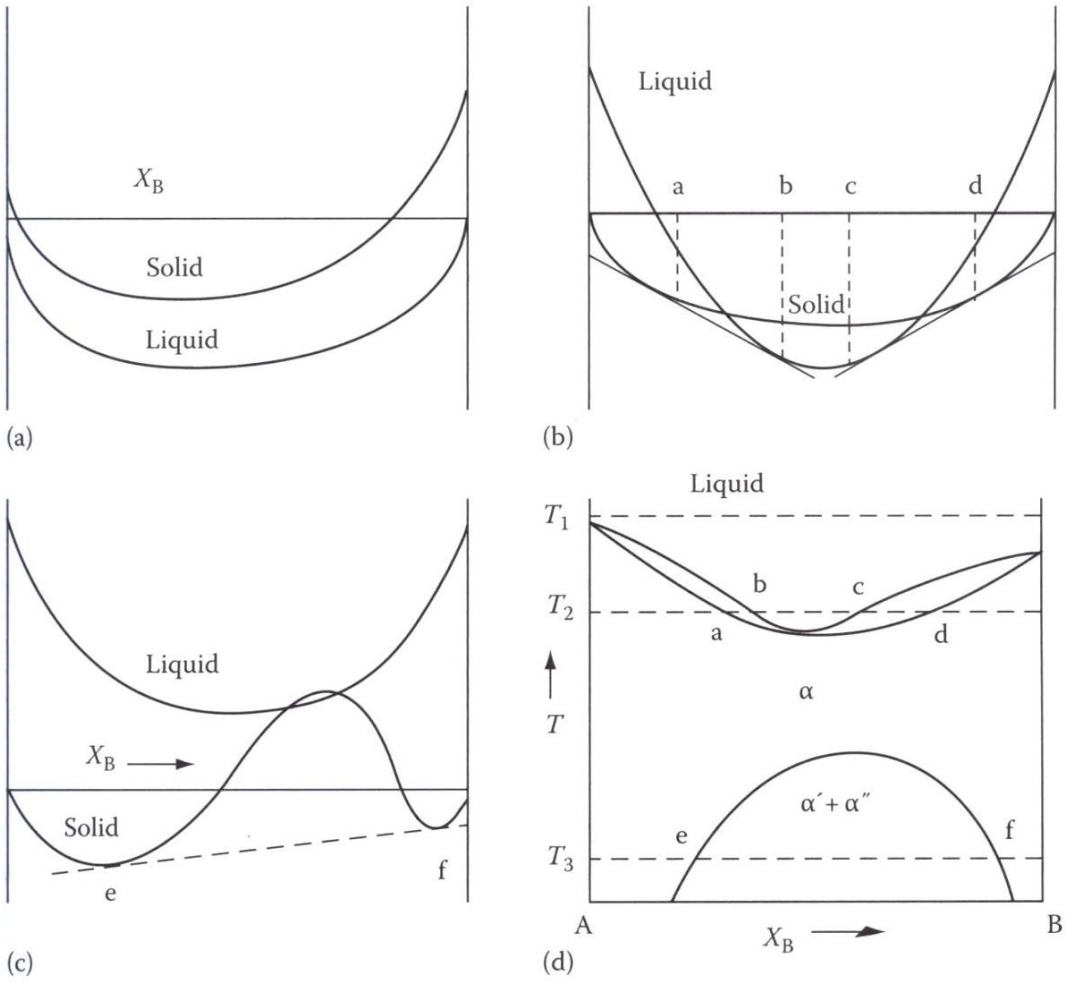

Figure 2.11 – Derivation of the binary phase diagram (d) in which the liquid phase is nearly ideal but, from the free energy curves (a), (b) and (c) [100]

Eutectic and peritectic phase diagrams – If ΔH_{mix} is much more positive in figure 2.11, the miscibility region (gap) may extend into the liquid phase. A eutectic system results when the melting points between the two components are closer to each other. The liquidus temperature of solid i is given by equation 2.35a [38, 109]. When there is appreciable solid solubility between the components, equation 2.35a is changed according to equation 2.35b [109].

$$\ln N_i = -\frac{\Delta H_f (T_m - T)}{RTT_m} \qquad 2.35a$$

$$\ln \frac{N_i}{N_i'} = -\frac{\Delta H_f (T_m - T)}{RTT_m} \qquad 2.35b$$

Where T_m is the melting temperature, N_i is the composition for the liquidus line, $N_i^{'}$ is the solid solubility of component i at temperature, T [109].

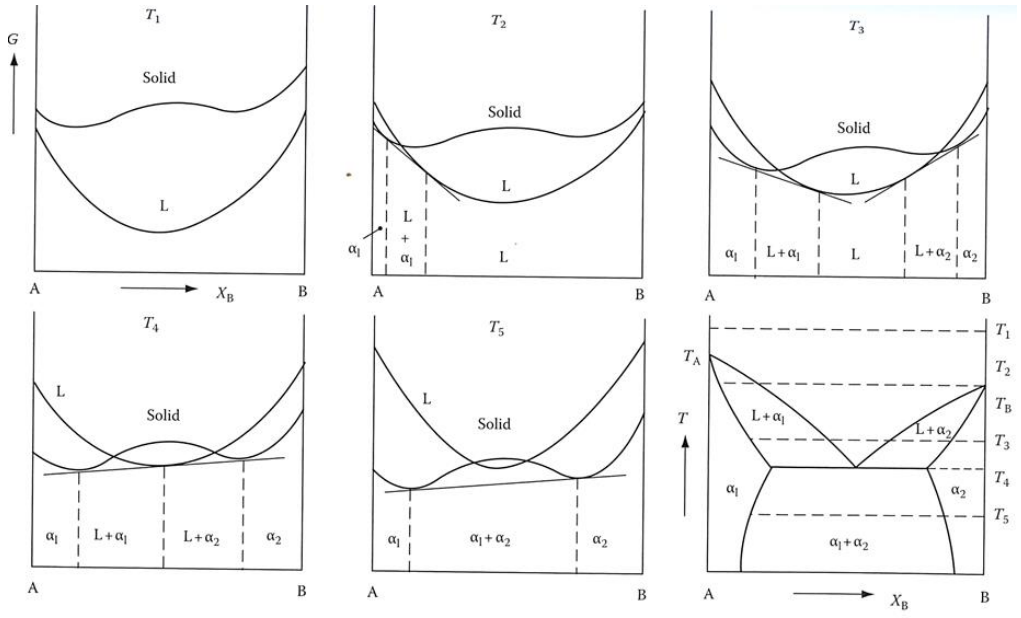

Figure 2.12 – Derivation of the binary phase diagram from the free energy curves at T_1, T_2, T_3, T_4 and T_5 [100]

A peritectic system is formed when there is a significant difference in the melting points between the components because the free energy curves are more skewed [10] (see appendex A.2.1). The Cu-Fe binary system is a good example of the peritectic system due to the marked difference between the melting points of Cu and Fe.

2.9 Smelting slags

It has been stated in chapter one that copper smelting slags are the major sources of cobalt. Slag has been defined as molten mixtures of silicates and metal oxides [28, 69, 110]. Slag acts as the receptacle for the unwanted compounds (gangue minerals), in metal extraction process [110]. In practice, slag from metal extraction process may contain halides and sulphides depending on the ore composition and the operating conditions. A good slag should be completely immiscible with the liquid metal phase and should therefore have the following properties [11]: (i) low melting temperature than the molten metal so as to maintain high fluidity [110] (ii) low viscosity (iii) low density and (iv) correct composition in order to accept and react with the impurities

from the liquid metal [110]. The above named slag properties are attained through control of slag structure and this is achieved by adding fluxes during the smelting process [11]. The common types of fluxes in copper smelting process are lime (CaO) and silica (SiO_2) even through CaF is added, sometimes [111].

Molten slag consist of cations (Fe^{2+}, Ca^{2+}, Mg^{2+} etc.) and anions (SiO_4^{4-}, PO_4^{3-}, O^{2-} etc.) [108, 112]. The SiO_4^{4-} tetrahedral unit structure is formed when silicon is coordinated by four O^{2-} ions. The SiO_4^{4-} unit structures may be connected as rings or chains depending on the SiO_2 content, to form a large polymerised ion as shown in figure 2.13 [108]. It can be observed in figure 2.13 that the structure of silicate ions depends on the degree of polymerization. The viscosity of the slag increases with increase in the size of the silicate ion or polymerisation [108].

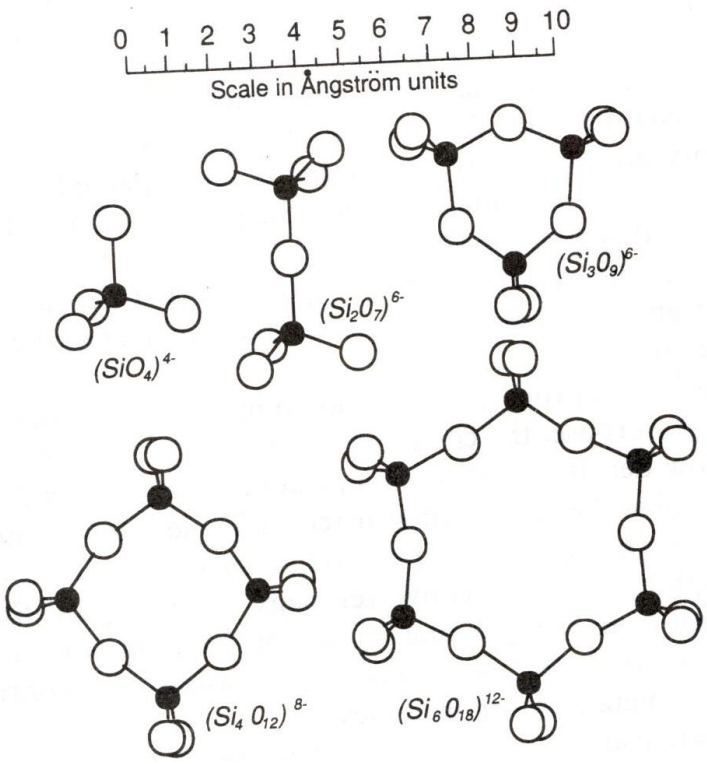

Figure 2.13 – Crystalline silicates, the silicon and oxygen atoms are shown in black and white circles, respectively [108]

The oxides in the slag can be classified as acidic, basic or neutral [10, 15, 108, 110]. The basic oxide is the O^{2-} ion donor (supplier) and the acid oxide is the O^{2-} ion acceptor (consumer) as shown in equations 2.35a and 2.35b [69, 108, 110], respectively. Neutral

oxides are also known as amphoteric oxides and they can combine with both the basic and acid oxides [15, 108].

$$MO = M^{2+} + 2O^{2-} \quad 2.35a$$

$$SiO_2 + 2O^{2-} = SiO_4^{4-} \quad 2.35b$$

A slag is therefore considered as acidic when it is rich in the acidic oxides (SiO_2, P_2O_5 etc.) and basic when it is rich in basic oxides (CaO, Na_2O, K_2O etc.) [110]. The basic slag contains a lot of O^{2-} ions and the acidic slag contains fewer O^{2-} ions [105, 111]. The basic metal oxides will be absorbed in the acidic slag and the acidic oxides will be absorbed in the basic slag.

The bond in the Si-O-Si chain is broken to form smaller units [108] such as SiO_4^{4-}, with the addition of CaO as shown in equation 2.36 and, the viscosity of the slag decreases.

$$Si_2O_7^{6-} + O^{2-} = 2SiO_4^{4-} \quad 2.36$$

Similarly, the addition of CaF_2 breaks down the bond in the Si-O-Si chains to release free O^{2-} ions as shown in equation 2.37. The free O^{2-} ions from equation 2.37 may bring more depolymerisation according to equation 2.36 such that the addition of CaF_2 significantly decreases the viscosity of silicate melts.

$$Si_2O_7^{6-} + 2F^- = 2SiFO_3^{3-} + O^{2-} \quad 2.37$$

The chemical composition of the slag depends on a number of factors such as mineralogical composition of the ore/concentrates, the extraction method and the type of the furnace. The different types of slags have been discussed by Rosenqvist [28].

2.9.1 Solubility of CaS in slag

Calcium sulphide (CaS) is one of the main reaction products from the carbothermic reduction of mineral sulphide concentrates in the presence of CaO. However, the solubility of CaS in slag is low even at 1573 K. The highest solubility of CaS at 1573 K

occurs in the $CaO\text{-}SiO_2\text{-}CaF_2$ system (figure 2.14) and this means that CaF_2 must be added as a fluxing agent in order to produce CaS containing slag. Even though figure 2.14 shows that the $CaO\text{-}SiO_2\text{-}CaF_2$ system can dissolve up to 10 wt. % CaS, there is yet another obstacle for achieving liquid metal / molten slag separation in the reduction of Cu-Fe-Co sulphide concentrates because, the Cu-Co-Fe alloys have high melting temperatures.

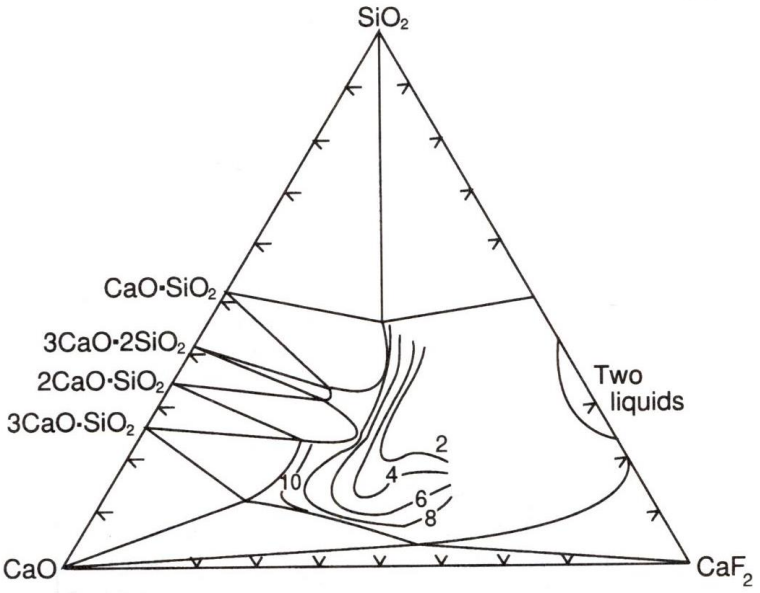

Figure 2.14 - Calcium sulphide (CaS) solubility contours for the $CaO\text{-}SiO_2\text{-}CaF_2$ system at 1573 K, in weight percent [108]

2.10 Recovery of metallic phases from slag

As stated in the introduction (chapter one), copper smelting and converting slag dumps contain significant quantities of copper and cobalt. In addition, the slag from the copper smelting and converting processes, contain more than 20 wt. % Fe. The metallic values (Cu, Co and Fe) in the slag are mainly present in the oxide form. Microscopic examinations of copper smelting and converting slag have revealed that the Cu and Co oxides are either dissolved in the oxide (fayalite, glassy) phases or exist as small spinel phases enclosed within the oxide phases [20, 25].

As a majority of Cu and Co from the slag are mainly in the oxide form [3], the carbothermic reduction (equation 2.38) may be employed to produce metallic/alloy

phases (M) of Cu, Co and Fe. The thermodynamic prediction indicates that Cu,Co and Fe oxides can be reduced to metallic state at temperatures as low as 1073 K [24, 28, 85].

$$MO + C = M + CO(g) \qquad 2.38$$

However, the solid state carbothermic reduction of metal (Cu, Co and Fe) oxides from the slag phase may not be straight forward. This is due to lack of contact between the metal oxides in the silicate phase(s) and the solid carbon. It may be suggested that the reduction of the metal oxides may require different mechanism(s), other than the direct contact between metal oxides and solid carbon. Therefore, metallisation may proceed as follows: (i) the diffusion of the O^{2-} and metal (M^{2+}) ions from the metal oxide (MO) to the slag/carbon interface (figure 2.15a). The rate of reaction may be determined by the diffusion of O^{2-} and metal (M^{2+}) ions through the slag matrix and/or gasification of carbon and (ii) diffusion of carbon/CO gas in the slag matrix so that the metallic phase is formed within the slag phase (figure 2.15b). This mechanism may be undesirable for solid state reduction as a result of the lack of separation of the metallic phases from the slag phase.

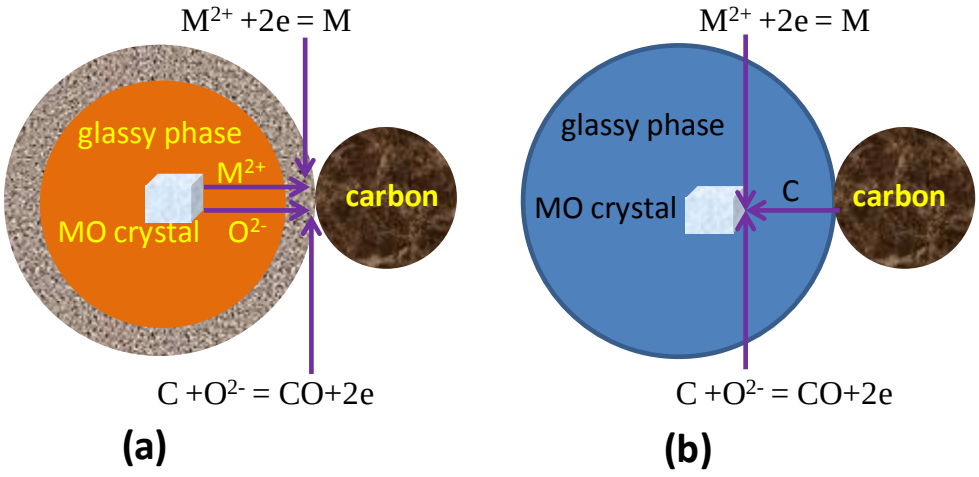

Figure 2.15 – Illustration of reduction mechanism of the metal oxide crystal in slag

2.10.1 Thermodynamic consideration

The Cu-Co-Fe-Ca-O-S predominance area diagram at 1273 K is shown in figure 2.16, from which the following observations can be made:

i. Metal oxides ($CoFe_2O_4$ and Cu_2O) co-exist with $CaSiO_3$ and SiO_2 at $\log_{10}(P(O_2))$ > -6.4.

ii. Metal sulphides ($CuFeS_2$, Cu_5FeS_4, Co_9S_8, FeS) co-exist with $CaSiO_3$ and SiO_2.

iii. Metal sulphides ($CuFeS_2$, Cu_5FeS_4, Co_9S_8, FeS) co-exist with CaS and SiO_2 at lower partial pressure of O_2 gas.

iv. Preferential sulphidisation of Cu and Co may be achieved based on the partial pressures of SO_2 and O_2 gases.

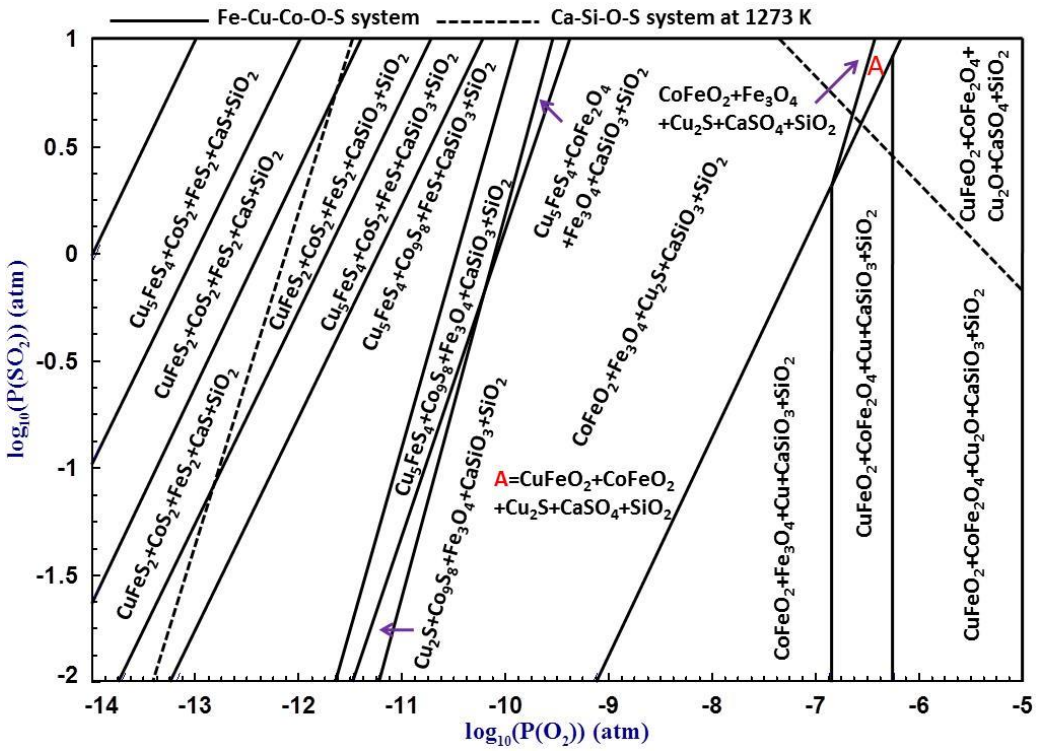

Figure 2.16 – The Fe-Co-Fe-Ca-Si-O-S predominance area diagram at 1273 K constructed by superimposing the Fe-Co-Fe-O-S (continuous line) and the Ca-Si-O-S (dotted line) predominance area diagrams, computed using FactSage software [24]

2.10.2 Sulphidisation of metal oxides

Based on the Cu-Co-Fe-Ca-O-S predominace area diagram in figure 2.16, carbon and SO_2/S_2 are required for the sulphidisation of the metal oxides because: (i) the partial pressure of O_2 gas should be lower ($\log_{10}PO_2$))(atm) < -6.1) and (ii) the partial pressure of SO_2/S_2 gas should be high as shown in figure 2.16. SO_2 and S_2 gases can be obtained from the reduction calcination of $CaSO_4$ [30] and from the thermal decomposition of FeS_2, respectively.

2.10.2.1 Sulphidisation of metal oxides with pyrite (FeS_2)

As already stated, pyrite (FeS_2) evolves S_2 gas as it decomposes to FeS above 1016 K (reaction 2.39a) such that it has been used for sulphidizing the metal oxides into the metal sulphides (equation 2.39b) [113, 114]. The iron sulphide ($Fe_{1-x}S$) from the thermal decomposition of FeS_2 may further react with Cu-O and Co-O according to equations 2.39a and 2.39d, respectively. The un-oxidised FeS reacts with Cu_2S and CoS to form Cu-Co-Fe-S matte phase.

$$FeS_2 = FeS + 0.5S_2(g) \quad \text{2.39a}$$

$$MO + 0.5S_2(g) + C = MS + CO \quad \text{2.39b}$$

$$FeS + Cu_2O = Cu_2S + FeO \quad \text{2.39c}$$

$$FeS + CoO = CoS + FeO \quad \text{2.39d}$$

The sulphidisation of metal oxides in the presence of pyrite (FeS_2) has three major draw backs: (i) the S_2 gas may escape out, without reacting with the metal oxides, because of the rapid decomposition of pyrite (FeS_2) above 1016 K, (ii) large quantities of FeO rich slag may be generated because of the presence of FeO from reactions 2.39c and 2.39d, at low addition of FeS_2 and (ii) a FeS rich matte may be generated at high addition of FeS_2, because of the FeS from the sulphidisation of FeO in the slag phase and, from equation 2.39a.

As pyrite (FeS_2) decomposes at low temperature, it has been used for sulphate roasting of the slag, in which Cu and Co are converted to sulphates. However, studies by Tumen and Bailey have showed that even though more than 90 % of copper can be recovered through sulphate roasting of slag with pyrite (FeS_2), the recovery of Co and Ni were very poor [115].

2.10.2.2 Sulphidisation of metal oxides with $CaSO_4$

Even though the thermal decomposition of calcium sulphate ($CaSO_4$) takes place at about 1473 K, the decomposition can occur at temperature as low as 1073 K, in the

presence of carbon (equation 2.40). Reaction 2.40 is known as reduction calcination [30].

$$CaSO_4 + 0.5C = CaO + SO_2 + 0.5CO_2(g) \qquad 2.40$$

The SO_2 gas from the reduction calcination of $CaSO_4$ will react with the metallic oxides to give metal sulphides as shown in equation 2.41a. The summation of equation 2.40 and 2.41a gives the overall equation 2.41b.

$$MO + SO_2(g) + 1.5C = MS + 1.5CO_2(g) \qquad 2.41a$$

$$MO + CaSO_4 + 2C = MS + CaO + 2CO_2(g) \qquad 2.41b$$

The use of $CaSO_4$ is attractive because: (i) $CaSO_4$ is readily available, (ii) sulphidisation may be achieved with minimal or no generation of SO_2 gas via reaction 2.41b i.e., by carefully controlling the molar ratio of $CaSO_4$/C [85] and (iii) a calcium silicate slag may be produced which may be used for construction and glass making. The sulphidisation of slag in the presence of $CaSO_4$, has been carried out by Matusewicz and Mounsey [113]. However, it was found that $CaSO_4$ was inappropriate for facilitating matte production [113] but no details were given out, regarding the type of carbon, stoichiometric ratios of $CaSO_4$ and carbon.

The reduction calcination of $CaSO_4$ has been studied by Turkdogan and Vinters [85] using various types of carbon. The reaction was completed in about 40 minutes and 120 minutes at 1373 K and 1273 K, respectively, in the presence of graphite. The reduction calcination of $CaSO_4$ with graphite yielded, mainly CaO and SO_2 gas. However, only 20 – 40 % of SO_2 gas was given off in the presence of more reactive carbon such as coke and coconut charcoal because part of $CaSO_4$ was calcined to CaS (figure 2.17a). Turkdogan and Vinters also studied the effect of changing the molar ratio of graphite in equation 2.40, the amount of SO_2 gas decreased at $C/CaSO_4 > 0.5$ mole ratio, (figure 2.17b) because of the calcination of $CaSO_4$ to CaS.

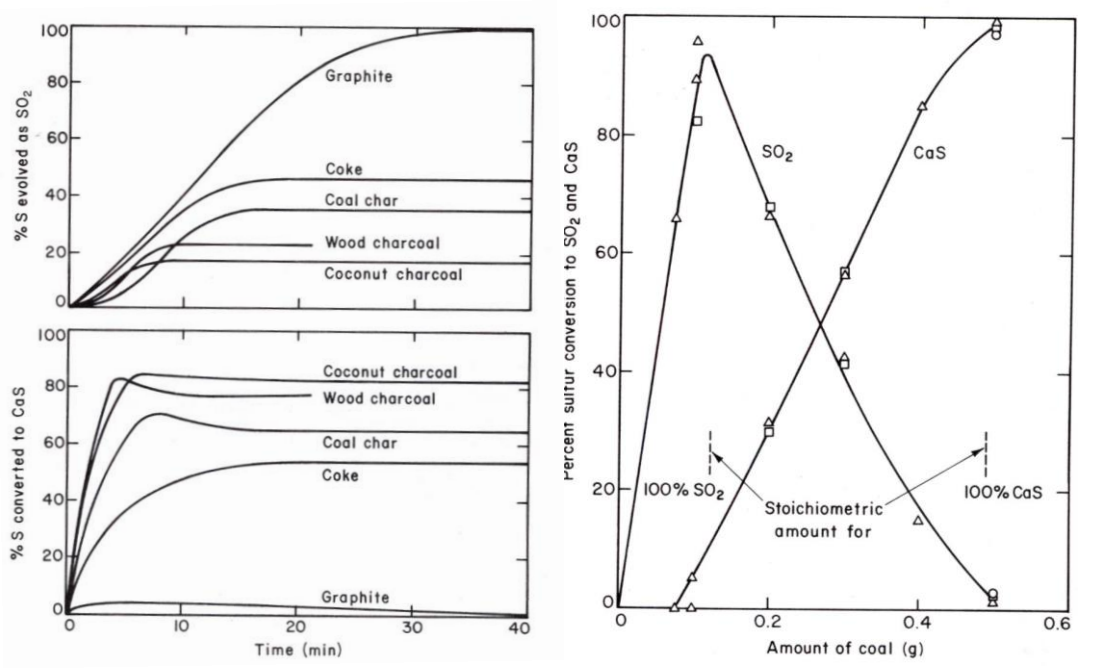

(a) (b)

Figure 2.17 – (a) Reduction calcination of $CaSO_4$ according to equation 2.40 with various types of carbon and (b) effect of changing the quantity of graphite during reduction calcination of 1.65g of $CaSO_4$ [85]

2.11 Equilibrium phase system

The froth flotation mineral concentrates consist of various phases and hence several phases are expected to form during reduction at high temperatures (above 1073 K). It is for this reason that various phase systems are discussed in the section.

2.11.1 Cu-Fe-S system

There are several phases in the Cu-Fe-S system, depending on temperature and composition of Cu, Fe and S. A liquid phase is formed in the region of 55 at. % - 60 at. % Cu, 15 at. % - 28 at. % Fe and 40 at. % - 45 at. % S, at 1073 K as shown in figure 2.18. The liquid phase is in equilibrium with Cu, Fe, Cu and Fe, $Fe_{1-x}S$ (Po) phases, depending on composition. Part of the liquidus surface of the copper-iron-sulphur system is shown in figure 2.19 [28] and it is evident that the liquidus temperature increases towards the Cu-Fe line. Copper mattes are metal rich and have composition lying between the FeS and Cu_2S line [111].

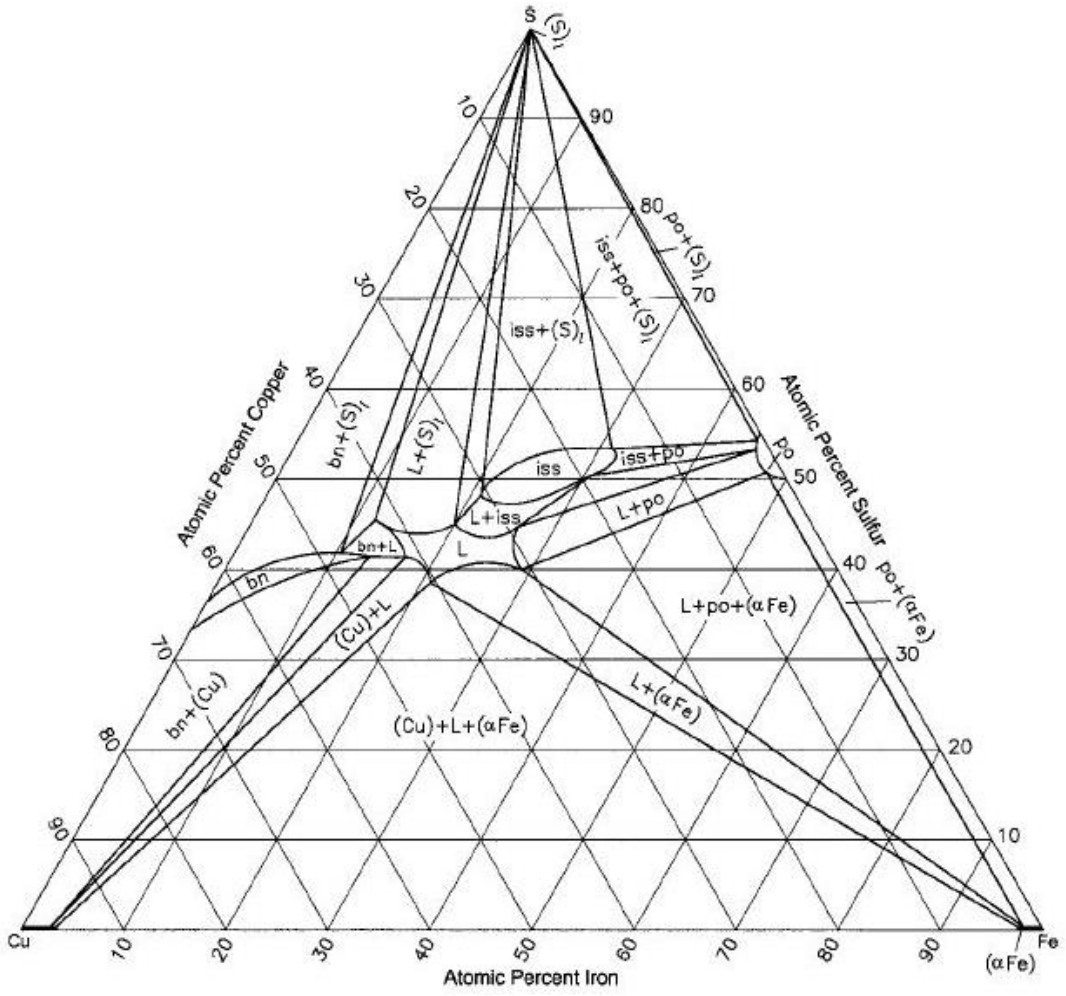

Figure 2.18 - The copper-iron-sulphur tenary system at 1073 K [91], bn is bornite (Cu_5FeS_4) and Po is pyrrhotite ($Fe_{1-x}S$)

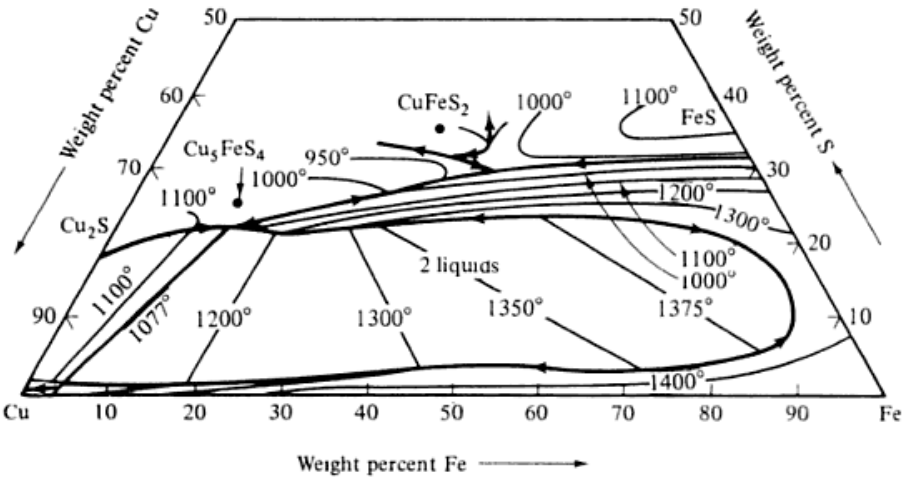

Figure 2.19 – Part of the Cu-Fe-S system showing the liquidus surface [28]

The Cu_2S-FeS pseudo binary phase diagram is shown in figure 2.20 [15]. The Cu_2S and FeS liquid phases are completely miscible because of the slight negative deviation from ideal behaviour [14]. The solid solubility of FeS in Cu_2S and Cu_2S in FeS are about 50 wt. % and 10 wt. %, respectively. There is a eutectic reaction at about 1198 K. The eutectic melt may be formed during carbothermic reduction of $CuFeS_2$ since Cu_2S and FeS can be produced via equation 2.42, at low addition of CaO or low reaction.

$$2CuFeS_2 + CaO + C = Cu_2S \bullet 2FeS + CaS + CO \qquad 2.42$$

It can be deduced from the Cu_2S-FeS pseudo binary phase diagram in figure 2.20 that: (i) Cu_5FeS_4 or Cu_2S + Cu_5FeS_4 are the main phases that can be obtained after heating the Cu_2S rich mineral sulphide concentrates and (ii) $CuFeS_2$ + Cu_5FeS_4 + FeS are the main phases than can be obtained after heating the FeS or FeS_2 rich mineral sulphide concentrates.

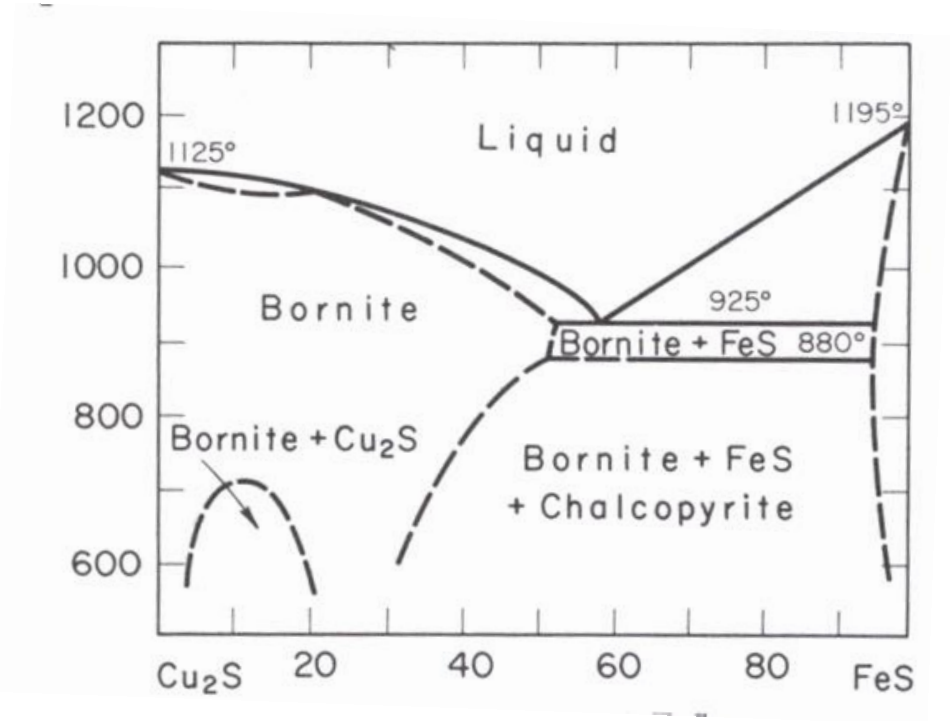

Figure 2.20 – The Cu_2S-FeS pseudo binary phase diagram [15]

2.11.1.1 Copper-sulphur (Cu-S) system

The copper-sulphur (Cu-S) system has been studied by Chakrabarti and Laughlin [116] and is shown in figure 2.21. There are a number of intermediate compounds in the Cu-S

system and they are; covellite (CuS) and chalcocite (Cu_2S) [117], djurleite ($Cu_{1.96}S$), digenite ($Cu_{2-\delta}S$), anilite ($Cu_{1.75}S$) [116]. Covellite (CuS) decomposes to digenite ($Cu_{1.96}S$) and S_2 gas at about 780 K (507 °C) [116]. There are two miscibility gaps [118] or immiscibility regions between L_1 and L_2 above 1378 K [10, 28, 116, 119] and between L_2 and L_3 above 1086 K [116]. There is a eutectic reaction at 1340 K (1067 °C) and 0.75 wt. % S. The solid solibility is very low in the Cu-S system due to the high tendency of compound formation [10].

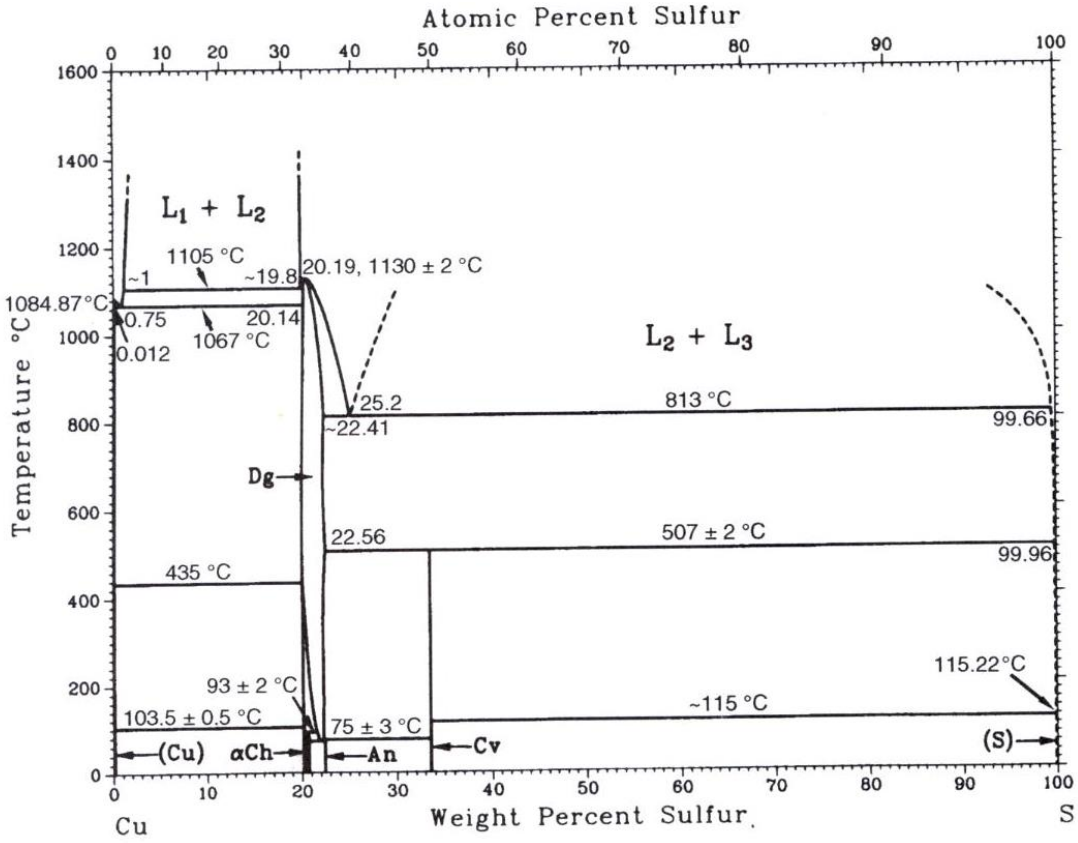

Figure 2.21 – Copper-sulphur binary phase diagram [7]

2.11.1.2 Iron-sulphur (Fe-S) system

The iron-sulphur system is shown in figure 2.22. There are two intermediate compounds in the system (pyrite (FeS_2) and the non-stoichiometric pyrrhotite ($Fe_{1-x}S$)), and both are stable at room temperature. $Fe_{1-x}S$ melts congruently at about 1462 K whereas FeS_2 decomposes at about 1016 K to give $Fe_{1-X}S$ and S_2 gas. The region between $Fe_{1-X}S$ and Fe is important during carbothermic reduction of the mineral sulphides in the presence of CaO, considering the fact that FeS_2 decomposes at above 1016 K. There is a eutectic reaction between Fe and $Fe_{1-x}S$, at about 1261 K and 31.6 wt. % S.

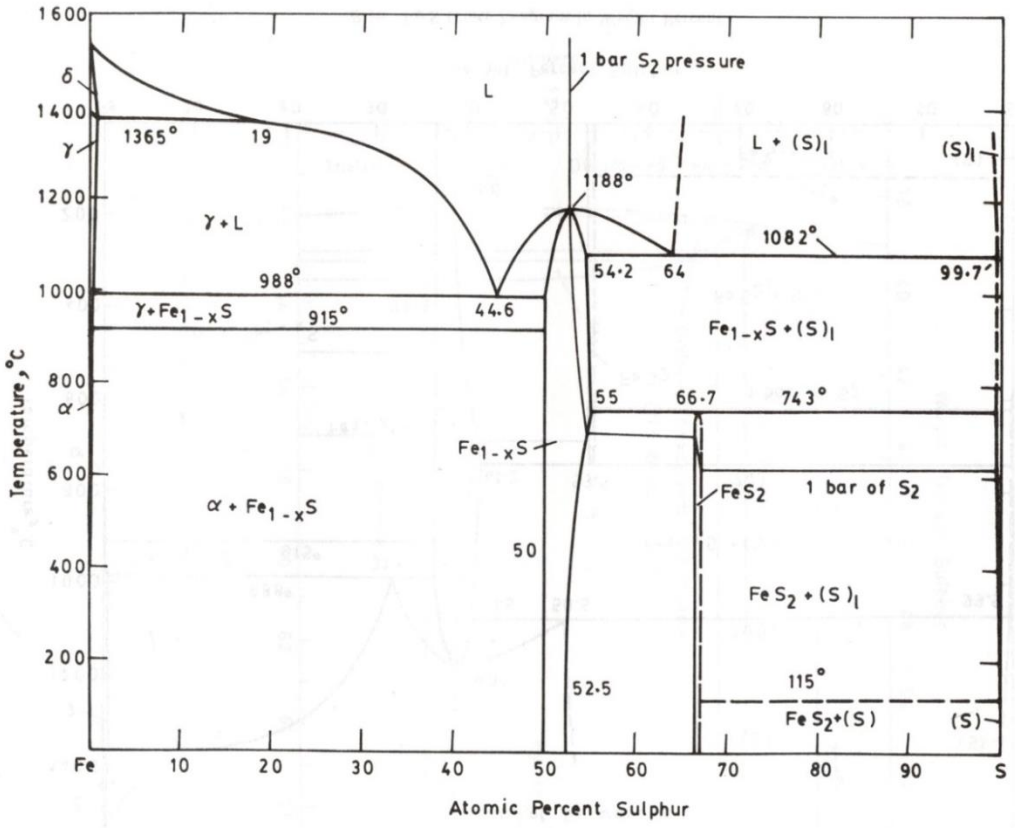

Figure 2.22 – The iron-sulphur binary phase diagram [120]

2.11.2 Copper-cobalt-sulphur system

The copper-cobalt-sulphur system is essential as it constitutes the major cobalt sulphide mineral ($CuCo_2S_4$) [13]. The system has been studied by Claig et al. and is shown in figure 2.23 at 1173 K [121, 122]. There are two liquid phases in the system at 1173 K. Liquid i has 70 wt. % - 74 wt. % Cu and extends from the Cu-S line, to a point with about 18 wt. % Co. Liquid ii has about 26 wt. % - 30 wt. % S and extends from the Co-S.

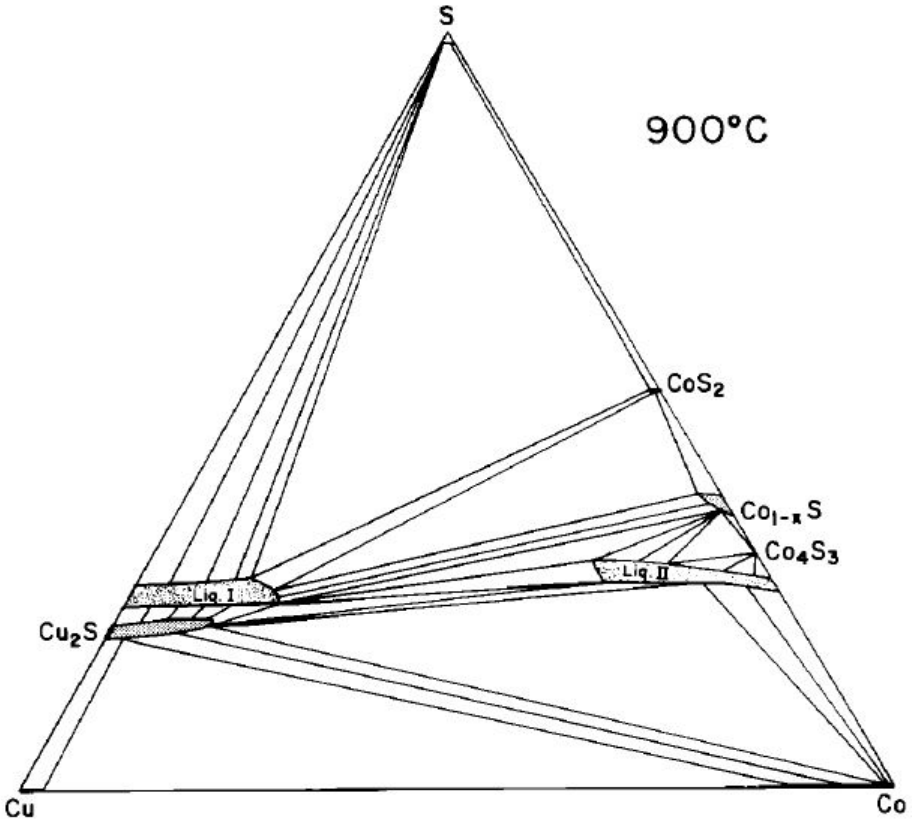

Figure 2.23 – The copper-cobalt-sulphur (Cu-Co-S) system at 1173 K [121, 122]

2.11.2.1 Cobalt-sulphur (Co-S) system

The cobalt-sulphur system is shown in figure 2.24 [120]. It consists of five intermediate phases namely $Co_{1-x}S$ (non-stoichiometric), CoS_2, Co_9S_8, Co_4S_3 and CoS_2) [123]. Cobalt disulphide (CoS_2) has a pyrite (FeS_2) type of structure [5] and hence they form solid solution. The solubility of sulphur in cobalt is very limited (about 0.04 wt. %) [5] because of high tendency to compound formation in the Co-S system. There is a eutectic reaction involving Co_4S_3 and Co at 1148 K (875 °C) and 26.6 wt. % sulphur. Co_4S_3 is stable between 1058 K (785 °C) and 1203 K (930 °C). Co_9S_8 decomposes to Co_4S_3 and $Co_{1-x}S$ upon heating to 1107 K wheras Co_3S_4 decomposes to CoS_2 and $Co_{1-x}S$ upon heating to 930 K. CoS_2 is stable down to room temperature.

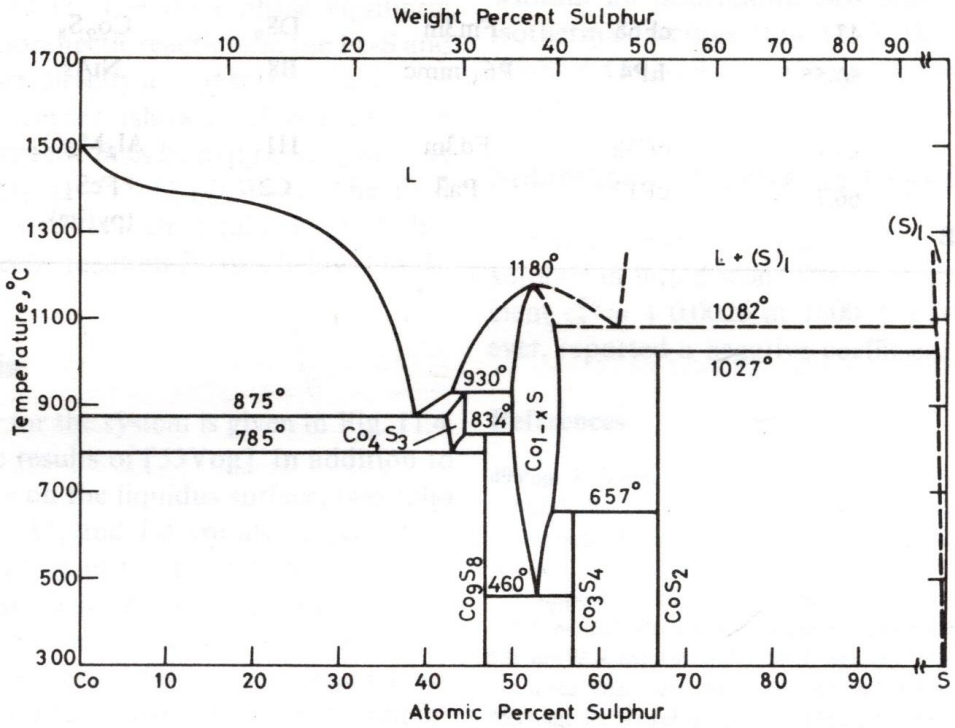

Figure 2.24 – Cobalt-sulphur (Co-S) binary phase diagram [120]

2.11.3 Copper-cobalt-iron (Cu-Co-Fe) system

The copper-cobalt-iron system is very important in the present investigation as it constitutes the metallic phases (Cu,Co and Fe) from the reduction of the mineral sulphide concentrates. The only phases in the Cu-Co-Fe system are those from the binary systems of Cu-Fe, Cu-Co and Co-Fe and they are γ-Cu, α-Co, ε-Co, α-Fe, γ-Fe and δ-Fe [124]. The solubility of Cu in α-(Fe-Co) and γ-(Co-Fe) and, of Fe and Co in Cu are still small [124]. The Cu-Co-Fe ternary systems at 1073 K and 1273 K are shown in figures 2.25a and 2.25b, respectively [124]. It can be observed from figures 2.25a and 2.25b that the solubility of Cu in Co-Fe alloy phase is very low as discussed above and hence the Co-Fe and Cu phases can be produced during carbothermic reduction of the mineral sulphides concentrates at lower temperatures.

The liquidus temperature for the Cu-Co-Fe system has been investigated by Banda et al. using differential thermal analysis (DTA) [125]. The liquidus temperature increases with increase in the Fe/Cu ratio, at constant cobalt content [125]. Cobalt has less influence on the liquidus temperature [125]. There is liquid separation between the Co-Fe and Cu molten phases in the system [126].

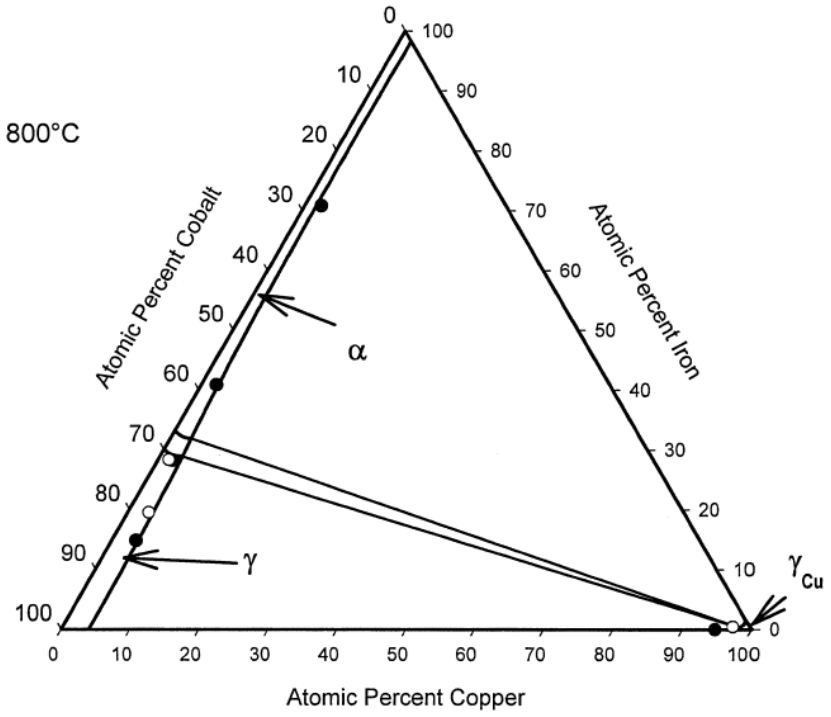

(a)

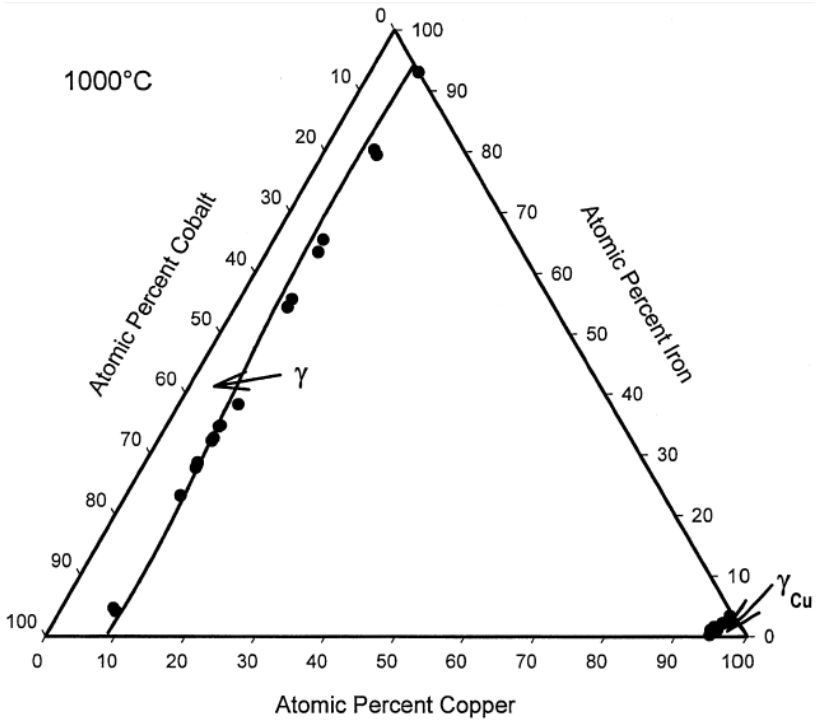

(b)

Figure 2.25 – The Cu-Co-Fe ternary system at; (a) 1073 K and (b) 1273 K. (──) calculated phase boundaries [127] and, compositions of the phases in equilibrium in the; (●) two phase region and (o) three phase region

2.11.3.1 Copper-cobalt phase diagram

The Cu-Co system is shown in figure 2.26. There are two crystalline forms of Co and they are ε-Co with a hexagonal closed packed structure and α-Co a face centered cubic structure [5, 6, 128]. The ε-Co phase is stable from room temperature to 695 K (422 °C) and the γ-Co phase is stable above this temperature [128]. There are three phases in the Cu-Co system above 695 K and they are: (i) α-cobalt (0 wt. % – 20.9 wt. % Cu), (ii) copper (0 wt. % – 7 wt. % Co) and (ii) liquid phase [23]. The three phases are in equilibrium at 5.1 wt. % Co, 8.4 wt. % Co and 87.4 wt. % Co [129]. The liquidus temperature is depressed with increase in copper content, reaching minimum at 100 wt. % Cu.

The variation of the lattice parameter in the Cu-Co system has been shown by Nishizawa and Ishida [130]. The lattice parameter of FCC cobalt from the quenched melt increases with increase in the Cu content and thus the 2θ angle peak position shift to the lower angle, in the XRD pattern. The Cu-Co system has the positive enthalpy of mixing which is an indication of phase separation [23, 131]. The curie temperature decreases within the α-Co phase, with increase in the copper content [130].

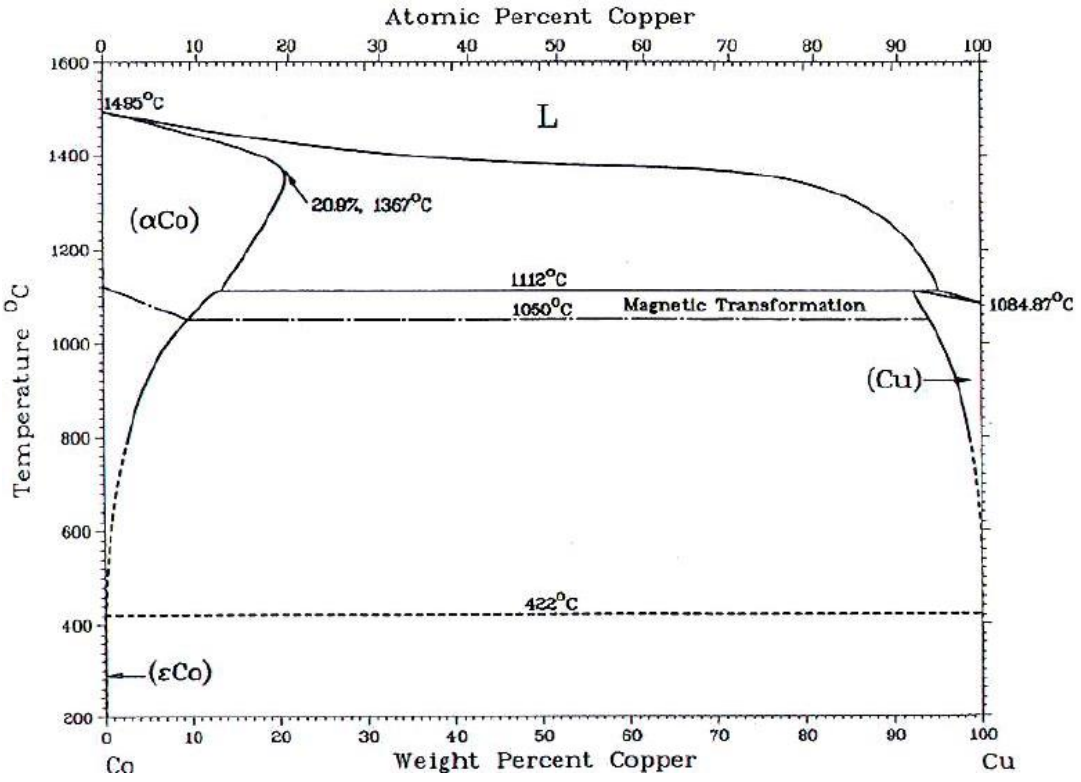

Figure 2.26 – The copper-cobalt binary phase diagram [23]

2.11.3.2 Iron-copper (Cu-Fe) system

The iron-copper system is shown in figure 2.27 and is important as it consistitute the metallic phases resulting from the reduction of the $CuFeS_2$ and Cu_5FeS_4 mineral phasess. The Cu-Fe system has five phases and they are; three iron rich phases (α-Fe, γ-Fe and δ-Fe), copper rich (FCC) and the liquid phase. The maximum solubility of Cu in Fe is about 12 wt. % at 1683 K [23]. The α-Fe phase has the lowest solubility of copper (2.2 wt. %) at the eutectoid temperature (1123 K). The maximum solubility of copper in δ-Fe is about 8.1 wt. %, at the peritectic temperature (1758 K). There is another peritectic at about 1369 K. The copper-iron system has positive deviation fron ideal and hence it has a de-mixing tendency [23, 131-135].

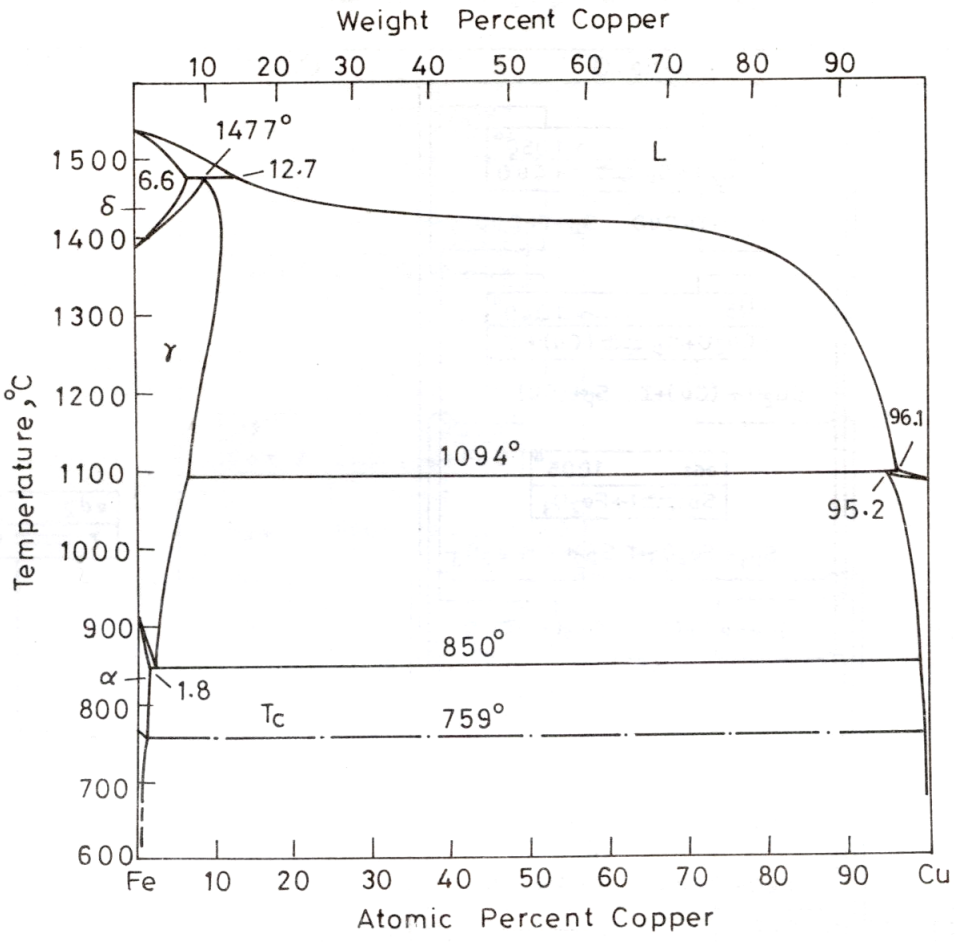

Figure 2.27 – Copper-iron phase diagram [136]

2.11.3.3 Iron-cobalt (Fe-Co) system

The iron-cobalt system is shown in figure 2.28. It has a very narrow solidification temperature range [137] of 2 K - 3 K, between 30 at. % to 100 at. % Co [23]. The liquidus line falls from the melting points of iron 1811 K (1538 ºC) and cobalt 1768 K (1495 ºC) and reaches minimum temperature of 1749 K at 66.8 at. % Co [129]. The maximum solid solubility of α-cobalt in α-iron is about 75 wt. % but there is complete solid solubility between α-cobalt and γ-iron [23]. The ordering of equiatomic (CoFe) alloy takes place below 730 °C [129, 138]. The iron atoms take up the corner atoms while cobalt atoms take up the cube-centre positions in the ordered CoFe phase (α′) [138]. There is random arrangment of the atoms on the corners and center of the cubic unit cell [138]. The curie temperature (T_c) increases as Co dissolves in Fe. As there is extensive solid solubility in Co-Fe system, the Co-Fe alloy phase will be formed during reduction of mineral sulphides.

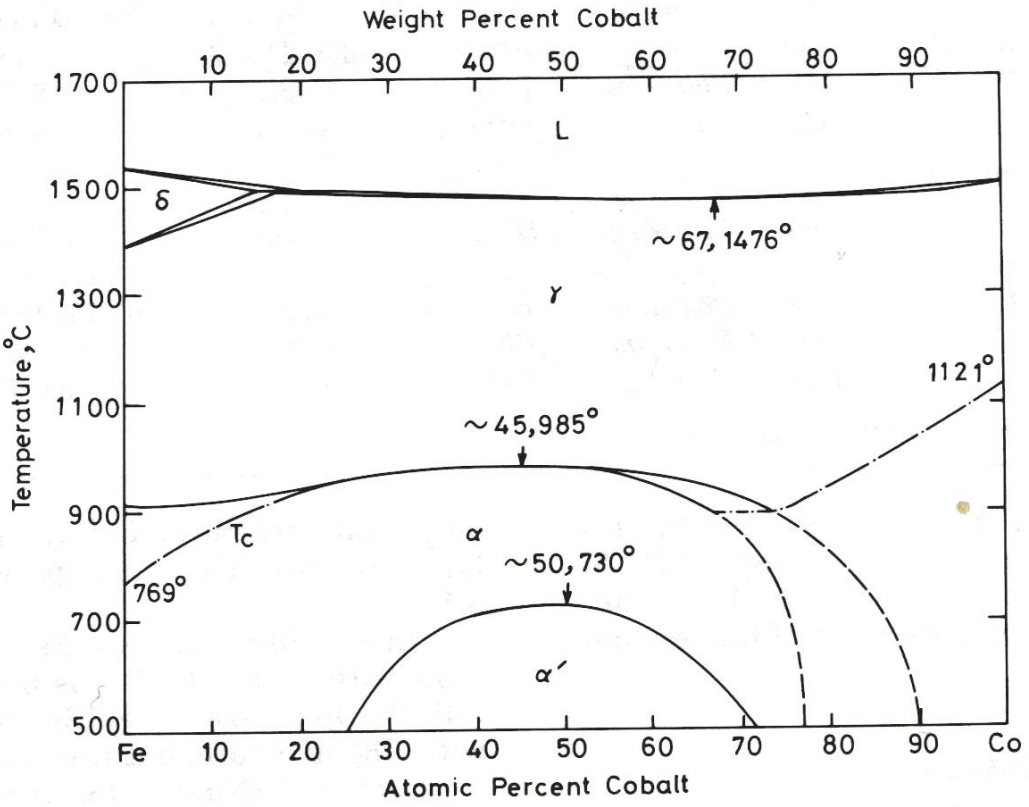

Figure 2.28 – The iron-cobalt binary phase diagram [120]

2.11.4 Iron-oxygen-sulphur (Fe-O-S) system

The iron-oxygen-sulphur system is important because the reduction of FeS or FeS_2 mineral phases may yield the FeO phase (equation 2.43) which may react with FeS. There is a eutectic reaction between FeO and FeS at 1193 K [139]. There is also a Fe-FeO-FeS tenary eutectic at about 1188 K, with a composition of about 68 wt. % Fe, 24 wt. % S and 8 wt. % O [140]. The presence of the Fe-O-S liquid phase may enhance the reduction of the FeS_2/FeS mineral phases.

$$FeS + CaO = FeO + CaS \qquad 2.43$$

2.11.5 Calcium-sulphur-oxygen (Ca-O-S) system

The Ca-O-S system is important as it shows how CaO reacts with sulphur gas under low and high partial pressure of O_2 gas or under oxidising and reducing atmosphere. The Ca-O-S stability diagram is presented in figure 2.29 [28, 41] and it can be observed that for a fixed partial pressure of O_2 gas, CaO may react with sulphur gas, to form $CaSO_4$ and CaS at low and high temperatures, respectively. Similarly, CaO may react with sulphur gas to form $CaSO_4$ and CaS at high and low partial pressure of O_2 gas, respectively. Figure 2.29 shows that CaS can be converted to CaO (regeneration of CaO) and $CaSO_4$ by controlling the partial pressure of O_2 gas. The stability region of CaO increases with decrease in the activity of CaO and partial pressure of O_2 gas. Based on figure 2.29, the mineral sulphides may react with CaO to form CaS or $CaSO_4$ depending on temperature and, partial pressures of O_2 and SO_2 gases.

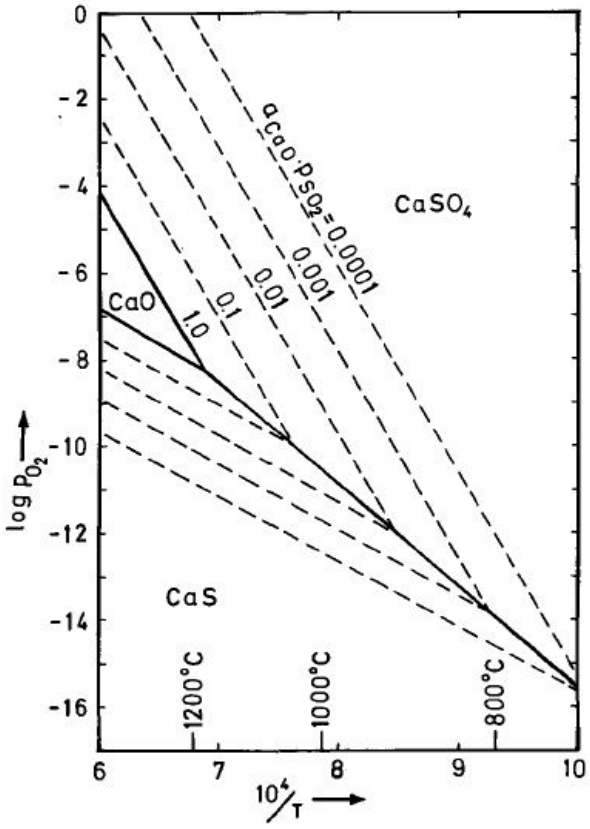

Figure 2.29 – Calcium-oxygen-sulphur system phase stability diagram [41]

2.11.6 Iron-calcium-oxygen-sulphur system

The Ca-Fe-O-S system is important as it relates to the reduction of pyrite (FeS_2) mineral phase in the presence of CaO. Previous study by Jha and Abraham [141] has showed that there is a eutectic between FeO and C_1 (3CaS•4FeO) at temperature of 1153 K (figure 2.30). The presence of the liquid phase may enhance the reduction of the FeS phase during carbothermic reduction. The Ca-Fe-O-S phase stability system has been computed by Kutsovskaya [53]. It was showed that Fe co-exists with CaS at low partial pressure of O_2 and S_2 gases.

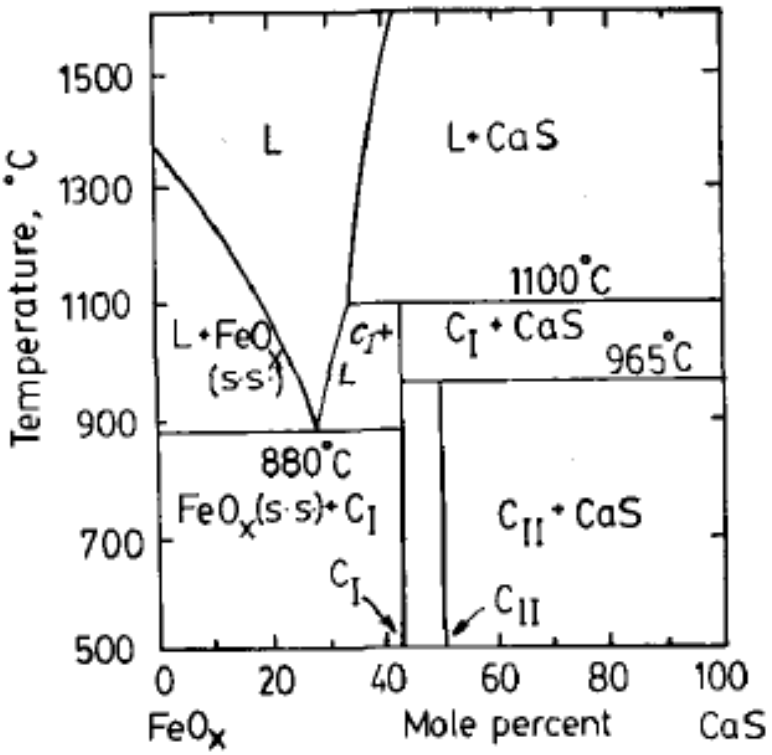

Figure 2.30 – The FeOx-CaS binary phase diagram published by Jha and Abraham [141]

Where C_1(3CaS•4FeO) and C_{11}(CaS•FeO)

2.11.7 Cu-Fe-Ca-O-S system

The Cu-Fe-Ca-O-S system is important for the reduction of Cu-Fe-S mineral sulphides in the presence CaO. The predominance area diagram for the Cu-Fe-Ca-O-S system at 1100 K has been computed by Morris and Flynn [142] and it was showed that sulphur can be fixed as CaS or $CaSO_4$ at low and high partial pressure of O_2 gas, respectively. The computed Cu-Fe-Ca-O-S system by Morris and Flynn [142] further showed that metallisation of copper and iron requires low partial pressure of O_2 and S_2 gases. Therefore, metallisation of copper and iron may not take place if the thermal decomposition of mineral sulphides is higher than the absorption of sulphur by lime.

The plot of oxygen potential against the reciprocal of temperature for the univalent equilibria of the Cu-Fe-Ca-O-S system has been computed by Rosenqvist [41] (figure 2.31). The major observations in figure 2.31 are: (i) metal oxides (CuO, $CuFe_2O_4$) co-exist with $CaSO_4$ at high partial pressure of O_2 gas, (ii) Cu co-exists with $CaSO_4$ and Fe_3O_4 and (iii) Cu co-exists with Fe and CaS at very low partial pressure of O_2 gas. Therefore, mineral sulphides can be roasted in O_2 gas, in the presence of CaO to

obtain metal oxides (CuO, $CuFe_2O_4$, Fe_2O_3) and $CaSO_4$. The lime roast calcine can be treated pyrometallurgically via:

i. Preferential metallisation of Cu, because Cu co-exists with the Fe_3O_4 and $CaSO_4$ phases. This is possible by adding just enough carbon for the reduction of CuO to Cu and, Fe_2O_3 to Fe_3O_4 (equation 2.44).

$$CuO + Fe_2O_3 + CaSO_4 + \frac{4}{3}C = Cu + \frac{2}{3}Fe_3O_4 + CaSO_4 + \frac{4}{3}CO(g) \qquad 2.44$$

ii. Complete metallisation of Cu and Fe as these phase co-exists with CaS. Metallisation may be achieved by adding carbon according to equation 2.45.

$$CuO + Fe_2O_3 + CaSO_4 + 8C = Cu + Fe + CaS \ + 8CO(g) \qquad 2.45$$

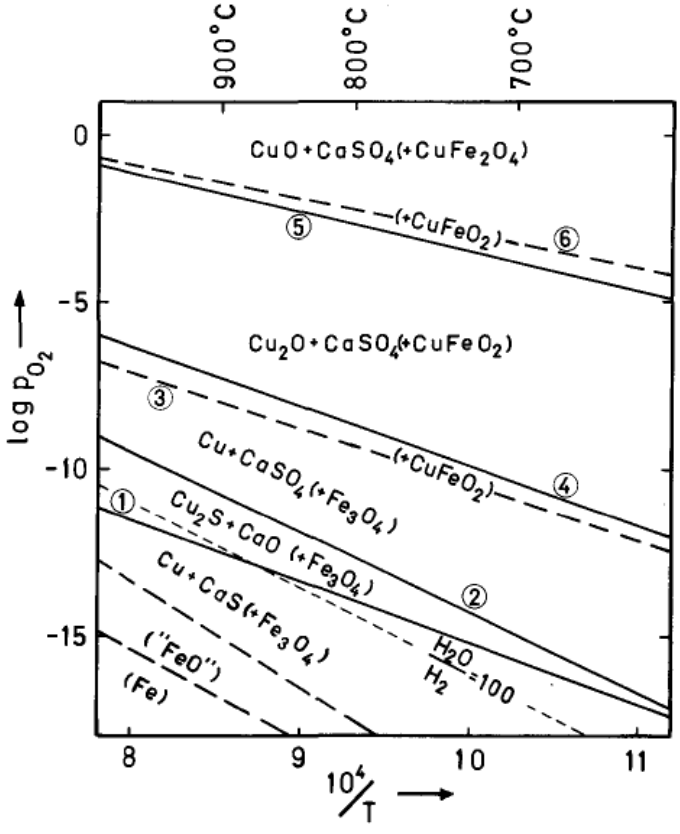

Figure 2.31 – Plot of oxygen potential against the reciprocal of absolute temperature, Cu-Ca-O-S (continuous lines) and Cu-Fe-O (dashed lines) [41]

2.11.8 Cu-Fe-S-O system

The Cu-Fe-O-S system is relevant during reduction of Cu-Fe-S ($CuFeS_2$ and Cu_5FeS_4) type of minerals. The liquidus line for the Cu-Fe-S-O system is shown in figure 2.32 [111] and it can be observed that the lowest liquidus temperature is towards the FeS. There are two eutectics in the system, between Cu_2S and FeS at 1183 K and, between FeO and FeS at 1193 K [139]. The Cu-Fe-O-S liquid phase may therefore be formed during carbothermic reduction of Cu-Fe-S mineral particles via diffusion of the O^{2-} ions into the mineral phase. It can also be observed in figure 2.32 that Cu_2S and FeO are highly soluble in FeS.

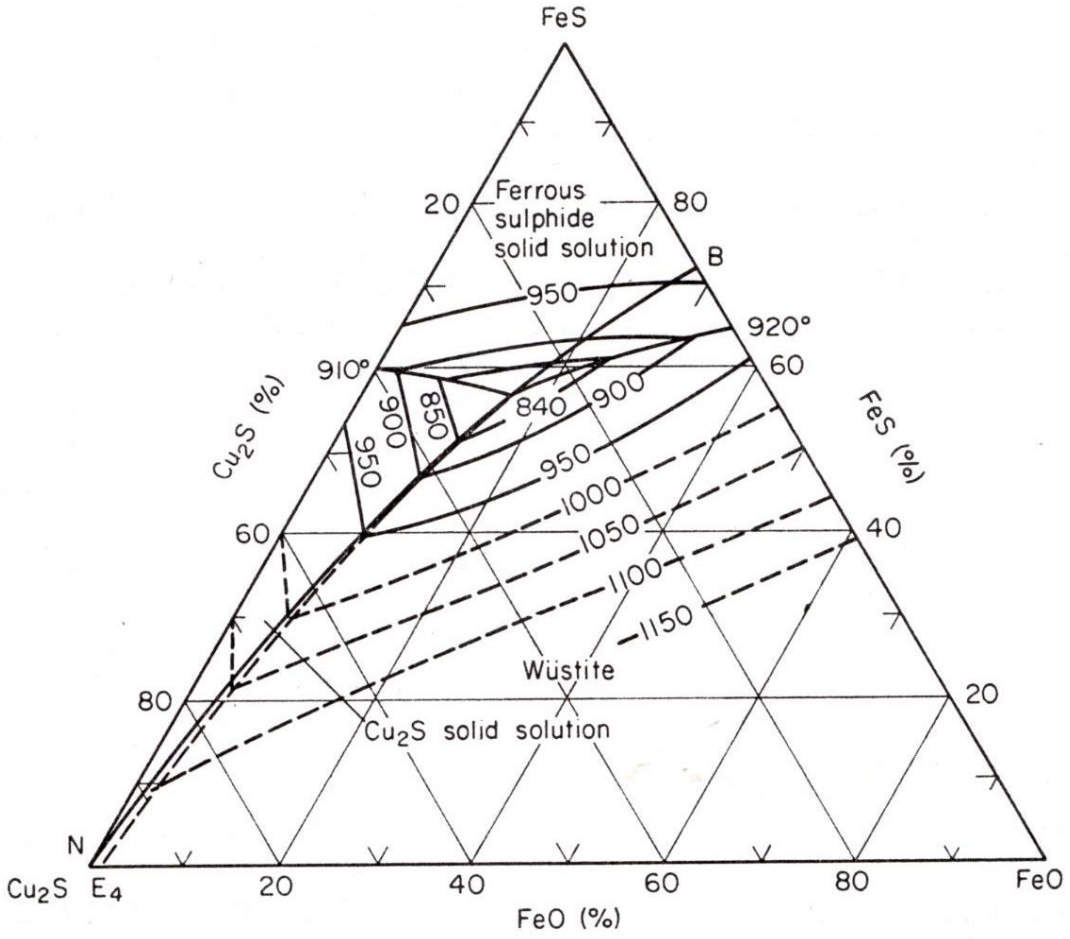

Figure 2.32 – The liquidus surface for the Cu_2S-FeS-FeO system, the BN line represents the composition of matte in equilibrium with SiO_2 saturated SiO_2 + FeO melt [111]

2.11.9 Iron–oxygen system

The iron-oxygen system has been extensively studied by Wriedt [143] and is shown in figure 2.33. There are three intermediate phases in the system and they are hematite (Fe_2O_3), magnetite (Fe_3O_4) and wustite (FeO) [144]. Wustite is the non-stoichiometric compound and can be designated as Fe_xO, where x is between 0.835 and 0.945 [144]. The wustite phase is unstable below 833 K (560 °C), it decomposes to Fe_3O_4 and Fe. As a result, Fe is in equilibrium with Fe_xO and Fe_3O_4, above and below 833 K, respectively. Any FeO phase that forms via ion exchange reaction might be retained or transformed to Fe_3O_4 and Fe, depending on the rate of cooling of the sample. Magnetite (Fe_3O_4) melts congruently at about 1869 K (1596 °C). On the other hand, hematite decomposes to magnetite and oxygen gas at 1730 K (1457 °C).

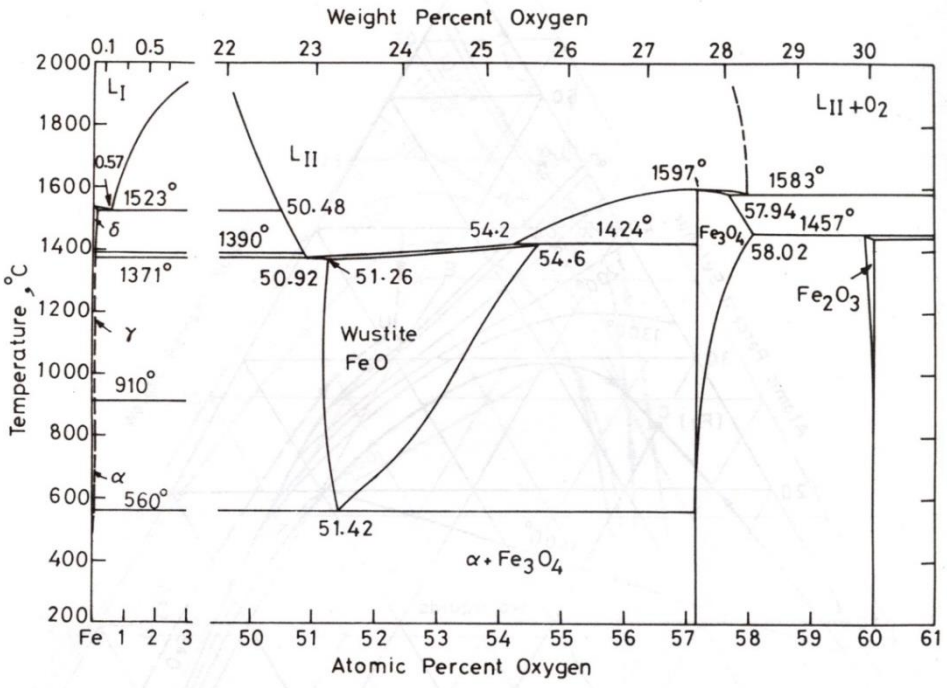

Figure 2.33 – The iron-oxygen binary phase diagram [120]

2.11.10 Calcium-oxygen-iron (Ca-O-Fe) system

The calcium-oxygen-iron system has been discused by Raghavan [120]. The FeO-CaO phase diagram is shown in figure 2.34 and it can be observed that there is a larger solubility between wustite (FeO) and CaO. The only intermediate phase is $Ca_2Fe_2O_5$ and it co-exists with either CaO or FeO. Based on the phase diagram in figure 2.34,

$Ca_2Fe_2O_5$ is expected to be one of the main phase after heat treatment of the Fe-S rich mineral sulphide concentrates in the presence of CaO, assuming that there is no formation of oxysulphide phases. The $Ca_2Fe_2O_5$ phase can also be produced during carbothermic reduction of the mineral sulphides in the presence of CaO, when the reduction reaction is slower than the FeS – CaO exchange reaction, The liquid phase in the FeO-CaO system appears at about 1388 K (1115 °C).

There is a limited solid solubility between CaO and Fe_2O_3 as shown in figure 2.35 because of high tendency to compound formation. The intermediate compounds in the CaO-Fe_2O_3 system are $CaFe_4O_7$, $CaFe_2O_4$ and $Ca_2Fe_2O_5$. $CaFe_4O_7$ is unstable below 1388 K (1155 °C). $CaFe_2O_4$ melts incongruently 1489 K (1216 °C) and $Ca_2Fe_2O_5$ melts congruently at 1722 K (1449 °C). A liquid phase appears at 1478 K (1205 °C) because of the eutectic between $CaFe_2O_4$ and $CaFe_4O_7$.

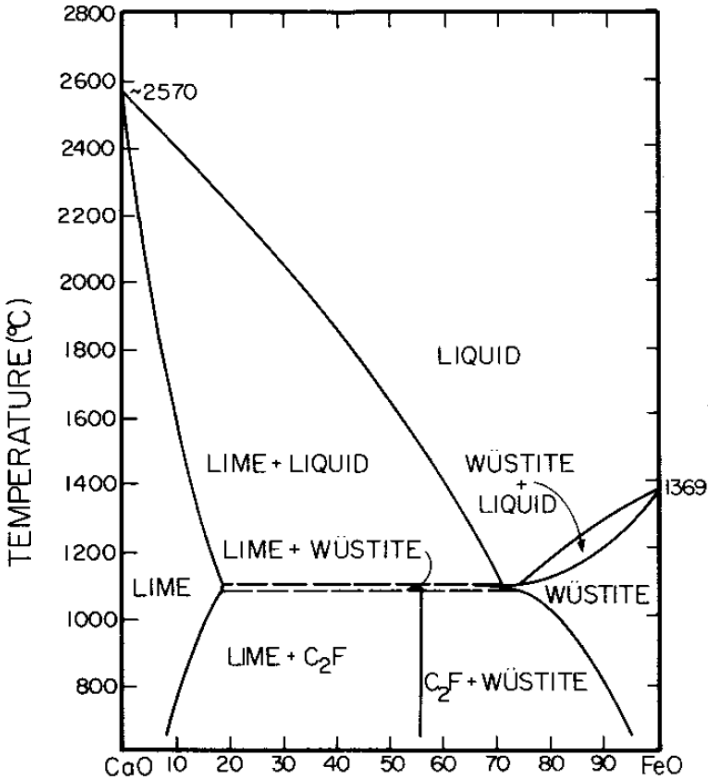

Figure 2.34 - FeO-CaO phase diagram in wt. % [145]

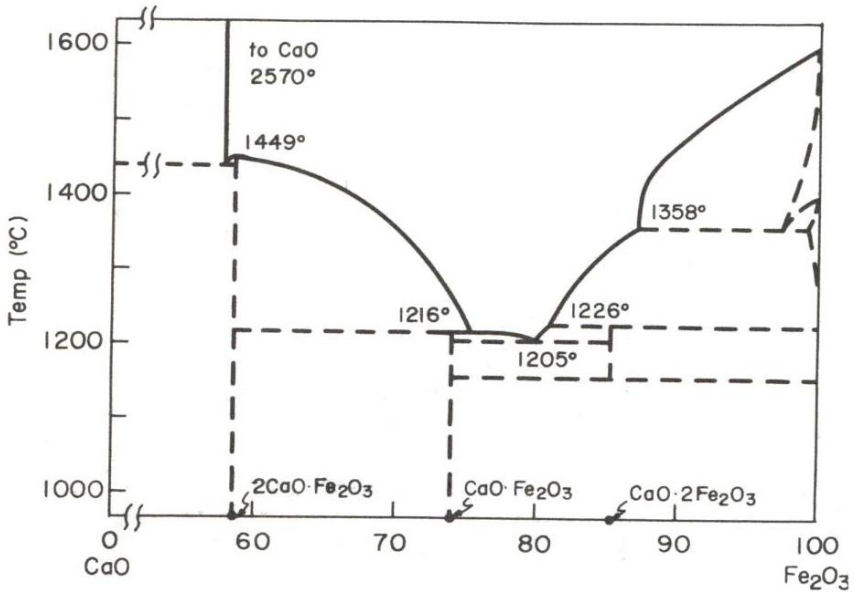

Figure 2.35 - Fe_2O_3-CaO phase diagram in wt. % [146]

2.11.11 Copper-oxygen (Cu-O) system

The Cu-O systen is of importance for the carbothermic reduction of Cu-S mineral phase because, the reduction reaction may proceed via formation of Cu_2O. The copper-oxygen system has been studied by many authors [147-150] and is shown in figure 2.36. The maximum solubility of O in Cu is 0.03 wt. %, at the eutectic temperature, 1339 K (1066 $^{\circ}$C) [150]. There is a liquid miscibility gap above 1496 K (1223 °C). There are two intermediate phases in the system and they are CuO and Cu_2O [150, 151]. The required oxygen potential for the formation (oxidation) of the two intermediate compounds are shown in equations 2.46b - 2.46c. The partial presssure of oxygen should therefore be kept low to avoid the oxidation of copper during reduction, particularly at the low stoichiometric ratio of carbon.

$$4Cu + O_2 \Leftrightarrow 2\,Cu_2O \qquad 2.46a$$

$$Log[PO_2 / bar] = 7.42 - \frac{17400}{T}\ , (1000 - 1339\ K) \qquad 2.46b$$

$$2Cu_2O + O_2 \Leftrightarrow 4\,CuO \qquad 2.46c$$

$$Log[PO_2/bar] = 9.53 - \frac{13300}{T}, (1000 - 1364\ K) \qquad 2.46d$$

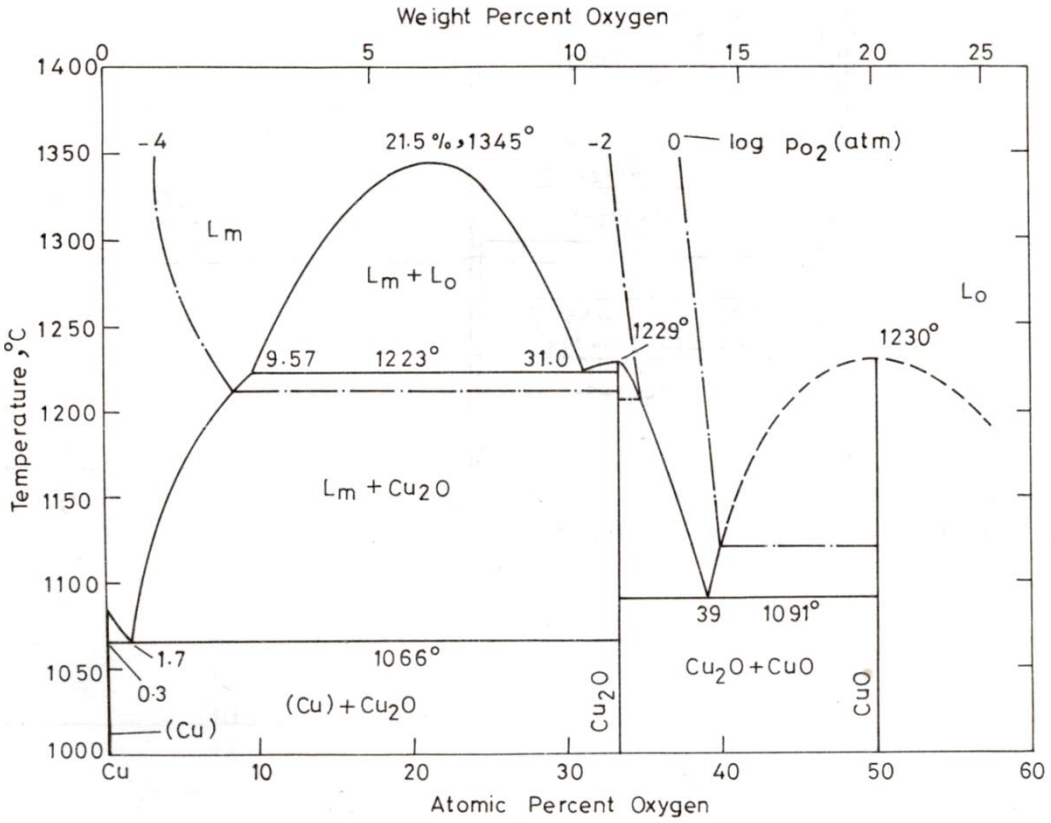

Figure 2.36 – The copper-oxygen (Cu-O) phase diagram [7]

2.11.12 CaO-SiO_2-Al_2O_3 system

The CaO-SiO_2-Al_2O_3 system is shown in figure 2.37 and it is important for producing FeO free slag, such as the blast furnace slag [28]. The lowest liquidus temperature, 1473 K – 1673 K (1200 °C - 1400 °C) and is found in the mixture containing 40 wt. % – 70 wt. % SiO_2 [28]. The activity of pure SiO_2 in the CaO-SiO_2-Al_2O_3 system has been shown by Rosenqvist and it decreases rapidly when the mole ratio of CaO exceeds that of $CaSiO_3$ [28].

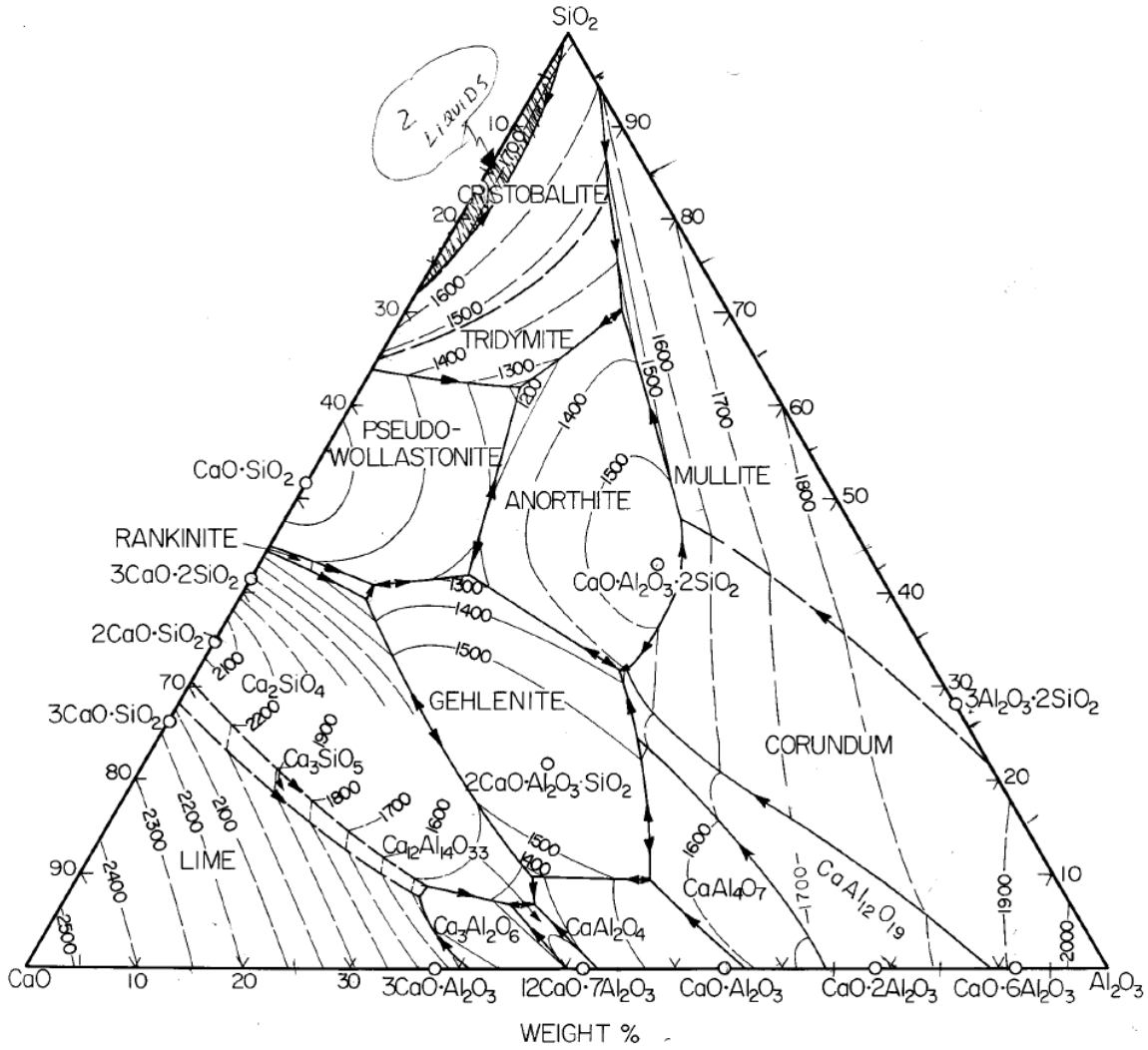

Figure 2.37 – $CaO\text{-}Al_2O_3\text{-}SiO_2$ phase diagram [145]

2.11.13 $CaO\text{-}SiO_2$ system

Silica (SiO_2) is the major gangue consitituent in the mineral sulphide concentrates from the Copperbelt province in Zambia. As the current investigation focuses on reduction of the mineral sulphide concentrates in the presence of CaO, it is important to discuss the $CaO\text{-}SiO_2$ phase diagram. The $CaO\text{-}SiO_2$ system is shown in figure 2.38 [152] and it is evident that there is very limited solid solubility between the CaO and SiO_2 phases because of the high tendency for compound formation in the system. The intermediate compounds are Ca_2SiO_4, $Ca_3Si_2O_7$, $CaSiO_3$ and Ca_3SiO_5 [153]. The lower and upper limit of stability for the Ca_3SiO_5 intermediate compound are 1523 K and 2343 K [153], respectively. $CaSiO_3$ and Ca_2SiO_4 melt congruently at 1817 K and 2403 K, respectively.

The enthalpy and entropy changes for the formation of intermdiate products are given in table 2.1.

Table 2.1 – Enthalpy and entropy changes for the formation of calcium silicate compound

	ΔH (J)	ΔS (J)	Temperature range (K)
$CaO + SiO_2 = CaSiO_3$	-92422	-2.5	298 - 1813
$2CaO + SiO_2 = Ca_2SiO_4$	-118769	11.3	298 - 2403
$3CaO + SiO_2 = Ca_3SiO_5$	-118769	6.7	298 - 1773
$3CaO + 2SiO_2 = Ca_3Si_2O_7$	-236701	-9.6	298 - 1773

Based on the thermodynamic data in table 2.1, it can be deduced that the Gibbs energy changes are negative for the reaction between CaO and SiO_2. As a result, the reaction between CaO and SiO_2 may decrease the availability of lime during carbothermic reduction. A large quantity for CaO might be necessary, for the formation of calcium silica and for the MS-CaO ion exchange reaction, if the driving force for formation of calcium silicate is higher than for the carbothermic reduction,

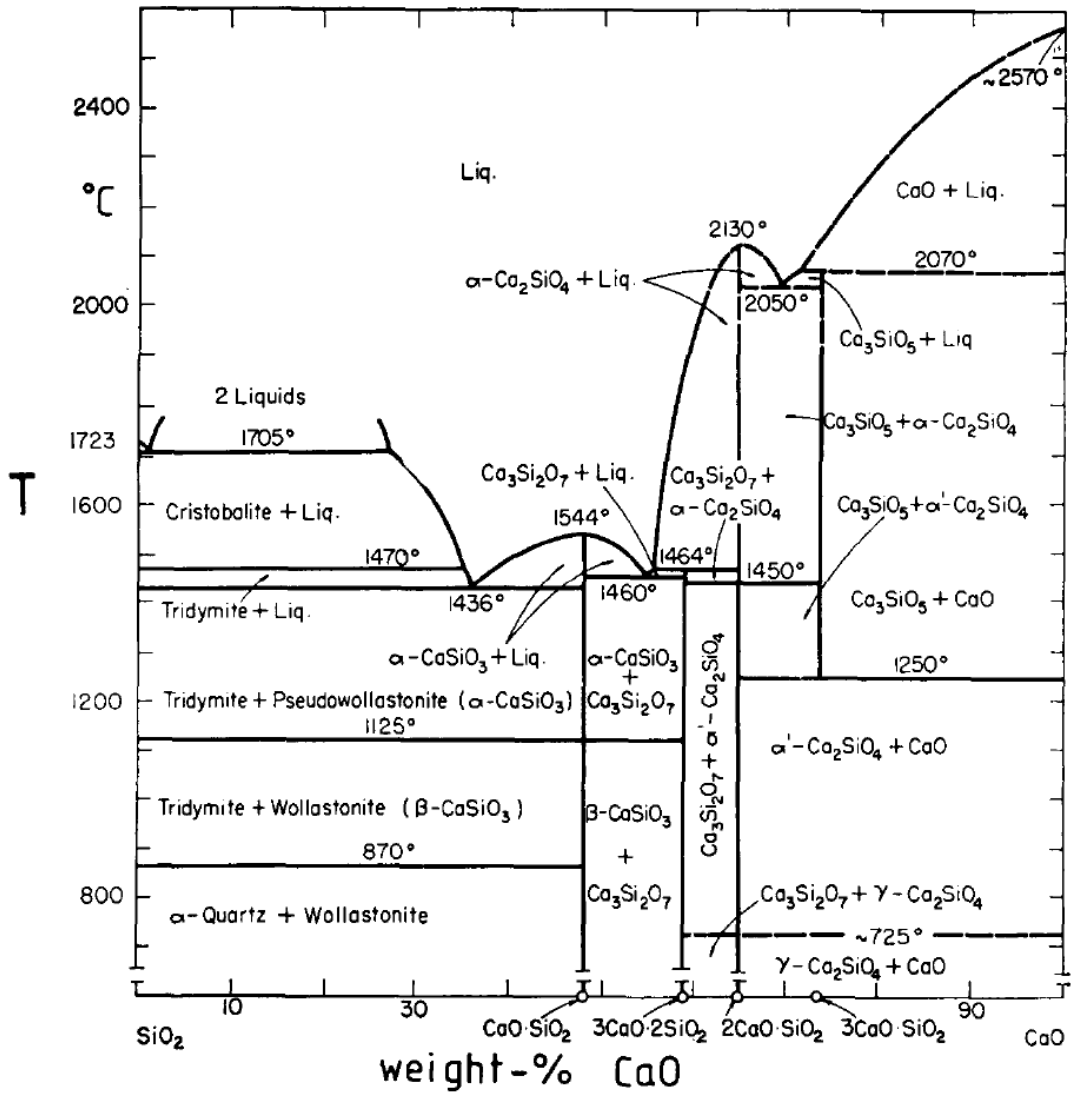

Figure 2.38 – The CaO-SiO_2 phase diagram [152]

2.11.14 FeO-SiO_2-CaO system

The FeO-SiO_2-CaO system constitutes the main components of copper smelting slag [28] and is shown in figure 2.39. The lowest liquidus temperature is near the FeO·SiO_2 composition. In copper smelting process, SiO_2 or FeO (in the form of FeS_2) is added to bring the slag composition closer to FeO·SiO_2, depending on the chemical composition of the mineral sulphide concentrates. The liquidus temperatures increase towards the SiO_2 and CaO regions. Olivine refers to the silicate minerals with a general formula of M_2SiO_4, where M is commonly Fe and Mg [154].

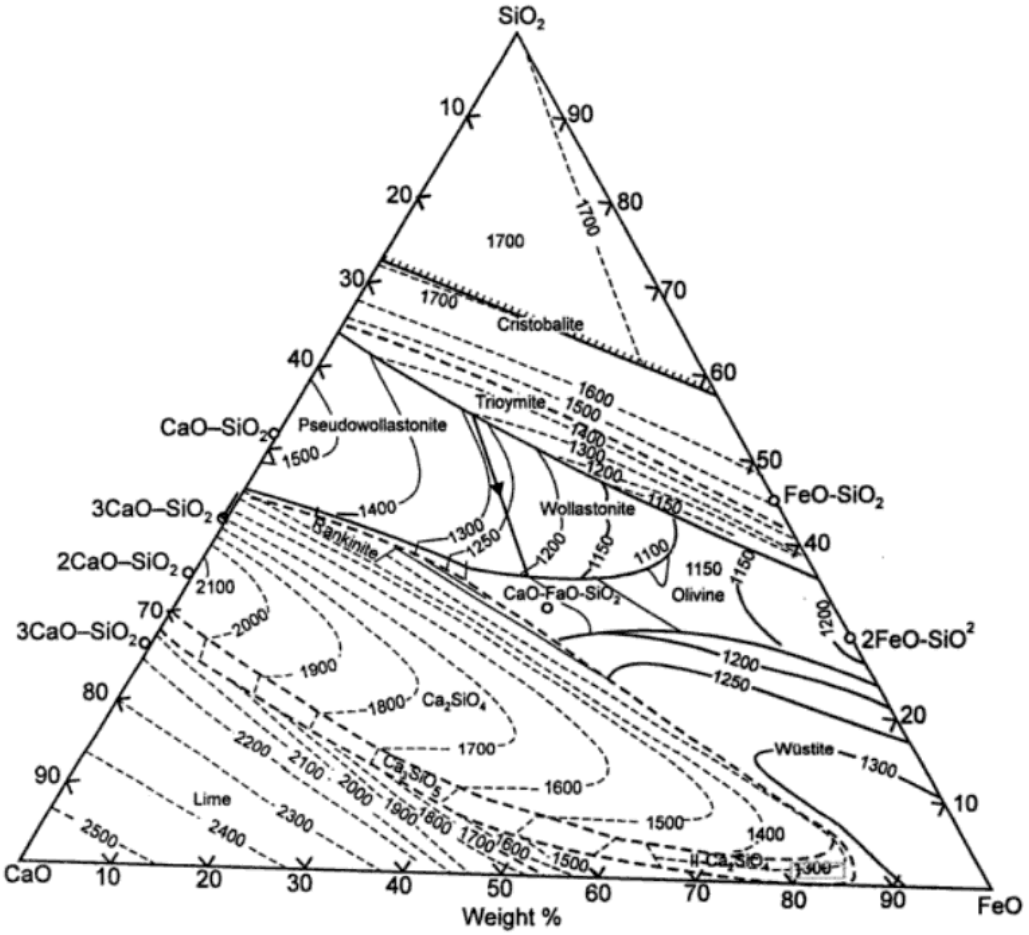

Figure 2.39 – The $FeO\text{-}SiO_2\text{-}CaO$ tenary phase diagram

3.0 Experimental procedure

3.1 Materials

The mineral sulphide concentrates were obtained from the Nchanga, Nkana and Baluba concentrators, on the Copperbelt region in Zambia. The mineral sulphide concentrates were derived from froth flotation and the mineralogical data is given in tables 3.1 – 3.3. Carrollite ($CuCo_2S_4$) is the main Co bearing mineral in all the three mineral concentrates. The other Co bearing mineral is pyrite (FeS_2) as shown in table 3.2.

Table 3.1- Mineralogical data for the Nchanga concentrates

	Wt. %	% TCu	% ASCu	F: L
Chalcopyrite ($CuFeS_2$)	5.8	2.0	-	97:3
Bornite (Cu_5FeS_4)	11.1	7.0	0.14	100:0
Chalcocite (Cu_2S)	28.3	22.6	0.3	96:4
Pyrite (FeS_2)	4.9	-	-	92:8
Carrollite ($CuCo_2S_4$)	0.2	0.1	-	100:0
Native copper	0.3	0.4	-	100:0
Malachite ($Cu_2CO_3(OH)_2$)	2.6	1.5	1.5	98:2
Cuprite (Cu_2O)	1.3	1.1	0.7	97:3
Gangue (45.3 wt. %)				
Quartz/feldspar	34.53			
Carbonates	1.20			
Micas	5.15			
Talc	2.81			
Carbonaceous shale	1.00			
FeO_x	0.40			
TOTAL	**100.0**	**34.7**	**2.8**	-

F:L = Ratio of free to locked sulphide mineral particles, TCu = total copper and ASCu = acid soluble copper

Table 3.2 - Mineralogical data for the Nkana concentrate

	Wt. %	% TCu	%	% TCo
Chalcopyrite ($CuFeS_2$)	8.6	3.0	-	-
Bornite (Cu_5FeS_4)	5.0	3.2	0.06	-
Chalcocite (Cu_2S)	0.7	0.6	0.01	-
Pyrite (FeS_2)	10.1	-	-	0.4
Carrollite ($CuCo_2S_4$)	2.0	0.4	-	0.8
Pyrrhotite (Fe_{1-xS})	0.2		-	-
Malachite ($Cu_2CO_3(OH)_2$))2.	0.6	0.3	0.3	-
Gangue (72.8 wt-%)				
Quartz/Feldspars	~19			
Carbonates	~10			
Micas	~31			
Talc ($Mg_3Si_4O_{10}(OH)_2$)	~1			
Carbonaceous Shale	~12			
Iron Oxides	<<1			
Total	**100.0**	**7.6**	**0.4**	**1.2**

Table 3.3 - Mineralogical data for the Baluba concentrate

MINERALS	**Cobalt concentrate**
	Wt %
Chalcopyrite ($CuFeS_2$)	51.6
Bornite (Cu_5FeS_4)	0.5
Chalcocite (Cu_2S)	5.8
Pyrite (FeS_2)	15.5
Carrollite ($CuCo_2S_4$)	1.5
SiO_2	9.8
Carbonates and hydrates	15.3
Total	**100.0**

The particles sizes of the mineral sulphide concentrates were between 5 µm and 500 µm. Graphite with particles size of less than 50 µm was obtained from Leeds university

laboratory. Carbon black - X72 was supplied by Evonik Company (Germany) whereas activated charcoal was purchased from Alfa Aesar (UK). The list of other chemicals which were used in the investigations is presented in table 3.4.

Table 3.4 – List of chemicals used in the investigation

Chemical	Supplier	Purity (wt. %)	Particle size (µm)
CaO	Vickers laboratory limited	> 95	-
$CaSO_4$	Alfar Aesar (UK)	>99	-
Fe_2O_3	Sigma-Aldrich (UK)	>99	< 5
CoO	Sigma-Aldrich (UK)	-	-
CuO	Sigma-Aldrich (UK)	>99	< 5
SiO_2	Sigma-Aldrich (UK)	-	-
Al_2O_3	Sigma-Aldrich (UK)	99.99	-

3.2 Carbothermic reduction experiments

The carbothermic reduction of the mineral sulphide concentrates were carried out in the thermal gravimetric analysis (TGA) equipment and in the elevating hearth furnace. The TGA equipment was used for the carbothermic reduction of smaller samples (less than 3 g) and for low temperature reduction ($T \leq 1323$ K). The elevating hearth furnace was used for larger samples (above 3 g) and for higher temperature experiments (above 1323 K) because, the quartz reaction tube in the TGA equipment cannot withstand temperatures, higher than 1323 K. The mixing procedure for the samples was the same, for the experiments carried out in the TGA equipment and in the elevating hearth furnace.

3.2.1 Sample preparation

For reduction experiments in the TGA equipment, 0.8 g of the mineral sulphide concentrates were mixed with lime and carbon by following equation 1.5a. The required lime and carbon were calculated according to equations 3.1a and 3.1b, respectively.

$$wt_{CaO} = \frac{wt\%\ of\ S\ in\ conc.}{100\%} \times \frac{56\,(RMM\ of\ CaO)}{32\,(RMM\ of\ S)} \times weight\ of\ conc. \qquad 3.1a$$

$$wt_{C} = \frac{wt\%\ of\ S\ in\ conc.}{100\%} \times \frac{12\,(RMM\ of\ C)}{32\,(RMM\ of\ S)} \times weight\ of\ conc. \qquad 3.1b$$

Where wt_{CaO} is the weight of CaO, wt_C is the weight of carbon, Conc. is the concentrates and RMM is relative molecular mass.

The mixture of mineral sulphide concentrates, lime and carbon were intimately mixed by grinding in a mortar and pestle for about 5 minutes. The mixed and ground samples were then transferred into the 13 mm diameter pressing steel die. The pellets were formed by pressing the samples at a load of 8 tons and for a period of about 35 minutes. The pressed pellets were between 6 mm and 10 mm in height.

3.2.2 Thermal gravimetric analysis (TGA) studies

Thermogravimetric analysis (TGA) is a technique where the sample weight or weight change (loss or gain) is measured either as a function of time (isothermal reaction) or as a function of temperature [155, 156]. In essence, the sample is either suspended from or placed on the balance during the reaction and, the weight changes are recorded on the computer with the help of the software. The recording of the sample may be carried out at different intervals such as 1 s, 10 s, 20 s, 60 s and so on, depending on the rate of reaction.

The reduction experiments were carried out isothermally, in order to examine the rate of reaction as a function of temperature. The schematic arrangement of the TGA equipment is shown in figure 3.1. The thermal gravimetric analysis unit consists of the temperature controller, Sartorius micro-balance which has a sensitivity of 0.1mg, pico data recorder which is connected to the computer, a vertical resistance furnace which is fitted with the quartz reaction tube [157]. The quartz reaction tube has a volume of 0.5 litres. The alumina crucible containing the sample pellet was suspended from the Sartorius micro-balance using a stainless steel wire in such a way that when the furnace is raised to its uppermost level, the crucible occupies the equi-temperature zone.

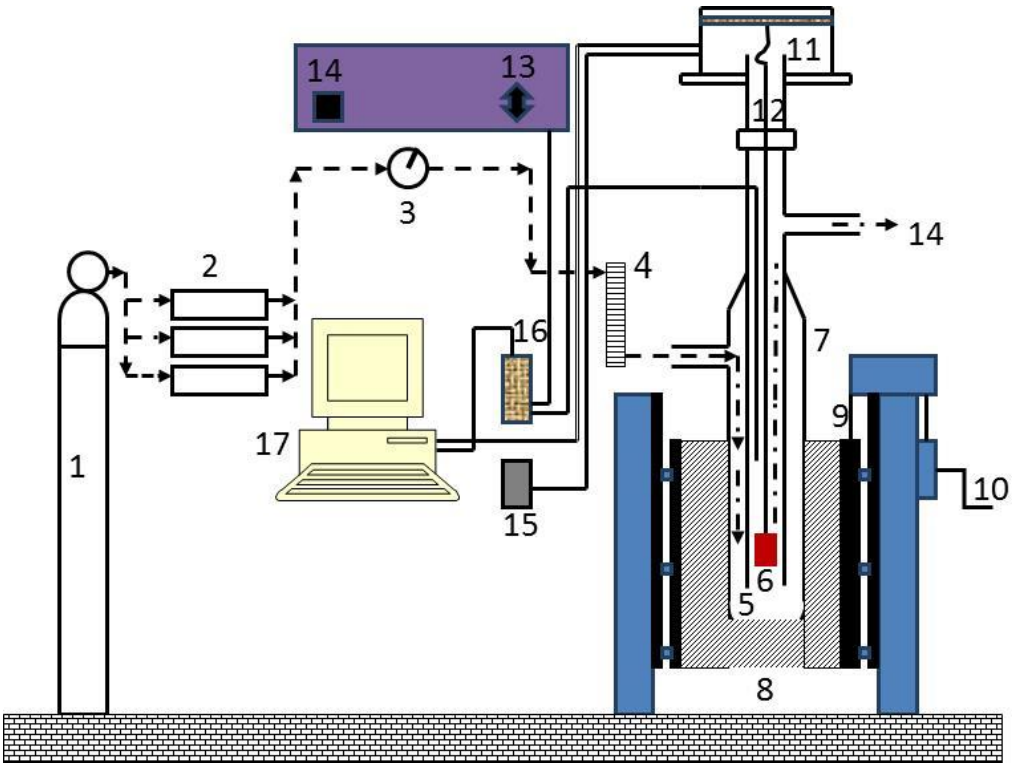

Figure 3.1 - Thermogravimetric analysis (TGA) equipment

1- argon/nitrogen/air gas cylinders, 2-gas purifier 3-gauge pressure, 4-flowmeter, 5-quartz inner tube, 6-sample crucible, 7-quartz outer tube, 8-furnace, 9 and 10 – driving mechanism, for raising the furnace up and down, 11- Sartorius micro-balance, 12-stainless steel wire, 13-furnace controller, 14 – on/off switch, 15-balance display, 16 pico data recorder, 17-personal computer.

The furnace was switched on using the on/off button (14) and adjusted to the required temperature by the furnace program controller (13). The furnace was allowed to heat to the required temperature and could take between 1 and 2 hours, depending on the reaction temperature. Upon reaching the required temperature, argon gas was purged into the quartz reaction chamber. The inert (argon) gas was opened from the gas cylinder (1) and then passed though the gas purifier (2) so as to remove any oxygen or moisture. The gauge pressure was adjusted using the gauge meter (3) and the flow rate was adjusted by the flow meter (4). The argon gas gauge pressure was set at a pressure of 1.2 bars and flow rate of 600 mL $(minute)^{-1}$. The argon gas entered the reaction vessel though the space between the inner (5) and outer (7) reaction quartz tube.

The alumina crucible was suspended from the microbalance (11) using the stainless steel (12). The furnace (8) was raised up and down using the driving

mechanism (10) which is attached to the wire rope (9). Once the crucible is well suspended in the reaction quartz reaction tube, the balance was zeroed using balance display (15) so that only sample weight can be recorded. The furnace was lowered down and the sample crucible attached to the stainless steel wire was removed from the furnace. The sample pellet was placed inside the alumina crucible, taken inside the quartz reaction tube and suspended from the micro-balance. The furnace was immediately raised up and, the sample weight was recorded on the personal computer (17) using Sartoconnect software, at the interval of 10 seconds.

The weight percentage of CO gas given out during the reaction or percentage reduction can be calculated by taking the ratio of the apparent reduction in weight at a given time "t" due to the loss of CO gas, with respect to the stoichiometric weight loss via reaction 1.5a (equations 3.2a and 3.2b). However, the mineral sulphide concentrates contain volatile constituents in the form of moisture, hydrates and carbonates which also contribute to the overall weight loss during the reactions. The theoretical weight loss is therefore the sum of the weight loss from CO gas and volatile constituents. The total weight from the volatile constitutes were found as 15 wt. %, 14 wt. % and 12 wt. % for the Nchanga, Nkana and Baluba concentrates, respectively. As a result, the % reduction was calculated according to equation 3.2c.

$$\%CO\ gas\ at\ any\ time = \frac{Weight\ loss\ at\ any\ time}{Wt_{CO}} \times 100 \qquad 3.2a$$

$$Wt_{CO} = \frac{\%S\ in\ the\ sample}{100\%} \times Wt_{sample} \times \frac{28(RMM\ of\ CO)}{32(RMM\ sulphur)} \qquad 3.2b$$

$$\%\,\mathrm{Re}duction\ at\ any\ time = \frac{Weight\ loss\ at\ any\ time}{Wt_{CO} + Wt_{V}} \times 100 \qquad 3.2c$$

where Wt_{CO} is the theoretical weight loss of CO gas from equation 1.5a and, Wt_V is the weight loss of the volatile consitituents in the mineral concentrates and RMM is the relative molecular mass.

3.2.3 High temperature reduction

As already stated, the high temperature (> 1323 K) reduction experiments were carried out in the elevating hearth furnace. The major drawback of the elevating hearth furnace is that it is not completely air tight. Therefore, the experiments were carefully designed so as to prevent air from oxidising the samples during reactions and this was achieved by placing the alumina crucibles containing the samples, inside the big salamander super (clay graphite) crucible as shown in figure 3.2. In addition, graphite powder and blocks were placed between the alumina crucible containing the sample and salamander super crucible. The furnace was further purged with argon gas at a flow rate of 2.0 litres per minute and a gauge pressure of 1.2 bars. At the end of experiment, the samples were taken out of the furnace and cooled down to room temperature under the graphite crucible. The cooled samples were weighed and the final weights were subtracted from the initial weights, to determine the experimental weight loss. The experimental weight loss of the samples was compared with the stoichiometric weight loss.

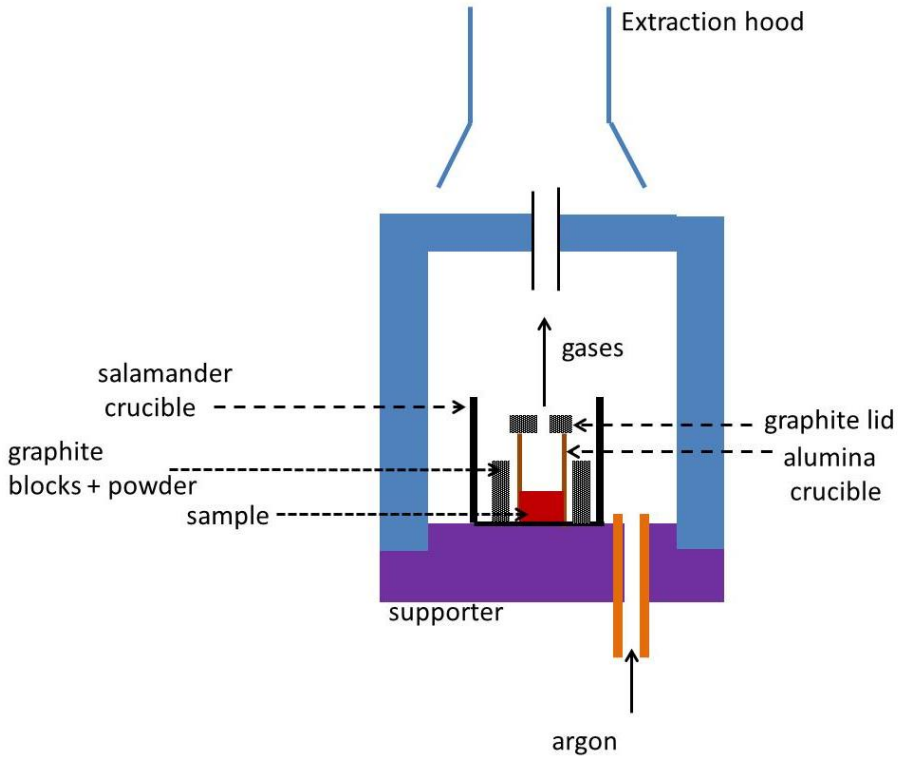

Figure 3.2 – Schematic arrangement for the experiments carried out in the elevating furnace, in G56 laboratory

3.3 Treatment of Cu-Co slag for the recovery of metallic values

As stated in chapter one, copper smelting slags are a major source of copper and cobalt, such that the recovery of copper and cobalt from slag was investigated. The Cu–Cu slag was synthesized by mixing metal oxides ((Cu,Cu,Fe)-O), CaO, Al_2O_3 and SiO_2 according to the composition in table 3.5. The composition in table 3.5 is typical of Nkana copper smelting slag dump except that CuO and CoO were added in higher quantities for easy analysis and understanding of the metal oxide during recovery. The mixed powders were transferred into the alumina crucible and melted for 2 hours at 1523 K, in air. The furnace was switched off and the sample was taken out the furnace at 1323 K. The cooled sample was crushed and ground to less than 300 µm.

Table 3.5 – Composition of synthetic slag in wt. %

Constituent	SiO_2	CaO	Fe_2O_3	Al_2O_3	CoO	CuO
Weight (%)	40	10	30	6	7	7

Carbothermic reduction of slag – 1.4 g of slag was thoroughly mixed with 0.44 g of carbon (carbon black - X72 and active charcoal), which is equivalent to the molar ratio of MO:C = 1:3, where MO is the metal oxide. The mixed samples were reduced isothermally under the flow of argon gas at 660 litres $(minute)_{-1}$ in the thermogravimetric analysis equipment so as to measure the weight loss (% reduction) as a function of time. The samples were removed from the furnace when there was no significant weight loss.

Sulphidisation of slag – 0.7 g of slag was mixed with $CaSO_4$ and C (activated charcoal or graphite) by following equation 2.41b. The experiments were carried out in the thermogravimetric analysis equipment and in the elevating furnace.

3.4 Magnetic separation of the reduced samples

The metallic phases in the reaction products were separated from CaS and gangue minerals using the hard drive magnet. The reacted samples were weighed and placed in a beaker and mixed with water. The beaker containing the sample and water was placed on top of the hard drive magnet. The sample in the beaker was stirred for nearly 30

seconds, for the purpose of taking magnetic constituents to the bottom of the beaker while taking the non-magnetic samples into the suspension. While holding the beaker against the hard drive magnetic, the water and non-magnetic fraction were poured out into another beaker. The procedure was repeated for 2 - 3 times to remove as much non-magnetic constituents as possible. The magnetic fraction became highly magnetic as more non-magnetic constituents were removed and, a brownish colour was observed due to the presence of metallic copper. At the end of separation process, the non-magnetic fractions were filtered off to removal water. The magnetic and non-magnetic fractions were dried at 323 K. The dried samples were then weighed and characterised.

3.5 Characterization of reacted samples

The as-received and reacted samples were characterized by the X-ray diffraction (XRD) analysis, X-ray fluorescence (XRF), scanning electron microscopy (SEM) and optical microscopy techniques.

3.5.1 X-ray diffraction (XRD) analysis

X-ray diffraction occurs when X-rays interact with the electrons of the atoms [158]. The crystalline phases diffract X-rays according to the Bragg's law (equation 3.3) [159, 160] .

$$\lambda = 2d \sin\theta \qquad 3.3$$

Where d is the interplanar spacing or d-spacing, λ is the wavelength of the incident beam and θ is the angle of incidence or the angle between the surface of the crystal and the incident rays.

The simple arrangement of the widely used X-ray diffraction machine is shown in figure 3.3. In some instruments, the sample is fixed and the diffraction angle (2θ) is obtained by rotating the X-ray source and the detector at angle θ, in the opposite directions (figure 3.3). In some machines, the X-ray source is fixed and the sample is rotated by θ whereas the detector is rotated by 2θ. The angle of diffraction (2θ) or the position of the detector is recorded against the X-ray intensity or counts per second. The

plot of X-ray intensity or counts per second is known as the diffraction pattern. The following can be determined from the X-ray diffraction patterns:

i. The crystalline phases in the sample because each phase has a unique diffraction pattern
ii. Presence of amorphous phase
iii. Phase quantification

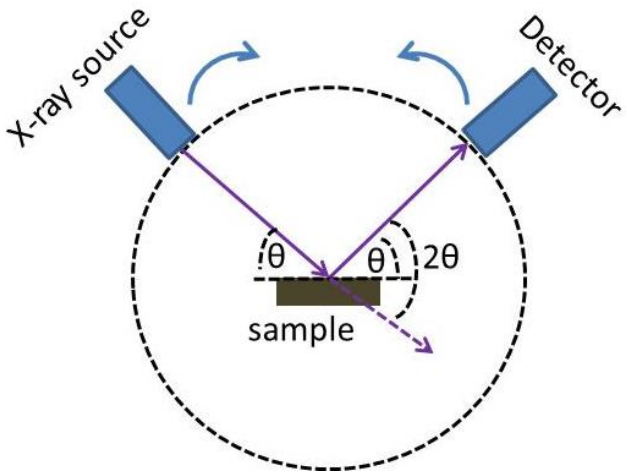

Figure 3.3 – Schematic illustration for the X-ray diffraction analysis

3. 5.1.1 Technical details

A representative portion of the sample or material was ground into fine powder in a mortar and pestle and, packed into the sample holder. X-ray diffraction analysis was carried out using the Philips X'pert machine with Cu K_α (0.15417 nm) radiation, at an acceleration voltage of 40 kV, current of 30 mA, step size of 2θ = 0.0334225 ° and time per step = 200.7 s. The samples were analysed for 2θ between 5° and 70° or 5° and 85°. The phases present in the powder diffraction patterns were identified by using the X'pert high score plus software which is supported by the JCPDS PDF-4+ database (RDB 2012).

3.5.2 Microscopy studies

Microscopic studies were carried out using the optical and scanning electron microscopy. Optical microscopy is used to study the microstructure of the sample [159]. However, with the ready availability [161] of the scanning electron microscopes, the use

of optical microscope has been decreasing [161]. In scanning electron microscopy (SEM), the sample is bombarded with a beam of electrons and the resultant interactions or signals are shown in figure 3.4.

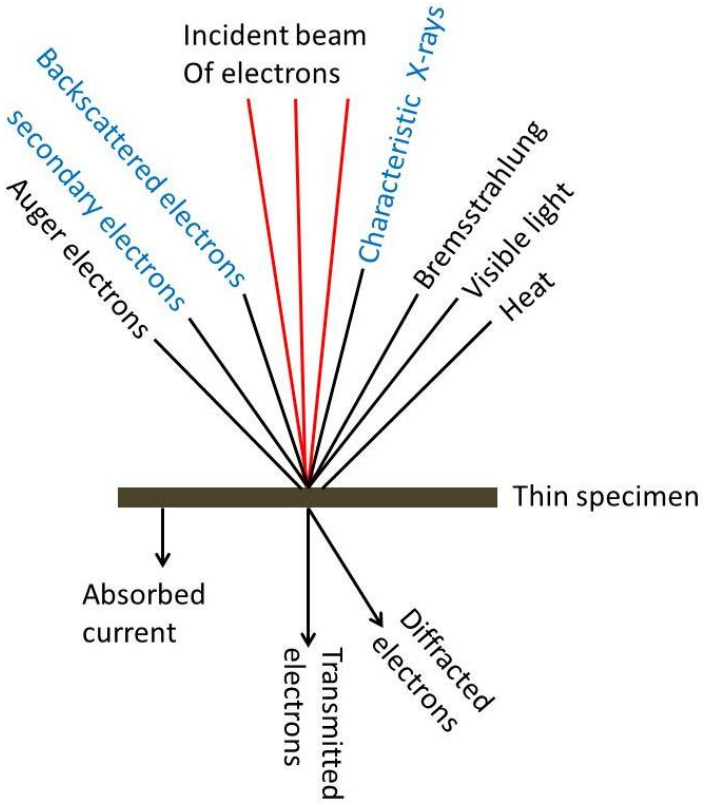

Figure 3.4 – Schematic illustration for the interraction of the beam of electrons with the sample, reproduced from Voutou and Stefanaki [162] and Rahaman [98], only backscattered and secondary electrons (in blue) are considered for SEM analysis

Even though several signals are produced from the interaction between the beam of electrons and the sample, the secondary electrons and the backscattered electrons are used in scanning electron microscopy imaging. The backscattered electrons (BSE) are the high energy, reflected beam of electrons and they vary directly [162, 163] with the atomic number and hence elements with the high atomic number appear brighter than those with low atomic number [162]. Therefore, backscattered electron imaging is good for showing phase contrast in a sample with different compositions or multiphase sample. Secondary electrons occur when the beam of energy knocks out or eject electrons from the outer shell of the atom [98, 163]. The ejected electrons that are closer to the surface of the sample may have sufficient energy to escape from the sample and thus become secondary electrons [98]. The secondary electrons are used to examine the

surface topography of the sample because the change in the surface topography, changes the yield of the secondary electrons [162]. X-rays occur when the electron from the inner, low energy shell is ejected by the incident beam of electrons leaving a hole or vacancy, which is filled by the electron from the outer, high energy shell [163]. The electron from the outer, high energy shell loses part of its energy as it moves to the inner, low energy shell in form of X-ray. The produced X-rays are characteristic of the difference in energy between the high and low energy shells and, the element atomic structure and elemental composition can be carried out. The full details of scanning electron microscopy are found in literature [163].

3.5.2.1 Technical details

A portion of the sample was mounted in a mixture of 3 parts epoxy resin and 1 part epoxy hardener and cured for about 8 hours. The mounted samples were gently ground on different grades of silicon carbide papers; P240, P400, P600, P800, P1200, P2500 and P4000. The grounded surfaces were further polished down to 1 µm and thoroughly cleaned with water. The polished samples were initially viewed under the Olympus BX51 optical microscopy. The optical images were taken at the magnifications of 50X, 100X, 200X and 500X by using the AxioVision SE64 REL.4.8 software.

For scanning electron microscopy (SEM), the polished sample surfaces were coated with a 5 nm layer of platinum to prevent charging during analysis. The scanning electron microscopy (SEM) was carried out using the Carl Zeiss Evo MA 15 (Germany) at the accelerating voltage of 20 kV, working distance of 8 mm and magnifications between 50 X and 6000 X. The SEM equipment is equipped with the energy dispersive X-ray (EDX) detector for the semi-quantitative elemental analysis and elemental mapping for the selected areas. The SEM-EDX analysis was very useful for analysing phases that were present in small concentrations (less than 3 wt. %) because they cannot be analysed by XRD analysis.

3.5.3 X-ray florescence (XRF)

The X-ray florescence (XRF) principle is similar to that of SEM-EDX technique. The main differences are that a larger sample (up to 10 g) and phases in smaller concentrations (parts per million) can be analysed in the X-ray florescence (XRF) technique. Therefore, XRF analysis was carried out for determining the overall

composition of the samples. The samples were analysed by the semi-quantitative pressed pellet method, which is a widely used method for determining sulphur in the samples. The samples were ground to very fine powders (< 100 µm) and mixed with EPM resin at a weight ratio of 2 parts sample and 1 part resin. The mixtures were then transferred into 3 cm diameter alumina caps and pressed into pellets at a pressure of 5 tons. The composition of the elements in the samples was executed in oxide form i.e. $CuFeS_2$ would be expressed as CuO, Fe_2O_3 and SO_3, CaS as CaO and SO_3, Cu as CuO.

4.0 Analysis of the as-received mineral sulphide concentrates

The Nchanga and Nkana mineral sulphide concentrates were weakly magnetic while the Baluba sulphide concentrates were non-magnetic. The Baluba sulphide concentrates were non-magnetic considering the fact that most of the Cu, Co, and Fe mineral sulphides ($CuFeS_2$, Cu_5FeS_4, $CuCo_2S_4$, FeS_2 and Cu_2S) are non-magnetic at room temperature, apart from pyrrhotite (Fe_{1-x}) [164]. However, the content of pyrrhotite ($Fe_{1-x}S$) is below 1 wt. % in all the mineral sulphide concentrates. It appears that the Nchanga and Nkana mineral sulphide concentrates were weakly magnetic due to the presence of the gangue minerals.

4.1 X-ray diffraction analysis

The X-ray diffraction patterns for the as-received mineral sulphide concentrates are shown in figure 4.1. It can be noted from the XRD patterns that there were many forms of copper sulphide in the Nchanga mineral sulphide concentrates namely Cu_2S (chalcocite) [165, 166], $Cu_{1.8}S$ or Cu_9S_5 (digenite) [166] and $Cu_{1.6}S$ or Cu_8S_5 (geerite) [166, 167]. Digenite (Cu_9S_5) and geerite (Cu_8S_5) can also be written as $4Cu_2S{\cdot}CuS$ and $3Cu_2S{\cdot}2CuS$ [167], respectively. Digenite ($4Cu_2S{\cdot}CuS$) and geerite ($3Cu_2S{\cdot}2CuS$) are considered stable when some of the Cu^{2+} ions are replaced by the Fe^{2+} ions in the Cu-Fe-S system [165, 167]. The XRD pattern in figure 4.1 shows that geerite (Cu_8S_5) is also present in the Nkana and Baluba mineral concentrates and, this is due to the stability of this mineral in the presence of Fe-S or in the Cu-Fe-S system [165]. On the other hand, the main mineral sulphide phases in the Baluba XRD pattern are $CuFeS_2$ (chalcopyrite) and pyrite (FeS_2) and this is in good agreement with the composition in table 3.3. Silica (SiO_2) is the main crystalline gangue mineral phase in the Nchanga and Nkana mineral concentrates and this agrees with the analyses in tables 3.1 and 3.2. Silica is in the form of alpha quartz (α-SiO_2), which is the most stable form of silica, below 846 K [168]. The XRD pattern for Nkana shows that CaO and MgO are in the form of dolomite mineral ($CaMg(CO_3)_2$).

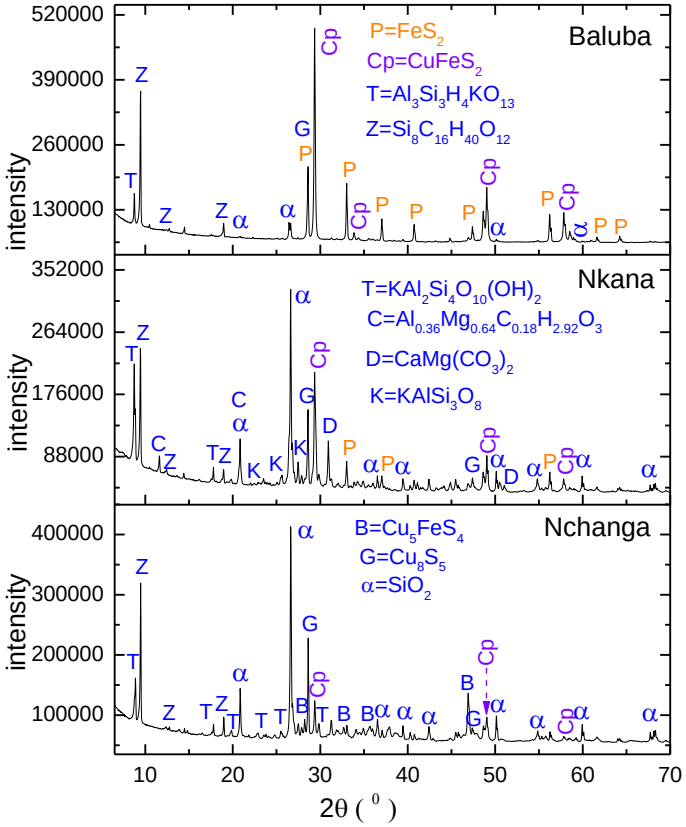

Figure 4.1 – XRD patterns for the as-received mineral sulphide concentrates

4.2 XRF semi-quantitative analysis

The XRF semi-quantitative composition of the mineral sulphide concentrates are presented in table 4.1. The XRF analysis agrees with the suppliers analyses (see tables 3.1 – 3.3). It can be observed from table 4.1 that the Nkana concentrates have the highest cobalt content (1.3 wt. %) followed by the Baluba concentrates (1.1 wt. %).

Table 4.1 – XRF semi-quantitative analysis (in wt. %) of the mineral sulphide concentrates

	Cu	Fe	Co	S	SiO_2	CaO	Al_2O_3	MgO	TiO_2	K_2O
Nchanga	35.4	6.9	0.3	9.9	34.7	0.5	5.4	4.1	0.3	2.4
Nkana	8.3	12.4	1.3	10.2	39.4	7.6	8.2	7.5	0.4	4.3
Baluba	25.5	27.7	1.1	20.8	13.3	2.8	2.3	5.7	0.1	0.6
Error = ±2 wt. %										

4.3 Microscopic examination

The optical micrographs for the as-received mineral sulphide concentrates are presented in figure 4.2. It is evident from figure 4.2 that copper sulphide (Cu_2S, Cu_8S_5) is the main mineral sulphide phase in the Nchanga concentrates because there are many bluish [169] particles under the reflected light microscope. The optical images in figure 4.2 clearly shows that $CuFeS_2$ (chalcopyrite) is the main mineral sulphide phase in the Baluba concentrates, as there are many brass yellow particles.

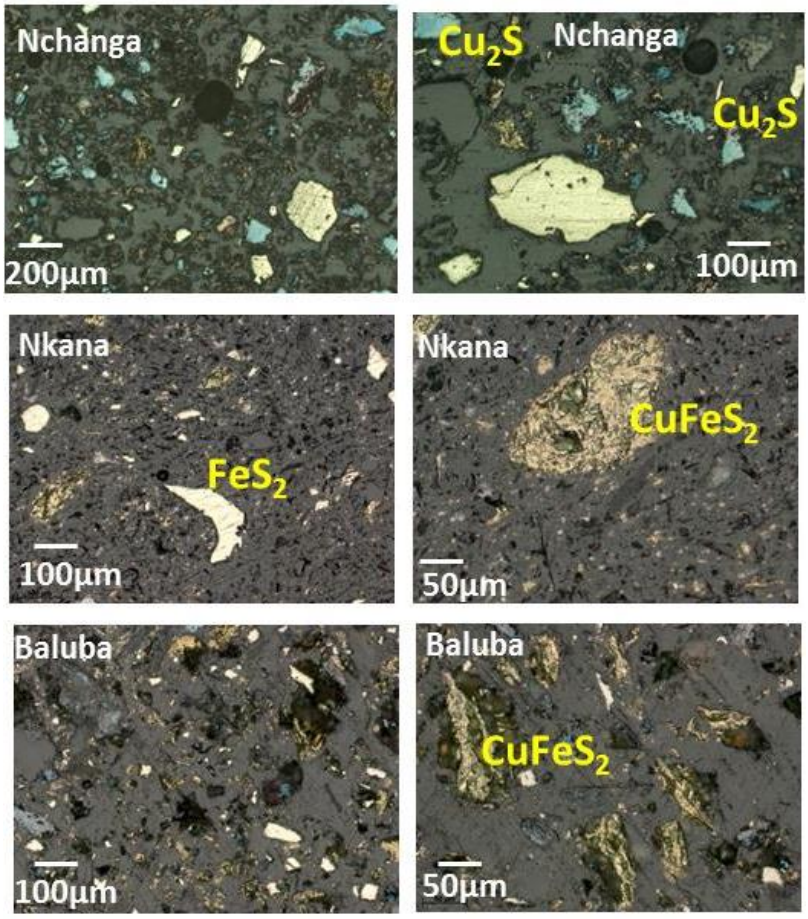

Figure 4.2 - Optical micrographs of the as-received mineral sulphides concentrates, under reflected light

The elemental maps for the as received Nchanga mineral sulphide concentrates are presented in figure 4.3. The elemental maps for the as received Nchanga sample agrees with the XRD (figure 4.2) results, as the main phases are Cu-S and SiO_2. The SEM-EDX point analysis of the Nchanga sulphide concentrates showed that Fe was dissolved in some Cu-S mineral particles. The presence of Fe in the Cu-S mineral particles is

because the Fe^{2+} ions can substitute the Cu^{2+} ions in Cu_9S_5 ($4Cu_2S{\cdot}CuS$) and Cu_8S_5 ($3Cu_2S{\cdot}2CuS$) [165, 167], as mentioned above. The Nkana mineral sulphide concentrates has the highest gangue content and it is for this reason that the concentrations of Al, K, Si, Mg, Ca are high, from the elemental maps in figure 4.4a. The analysed area in figure 4.4a contains TiO_2 and ZrO_2 because these compounds are present in the mineral sulphide concentrates, although in very low concentrations. As noted in tables 3.2 and 4.1, the Nkana mineral sulphide concentrates has the highest Co content and hence an area containing cobalt was analyzed and the elemental maps are presented in figure 4.4b. The elemental maps in figure 4.4b clearly shows the presence of Cu-Co-S and Co-Fe-S phases, and they were analyzed as carrollite ($CuCo_2S_4$) and cobaltian pyrite $(Fe,Co)S_2$ minerals, respectively, by SEM-EDX analysis. It is worth noting that both carrollite ($CuCo_2S_4$) and cobaltian pyrite $(Fe,Co)S_2$ are stable minerals at room temperature. The Baluba sulphide concentrates have the lowest gangue content and hence the analysed area in figure 4.5 contains less gangue minerals. It can be observed from the elemental maps in figures 4.3 – 4.5 that the mineral sulphide particles have various shapes and sizes and this is due to the fact that non-uniform shapes and sizes are produced during the grinding stage.

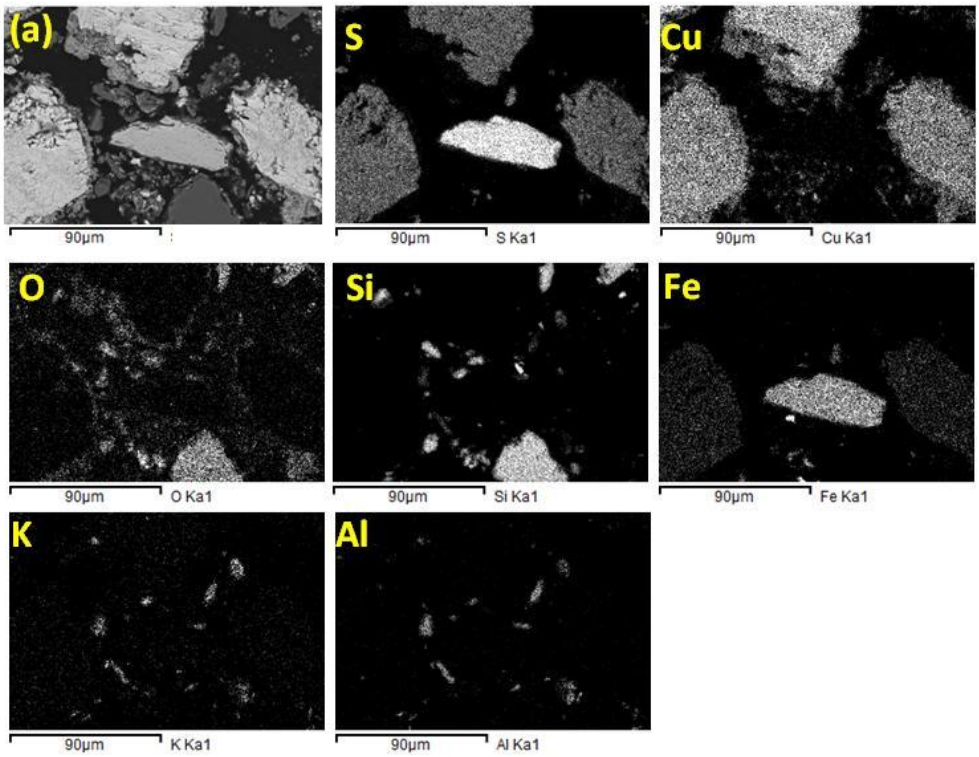

Figure 4.3 – Elemental mapping for the as received Nchanga mineral concentrates, (a) is the analysed area under backscattered electron imaging

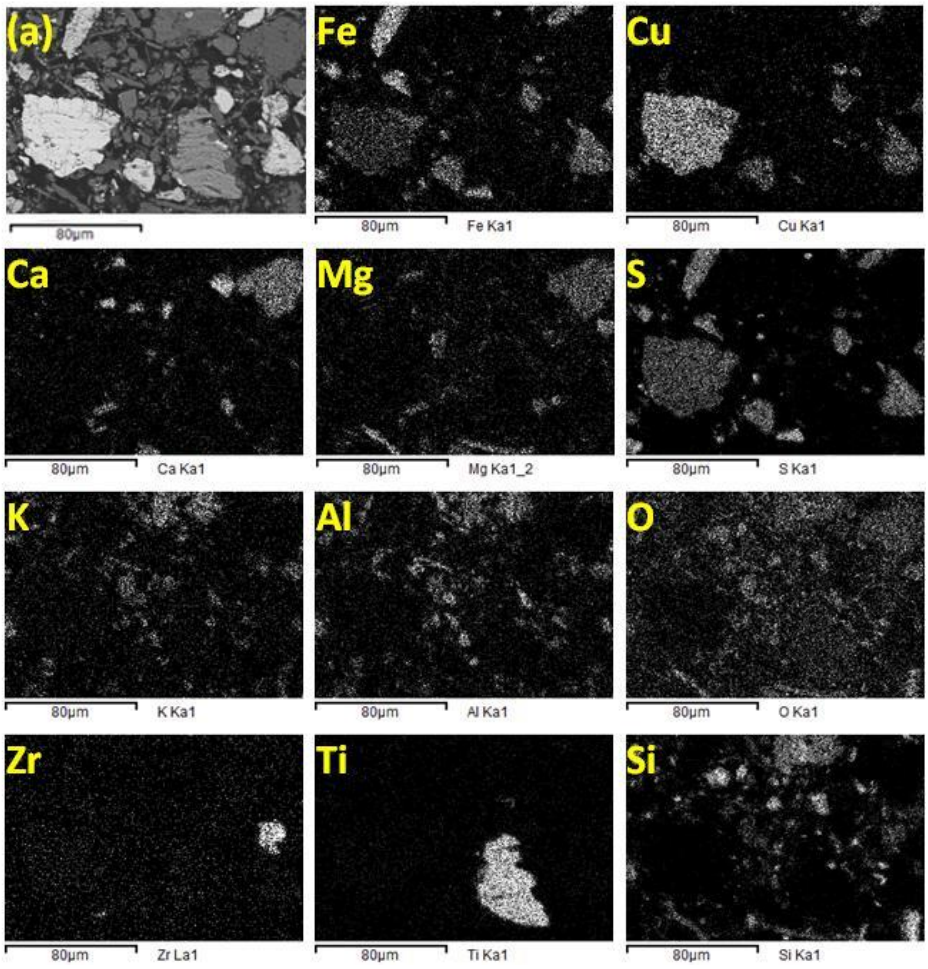

Figure 4.4a - Elemental mapping for the as received Nkana mineral concentrate, (a) is the analysed area under backscattered electron imaging

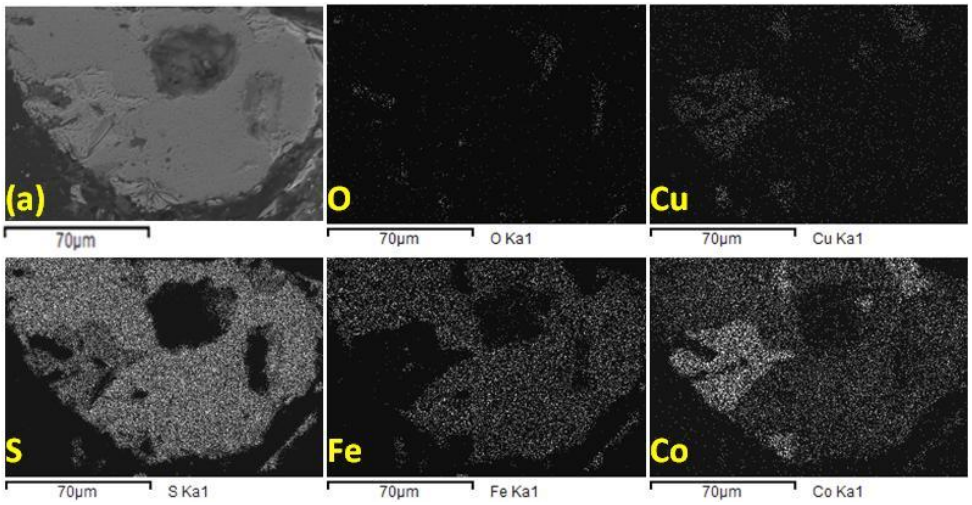

Figure 4.4b - Elemental mapping for the as received Nkana mineral concentrates, (a) is the analysed area under backscattered electron imaging

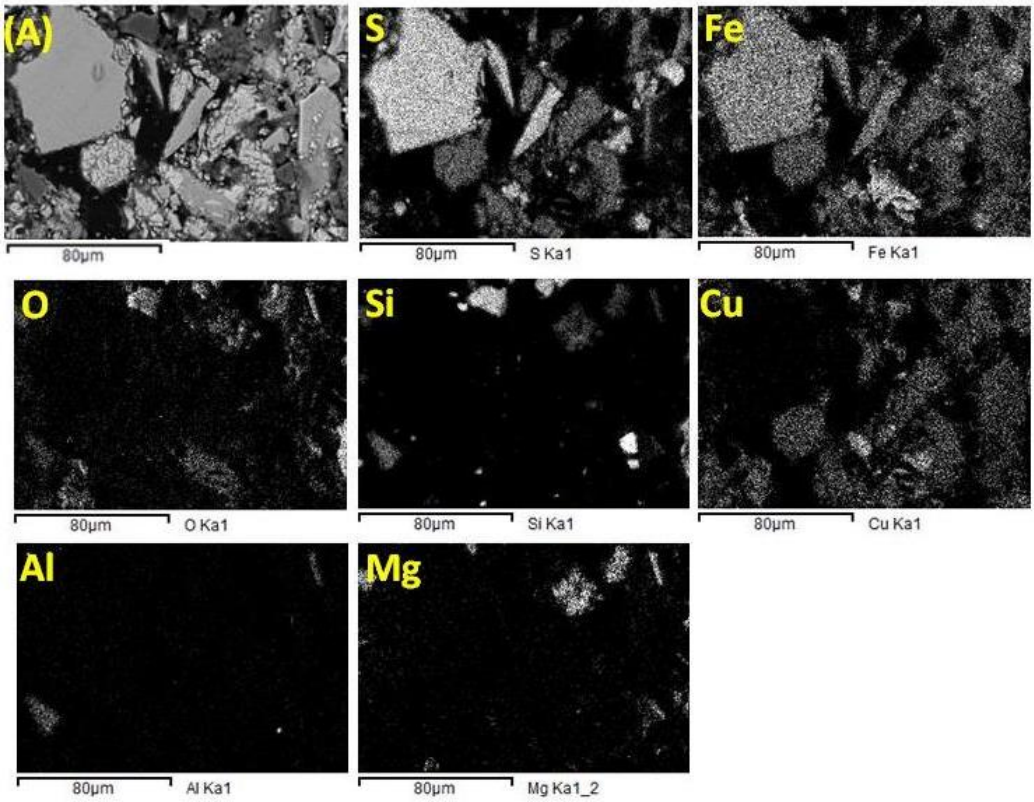

Figure 4.5 – Elemental mapping for the as received Baluba mineral concentrates; (A) is the analysed area under backscattered electron imaging

4.1.4 Determination of moisture content

It was important to determine the moisture content in the mineral sulphide concentrates, as moisture may alter the reactions during the carbothermic reduction in the presence of CaO. The moisture content was estimated by heating the mineral sulphide concentrates at 413 K, under argon atmosphere. The plots of % weight loss against time are presented in figure 4.6 and it can be observed that the weight losses occurred, within 30 minutes, suggesting that it was mainly due to the loss of water. It can be noted from figure 4.6 that the Nchanga mineral sulphide concentrates had the highest moisture content whereas the Nkana mineral sulphide concentrates had the lowest moisture content.

4.1.5 Determination of volatile constituents

The weights of the volatile constituents in the mineral sulphide concentrates were estimated by heating the mineral sulphide concentrates at 973 K, under argon

atmosphere and the plots of the % weight loss against time curves are presented in figure 4.6. The precise determination of the volatile constituents require heating of the mineral sulphide concentrates above 1173 K [170] but the challenge is that there is loss of sulphur at this temperature, resulting from the thermal decomposition of pyrite (FeS_2) and chalcopyrite ($CuFeS_2$) minerals when heated above 773 K [78]. The weight loss occurred in about 240 seconds (4 minutes) in the Nchanga sample. The sharp weight loss in the Nchanga sample was mostly due to the thermal decomposition of the gangue minerals because; (i) the concentrates are rich in the Cu_2S and Cu_5FeS_4 minerals, which are stable at 973 K and (ii) the thermal decomposition of the $CuFeS_2$ and FeS_2 minerals is very slow at 973 K.

There was a sharp weight loss in the first 480 seconds (8 minutes), followed by a gradual weight loss in the Nkana and Baluba samples at 973 K (figure 4.6). The sharp weight loss is mainly due to the thermal decomposition of the gangue minerals whereas the gradual weight loss might be due to the thermal decomposition of the sulphide and gangue minerals. The phases obtained after heating the mineral sulphide concentrates at 973 K, were similar to the ones in the as-received mineral sulphide concentrates, implying that the thermal decomposition of the mineral sulphides was very low. In summary, the weight loss of the samples at 973 K is mainly contributed by the thermal decomposition of the gangue minerals.

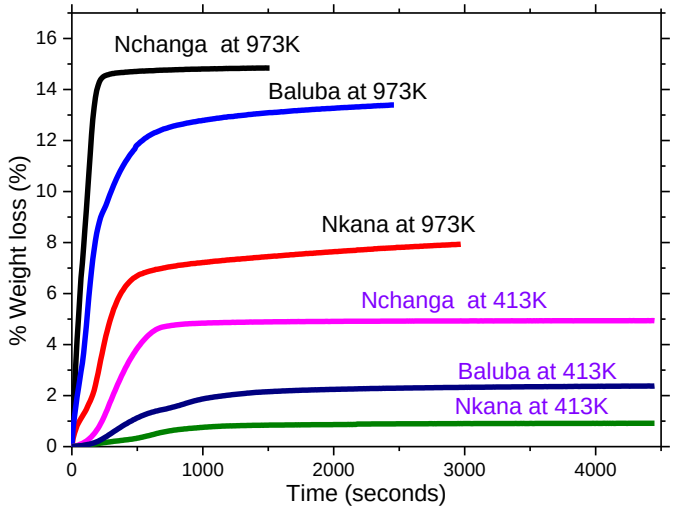

Figure 4.6 – Plot of the % weight loss versus time for the mineral sulphide concentrates, heated under argon atmosphere at 413 K and 973 K in the TGA equipment. Argon flow rate = 0.6 litre min^{-1}

5.0 Heat treatment of the mineral sulphide concentrates

This chapter has two main sections: (i) thermal decomposition of the mineral sulphide concentrates under argon atmosphere at 1273 K (in the absence of CaO and C) and (ii) heat treatment of the mineral sulphide concentrates in the presence of CaO at a temperature range of 1073 K – 1323 K. The aim(s) are discussed in each section.

5.1 Thermal decomposition of the mineral sulphide concentrates

The main purpose of heating the mineral sulphide concentrates under inert (argon) atmosphere at 1273 K was to analyse the thermal decomposition of the mineral sulphide concentrates and the high temperature phases. Analysis of thermal decomposition of the mineral sulphide concentrates was very necessary as it may influence the reaction mechanism during carbothermic reduction in the presence of CaO. The phase formation occurring via internal oxidation was analysed after heating the mineral sulphide concentrates in the absence of CaO and C.

As stated above, the mineral sulphide concentrates were heated under argon atmosphere at 1273 K and the plot of the % weight loss versus time curves are presented in figure 5.1a. The results in figure 5.1a show that the % weight loss was highest and lowest for the Nchanga and Nkana samples, respectively. The major observation from the results in figure 5.1a is that a significant weight loss occured in the first 300 seconds (5 minutes) and this is due to the rapid evolution of S_2 gas from FeS_2 and $CuFeS_2$ minerals and, H_2O and CO_2 gas from moisture and the gangue minerals.

The X-ray diffraction patterns for the mineral sulphide concentrates heated under argon atmosphere at 1273 K are presented in figure 5.1b. There are no XRD peaks for the $CuFeS_2$ phase in the Nchanga diffraction pattern and this can be because of the thermal decomposition of this mineral phase to the Cu_5FeS_4 and FeS phases at high temperatures [32, 89, 90] (see section 2.7). However, the FeS phase was absent in the heated Nchanga sample so that it can be suggested that there was:

i. Dissolution of FeS in Cu_2S because the two phases have extensive solid solubility [15, 78].
ii. Formation of another phase according to equations 5.1 and 5.2.

$$4FeS + 10Cu_2S + S_2(g) = 4Cu_5FeS_4, \quad \Delta G_{1273K} = -80.5 \text{ kJ} \qquad 5.1$$

$$CuFeS_2 + 2Cu_2S = Cu_5FeS_4, \quad \Delta G_{1273K} = -12.2\ kJ \qquad 5.2$$

From the phase analysis in the XRD patterns in figure 5.1b, it appears that the absence of the FeS phase in the heated Nchanga sample is as result of formation of the Cu_5FeS_4 phase as shown in equations 5.1 and 5.2. This is due to the decrease and increase in the XRD peak intensities for the Cu_2S and Cu_5FeS_4 phases, respectively. Note that the major mineral sulphide phase in the as-received Nchanga concentrates was Cu_2S but this is not the case, after heating the sample.

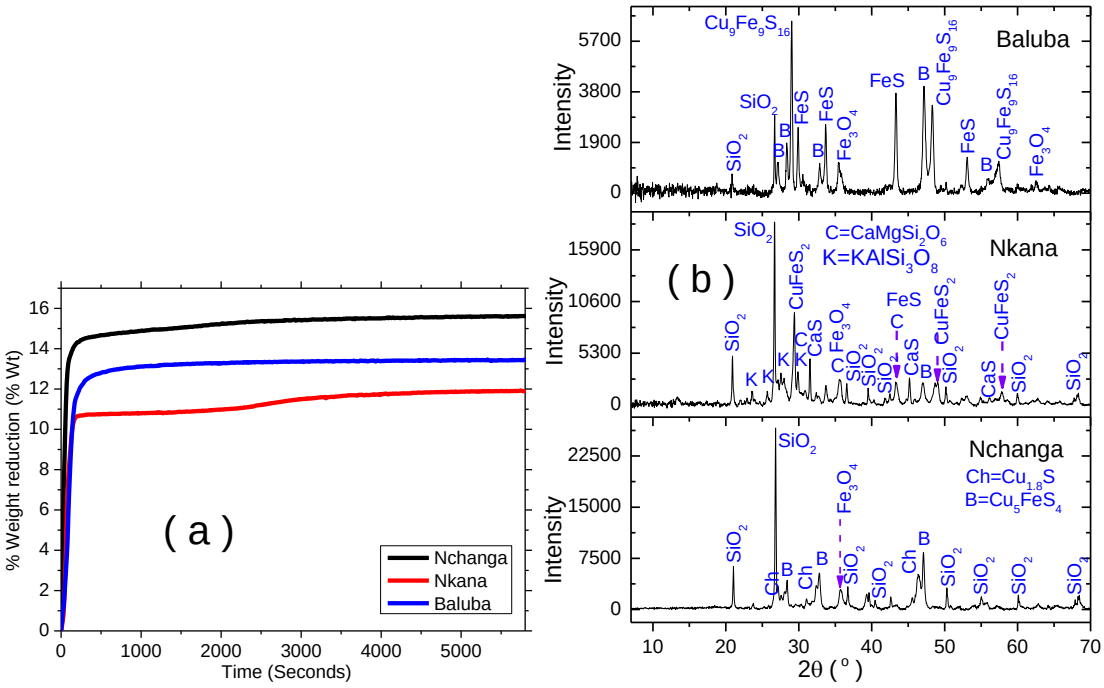

Figure 5.1 – (a) Plot of % weight loss versus time curves at 1273 K, under argon atmosphere in the TGA equipment and (b) XRD patterns for the samples in (a)

The main phases in the Cu_2S rich area of the Cu_2S-FeS pseudo binary phase diagram are Cu_5FeS_4 or Cu_5FeS_4 + Cu_2S [15] (see figure 2.20) and this agrees with the XRD results for Nchanga. The Nchanga mineral sulphide concentrates are rich in the $Cu_2S/Cu_{1.6}S$ minerals (see table 3.1) and hence the main sulphide phases in the heated sample are Cu_5FeS_4 + Cu_2S. As the Nchanga concentrates are rich in Cu, the Cu rich Cu-Fe-O-S predominance area diagram (PAD) was computed at 1273 K and is shown in figure 5.2a. It can be observed from the thermodynamic prediction in figure 5.2a that the Cu_5FeS_4 phase co-exists with the Cu_2S phase at $0.2 < \log_{10}P(S_2)(atm) < 5$ and $-8 <$

$\log_{10}P(O_2)(atm) < -10$. From the computed value of Gibbs energy change at 1273 K for the formation of Cu_5FeS_4 from FeS and Cu_2S in equation 5.1, the equilibrium partial pressure of S_2 gas is 2004 atm [$(\log_{10}P(S_2)(atm)) = 3.3$]. The value of $(\log_{10}P(S_2)(atm)) = 3.3$ is within the $Cu_2S + Cu_5FeS_4$ phase field ($0.2 < \log_{10}P(S_2)(atm) < 5$). The above analysis clearly shows that there is good agreement between the experimental results and the thermodynamic predictions.

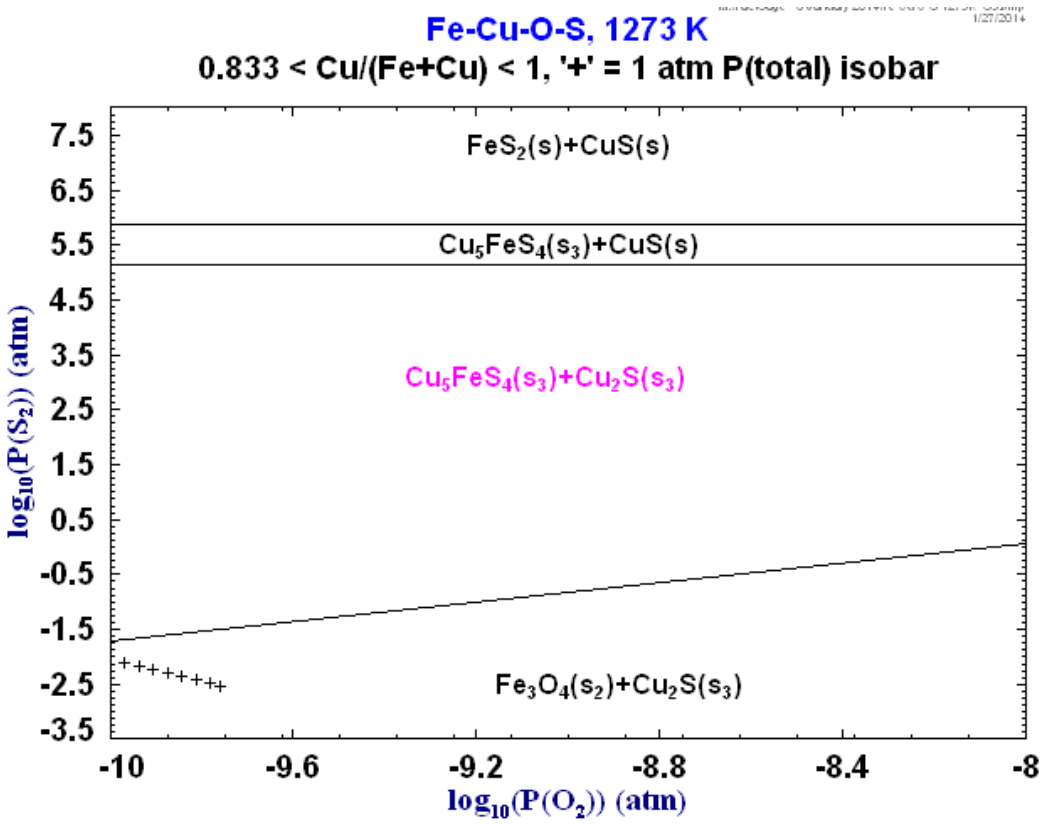

Figure 5.2a – Cu rich Fe-Cu-O-S predominance area diagram at 1273 K, computed using FactSage software 6.1 [24]

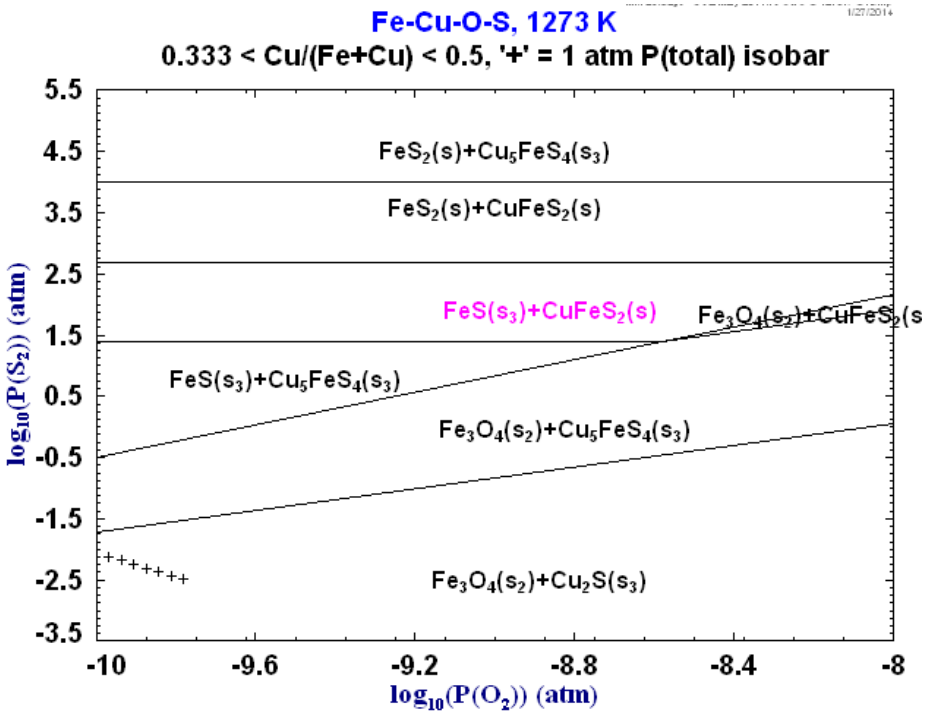

Figure 5.2b – Fe rich Fe-Cu-O-S predominance area diagram at 1273 K, computed using FactSage software 6.1 [24]

Nevertheless, the major copper bearing mineral phase in the heated Nkana concentrates was $CuFeS_2$. The presence of $CuFeS_2$ in the heated Nkana sample suggests that the thermal decomposition of $CuFeS_2$ to Cu_5FeS_4 and FeS did not occur. Even though many studies have showed that $CuFeS_2$ decomposes to Cu_5FeS_4 and FeS at 1273 K [15, 76, 88], the Cu_2S-FeS pseudo binary phase diagram (see figure 2.20) [15, 78] shows that $CuFeS_2$ is stable towards the FeS rich area. As the Nkana concentrates are rich in the FeS_2 mineral, $CuFeS_2$ is expected to be present in the heated sample.

Calcium sulphide (CaS) was identified in the heated Nkana sample and its presence was due to the ion exchange reaction between CaO and the mineral sulphide (MS). The exchange reaction occurred between CaO and mineral sulphide in the Nkana sample, as the concentrates have nearly 6 wt. % CaO in the form of $CaCO_3$ and $CaMg(CO_3)_2$ minerals. The ion exchange reaction between mineral sulphides and CaO yields CaS and metal oxide(s) (see equation 1.5b) and hence Fe_3O_4 is present in the X-ray diffraction in the Nkana heated sample. $CaMgSi_2O_6$ was also identified in the Nkana heated sample suggesting that part of MgO and CaO reacted with SiO_2 at 1273 K.

The major phases in the heated Baluba sample were FeS, Cu_5FeS_4 and $Cu_9Fe_9S_{16}$. The presence of FeS is due to the thermal decomposition of FeS_2 and $CuFeS_2$ (see equations 2.19b and 2.22). Cu_5FeS_4 was formed by the thermal decomposition of the $CuFeS_2$ mineral since Cu_5FeS_4 was absent in the as-received

Baluba concentrates (see figure 4.1). It can be suggested that the thermal decomposition of $CuFeS_2$ via reaction 2.19b, was incomplete because of the presence of the $Cu_9Fe_9S_{16}$, in the heated sample. $Cu_9Fe_9S_{16}$ was formed due to loss of sulphur from the $CuFeS_2$ (see equation 2.19a). The Baluba sample has about 3 wt. % CaO and it is for this reason that both the CaS and Fe_3O_4 phases were obtained in the heated sample, as for the case of Nkana.

Similar metal bearing phases ($CuFeS_2$, $Cu_9Fe_9S_{16}$, FeS and Fe_3O_4) were obtained in the Nkana and Baluba heated samples. Note that the Fe content is slightly higher than the Cu content in the Nkana and Baluba samples and hence the Fe rich Cu-Fe-O-S system was computed at 1273 K (figure 5.2b). It is evident from the thermodynamic prediction in figure 5.2b that the FeS + $CuFeS_2$ phase field is in equilibrium with the Fe_3O_4 + Cu_5FeS_4 phase field and hence these phases were obtained in the heated Nkana and Baluba samples (see figure 5.1b). From the XRD results in figure 5.1b and the Cu-Fe-O-S system in figure 5.2b, it can be concluded that there is a very broad agreement between the experimental results for the heated mineral concentrates and the thermodynamic prediction.

5.1.1 SEM analysis

The elemental mapping for the mineral sulphide concentrates heated at 1273 K, under argon atmosphere are shown in figures 5.3 – 5.5. It can be deduced from the elemental maps in figure 5.3 that the main metal sulphide phase in the heated Nchanga sample is bornite (Cu_5FeS_4) and this agrees with the XRD results in figure 5.2b. A thin ring of iron oxide surrounds the bornite phase in some particles and this might have been caused by the internal oxidation of the sample. The iron oxide phase was identified as Fe_3O_4 in the XRD pattern (see figure 5.1). It is evident from the SEM images that the heated Baluba sample was completely molten and this is due to the fact that the mineral sulphide concentrates are dominated by the $CuFeS_2$ mineral which melts at 1223 K [171]. On the other hand, the Nkana sample was partially molten because of the presence of the gangue mineral phases e.g. SiO_2 and Al_2O_3 are solid at 1273 K. The SEM results in figure 5.3 show that the volume of the liquid phase is very small in the Nchanga sample and this is because the mineral sulphide concentrates are dominated by the Cu_2S mineral which melts at 1403 K.

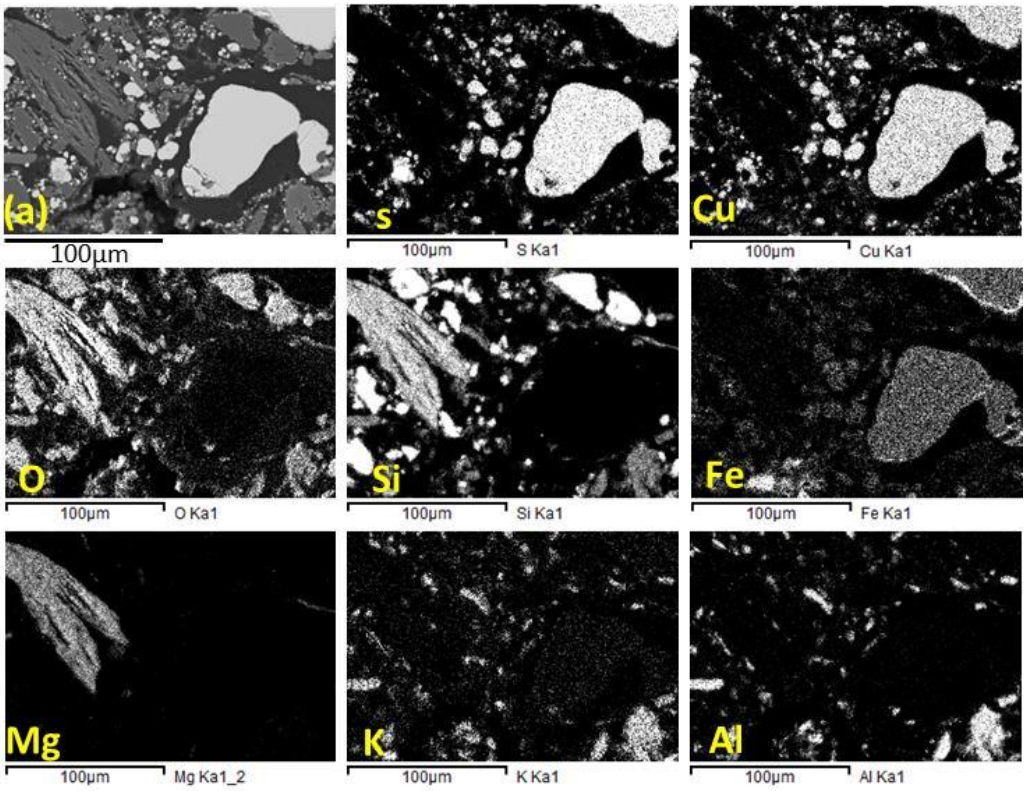

Figure 5.3 – Elemental mapping for the Nchanga sample after heating the mineral concentrates at 1273 K, (a) is the analysed area under backscattered electron imaging. Argon flow rate = 0.6 litre min^{-1}

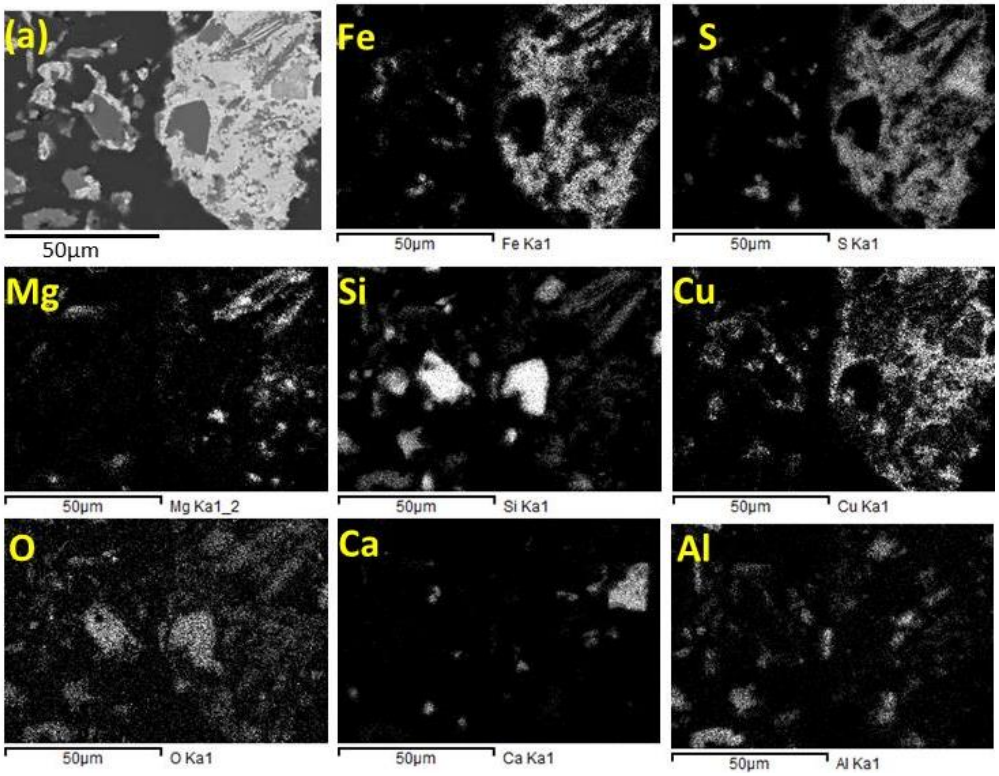

Figure 5.4 – Elemental mapping for the Nkana sample after heating the mineral concentrates at 1273 K, (a) is the analysed area under backscattered electron imaging. Argon flow rate = 0.6 litre min^{-1}

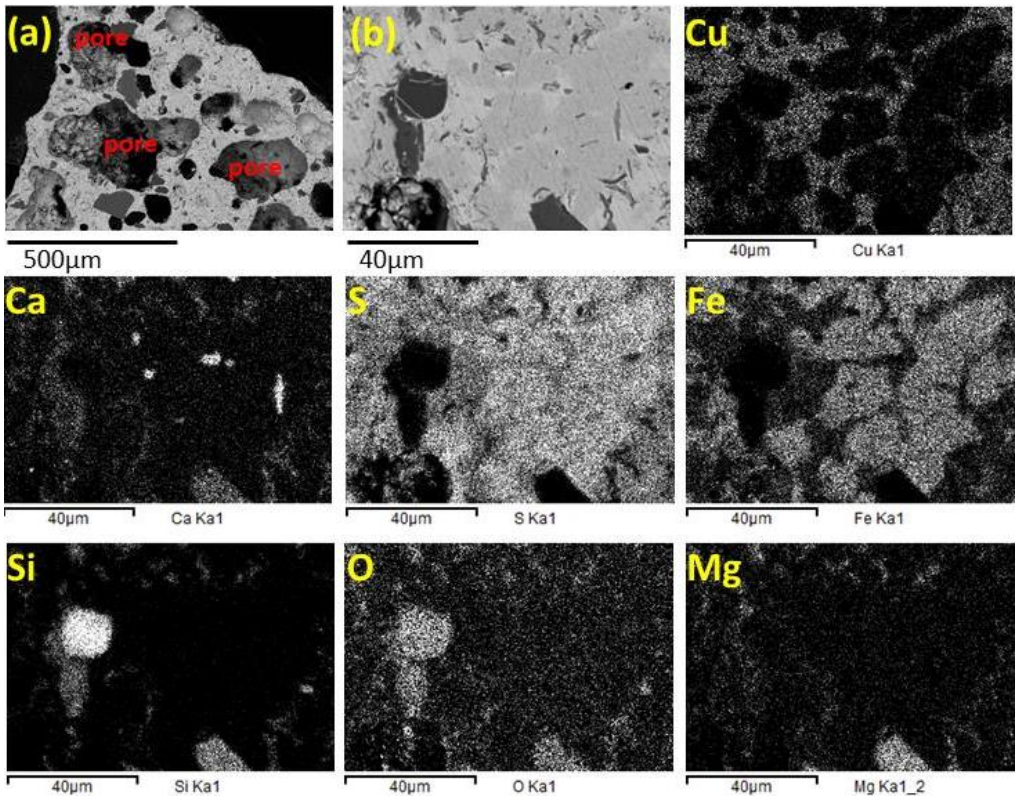

Figure 5.5 – Elemental mapping for the Baluba sample after heating the mineral concentrates at 1273 K, (b) is the analysed area under backscattered electron imaging. Argon flow rate = 0.6 litre min^{-1}

5.2 Heat treatment of mineral sulphide concentrates in the presence of CaO

The carbothermic reduction of the mineral sulphide concentrates cannot occur in the absence of CaO. However, metallisation can take place in the absence of carbon via metal sulphide (MS) – metal oxide (MO) and MO - CaS reactions as reported by Jha [35, 172] and Machingawuta et al. [38]. Moreover, the MS - CaO ion exchange reaction may yield liquid phase(s) which can influence the rate of metallisation during reduction of the mineral sulphides. Therefore, the heat treatment of the mineral sulphide concentrates in the presence of CaO was studied, for understanding the phase formation in the absence of carbon.

To understand the reactions between mineral sulphide and CaO, the mineral sulphide concentrates were mixed with CaO at the molar ratio of MS:CaO = 1:2 and, heated isothermally, in the thermogravimetric analysis equipment in the temperature

range of 1073 K – 1323 K. The plots of the % weight loss versus time curves are shown in figure 5.6.

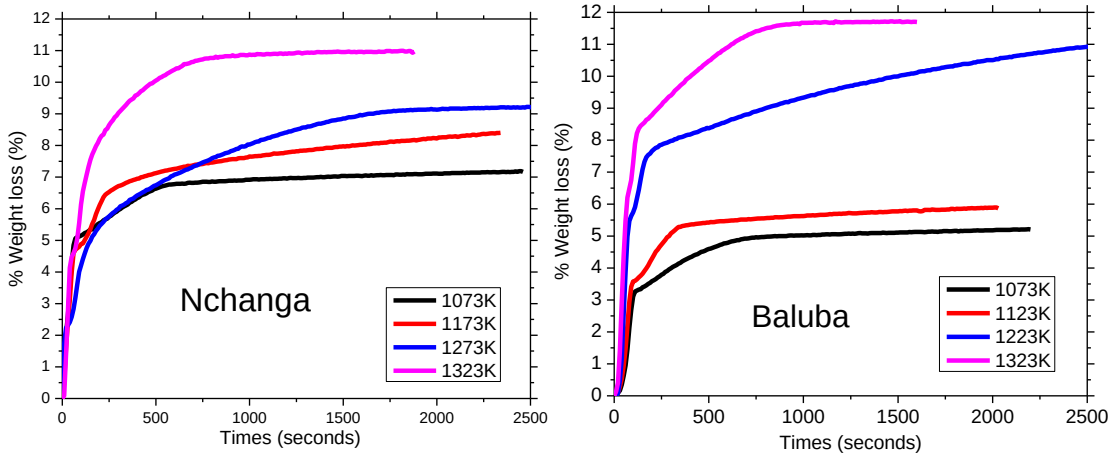

Figure 5.6 – Plots of the % weight loss against time for heat treatment of the mineral sulphide concentrates in the presence of CaO, molar ratio of MS:CaO = 1:2. Argon flow = 0.6 litre min^{-1}

It is evident from figure 5.6 that the % weight loss increases with increase in the reaction temperature. The weight loss of the samples during heat treatment of the mineral sulphide concentrates in the presence of CaO can be caused by: (i) evolution of SO_2 gas (equations 5.3 – 5.5) [172] and (ii) thermal decomposition of the volatile species, such as H_2O or CO_2 gas that were present in the mineral sulphide concentrates.

$$1.5S_2(g) + 2CaO = 2CaS + SO_2(g),\ \Delta G_{1273K} = -96\ kJ \qquad 5.3$$

$$2Cu_2O + Cu_2S = 6Cu + SO_2(g), \quad \Delta G_{1273K} = -21\ kJ \qquad 5.4$$

$$3Cu_2O + CaS = 6Cu + CaO + SO_2(g), \quad \Delta G_{1273K} = -127\ kJ \qquad 5.5$$

The XRD patterns for the mineral sulphide concentrates heated in the presence of CaO at 1073 K and 1273 K are presented in figure 5.7a and 5.7b, respectively.

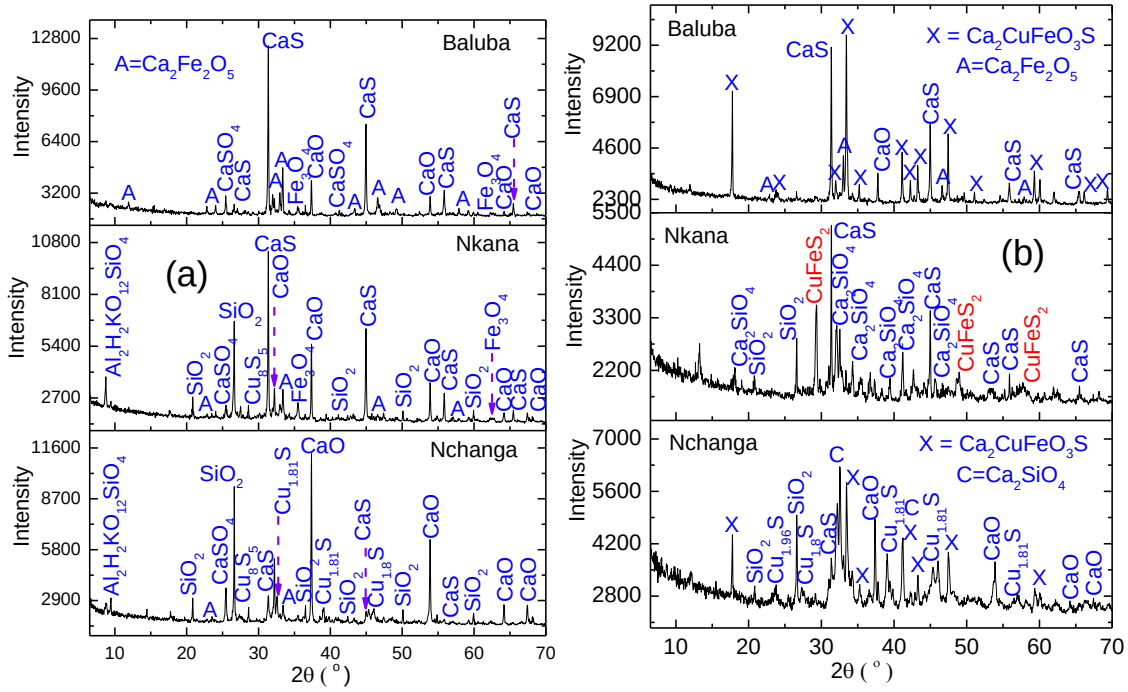

Figure 5.7 – XRD patterns for the mineral sulphide concentrates heat treated in the presence of CaO, molar ratio of MS:CaO = 1:2; (a) 1073 K and (b) 1273 K. Argon flow = 0.6 litre min^{-1}

The main phases in the samples at 1073 K and 1123 K were CaS, Fe_3O_4, $Ca_2Fe_2O_5$, $CaSO_4$, excess CaO, Cu-S. The formation of CaS and $Ca_2Fe_2O_5$ are due to the MS – CaO exchange and Fe-O - CaO reactions, respectively. $CaSO_4$ might have been formed via equation 5.6. Since the $CaSO_3$ is stable at 1173 K, in the presence of SO_2 gas, reaction 5.6 might have occurred via equations 5.7 and 5.8. The CaO – FeS system as a function of partial pressures of O_2 and SO_2 gas, has been constructed by Rosenqvist [41] and it was shown that the stable phases in the CaO rich region are CaS, Fe_3O_4, $Ca_2Fe_2O_5$, $CaSO_4$ and CaO and, this agrees with the results in figure 5.7a at 1073 K.

$$4CaO + 4SO_2(g) = CaS + 3CaSO_4, \qquad \Delta G_{1073K} = -261\,kJ \tag{5.6}$$

$$CaO + SO_2(g) = CaSO_3 \qquad \Delta G_{1073K} = -34\,kJ \tag{5.7}$$

$$4CaSO_3 = CaS + 3CaSO_4 \qquad \Delta G_{1073K} = -126\,kJ \tag{5.8}$$

Copper sulphide ($Cu_{1.6}S$ and $Cu_{1.8}S$) is present in the samples at 1073 K as shown in the XRD patterns in figure 5.7a. The copper sulphides in figure 5.7a co-exist with CaO indicating that the Cu-S – CaO reaction was extremely slow at 1073 K.

There was no $CaSO_4$ in the samples at higher reaction temperatures ($T \geq 1223$ K) as shown in figure 5.7b. The absence of the $CaSO_4$ phase at $T \geq 1223$ K appears to be due to reaction 5.9 [84, 85]. Reaction 5.9 has been studied by Jha [84] under the flow of argon atmosphere and the reaction reached about 30 % conversion, in 2 hours at 1223 K. The presence of SiO_2 can further force reaction 5.9 in the forward direction because of the formation of calcium silicate as shown in equation 5.10. The possibility of reactions 5.9 and 5.10 can be confirmed by the fact that $CaSO_4$ was only present in the samples which were reacted for less than 15 minutes at $T \geq 1223$ K.

$$CaS + 3CaSO_4 = 4CaO + 4SO_2(g), \qquad \Delta G_{1273K} = +121.5 \text{ kJ} \qquad 5.9$$

$$CaS + 3CaSO_4 + 4SiO_2 = 4CaSiO_3 + 4SO_2(g), \ \Delta G_{1273K} = -241.5\text{kJ} \qquad 5.10$$

It is important to note that $CuFeS_2$ was absent and present in the Nkana sample at $T \leq 1173$ K and $T > 1173$ K, respectively (see figures 5.7a and 5.7b). In addition, there was no excess CaO in the Nkana sample at $T > 1173$ K and Ca_2SiO_4 was observed. Therefore, the presence of $CuFeS_2$ and the absence of CaO in the Nkana sample at $T > 1173$ K, can be due to two reasons: (i) consumption of part of CaO by the gangue minerals (SiO_2 and Al_2O_3) and (ii) re-sulphidisation of the metal oxides via CaS - metal oxide (MO) reaction from the liquid phase.

The presence of metal sulphides ($CuFeS_2$) in the Nkana sample was analysed by stopping the reactions at various times at 1273 K. The phases obtained after 3 and 5 minutes are presented in the XRD patterns in figure 5.8. There were no metal sulphide phases at time ≤ 3 minutes and the main phases were Fe_3O_4, $Ca_2Fe_2O_5$, Ca_2SiO_4 and CaO. Since the metal sulphides are absent at $t \leq 3$ minutes (figure 5.8), it can be concluded that all the mineral sulphides reacted with CaO via the MS - CaO exchange reaction. In short, the MS - CaO exchange reaction was complete in the Nkana sample at $t \leq 3$ minutes. However, excess CaO was absent and $CuFeS_2$ was present in the samples that were reacted for $t \geq 5$ minutes. The XRD peak intensities for $CuFeS_2$ were increasing with increase in reaction time. As a result, the formation of metal sulphides

or re-sulphidisation of the metal oxides are due to the reaction involving CaS, SiO_2, metal oxides and, can be represented by equations 5.11 and 5.12.

$$3Ca_2Fe_2O_5 + 7CaS + 13SiO_2 = 6FeS + 13CaSiO_3 + SO_2(g) \quad 5.11$$

$$4CaS + Cu_2O + Ca_2Fe_2O_5 + 6SiO_2 = 2CuFeS_2 + 6CaSiO_3 \quad 5.12$$

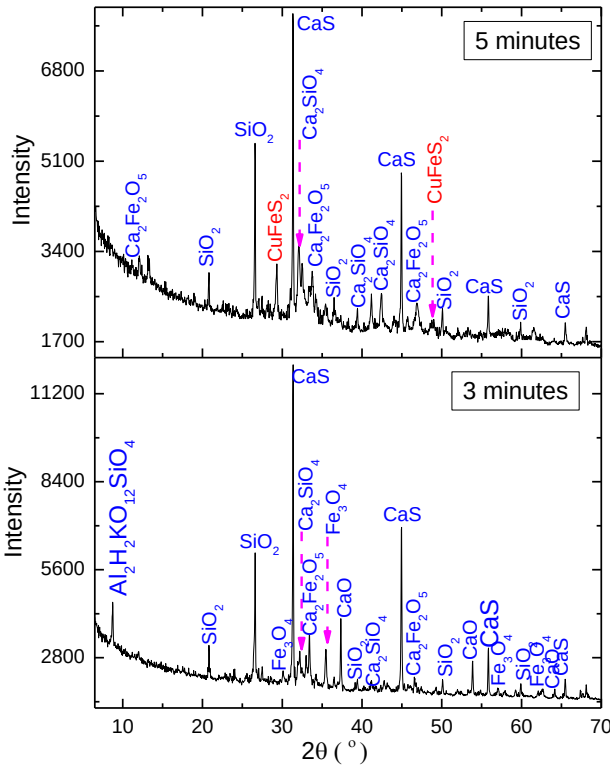

Figure 5.8 – XRD patterns after heat treatment of the Nkana sample for 3 minutes and 5 minutes at 1273 K, molar ratio of MS:CaO = 1:2. Argon flow = 0.6 litre min^{-1}

The XRD peak intensities for CaS are highest in the Baluba sample because nearly all mineral sulphides reacted with CaO. Apart from CaS, the other major phase in the heat treated Baluba sample at 1273 K, was Ca_2CuFeO_3S. The Ca_2CuFeO_3S liquid phase was also present in the Nchanga sample at 1273 K (figure 5.7b).

5.2.1 Formation of the Ca_2CuFeO_3S liquid phase

The Ca_2CuFeO_3S liquid phase has never been reported in the heat treatment or reduction of the mineral sulphides in the presence of CaO. It was therefore necessary to

understand the mechanism leading to the formation of this phase and this was achieved by stopping the reactions/experiments at various times (between 1 to 15 minutes). The XRD patterns obtained after heat treatment of the Baluba mineral sulphide concentrates in the presence of CaO, for various times at 1273 K, are given in figure 5.9. The main phases that were formed after reacting the samples for 1 minute were CaS, $CaSO_4$ and Fe_3O_4 (figure 5.9). However, Fe_3O_4 was absent and $Ca_2Fe_2O_5$ was observed after increasing the reaction time to 2 minutes. The formation of Fe_3O_4 and $Ca_2Fe_2O_5$ can be represented by equations 5.13a and 5.13b, respectively. The XRD peak intensities for $Ca_2Fe_2O_5$ increased after 4 minutes and, Ca_2CuFeO_3S was observed after the sample was reacted for 7 minutes. The XRD peak intensities for Ca_2CuFeO_3S were increasing with increase in the reaction time.

$$4.5FeS_2 + 8CaO = 1.5Fe_3O_4 + 8CaS + SO_2(g), \quad \Delta G_{1273K} = -418\,kJ \qquad 5.13a$$

$$8Fe_3O_4 + 24CaO + 2SO_2(g) = 12Ca_2Fe_2O_5 + S_2(g), \quad \Delta G_{1273K} = -507\,kJ \qquad 5.13b$$

$$CaS + 3CaO + Cu_2S + Fe_2O_3 = 2Ca_2CuFeO_3S \qquad 5.13c$$

$$2CaS + 2CaO + Cu_2O + Fe_2O_3 = 2Ca_2CuFeO_3S \qquad 5.13d$$

$$CaS + Cu_2S + CaO + Ca_2Fe_2O_5 = 2Ca_2CuFeO_3S \qquad 5.13e$$

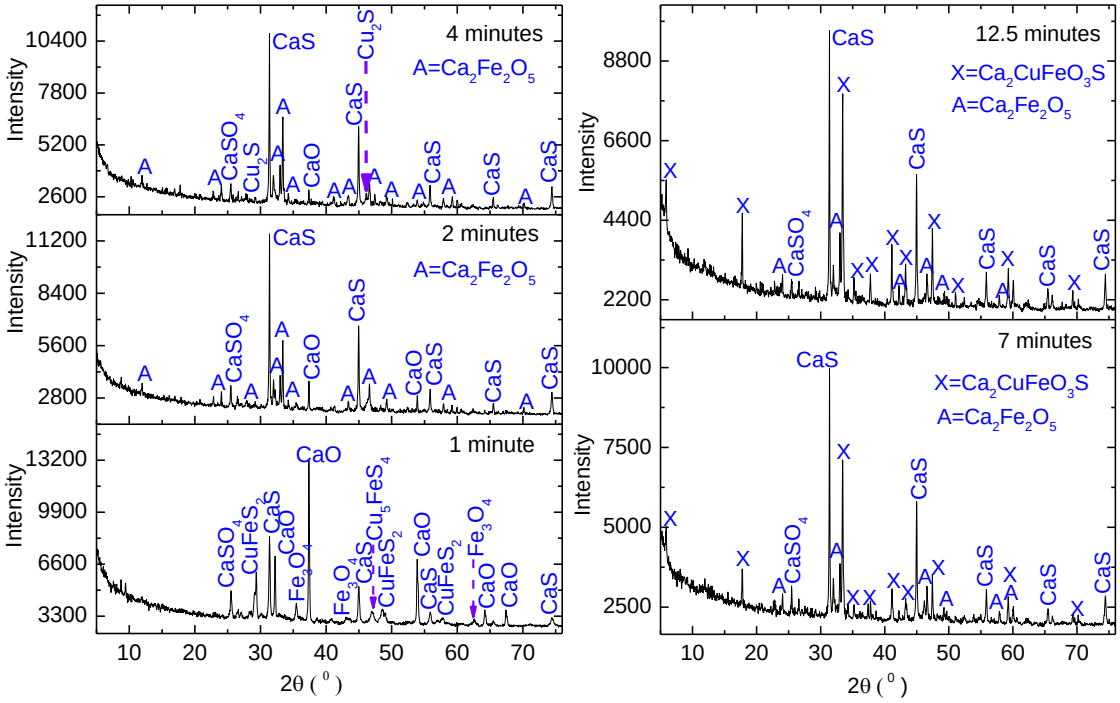

Figure 5.9 – XRD patterns for Baluba mineral sulphide concentrates after heating in the presence of CaO for MS:CaO = 1:2, for various times at 1273 K. Argon flow = 0.6 litres min^{-1}

The Ca-Fe-Cu-O-S predominance area diagram at 1273 K is shown in figure 5.10 and it can be observed that the stable phases at high partial pressure of O_2 and SO_2 gases are Cu_2S, Fe_3O_4 and $CaSO_4$. Note that the partial pressures of O_2 and SO_2 gases are expected to be higher at the start of the reaction (experiment) owing to the thermal decomposition of the gangue minerals and mineral sulphides ($CuFeS_2$ and FeS_2), respectively, and hence Cu_2S, Fe_3O_4 and $CaSO_4$ were obtained in the first minute. $Ca_2Fe_2O_5$ was obtained in the second minute at 1273 K and the thermodynamic prediction in figure 5.10 shows that this is only possible when the partial pressure of SO_2 decreases. The partial pressure of SO_2 gas decreases with increase in reaction time, due to decrease in the thermal decomposition of the mineral sulphides. As observed in figure 5.9, Ca_2CuFeO_3S co-exist with $CaSO_4$, Cu_2S, CaS, CaO and $Ca_2Fe_2O_5$, suggesting that it is formed at the equilibrium point of the ($\log_{10}(P(O_2))$(atm) ≈ -10.4 and $\log_{10}(P(SO_2))$(atm) ≈ -1.1) of the $CaSO_4$ + $Ca_2Fe_2O_5$ + Cu_2S, CaS + $Ca_2Fe_2O_5$ + Cu_2S and CaO + $Ca_2Fe_2O_5$ + Cu_2S phase fields (figure 5.10). In summary, the phases obtained at various times (figure 5.9) correspond with the phase fields in figure 5.10 and this shows that there is good agreement between the experimental results and the thermodynamic prediction.

Metallic copper has been reported by Jha [35, 172] and Payne [47] after heat treatment of the $CuFeS_2$ mineral in the presence of CaO. However, metallic copper was not observed in the present study and this shows that the partial pressure of O_2 gas was lower compared to the work by Jha and Payne, based on the thermodynamic prediction in figure 5.10. The difference in the partial pressure of O_2 gas can arise because of the difference in the argon flow rate and the presence of gaps in the TGA equipment.

It is worth noting that the Ca_2CuFeO_3S phase can be represented as $0.5(CaS{\cdot}Cu_2S{\cdot}3CaO{\cdot}Fe_2O_3)$ or $0.5(2CaS{\cdot}Cu_2O{\cdot}2CaO{\cdot}Fe_2O_3)$ as shown in equations 5.13c and 5.13d, respectively. Based on the XRD results in figure 5.9, it is more reasonable to represent the Ca_2CuFeO_3S phase as $0.5(CaS{\cdot}Cu_2S{\cdot}3CaO{\cdot}Fe_2O_3)$ since this phase is similar to $0.5(CaS{\cdot}Cu_2S{\cdot}CaO{\cdot}Ca_2Fe_2O_5)$. Therefore, the formation of the Ca_2CuFeO_3S phase can be represented by equation 5.13e. As shown from the XRD pattern in figure 5.2, the Ca_2CuFeO_3S phase was not observed in the Nkana sample and this is due to the absence of $Ca_2Fe_2O_5$, since part of CaO was consumed by the gangue minerals by forming complex calcium silicate phases.

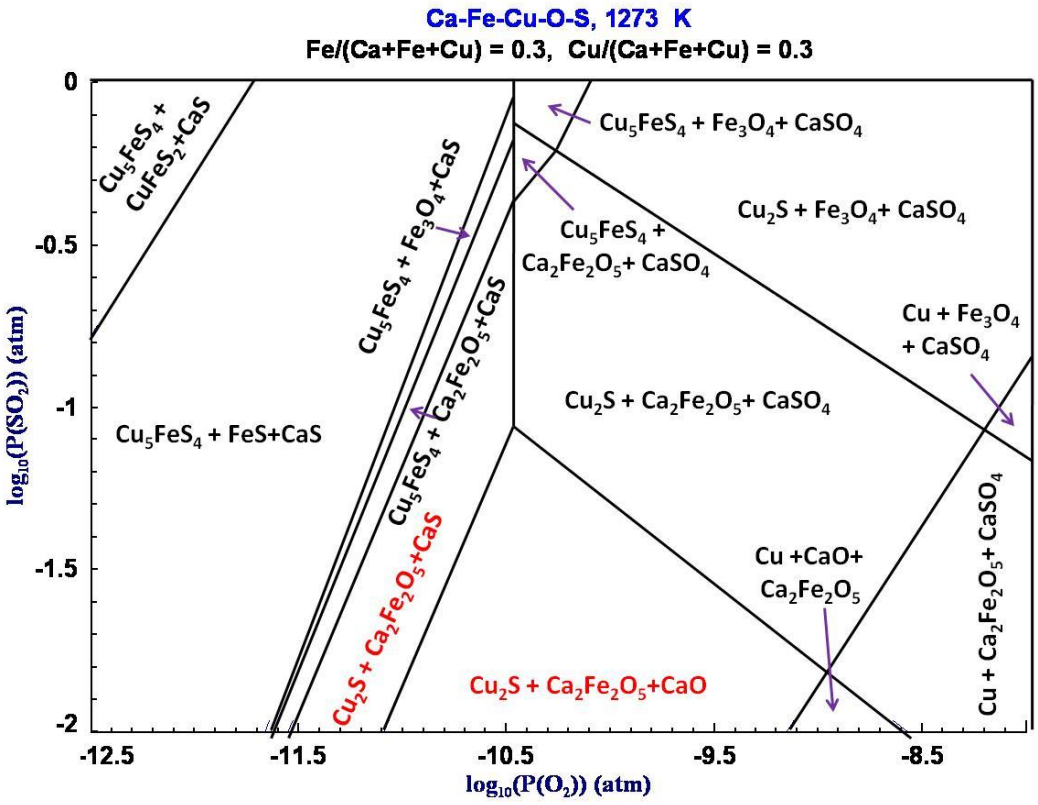

Figure 5.10 - Ca-Fe-Cu-O-S predominance area diagram at 1273 K, computed using FactSage software 6.1 [24]

5.2.2 SEM analysis

The scanning electron microscopy (SEM) images for the heat treated Nchanga sample are given in figures 5.11a and 5.11b. There was no evidence of the Cu_2O phase as the Gibbs energy is positive for the Cu_2S – CaO exchange reaction (see figure 2). However, precipiates of CaS and copper oxysulphide (Cu-O-S) were observed in the partially reacted Cu-S particles and these might have been formed during cooling of the Cu_2S - CaO eutectic melt. The CaS phase in area C (figure 5.12b) contains up to 18 wt. % Cu (table 5.1) and this might be as a result of ionic substitution between Ca^{2+} (0.99 Å) and Cu^{1+} (0.96 Å) ions. The SEM images for the Baluba sample are shown in figure 5.12 and it can be observed that the Ca_2CuFeO_3S phase is mostly surrounded by CaS. By comparions, the larger Cu-S particles did not fully react with CaO as they have smaller reacting surface area compared to the smaller particles.

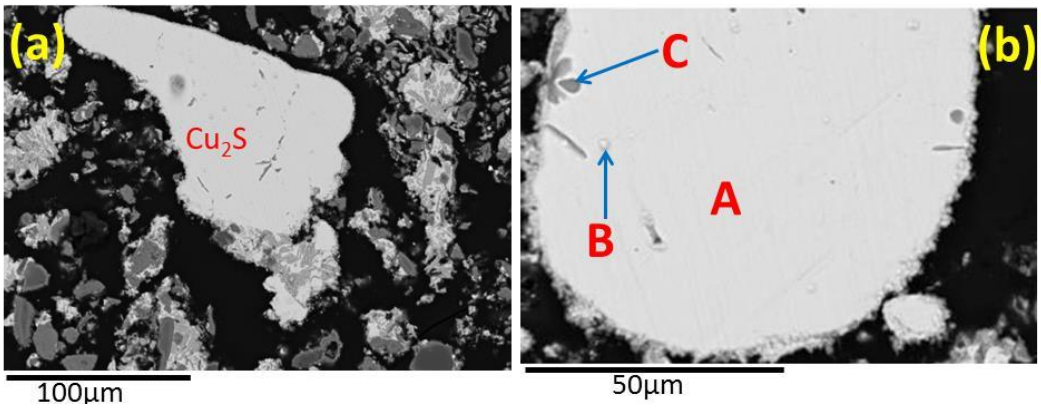

Figure 5.11 – Backscattered SEM images for the Nchanga sample, the mineral sulphide concentrates were heat treated in the presence of CaO at 1273 K, molar ratio of MS:CaO = 1:2, the composition of areas A, B and C are given in table 5.1. Argon flow = 0.6 litre min^{-1}

Table 5.1 – SEM-EDX semi-quantitative composition in wt. % from figure 5.11b

Area	Cu	Ca	O	S
A	76.3	-	-	23.7
B	63.7	-	15.7	20.6
C	17.9	40.9	-	41.2

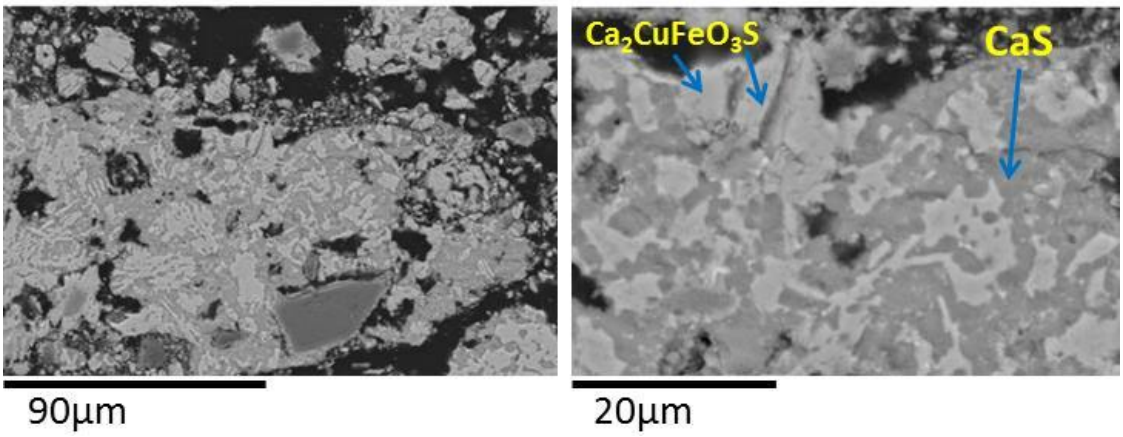

Figure 5.12 – Backscattered SEM images for the Baluba sample, the mineral sulphide concentrates were heat treated in the presence of CaO at 1273 K, molar ratio of MS:CaO = 1:2. Argon flow = 0.6 litre min^{-1}

The SEM-EDX elemental maps for the Nkana sample are shown in figure 5.12 and there is no evidence of the unreacted mineral sulphide phases. The mineral sulphide phase are found either at the periphery or interface of the calcium silicate phases suggesting that it was formed from the reactions involving CaS, SiO_2 and metal oxides (see equations 5.9 - 5.11). The unreacted SiO_2 is surrounded by a rim of Ca-Si-O phase and thus the reaction between SiO_2 and CaO follows a shrinking core model. Based on the SEM images in figure 5.12, it can be concluded that metal oxides can react with CaS in the presence of SiO_2 and Al_2O_3 to form metal sulphides ($CuFeS_2$) and calcium silicate compounds as for the case of Nkana sample.

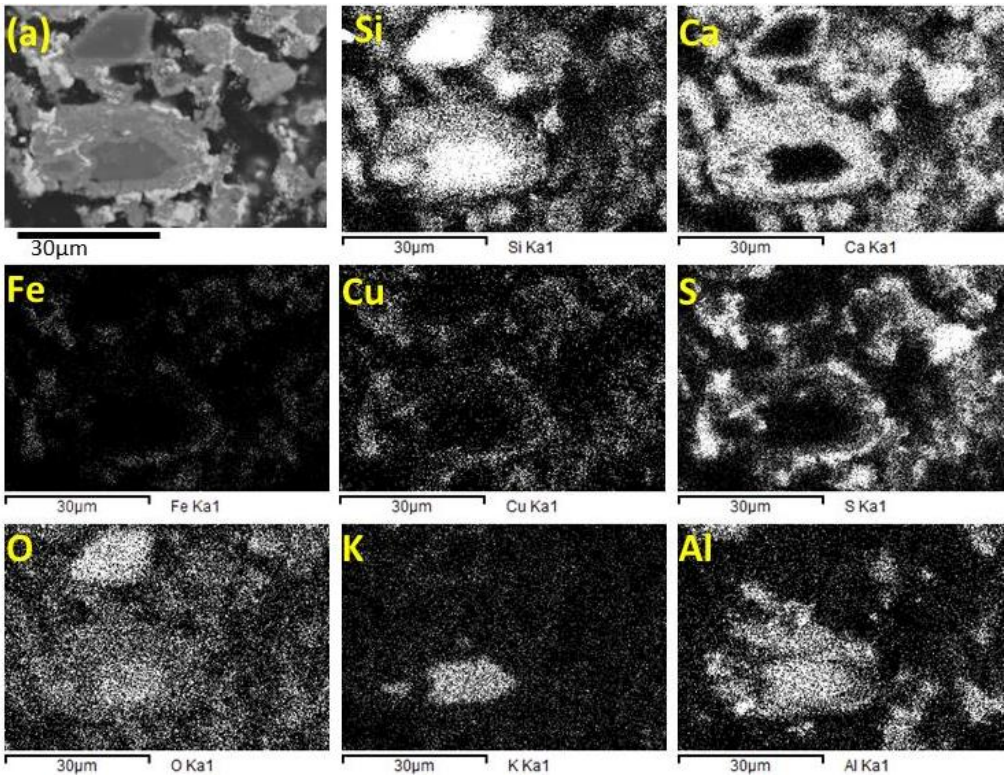

Figure 5.13 – Elememental mapping for the Nkana sample, the mineral sulphide concentrates were heat treated in the presence of CaO at 1273 K, molar ratio of MS:CaO = 1:2, (a) is the analysed area under backscattered electron imaging. Argon flow = 0.6 litre min^{-1}

6.0 Carbothermic reduction of mineral sulphide concentrates in the presence of CaO

This chapter focuses on carbothermic reduction of the mineral sulphide concentrates in the presence of CaO, under argon atmosphere. The reduction experiments were carried out in a temperature range of 1073 K – 1573 K. The low temperature (1073 K - 1323 K) reduction experiments were carried out in the thermogravimetric analysis (TGA) equipment for measuring the extent of reduction as a function of time. The reduction of larger samples (> 3g) and high temperature reduction experiments were carried out in the elevating hearth furnace. The separation of metallic phases from the reduced samples is discussed in this chapter. The energy balance for the carbothermic reduction of mineral sulphides was analysed and compared with the conventional copper smelting process.

6.1 Low temperature reduction (1073 K - 1323 K)

The thermogravimetric analysis was carried out for measuring the extent of reduction or metallisation with respect to time. All reacted samples were characterized by the X-ray diffraction technique. The XRD analysis confirmed that the metallisation was achieved for the samples reacted for more than 1.5 hours at T ≥ 1273 K. No XRD peaks for the starting mineral sulphides were identified in the fully reacted samples, which was characterized by defining the cessation of weight loss due to reaction 1.5a. The relative proportions of lime-to-sulphide and, sulphide-to-carbon mole ratios, types of carbon and finally the reduction temperature were the main parameters found to affect the overall metallisation process.

6.1.1 Effect of reduction temperature

The effect of temperature during carbothermic reduction of mineral sulphide concentrates in the presence of CaO, was studied by keeping MS:CaO:C mole ratio constant. By fixing reaction parameters, the percentage reduction (%R) was recorded continuously against time (t, seconds) at each temperature and the results are presented in figures 6.1a and 6.1b. It is evident from figures 6.1a and 6.1b that the carbothermic

reduction of mineral sulphide concentrates in the presence of CaO is strongly temperature dependent. The percentage reduction (%R) of mineral sulphide concentrates at 1073 K is lower than that at 1273 K or 1323 K as metallisation is incomplete even after holding the samples for 2.5 hours at 1073 K. From the %R versus time plot in figures 6.1a and 6.1b, the reduction reaction above 1223 K appears to progress nearly continuously, meaning that there is no apparent barrier to the overall reaction. By comparison, at and below 1223 K the slope in the %R versus time curve changes after about 15 % reduction and 50 % reduction. From the comparison of plots between 1073 K and 1223 K in figures 6.1a and 6.1b, it can be concluded that the overall rate of reduction increases with increasing temperature.

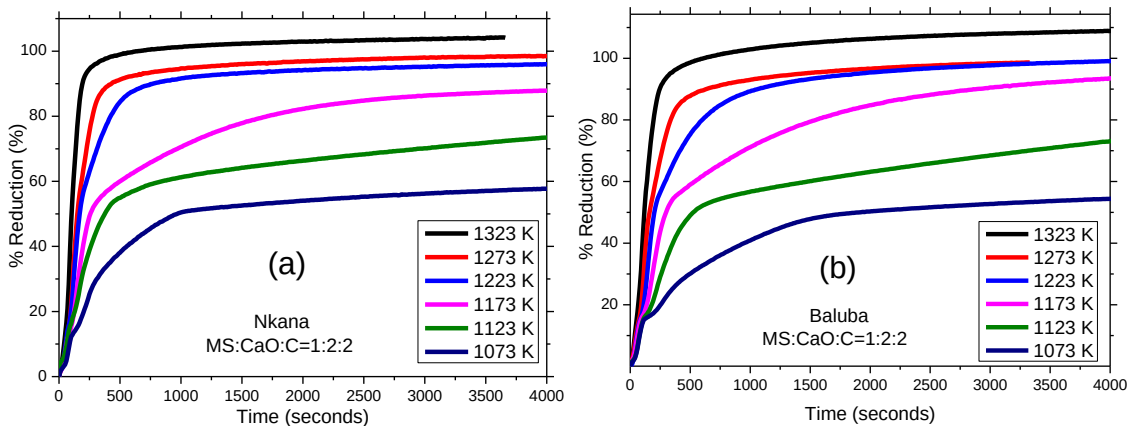

Figure 6.1 – Effect of reduction temperature during reduction of mineral sulphide concentrates in the presence of CaO and carbon black at molar ratio of MS:CaO:C = 1:2:2. Argon flow rate = 0.6 litre min^{-1}

The reduction reactions were stopped after 1.5 hours at 1273 K and 2.5 hours at 1073 K, and the reaction products were analyzed using the X-ray powder diffraction (figures 6.2a and 6.2b) and microscopic techniques. There were no mineral sulphides found after holding the samples for 1.5 hours at 1273 K as shown in figure 6.2b. By comparison, the presence of copper sulphide (Cu-S) was verified from the XRD patterns in figure 6.2a, after 2.5 hours at 1073 K. In view of the relative abundance of Cu_2S in the Nchanga concentrate, which is at 28.3 wt. %, it is unsurprising that the copper sulphide is still abundant in the powder diffraction pattern. In figure 6.2a, it can also be observed that the relative intensities of powder diffraction peaks for CaS are the strongest which may suggest that if the accompanying exchange and reduction reactions, defined in equations 1.5b and 1.5c, respectively, have progressed then there should be sufficiently

high percentage of metallic phase present. However, on comparing the relative intensities of XRD peaks for metallic phases, copper was found to be weak, suggesting that there is little metallisation occurring at 1073 K. The lack of metallisation at 1073 K is evident from the much reduced weight loss, manifested by %R data in figure 6.1, also characterized by the rate of evolution of CO gas in accordance with reaction 1.5a.

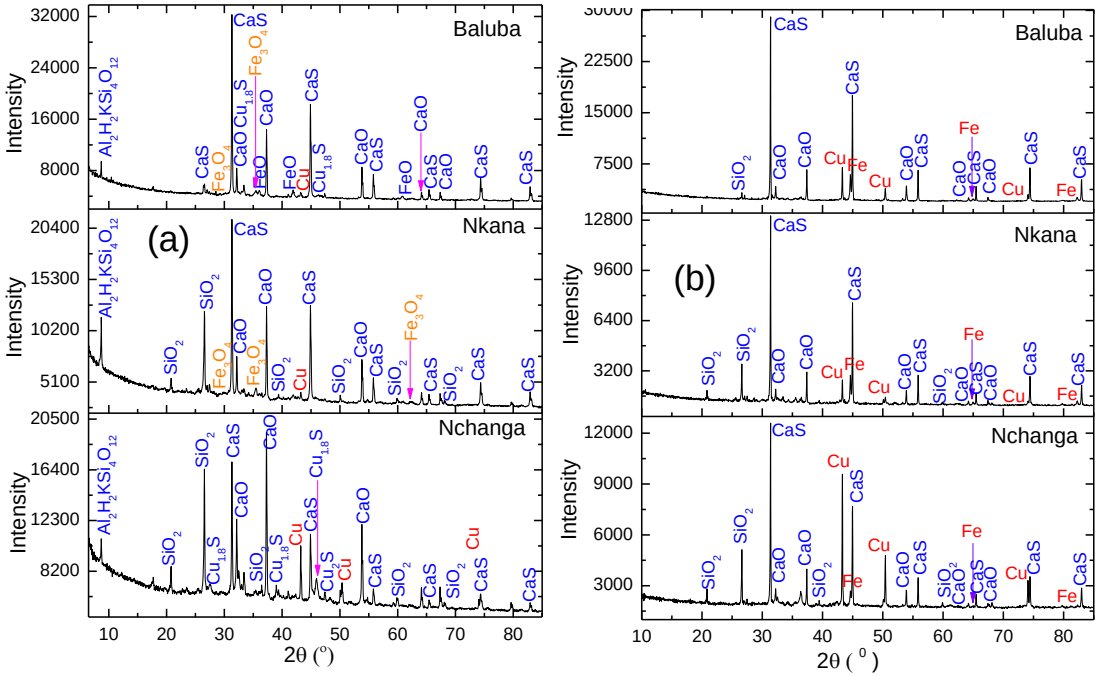

Figure 6.2 – XRD patterns for the samples after carbothermic reduction in the presence of CaO and carbon black at 1273 K, molar ratio of MS:CaO:C = 1:2:2; (a) 2.5 hours at 1073 K and (b) 1.5 hours. Argon flow rate = 0.6 litre min^{-1}

The abundance of CaS and presence of iron oxide (FeO and Fe_3O_4) in the powder diffraction patterns for the samples at 1073 K, confirms that the exchange reactions take place by forming wustite and magnetite first, which at 1073 K, do not reduce to metallic iron. The main barrier for the progression of metallisation of iron appears to be the ensuing reduction reactions (see equations 1.5c – 1.5e). From the literature [15], the solid-state reduction of iron oxide (magnetite/wustite) phase is reported to be very slow below 1173 K [15]. By increasing the temperature above 1173 K, the overall fraction of metallic phases present in the powder diffraction pattern increases due to increasing rate of reduction of the Fe-O phase.

6.1.2 Effect of mole ratio of lime (CaO)

The effect of mole ratio of CaO during carbothermic reduction of mineral sulphide concentrates was studied by maintaining the mole ratio of mineral sulphide:carbon at MS:C = 1:4. A range of mole ratios of CaO:MS, varying between 1.5 and 4, were investigated between 1073 K and 1323 K. It was established that at lower mole ratio of CaO such as MS:CaO = 1:1.5, the reduction reaction did not yield much metallic phase and this is due to smaller area of contact for sustaining the exchange reaction (see equation 1.5b), which is why a significant proportions of mineral sulphides remained unreacted. With the increasing lime-to-sulphide molar ratio, a majority of mineral sulphides were converted into metallic phases even at lower temperatures, e.g. at 1173 K.

The TGA results showing the % reduction versus time plots, obtained at different mole ratios of CaO are shown in figure 6.3. It is evident from figure 6.3 that the extent of metallisation increases with increase in the mole ratio of CaO. It can further be observed in figure 6.3 that the profile of the % reduction versus time curves is similar in the first 4 minutes, corresponding to about 60 % reduction for Nkana and Baluba, at 1273 K. The profile of the % reduction versus time curves, is the same in the first 4 minutes at 1273 K because of the thermal decomposition of the mineral sulphides ($CuFeS_2$ and FeS_2), so that the exchange reaction proceeds mainly via CaO(s) - S_2(g) reaction. However, the exchange reaction essentially proceeds via CaO(s) - MS(s,l) reaction, after thermal decomposition of the mineral sulphides and hence good contact between MS(s,l) and CaO(s) is required for sustaining the exchange reaction. It is for this reason that the extent of metallisation against time greatly increases with increase in the mole ratio of CaO, after 4 minutes at 1273 K.

Nonetheless, the profiles of the % reduction versus time curves were only similar in the first 2.5 minutes corresponding to about 18 % reduction at 1073 K. This is because thermal decomposition of mineral sulphide is low at 1073 K compared to 1273 K.

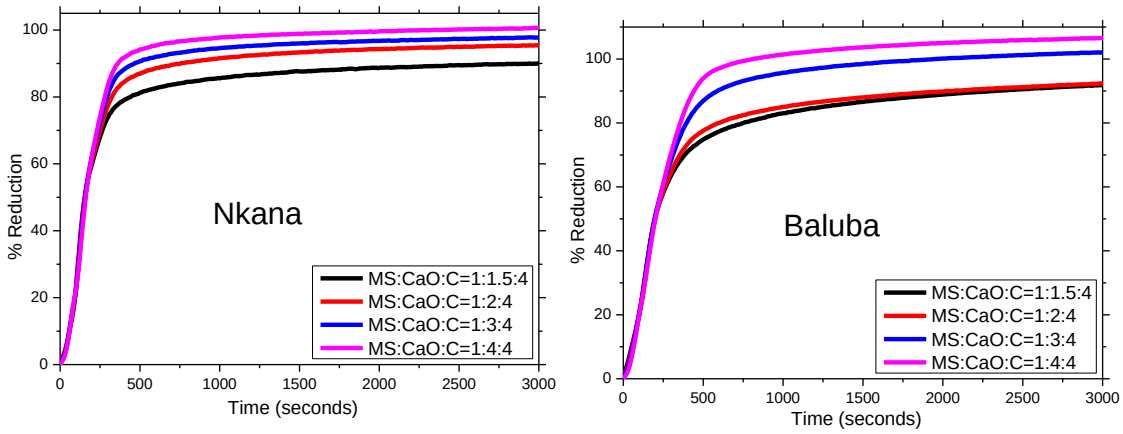

Figure 6.3 – Plot of % reduction against time curves at 1273 K, different mole ratio of CaO. Argon flow rate = 0.6 litre min^{-1}

6.1.3 Effect of mole ratio of carbon black

For studying the effect of carbon black, the MS:CaO mole ratio was kept at 1:2 (MS:CaO = 1:2) and the reduction reactions were analysed between 1073 K and 1323 K. The plots of % reduction against time at different mole ratios of carbon black are shown in figure 6.4. It is evident from figure 6.4 that the extent of metallisation decreases as the mole ratio of carbon black increases between MS:CaO:C = 1:2:2 and 1:2:4 (MS:C = 1:2 and 1.4). The decrease in the extent of metallisation with increase in the mole ratio of carbon is due to the decrease in the contact area for the MS - CaO exchange reaction. It is very clear in figure 6.4 that the reduction reaction for Baluba sample stopped after reaching 90 % reduction in 5 minutes at molar ratio of MS:CaO:C = 1:2:1 and this could be due to sintering of the sample because the sample was excessively sintered after the experiment. By comparison, the Nkana or Nchanga samples were less sintered as result of high gangue mineral content. From the % reduction vs time plots in figure 6.4, it can be concluded that the extent of metallisation decreases with increase in the stoichiometric ratio of carbon black. Nonetheless, the mole ratio of carbon should be more than 1 for reaching 100 % reduction in the Baluba sample.

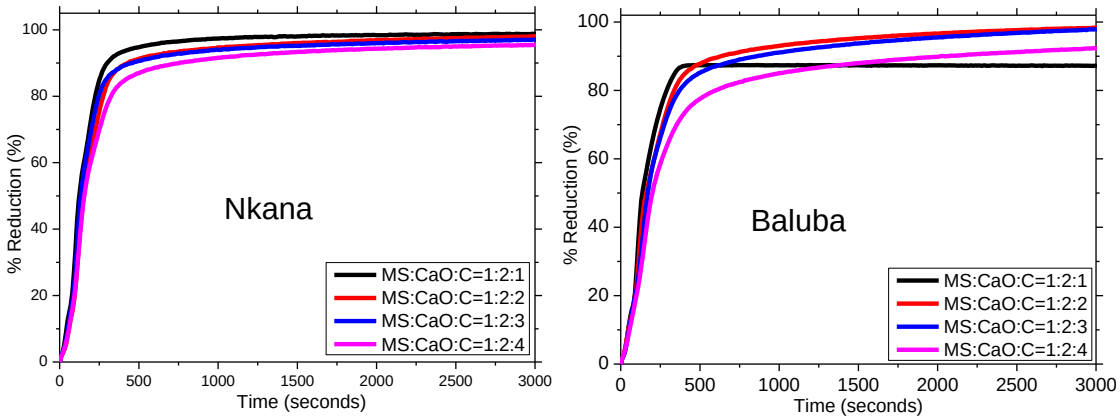

Figure 6.4 – Plot of % reduction against time curves at 1273 K, different mole ratio of carbon black. Argon flow rate = 0.6 litre min^{-1}

The XRD patterns for the mineral sulphide concentrates at molar ratio of MS:CaO:C =1:2:1 and 1:2:2 are compared in figures 6.5a and 6.5b, respectively. The metallic phases (Cu, Fe), CaS and excess CaO can be observed in the reacted samples at molar ratio of MS:CaO:C = 1:2:2 (figure 6.5b). Nonetheless, excess CaO from the reduction reaction was completely consumed by SiO_2 and Al_2O_3 at molar ratio of MS:CaO:C = 1:2:1, by forming calcium silicates, identified in the X-ray diffraction patterns in figure 6.5a as Ca_2SiO_4 and $Ca_2Al_2SiO_7$ phases. The Baluba sample has the lowest SiO_2 content but there was no excess CaO at molar ratio of MS:CaO:C = 1:2:1 due to the formation of $Ca_2Fe_2O_5$ phase as shown in figure 6.5a. The presence of the $Ca_2Fe_2O_5$ phase explains as to why the % reduction only reached about 90 % reduction at MS:CaO:C =1:2:1 (see figure 6.4b).

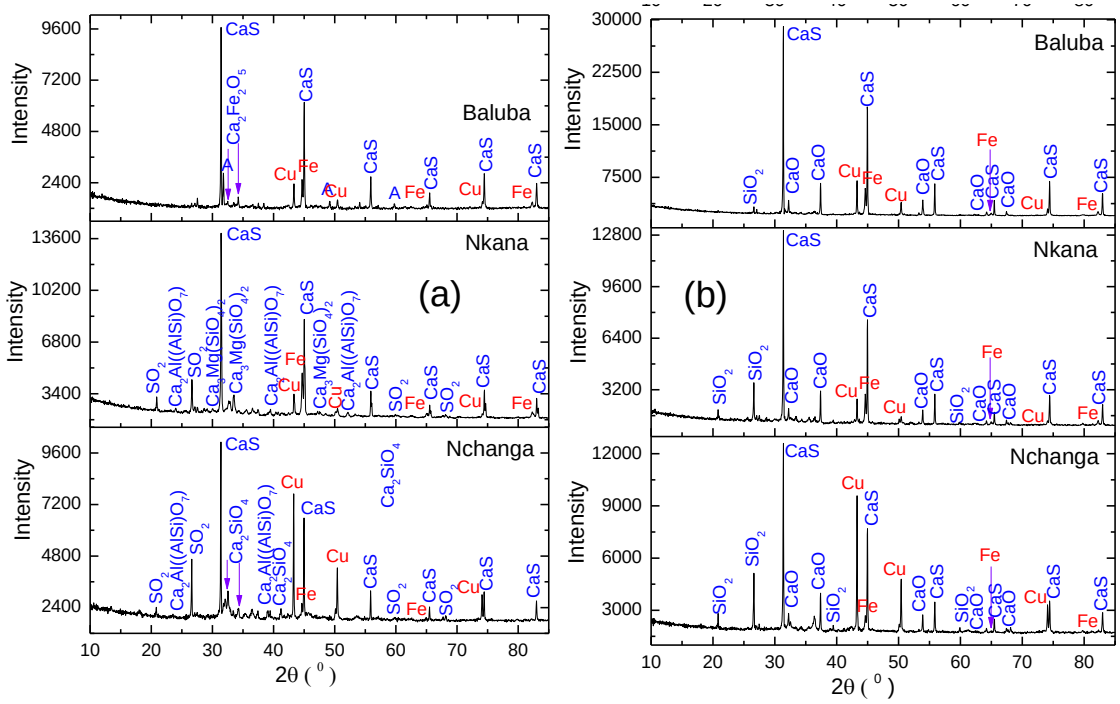

Figure 6.5 - Effect of changing the mole ratio of carbon at 1273 K; (a) MS:CaO:C = 1:2:1 and (b) MS:CaO:C = 1:2:2. Argon flow rate = 0.6 litre min^{-1}

The predominance area diagrams for Ca-Cu-Fe-O-S-Si systems at different activities of SiO_2 are shown in figure 6.6a and 6.6b. The Cu + Fe + CaS phase field is in equilibrium with the Cu + Fe + CaO phase field at low partial pressures of O_2 and SO_2 gases (figure 6.6a) and this is why the Cu + Fe + CaS + CaO phases were obtained at molar ratio of MS:CaO:C = 1:2:2, at 1273 K (see figure 6.5a). Based on the experimental results and the thermodynamic prediction in figure 6.6a, it can be estimated that $\log_{10}(P(O_2))$(atm) was less than -15.3 at molar ratio of MS:CaO:C = 1:2:2. On the other hand, the Cu + Fe + CaS phase field is in equilibrium with the Cu + CaS + $Ca_2Fe_2O_5$ phase field at $\log_{10}(P(O_2))$(atm) ≈ -15.3 and it is for this reason that $Ca_2Fe_2O_5$ was obtained in the Baluba sample at molar ratio of MS:CaO:C = 1:2:1. It can be concluded that the partial pressure of the O_2 gas increases as the molar ratio of MS:CaO:C = 1:2:2 changes to MS:CaO:C = 1:2:1. The SiO_2 content is high in the Nchanga and Nkana samples so that the Ca-Cu-Fe-O-S-Si system is shown in figure 6.6b at $\log(aSiO_2)$ = -5. The Cu + Fe + CaS phase field is in equilibrium with the Cu_2S+ Fe + Ca_2SiO_4 phase field in figure 6.6b and hence the metallic phases (Cu, Fe) co-exist with Cu_2S, CaS and calcium silicate phases in the Nchanga sample at molar ratio of MS:CaO:C = 1:2:1. The above analysis clearly shows that there is broad agreement between the experimental results at MS:CaO:C = 1:2:2 or 1:2:2 and the thermodynamic prediction.

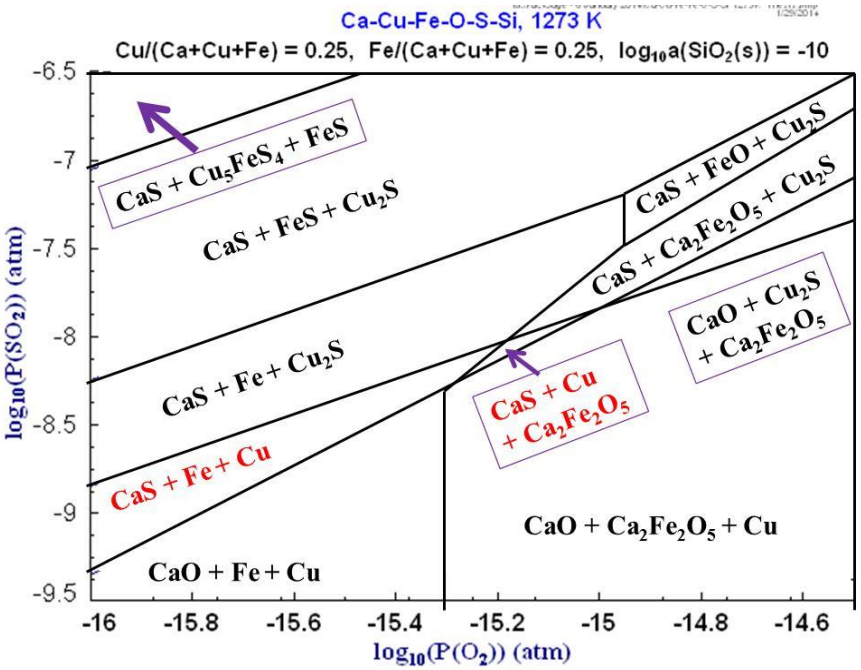

Figure 6.6a – The Ca-Cu-Fe-O-S predominance area diagram at 1273 K, computed using FactSage software 6.1 at log($aSiO_2$) = -10 [24]

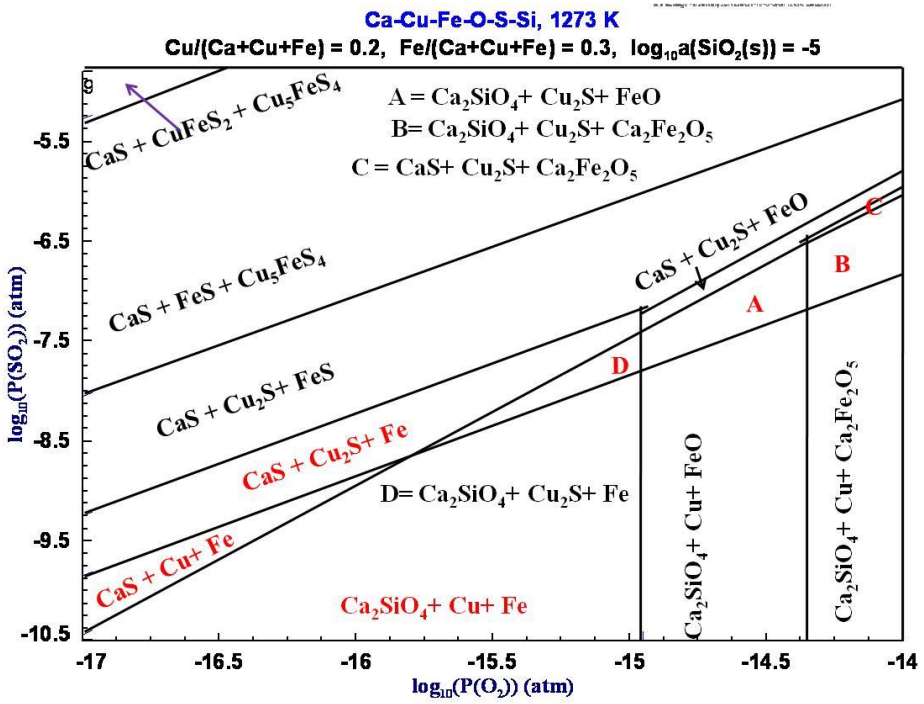

Figure 6.6b – The Ca-Cu-Fe-O-S predominance area diagram at 1273 K, computed using FactSage software 6.1 at log($aSiO_2$) = - 5 [24]

6.1.4 Effect of mole ratio of graphite

The effect of increasing the mole ratio of graphite was analysed at molar ratio of MS:CaO = 1:2 and the plot of % reduction versus time curves are shown in figure 6.7. As shown in figure 6.7, the extent of metallisation increases with increase in graphite-to-sulphur mole ratio and this was caused by the increase in the reduction reaction. It is evident from figure 6.7 that metallisation was completed within 15 minutes at molar ratio of MS:CaO:C = 1:2:2 or 1:2:4 which was not the case when carbon black was used (see figure 6.4) and this shows that the overall time for complete metallisation is shorter with graphite than with carbon black. It appears that metallisation of Cu and Fe proceeds via reduction of the Ca_2CuFeO_3S liquid phase at all mole ratios of graphite and hence the extent of metallisation increases with increase in the mole ratio of graphite. In short, the rate of reduction of the Ca_2CuFeO_3S liquid phase increases with increasing mole ratio of graphite.

The XRD and SEM-EDX analyses showed that excess CaO was consumed by SiO_2 at molar ratio of MS:CaO:C = 1:2:2 or 1:2:4 by forming Ca_2SiO_4 and $Ca_2Al_2SiO_7$ at 1273 K and above in the Nchanga and Nkana samples. The $Ca_2Fe_2O_5$ phase was observed in the Baluba samples and this is because of the equilibrium between Cu + Fe + CaS and Cu + $Ca_2Fe_2O_5$ phase fields (see figure 6.6a). The presence of calcium silicates in the Nchanga and Nkana samples and, $Ca_2Fe_2O_5$ in the Baluba sample, confirms that the partial pressures of O_2 and SO_2 gases are slightly higher for the reduction with graphite than with the carbon black.

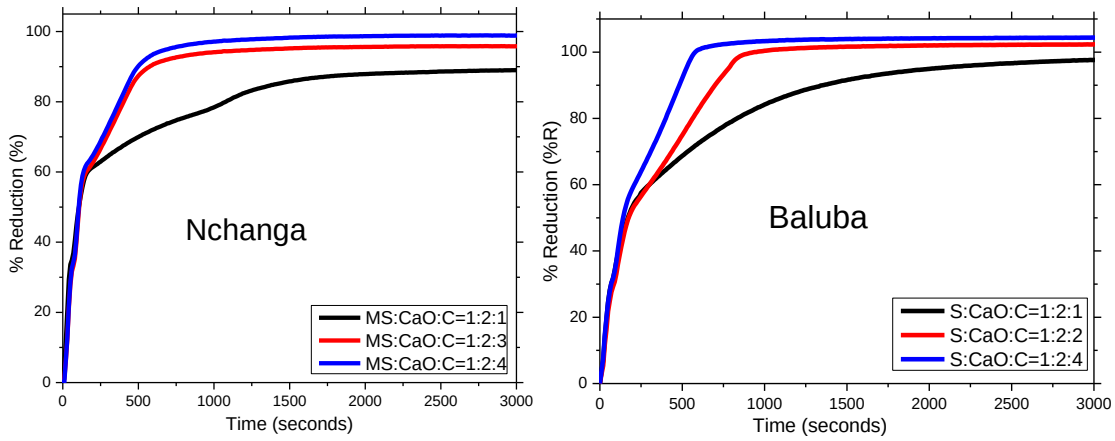

Figure 6.7 – The plot of % reduction versus time curves for the carbothermic reduction of mineral sulphide concentrates in the presence of CaO with graphite at 1273 K. Argon flow rate = 0.6 litre min^{-1}

6.1.5 Effect of particle sizes of the mineral sulphide concentrates

The effect of changing the particle sizes of the mineral sulphide concentrates was studied by further grinding the mineral sulphide concentrates to the particle sizes of -63 µm and -38 µm. The effect of changing the particle sizes of the mineral sulphide concentrates is compared in figures 6.8a and 6.8b at 1073 K, because the extent of metallisation is slowest at this temperature. It is evident from the XRD patterns in figures 6.8a and 6.8b that metallisation of copper increased as the mineral sulphide concentrates particle sizes decreased from -63 µm to -38 µm. As discussed above, the metallisation of copper was limited by the exchange reaction but the barrier decreases with decrease in particle sizes of the mineral sulphide concentrates.

The XRD patterns in figures 6.8a and 6.8b also show that metallisation of Fe is not affected by the particle size of the mineral sulphide concentrates as Fe is still in the oxide form at -38 µm. The fact that metallisation of Fe does not occur even at -38 µm confirms that the main barrier is the reduction reaction at 1073 K. The overall time taken for the complete reduction of the mineral sulphide concentrates particles decreased with the decrease in particle size of the mineral sulphide particles at higher temperatures ($T \geq 1223$ K). For example, metallisation was completed in about 45 minutes and 60 minutes at concentrate particles sizes of -38 µm and -63 µm, respectively, at 1273 K. Even though the total time for complete metallisation decreases with decrease in the particle size of the mineral concentrates, it is unnecessary to grind to -38 µm because of the energy cost for grinding is relatively high.

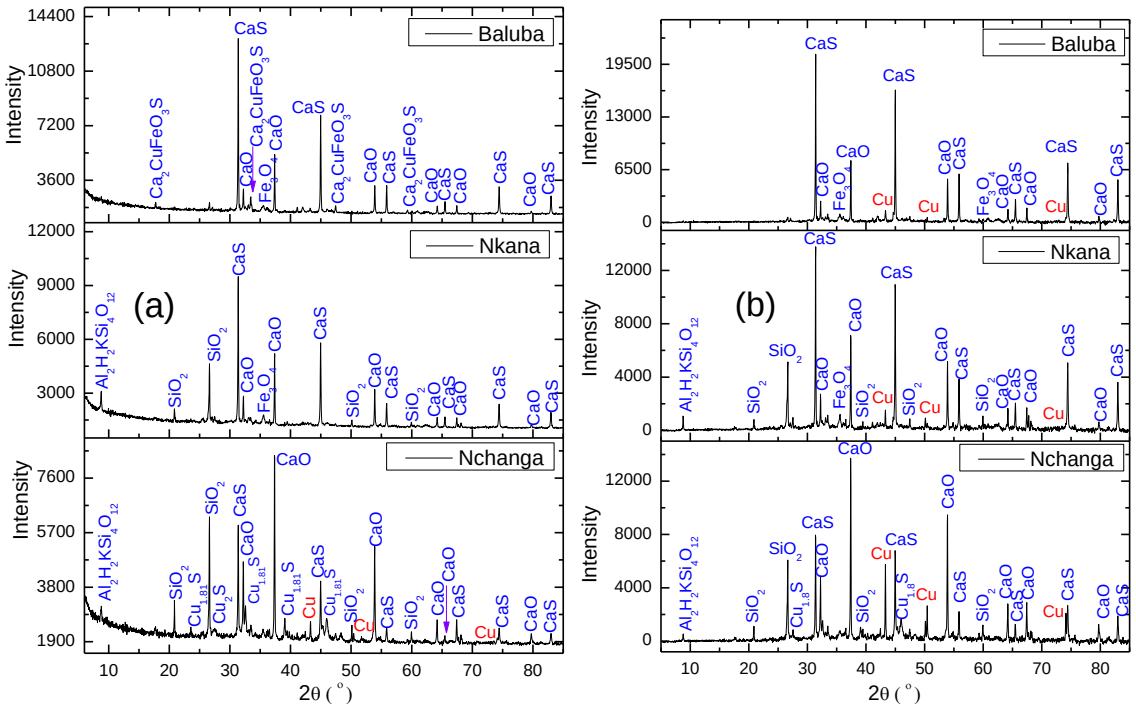

Figure 6.8 – XRD patterns for the samples reduced at different particle sizes, 2.5 hours at 1073 K and molar ratio of MS:CaO:C = 1:2:2; (a) at -63 µm and (b) at -38 µm. Argon flow = 0.6 litre min^{-1}

6.1.6 Phase analysis

The phases in the samples were characterised by X-ray diffraction (XRD) and scanning electron microscopy (SEM) techniques.

6.1.6.1 A summary of the analysis of phases using XRD

The comparison of phases present as a result of exchange reaction at 1073 K in figure 6.2a for different concentrates shows the strong presence of Fe-O (FeO and Fe_3O_4), which suggests that the mineral sulphides have undergone exchange reaction. Fe-O co-exists with CaS in the reduction with carbon black. At higher reduction temperatures, for example at 1273 K, Fe_3O_4 is less evident, as can be seen in figure 6.2b. Excess SiO_2 present in the gangue is evident at both 1073 K and 1273 K for MS:CaO:C = 1:2:2. As expected from the %R versus time plots in figure 6.1, the volume fractions of metallic phases increase in the reacted materials with increase in temperature and is confirmed by the presence of Cu/Fe in the XRD patterns in figure 6.2b.

Furthermore, it is noticeable from figures 6.2a and 6.2b that the excess CaO at MS:CaO:C = 1:2:2 did not react with the SiO_2 present in the minerals at 1073 K. From figure 6.5a the presence of calcium silicate confirms the reaction between CaO and SiO_2, by forming the Ca_2SiO_4 and $Ca_2Al_2SiO_7$ at 1273 K. The formation of complex silicates consumes the available CaO for facilitating the exchange reaction at a given temperature. As a result, the mineral sulphides do not reduce completely, by leaving a trail of evidence for incomplete reaction in the form of unreacted sulphides of copper and iron.

6.1.6.2 Summary of the phase analysis using SEM

In order to further analyse the mechanism of overall reduction reaction, shown in equation 1.5a, systematic analysis using SEM and EDX techniques were undertaken. In figure 6.9, the area analysed for the reaction product after 2.5 hours of reaction at 1073 K is compared with the elemental distribution map, obtained via the EDX spectroscopic technique. The elemental maps of Fe and O show a ring of iron oxide around the copper-sulphide rich phase, which explains that the ions of iron and copper diffuse towards the surface and centre, respectively, and this mechanism also takes place during oxidation/roasting of Cu-Fe sulphide minerals ($CuFeS_2$ and Cu_5FeS_4) [14, 28, 85]. It is caused by the higher stability of FeO than Cu_2O [14] so that FeS is preferentially oxidised. The brightest phase in image B of figure 6.9 is metallic copper. Part of copper was formed at the interface between the Cu_2S and Fe_3O_4 phases and this is because of the equilibrium between the Cu_2S + Fe_3O_4 and Cu + Fe_3O_4 phase fields at $\log_{10}P(O_2)(atm) < -17.9$, at 1073 (figure 6.10). It can be observed from image B in figure 6.9 that all the smaller Cu_2S particles (< 5 µm) were reduced to metallic copper due to the fact that the smaller particles have larger reacting surface area. The area analysed in figure 6.9 is devoid of cobalt, since the Nchanga concentrates contain the least amount of cobalt (0.4 wt. % of Co).

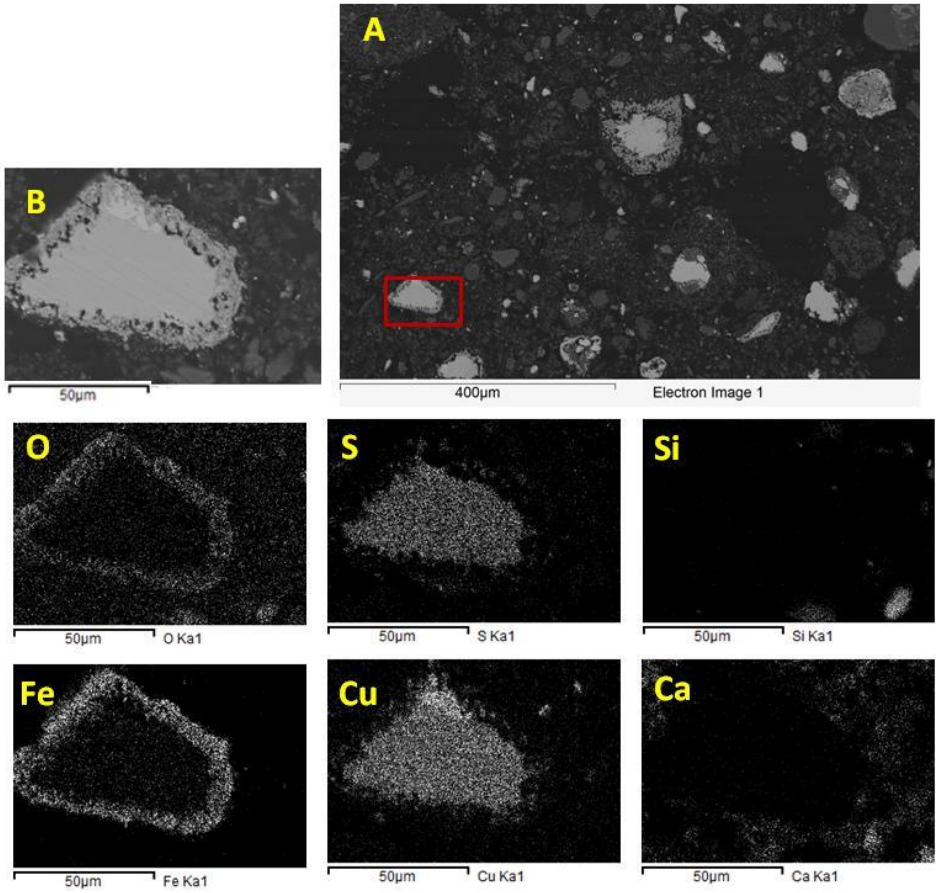

Figure 6.9 – Elemental mapping for Nchanga sample after reduction at 1073 K, molar ratio of MS:CaO:C = 1:1.5:1.5, (A) low magnification image, the analysed area is highlighted by the red box and (B) is the analysed area under BSE imaging

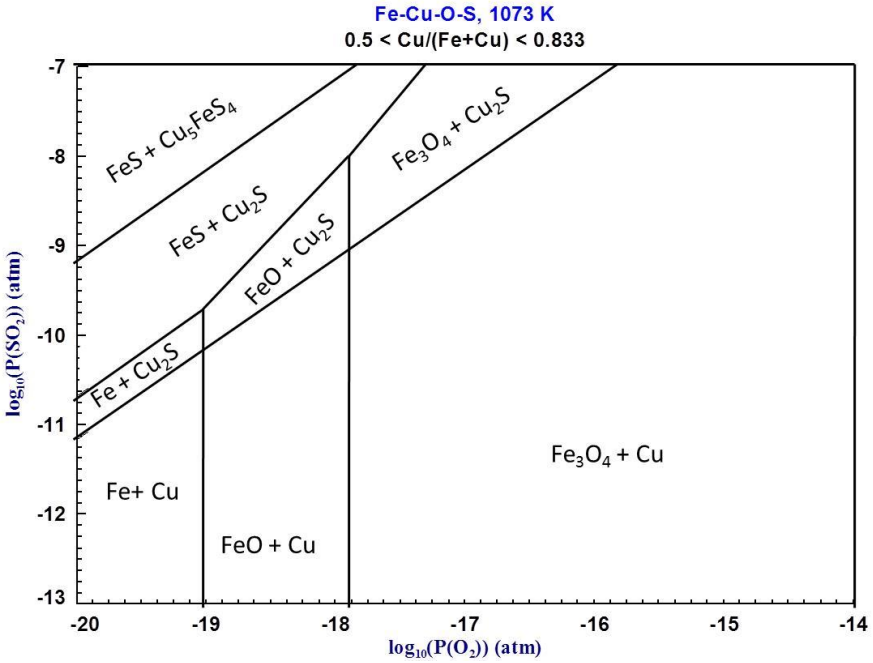

Figure 6.10 – The Fe-Cu-O-S predominance area diagram at 1073 K in relation to the phases obtained in figure 6.9, computed using the Factsage software 6.1 [24]

The SEM images for the Baluba sample after carbothermic reduction at 1073 K are presented in figures 6.11a and 6.11b. The FeS_2 particles in figure 6.11a were completely converted to Fe-O which was identified as FeO and Fe_3O_4 in the X-ray diffraction patterns in figure 6.2a. On the other hand, metallisation of cobalt occurred at 1073 K as shown in figure 6.11b. As noted in figure 6.11b, Co co-exists with Cu_2S and Fe_3O_4 and this agrees very well with the thermodynamic prediction in figure 6.12. The cobalt peaks did not appear in the X-ray diffraction patterns because cobalt is present in small concentration (< 2 wt. %), which is below the limit for XRD detection. SEM analysis for the Nkana sample at 1073 K also showed that the Co-S particles were reduced to Co at 1073 K. From the SEM analysis, it can be concluded that preferential metallisation of cobalt occurred at 1073 K but the metallisation of copper and iron were limited by the exchange and reduction reactions, respectively. Therefore, there is very good agreement between the experimental results and the thermodynamic prediction in figure 2.3a where, the Gibbs energy change is more negative for metallisation of cobalt than for iron and copper.

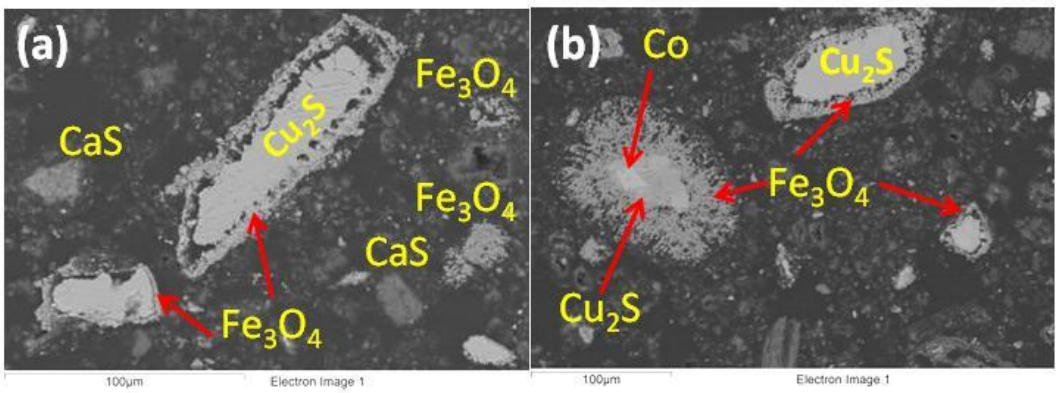

Figure 6.11 – Backscattered SEM images of the Baluba sample, after reduction at 1073 K and molar ratio of MS:CaO:C = 1:2:2. Argon flow rate = 0.6 litre min^{-1}

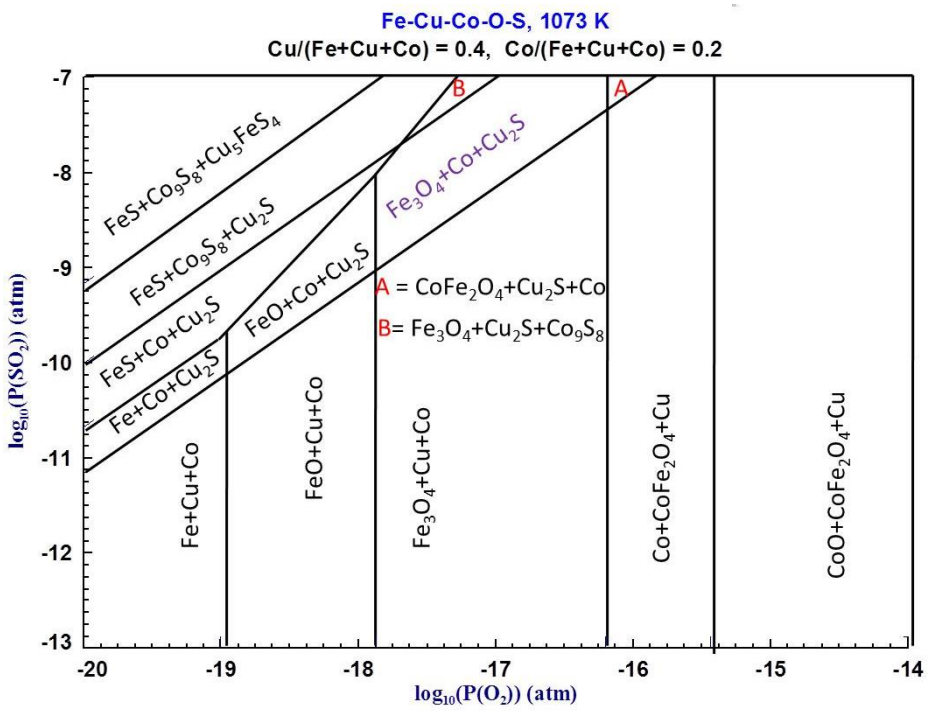

Figure 6.12 – The Fe-Cu-O-S predominance area diagram at 1073 K in relation to the phases obtained in figure 6.11, computed using the Factsage software 6.1 [24]

The elemental maps for the Nchanga and Nkana samples which were reacted for 2.5 hours at 1273 K for molar ratio of MS:CaO:C = 1:1.5:1.5, are shown in figures 6.13 and 6.14, respectively. Since the Nchanga sulphide concentrates have the highest copper content, the analysed area in image A of figure 6.13 contains a lot of copper particles which were reduced from the Cu_2S mineral particles. The reduced copper particles have various sizes and shapes which are similar to the mineral sulphide, in the as-received mineral concentrates. On the other hand, the Nkana concentrates are rich in iron such that the analysed area in figure 6.14 contains a lot of iron particles. Furthermore, the analysed area in figure 6.14 also contains significant amount of cobalt which is associated with iron as a result of high solid solubility between iron and cobalt. The shape of the reduced Fe or Fe-Co particles appear different from their respective mineral sulphides due to dominance of the liquid phase during reduction of (Co)FeS_2 mineral particles.

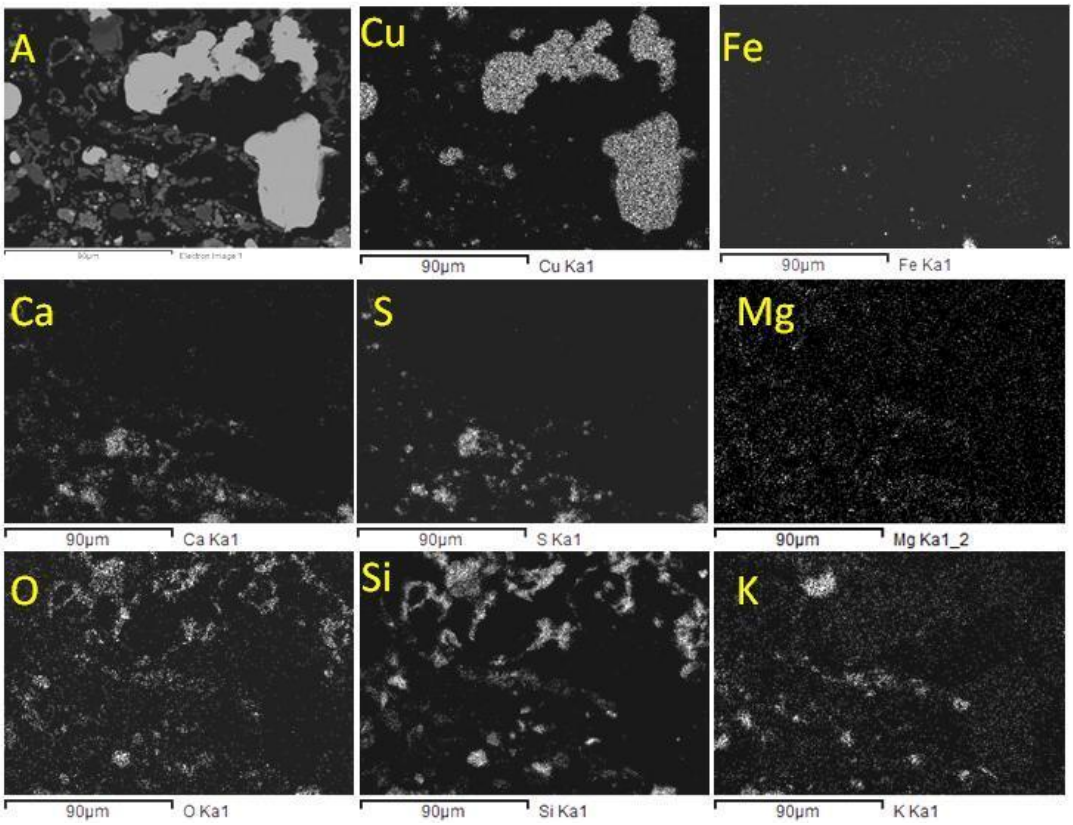

Figure 6.13 – Elemental mapping for Nchanga sample after carbothermic reduction at 1273 K for molar ratio of MS:CaO:C = 1:2:2, (A) is the sample area analysed from image A, under backscattered electron imaging. Argon flow rate = 0.6 litre min^{-1}

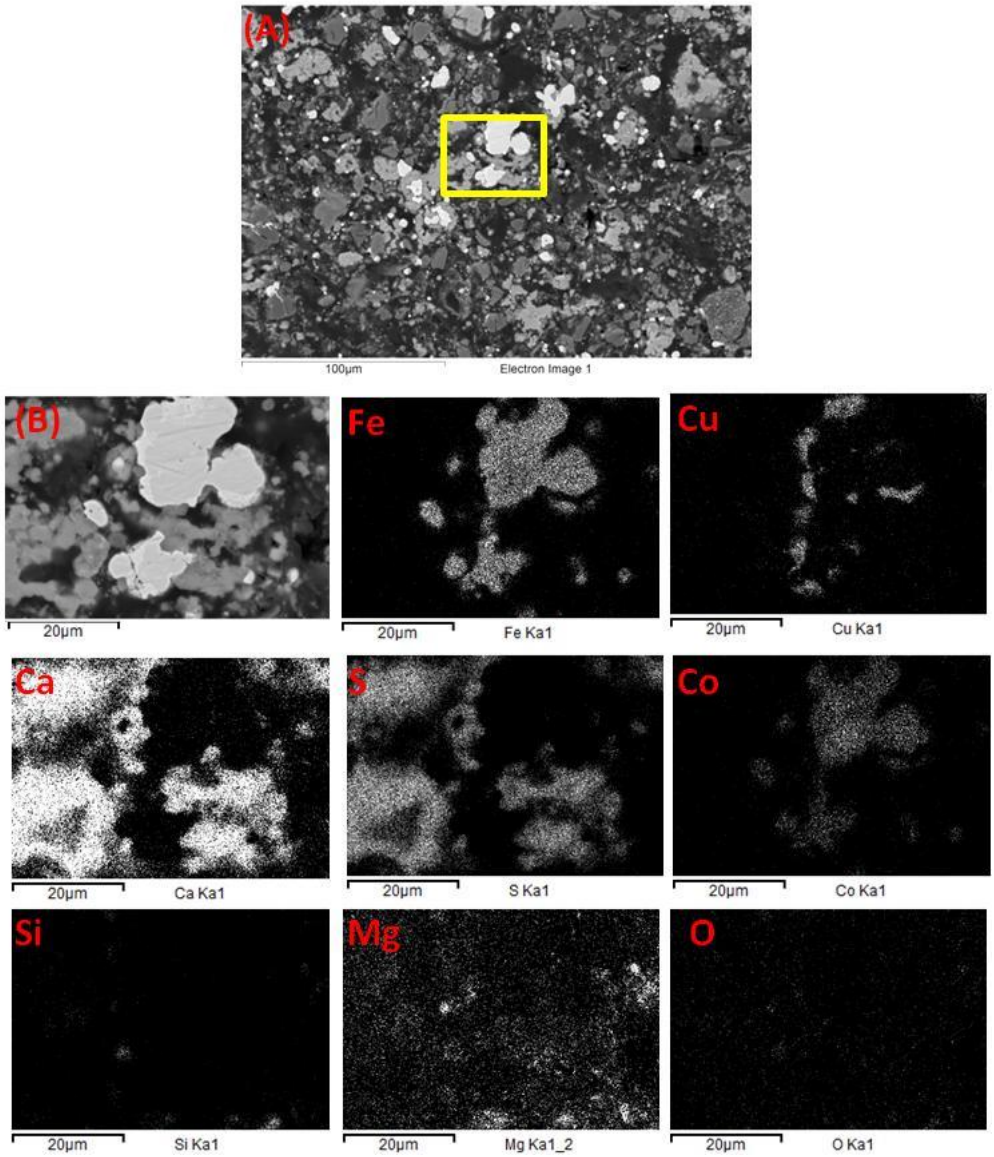

Figure 6.14 – Elemental mapping for Nkana sample after reduction at 1273 K, molar ratio of MS:CaO:C = 1:1.5:1.5, the analysed area is highlighted by the yellow box in (A) and (B) is the analysed area under BSE imaging. Argon flow rate = 0.6 litre min^{-1}

SEM-EDX semi-quantitative analysis was carried out in order to determine the compositions locally, a summary of the composition from figure 6.15 is presented in table 6.1. It can be observed in table 6.1 that a number of metallic phases had about 97 wt. % Cu in the Nchanga sample meaning that they were reduced from the Cu_2S mineral. It is worth noting that the purity of the copper phase is similar to that of blister copper [8, 10, 15], produced after conventional smelting and converting processes at temperatures above 1473 K. Most metallic phases in the Nkana and Baluba reduced samples had about 96 wt. % Fe meaning that they were reduced from the FeS_2 mineral

particles. The purity of iron produced by this process is much higher than that of the pig iron which contain about 93 wt. % Fe, produced by smelting of iron oxide above 1773 K [105]. It can be observed in table 6.1 that a metallic phase with 92 wt. % Co was produced in the Nkana sample at 1173 K. The semi-quantitative SEM-EDX analysis in table 6.1 further shows that the Co-Fe alloys were produced during reduction of the mineral sulphide concentrates, as observed from the elemental maping in figure 6.14.

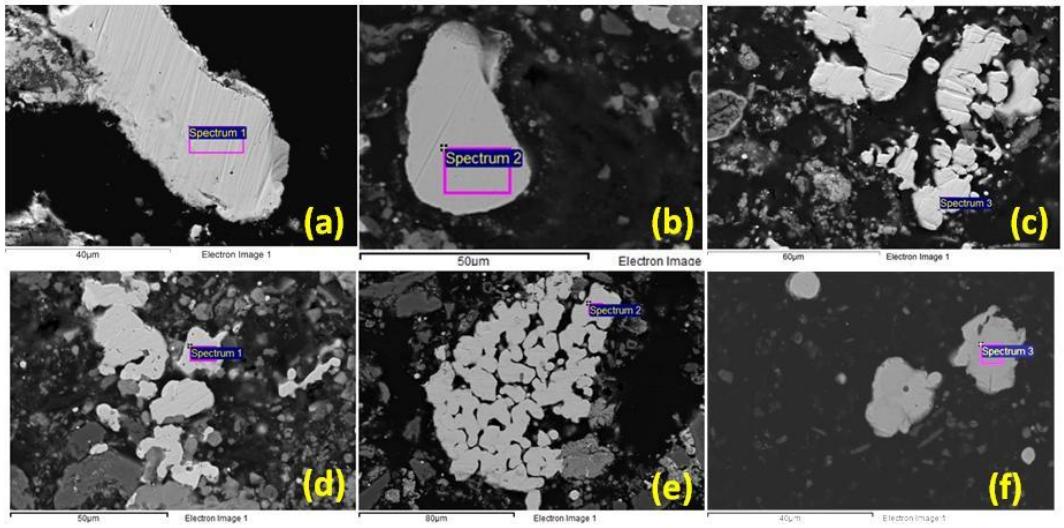

Figure 6.15 – Backscattered SEM images for the reduced samples, the compositions are given in table 6.1. Argon flow rate = 0.6 litre min^{-1}

Table 6.1 – SEM-EDX semi-quantitative results (wt. %) obtained from figure 6.1

	Cu	Co	Fe	O
(a) - Nchanga at 1273 K – spectrum 1	97	-	1	2
(b) - Nchanga at 1273 K – spectrum 2	97	-	2	1
(c) - Nkana at 1273 K – spectrum 2	3	-	97	
(d) - Nkana at 1273 K – spectrum 1	7	11	82	
(e) - Nchanga at 1273 K – spectrum 2	4	11	85	
(f) - Nkana at 1173 K – spectrum 1	3	92	3	2
Baluba at 1273 K (image not shown)	4	-	96	
Baluba at 1273 K (image not shown)	22	72	2	3

6.1.7 Reaction mechanism

In order to understand, the reaction mechanisms taking place during the carbothermic reduction of the mineral sulphide concentrates in the presence of CaO and C, some

experiments were stopped at various times, between 1 and 30 minutes at 1273 K, molar ratio of MS:CaO:C = 1:2:2. The partially reacted samples were characterised by XRD and SEM analyses. The XRD patterns for the samples which were reacted for 1 minute and 2 minutes at 1273 K, are shown in figures 6.16a and 6.16b, respectively. As shown from the XRD patterns in figure 6.16a, the major phases obtained after 1 minute were Fe_3O_4, Cu_2S, Cu_5FeS_4, CaS, $CaSO_4$, CaO (residual) and $CuFeS_2$ (residual). The presence of the $CaSO_4$ phase shows that the partial pressures of O_2 and SO_2 gases were high, corresponding to $\log PO_2(g)(atm) > -10.5$ and $\log PSO_2(g)(atm) > -2.5$, from the thermodynamic prediction in figure 6.17. The high partial pressure of SO_2 gas can be caused by the reaction between S_2 gas (from the thermal decomposition of FeS_2 and $CuFeS_2$ minerals) and CaO as shown in equation 6.1a. The absence of FeS_2 or FeS and high intensity peaks for Fe_3O_4 in the XRD patterns, after 1 minute at 1273 K show that reaction 6.1a and 6.1b occurred. The $CaSO_4$ phase might have been formed from the reaction between SO_2 and CaO (equation 6.1c). The minimum $\log PSO_2(g)(atm)$ for equation 6.1c is -1.25, assuming that the activities of CaO, CaS and $CaSO_4$ are equal to 1. The summation of equation 6.1a and 6.1c [173] gives equation 6.1d.

$$\frac{8}{3}CaO + 2S_2(g) = \frac{8}{3}CaS + \frac{4}{3}SO_2(g), \quad \Delta G_{1273K} = -128\ kJ \qquad 6.1a$$

$$4.5FeS_2 + 8CaO = 1.5Fe_3O_4 + 8CaS + SO_2(g), \quad \Delta G_{1273K} = -438\ kJ \qquad 6.1b$$

$$\frac{4}{3}CaO + \frac{4}{3}SO_2(g) = \frac{1}{3}CaS + CaSO_4, \quad \Delta G_{1273K} = -40.5\ kJ \qquad 6.1c$$

$$2S_2(g) + 4CaO = 3CaS + CaSO_4, \quad \Delta G_{1273K} = -168.5\ kJ \qquad 6.1d$$

The presence of $CaSO_4$ in the first minute at 1273 K, which is caused by the high partial pressures of O_2 and SO_2 gases, shows that the reactivity of carbon is very low in the initial stages of the reaction. In fact, similar phases were obtained after 1 minute at 1273 K, at molar ratios of MS:CaO:C = 1:2:2, 1:2:4 and in the absence of carbon (MS:CaO:C = 1:2:0) (see figure 6.4).

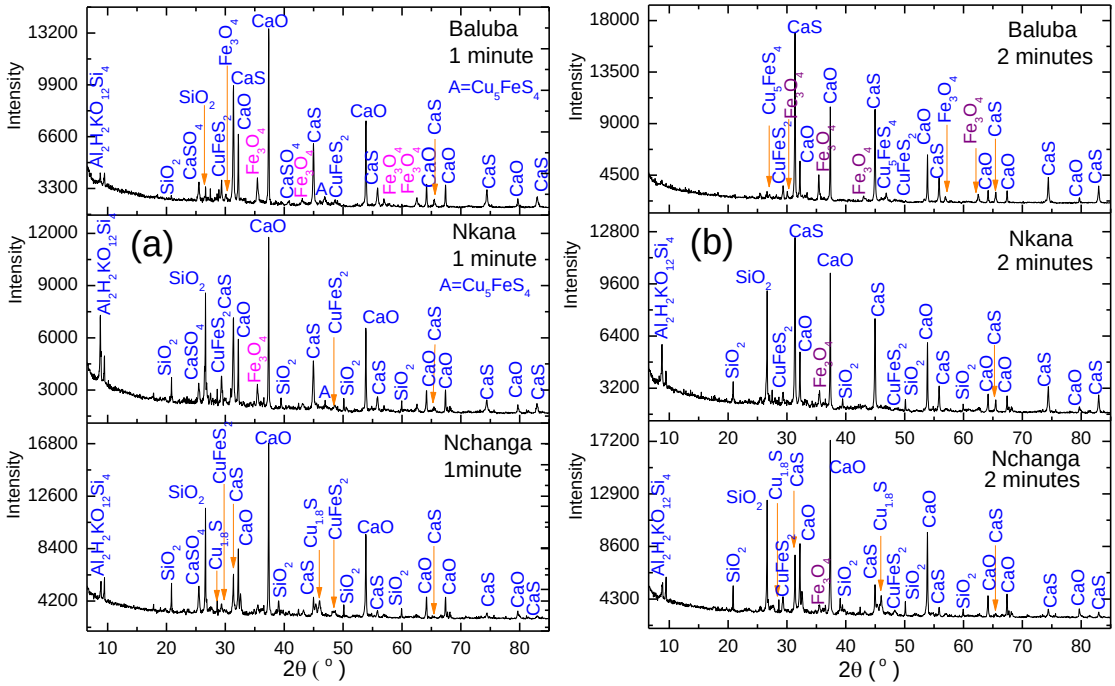

Figure 6.16 – XRD patterns for the partially reacted samples at 1273 K, molar ratio of MS:CaO:C = 1:2:2; (a) 1 minute and (b) 2 minutes. Argon flow rate = 0.6 litre min^{-1}

The phases obtained in the first minute at 1273 K can be represented by area A in the Cu-Ca-Fe-Co-O-S predominance area diagram in figure 6.17. In moving from area A in figure 6.17, three important things may happen as the partial pressures of O_2 and SO_2 gases changes:

i. Cobalt ferrite ($CoFe_2O_4$) can be produced when the partial pressure of SO_2 gas is decreased at constant partial pressure of O_2 gas.

ii. $CaSO_4$ can be calcined to CaS and, Cu_5FeS_4 can be formed as the partial pressure of O_2 gas decreases faster than that of SO_2 gas.

iii. $CaSO_4$ can be calcined to CaS and the CaS would co-exist with Fe_3O_4, Cu_2S and Co_9S_8 when the partial pressures of O_2 and SO_2 gases decreases nearly at the same rate.

However, cobalt ferrite ($CoFe_2O_4$) and Cu_5FeS_4 were not observed in the later stages of the reactions implying that the partial pressures of SO_2 and O_2 gases decreases nearly at the same rate at 1273 K. The partial pressures of SO_2 and O_2 gases decrease at the same rate because, the reactivity of carbon increases and the thermal decomposition of the mineral sulphides decreases with increase in reaction time. The partial pressures of SO_2 and O_2 gases continues decreasing with increase in reaction time such that the Co-O and Fe-O phases are reduced to metallic state at $\log_{10}(P(O_2))(atm) < -12.4$ (area C in figure

6.17) and -14.9 (area E in figure 6.17), respectively. Fe and Co co-exist with Cu_2S and CaS, as analysed by SEM and XRD techniques and this can be represented by area E. It appears that the partial pressure of O_2 gas does not decrease further upon reaching region E. However, the partial pressure of SO_2 gas continues decreasing due to absorption of sulphur by CaO such that region F is reached and hence metallisation of Cu occurs. Based on the XRD and SEM results, it can be concluded that the overall reaction follows the following path; A → B →C → D → E → F, from the Cu-Ca-Fe-Co-O-S system in figure 6.17.

The thermodynamic prediction in figure 6.17 shows that preferential metallisation of Cu can take place, only under very low partial pressure of SO_2 gas and high initial partial pressure of O_2 gas ($logPO_2(g)(atm) > -11.8$). However, this may not happen at 1273 K, owing to the initial high partial pressures of O_2 and SO_2 gases, resulting from the thermal decomposition of S_2 gas from the mineral sulphides ($CuFeS_2$ and FeS_2).

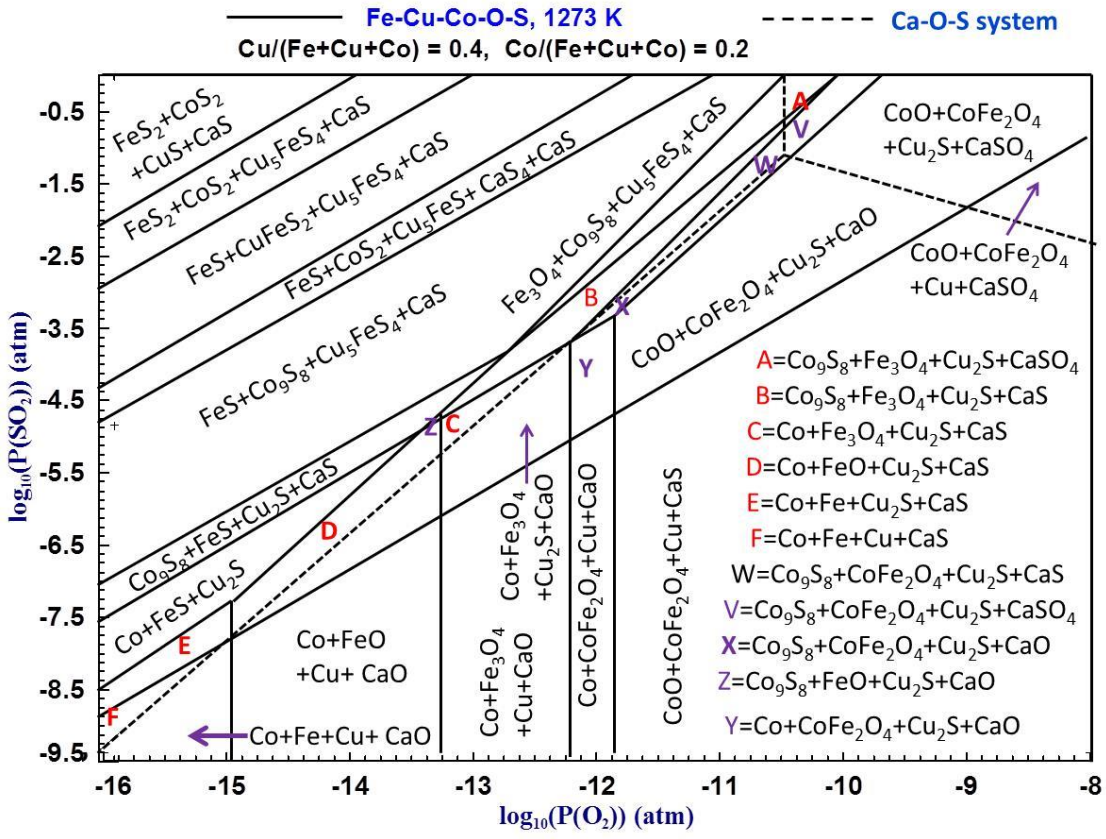

Figure 6.17 – The Cu-Co-Ca-Fe-O-S predominace area diagram at 1273 K, computed by superimposing the Fe-Cu-Co-O-S and Ca-O-S predominace area diagrams, using the FactSage software 6.1 [24]

The summary of SEM images for the samples reacted for various times at 1273 K are presented in figure 6.18. A rim of iron oxide (Fe-O) surrounds the un-reacted core of Cu-S in the first 2 minutes at 1273 K, for the reduction of the $CuFeS_2$ and Cu_5FeS_4 mineral particles. The rim of Fe-O on the periphery of the partially reacted samples confirms that there is preferential oxidation of Fe-S to Fe-O (FeO or Fe_3O_4) in the early stages of the reaction. The preferential formation of Fe-O on the periphery and Cu_2S phase at the core is driven by the higher stability of iron oxide than iron sulphide and the higher stability of copper sulphide than copper oxide [174]. As a result, the Fe^{2+} ions diffuse to the periphery where the oxygen potential is high and the Cu^{2+} ions diffuse to the centre where the oxygen potential is low, to form Cu_2S. The S^{2-} ions that are nearer to the surface of the mineral particle also diffuse to the lime particle as shown in figure 6.19. The Fe^{2+} ions react with O^{2-} ions at the periphery to form Fe_3O_4 as shown in figure 6.19. The preferential oxidation of iron to iron oxide at the periphery and, the formation of $Cu_{1.8}S$ at the core is similar to Kernel roasting [28, 85]. Thermodynamically, the oxidation of Cu-S can only take place when Fe is in the oxide form because the equilibrium for reaction 6.2 is always in the forward direction.

$$Cu_2O + FeS = Cu_2S + FeO \qquad 6.2$$

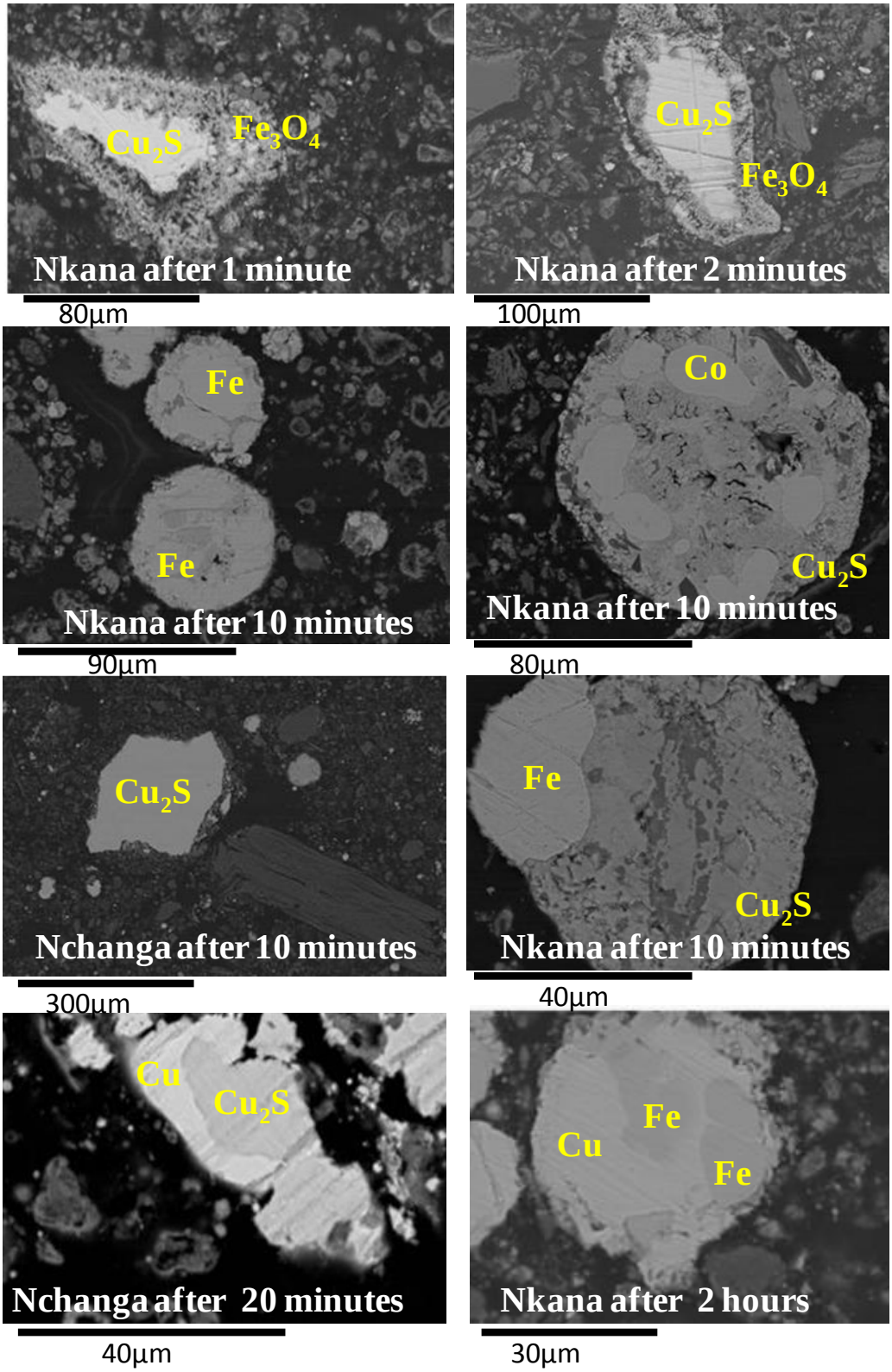

Figure 6.18 – Backscattered SEM images for the samples reacted for various times at 1273 K, molar ratio of MS:CaO:C = 1:2:2. Argon flow rate = 0.6 litre min^{-1}

It is very clear from figure 6.18 that the partially reacted Cu-Fe-S ($CuFeS_2$ and Cu_5FeS_4) and Cu-Co-S ($CuCo_2S_4$) type of mineral particles consist of Fe or Co in the Cu-S matrix and this broadly agrees with the Cu-Co-Fe-Ca-O-S predominance area diagram in figure 6.17. The Co and Fe are in the spherical and ovate shapes which is a characteristic of partial or complete melting [175]. It can be suggested that the reduction of Fe-O at the peripheral, result in the formation of low oxygen and metal rich Cu-Fe-O-S liquid phase. However, the reduction of the Cu-S from Cu-Fe(Co)-S was slower, taking up to 1.5 hours at 1273 K, probably due to depletion of the nearby CaO, from the ion exchange reaction between Fe-S/Co-S and CaO.

SEM-EDX analysis confirmed that the purity of the embedded Co and Fe phases was over 98 wt.%, implying that it is possible to obtain very high grade Co and Fe particles by carrying out magnetic separation of the partially reacted samples. Nevertheless, the Co and Fe particles are not large enough (< 30 µm) to be liberated by crushing and grinding. Succesful magnetic separation would require complete liberation of the magnetic particles of Co and Fe.

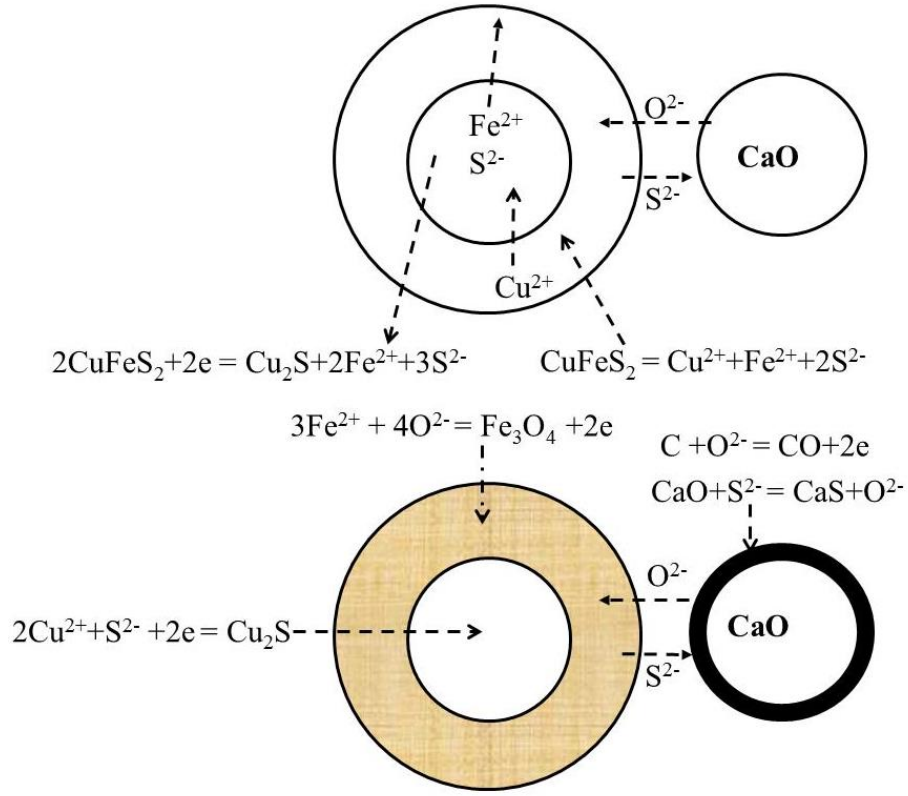

Figure 6.19 - Schematic illustration showing mechanism taking place during the initial stages of the reaction between $CuFeS_2$ and CaO, Fe_3O_4 is formed at the periphery and Cu_2S at the core

The reduction of Cu-S (Cu_2S and $Cu_{1.6}S$) mineral particles was found to take place via two mechanisms:

i. Diffusion of the S^{2-} ions away from the Cu_2S mineral particle when there is less contact between the Cu_2S and CaO particles or, when the rate of reduction reaction is faster than the rate of ion exchange reaction. For instance, the partially reacted Cu_2S particles were surrounded by a dense layer of metallic copper at molar ratio of MS:CaO:C = 1:2:4 as shown in figure 6.20a. The contact between Cu-S and CaO is decreased at molar ratio of MS:CaO:C = 1:2:4 and hence metallisation of Cu occur via diffusion of the S^{2-} ions.

ii. Formation of the Cu_2S – CaO eutectic melt as precipitates of CaS were observed in the partially reacted Cu_2S particles at molar ratios of MS:CaO:C(carbon black) = 1:2:1 and MS:CaO:C(graphite) = 1:2:2. The sample sinters at molar ratios of MS:CaO:C(carbon black) = 1:2:1 and MS:CaO:C(graphite) = 1:2:2 since the reduction reaction is slower and hence the Cu_2S – CaO eutectic melt is formed. The overall reactions can be represented by equations 6.3a and 6.3b. The possibility of equations 6.3a and 6.3b can be appreciated by the fact that, Cu was formed in the rich CaS phase, at molar ratios of MS:CaO:C(carbon black) = 1:2:1 and MS:CaO:C(graphite) = 1:2:2

$$Cu_2S(S) + CaO(s) = Cu_2O \bullet CaS(l) \qquad 6.3a$$

$$Cu_2O \bullet CaS(l) + C(s) = 2Cu(s) + CaS(s) + CO(g) \qquad 6.3b$$

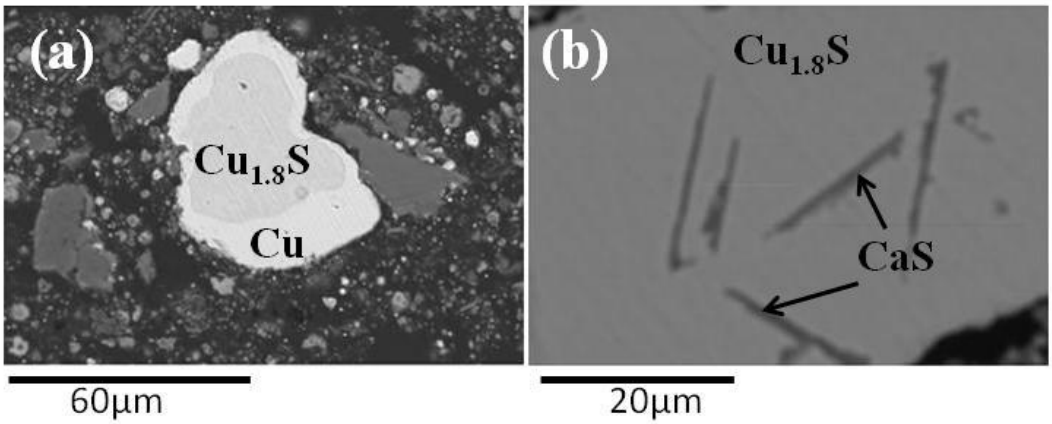

Figure 6.20 – Backscattered SEM images for the partially reacted samples at 1273 K; (a) molar ratio of MS:CaO:C (carbon black) = 1:2:4 and (b) molar ratio of MS:CaO:C(graphite) = 1:2:2. Argon flow rate = 0.6 litre min^{-1}

Based on the XRD and SEM results, the reduction of $CuCo_2S_4$ and Cu_5FeS_4 mineral particles can be summarised as follows:

i. Preferential oxidation of Fe-S and Co-S to form Fe-O and Co-O as shown in equation 6.4a and 6.4b, respectively.

ii. Reduction of Fe-O and Co-O to form Fe and Co as shown in equations 6.4c and 6.4d, respectively.

iii. Carbothermic reduction of Cu-S via a combination of ion exchange and reduction reactions (equation 6.4e).

$$6Cu_5FeS_4 + 9CaO + C = 15Cu_2S + 2Fe_3O_4 + 9CaS + CO \quad 6.4a$$

$$2CuCo_2S_4 + 7CaO + 3C = Cu_2S + 4CoO + 7CaS + 3CO \quad 6.4b$$

$$2Cu_5FeS_4 + 3CaO + 3C = 5Cu_2S + 2Fe + 3CaS + 3CO \quad 6.4c$$

$$2CuCo_2S_4 + 7CaO + 7C = Cu_2S + 4Co + 7CaS + 7CO \quad 6.4d$$

$$Cu_2S(s) + CaO(s) + C(s) = 2Cu(s) + CaS(s) + CO(g) \quad 6.4e$$

6.1.7.1 Further investigations of reaction mechanism

There is less contact between the mineral sulphide (MS) and lime (CaO) particles at high mole ratio of carbon than CaO such as at MS:CaO:C = 1:2:4. Similarly, there is less contact between the mineral sulphide and carbon particles, at high mole ratio of CaO than C e.g. at MS:CaO:C = 1:4:2. In order to understand the reaction mechanism that can occur, when there is little or no contact between MS and C or CaO particles, three types of experiments were carried out under argon atmosphere at 1273 K: (i) the mineral sulphide concentrates were pressed into cylindrical pellets and covered by the mixture of the CaO + C powders at molar ratio of CaO:C = 1:1 (figure 6.21a) and heated under argon atmosphere at 1273 K, (ii) the mixture of mineral sulphide concentrates + C at molar ratio of MS:C = 1:2 were pressed into cylindrical pellets and covered with the CaO powder (figure 6.21b) and (iii) repeating experiment (i) but using

either a piece of natural $CuFeS_2$ or Cu_5FeS_4, instead of the mineral sulphide concentrates.

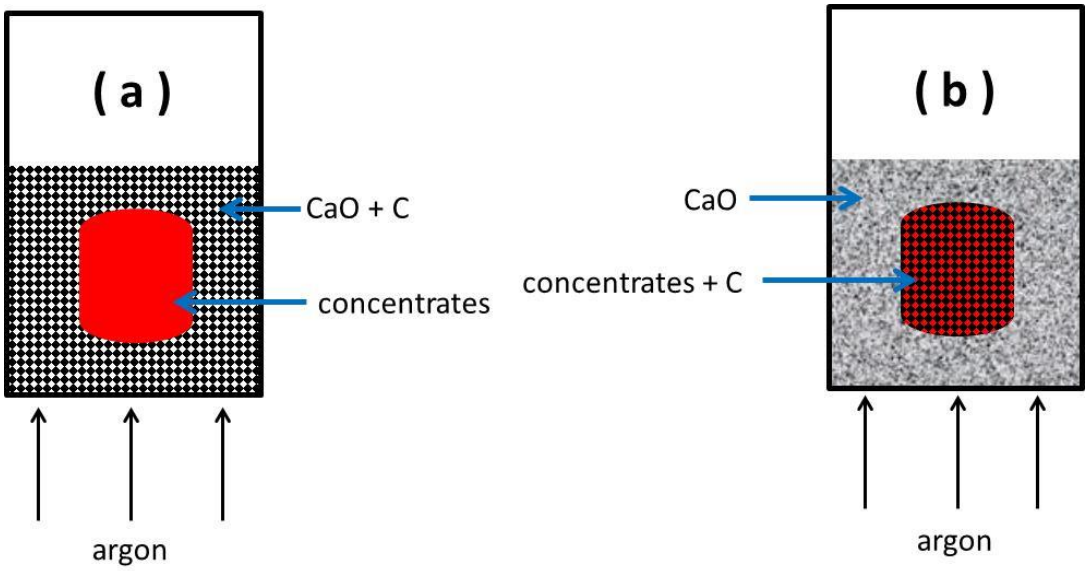

Figure 6.21 - Schematic arrangement of the experiments at 1273 K; (a) mineral sulphide concentrates pellet covered by the mixture of CaO + C during reduction and (b) mixture of mineral concentrate + C pellet, covered by CaO during experiment

The weight losses were recorded during the experiment and, the reacted samples were analysed by XRD and SEM techniques. Metallic copper was observed but metallic iron was absent for the experiments where, either pellets of the mineral sulphide concentrates or pieces of natural minerals ($CuFeS_2$ and Cu_5FeS_4) were covered by the mixture of the CaO + C powder (see figure 6.21a). The XRD analysis for the CaO + C powders, covering the pellets of the mineral sulphide concentrates or pieces of natural minerals, during the experiments showed clear evidence of CaS. However, there was no CaS in the mineral sulphide concentrates pellets or pieces of $CuFeS_2$ and Cu_5FeS_4, thereby suggesting that S^{2-} ions are the migrating species when there is less contact between mineral sulphide concentrates and CaO + C. The S^{2-} ions diffuse from the mineral sulphide to the lime particles and yield CaS which is a stable phase under reducing atmosphere. Since copper was the only metallic phase in experiment 6.21a, the reactions taking place in the mineral sulphide particle can be represented by equations 6.5a and 6.5b. The S_2 gas and S^{2-} ions from equations 6.5a and 6.5b, respectively, diffuse to the lime particles leading to reactions 6.4c - 7.4f at the lime - carbon interface.

The electrons from equation 6.5f [172] react with the Cu^{+} ions to yield metallic copper via reaction 6.5g.

In the mineral sulphide concentrates;

$$4Cu_5FeS_4 = 4FeS + 10Cu_2S + S_2(g) \quad 6.5a$$

$$Cu_2S = 2Cu^{+} + S^{2-} \quad 6.5b$$

At the CaO and C interface

$$2CaO + S_2(g) + 2C = 2CaS + 2CO(g) \quad 6.5c$$

$$CaO = Ca^{2+} + O^{2-} \quad 6.5d$$

$$Ca^{2+} + S^{2-} = CaS \quad 6.5e$$

$$C + O^{2-} = CO(g) + 2e \quad 6.5f$$

Nucleation of copper

$$2Cu^{+} + 2e = 2Cu \quad 6.5g$$

The SEM images obtained after pieces of natural $CuFeS_2$ and Cu_5FeS_4 were covered by the mixture of CaO + C powders, during the reaction are shown in figure 6.22. The only phases from the Cu_5FeS_4 experiment are Cu_5FeS_4 and Cu (figure 6.22a) and, these are the stable phases in the Cu rich region of the Cu-Fe-S tenary system (see figure 3.18). On the other hand, three phases were observed from the $CuFeS_2$ experiment and they are Cu_5FeS_4, FeS and Cu (figure 6.22b). The presence of Cu_5FeS_4 and FeS from the $CuFeS_2$ experiment is as a result of thermal decomposition (equation 6.6). Copper (Cu) was formed from the Cu_5FeS_4 phase (see equations 6.5a – 6.5g).

$$5CuFeS_2 = Cu_5FeS_4 + 4FeS + S_2(g) \quad 6.6$$

It can be observed from the SEM image in figure 6.22b that Cu is in the form of fibres and mostly at the interface between the Cu_5FeS_4 and FeS phases, as a result of diffusion of the Cu^{1+} ions from the Cu_5FeS_4 phase (see equations 6.5a - 6.5e). The copper particles grow by producing fibres due to high stress [176] at the Cu_5FeS_4/ FeS interface.

Both XRD and SEM (figure 6.22) analyses revealed that metallisation of copper was incomplete even though the experiments were stopped when there was no further weight loss from the samples. The weight loss stopped or the reaction ceased after about 1.5 hours at 1273 K. As the reactions ceased before reaching completion, another experiment was carried out whereby the mineral sulphide concentrates were pressed into pellets and covered by the mixture of the CaO + C powder during reduction. The experiment was stopped after there was no further weight loss from the sample. The crucible containing the sample was cooled down to room temperature and the CaO + C powder were stirred using a wire in order to expose the sample pellet to the un-reacted CaO + C powders. The samples were then put back into the furnace and the weight losses were observed for another 1.5 hours, meaning that the reaction continued because the sample was exposed to the un-reacted CaO + C powders after stirring. It can be suggested that the reaction ceases when the CaS layer is formed on the surface of the mineral sulphide concetrates pellet. Both the pellets and the mixture of CaO + C powders were analysed by X-ray diffraction. It was observed that the XRD peak intensities of Cu and CaS were higher in the pellets and CaO + C powders respectively, than the experiments carried out without stirring the CaO + C powder.

On the other hand, the XRD peak intensities for CaS in the CaO powder were extremely low for the experiments, where the pellets consisting of mineral sulphide concentrates + C were covered by the CaO powder. In addition, metallic copper was absent from the mineral sulphide concentrates pellets. The absence of Cu and very low concentration of the CaS phase for experiment in 6.21b explains that the diffusion of S^{2-} ions is very low when the lime and carbon particles are far from each other. This is because, the O^{2-} ions do not easily react with carbon to form a stable CO gas. In other words, CaO remains stable when the CaO and C particles are far from each other.

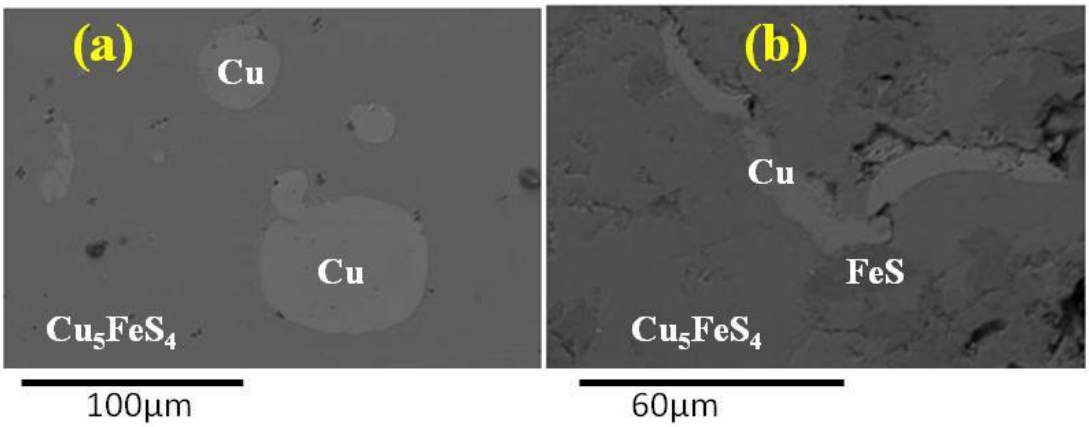

Figure 6.22 - Backscattered SEM images for the natural minerals heated in a mixture of CaO and C powders at 1273 K; (a) $CuFeS_2$ and (b) Cu_5FeS_4, the phases were analysed by SEM-EDX analysis. Argon flow rate = 0.6 litre min^{-1}

6.1.8 Liquid phase formation during reduction process

The formation of the liquid phase is very important since it enhances the reaction kinetics, because of the faster diffusion of cations and anions in the liquid than in the solid phase. The formation of liquid phase was investigated by using different mole ratios of lime and carbon and, different types of carbon (carbon black or graphite). From the experimental work carried out, the formation of the liquid phase appears to be as a result of; (i) melting of the mineral sulphide particles e.g. $CuFeS_2$ melts at 1223 K [171], so that a molten mineral sulphide phase reacts with CaO and C/CO gas and (ii) reaction between mineral sulphide particles and CaO, causing liquid matte phase (MO + MS) or eutectic melts as reported by Jha [32, 35, 172, 177, 178].

Chalcocite (Cu_2S) is a very stable mineral sulphide with a melting temperature of 1403 K but a liquid phase was observed during its reduction. In the earlier work by Jha, during the carbothermic reduction of Cu_2S in the presence CaO, a liquid phase belonging to the Cu-O-S system was suggested to be due to the binary eutectic at 1113 K, involving Cu_2S and Cu_2O [35, 172]. However, the Cu-O-S liquid phase may not exist if the rate of reduction reaction is faster than the ion exchange reaction, because the Cu_2O phase would be immediately reduced to Cu. In the present study, the Cu-Ca-O-S liquid phase was only observed at molar ratios of MS:CaO:C(carbon black) = 1:2:1 and MS:CaO:C(graphite) = 1:2:2 because, the rate of reduction reaction is slower than that of the exchange reaction. In addition to equation 6.3a, metallisation can also occur via reaction 6.7 [35, 172]. In summary, there is a liquid phase in the reduction of Cu_2S

mineral particles but the presence of this liquid phase is greatly influenced by the mole ratio of carbon and / or its reactivity.

$$3Cu_2O + CaS = 6Cu + CaO + SO_2(g) \qquad 6.7$$

Cenospheres were observed in the partially reacted samples at 1273 K as shown in figure 6.23. The formation of cenospheres was due to evolution of the S_2 or SO_2 gases from the molten mineral sulphide particles. The mechanism of cenosphere formation has been explained very well by Li and Wu [179]. Elemental mapping confirmed that cenospheres were formed from the larger $CuFeS_2$ mineral particles (> 30 µm) because, more gas is evolved from the larger molten particles than the smaller particles [179]. By comparison, the cenospeheres were more common in the Baluba sample as this sample is dominated by the $CuFeS_2$ which melts at 1223 K [171].

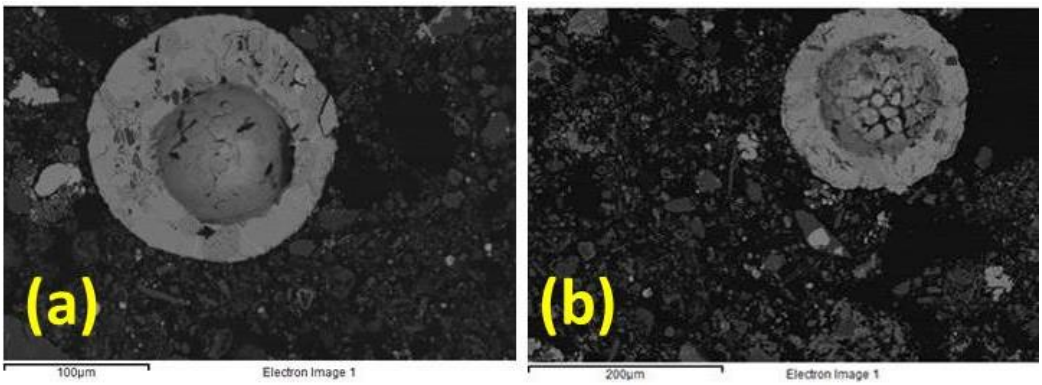

Figure 6.23 – Backscattered SEM images showing cenospheres in the partially reacted $CuFeS_2$ particles, after reduction for 10 minutes at 1273 K, MS:CaO:C = 1:2:2 (a) Nchanga and (b) Nkana. Argon flow rate = 0.6 litre min^{-1}

Both the SEM and XRD analyses confirmed that the reduction of the FeS_2 mineral particles was the fastest compared to other mineral particles ($CuFeS_2$, Cu_5FeS_4, Cu_2S), above 1173 K. The rapid reduction of the FeS_2 mineral particles above 1173 K is due to the presence of the liquid phase. As stated in chapter 2, liquid phases belonging to the Ca-Fe-O-S system have been observed by Jha, during carbothermic reduction of FeS [172]. The Ca-Fe-O-S liquid phases had compositions of 3FeO.3CaS and FeO.CaS [177]. However, the liquid phases belonging to the Ca-Fe-O-S system were not found in the partially reacted samples in the present study. The Ca-Fe-O-S liquid phase was not

observed because, CaO was added at more than its stoichiometric mole ratio (MS:CaO = 1:2), in order to compensate for the reactions between CaO and gangue minerals. According to Rosenqvist [41], the FeO.CaS or 4FeO.3CaS phases can only be formed at higher mole ratio of FeS than CaO [41]. Furthermore, the absence of the FeO.CaS or 4FeO.3CaS liquid phases in the present study might be as a result of formation of the Ca_2CuFeO_3S liquid phase which was observed at the higher mole ratio of CaO than C or in the absence of carbon (see section 6). On the other hand, a liquid phase belonging to the Fe-O-S system was found in the partially reacted FeS_2 mineral particles. SEM-EDX analysis showed that the Fe-O-S liquid phase had a composition of 56 wt. % Fe, 29 wt. % S and 9 wt. % O and this is slightly comparable with the eutectic composition of 68 wt. % Fe, 24 wt. % S and 8 wt. % O at about 1193 K [85].

A liquid phase belonging to the Cu-Fe-S-O system was determined during reduction of Cu-Fe-S type of mineral particles at equal mole ratios of CaO and C (MS:CaO:C = 1:2:2). The Cu-Fe-S-O liquid phases appear to form as a result of the reaction between the Fe-O phase at the periphery and the Cu-S phase at the centre. Two main observations were made during reduction of the Cu-Fe-O-S liquid phase:

i. The low oxygen, Cu-Fe-S-O liquid phase was found with the metallic iron spheres at higher reduction temperature (above 1173 K) as shown in figure 6.24(a).
ii. The oxygen rich Cu-Fe-S-O liquid phase was found with the metallic copper at lower reduction temperature (below 1173 K) as shown in figure 6.24(b).

Based on observations i and ii, it can be concluded that preferential metallisation of iron and copper from the Cu-Fe-O-S liquid phase, occurs at higher and lower reduction temperatures, respectively. From the thermodynamic prediction in figure 6.17, Fe co-exists with Cu_2S at lower partial pressure of O_2 gas whereas Cu co-exists with Fe-O and in equilibrium with Cu_2S, at higher partial pressure of O_2 gas. Therefore, the reactivity of carbon is high at higher temperatures e.g. 1273 K, such that the partial pressure of O_2 gas decreases, leading to the preferential metallisation of Fe from the Cu-Fe-O-S system Nonetheless, the reactivity of carbon is low at lower reduction temperature, and hence the partial pressure of O_2 gas remains high, and this is why metallic copper was found with the oxygen rich matte.

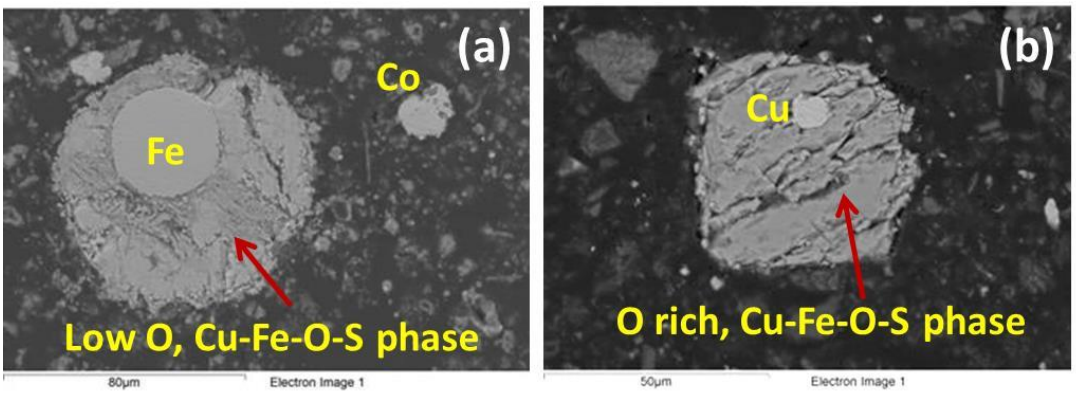

Figure 6.24 – Backscattered SEM images for the partially reduced samples at molar ratio of MS:CaO:C = 1:2:2; (a) 20 minutes at 1273 K and (b) 2 hours at 1073 K. Argon flow rate = 0.6 litre min^{-1}

6.1.9 Effect of CaO/C mole ratio on microstructure of reduced samples

The study of the microstructure of the reduced sample is very important for developing the right process of separating the metallic phases from impurities (CaS, excess CaO and gangue minerals). The overall microstructures of the carbothermically reduced samples were greatly affected by the CaO/C mole ratio.

The SEM images for the Nchanga and Nkana samples after carbothermic reduction at 1273 K, molar ratio of MS:CaO:C = 1:2:2 and 1:2:1 are compared in figure 6.25. It is evident in figure 6.25 that the metallic phases were embedded in the CaS rich phase at molar ratio of MS:CaO:C = 1:2:1 whereas the metallic phases are not surrounded by the CaS phase at molar ratio of MS:CaO:C = 1:2:2. The is due to the presence and absence of the intermediate Ca_2CuFeO_3S liquid phase at molar ratio of MS:CaO:C = 1:2:1 and MS:CaO:C = 1:2:2, respectively. To confirm the existence of the Ca_2CuFeO_3S liquid phase at different molar ratio of C/CaO, the samples were reacted for various times at 1273 K, molar ratio of MS:CaO:C = 1:2:1, 1:2:2 and 1:2:4. The Ca_2CuFeO_3S liquid phase was only observed at molar ratio of MS:CaO:C = 1:2:1 (figure 6.26a). However, the Ca_2CuFeO_3S phase was absent in the partially reacted sample at molar ratios of MS:CaO:C = 1:2:2 and 1:2:4 (figure 6.26b). The XRD peak intensities for Cu and Fe are higher in figure 6.26a than in figure 6.26b, after 5 minutes because of the presence of Ca_2CuFeO_3S liquid phase at molar ratio of MS:CaO:C = 1:2:1.

The microstructure obtained at molar ratio of MS:CaO:C = 1:2:1 and 1273 K, was found to be similar to the ones obtained by heat treating the mineral sulphide

concentrates in the presence of CaO (MS:CaO = 1:2) followed by the carbothermic reduction of the samples at MS:C = 1:2 (see appendix A.6.1). The Ca_2CuFeO_3S liquid phase is formed during heat treatment of the mineral sulphide concentrates in the presence of CaO and hence metallisation occours via reduction of the liquid phase. The addition of carbon whether at MS:C = 1:2 or 1:4 does not change the microstructure of the samples as the metallic phases were surrounded by the CaS phase. It can be concluded that the metallic phases can be free from CaS if the formation of Ca_2CuFeO_3S liquid phase is prevented during reduction.

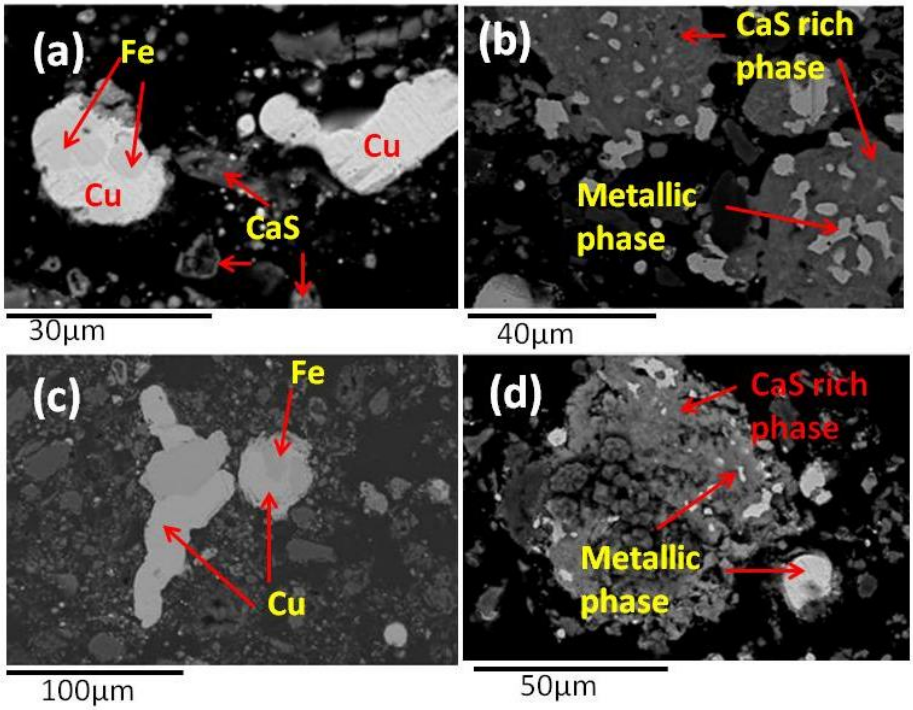

Figure 6.25 – Backscattered SEM images for the samples reduced at 1273 K; (a) Nchanga at MS:CaO:C = 1:2:2.5 and (b) Nchanga at MS:CaO:C = 1:2:1, (c) Nkana at MS:CaO:C = 1:2:2.5 and (d) Nkana at MS:CaO:C = 1:2:1. Argon flow rate = 0.6 litre min^{-1}

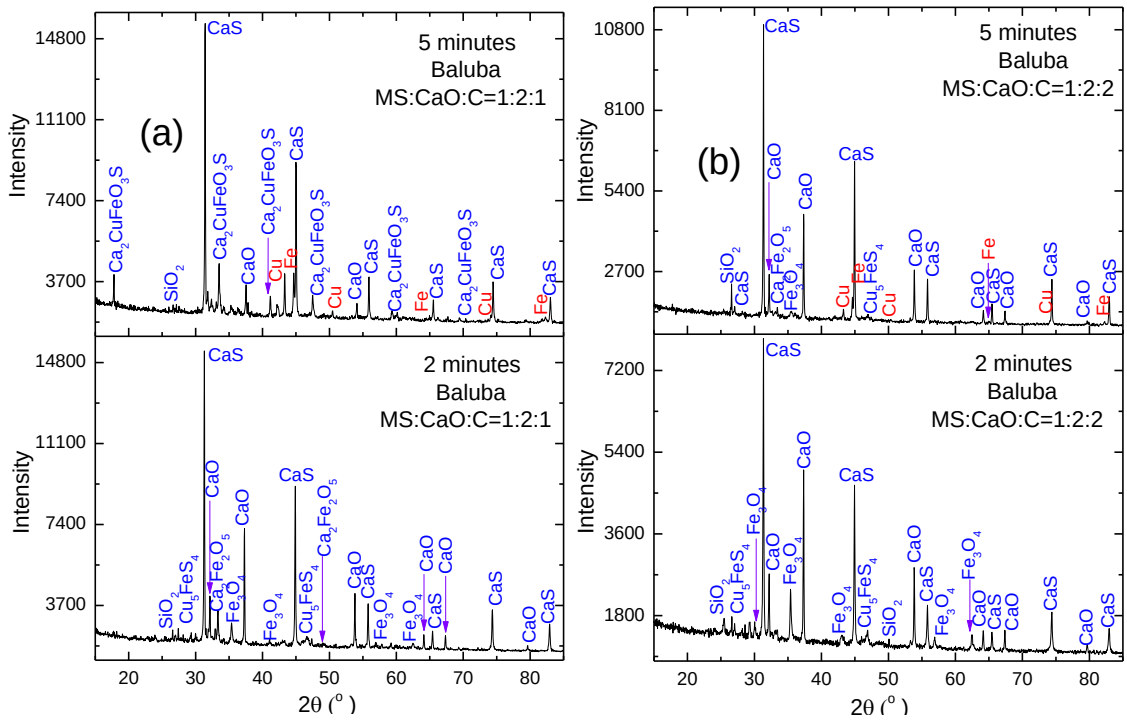

Figure 6.26 – XRD patterns for the partially reacted Baluba samples at 1273 K, mole ratio of; (a) MS:CaO:C = 1:2:1 and (b) MS:CaO:C = 1:2:2. Argon flow rate = 0.6 litre min^{-1}

Even though the X-ray diffraction analysis results in figure 6.26 indicate that metallisation was faster at the higher molar ratio of CaO than C, the microstructure in figure 6.25 clearly shows that the metallic phases were embedded in the CaS rich phase. The magnetic separation of the metallic phases which are surrounded by the CaS rich phase might be very difficult. As a result, it is very important that if the carbothermic reduction process is to be followed by the magnetic separation process, the C/CaO ratio should be equal to, or above 1.

6.1.10 Reaction Kinetics

The experimental isothermal data were fitted [180] into several kinetic equations (see equations 2.10a - 2.11b) in order to obtain the suitable reaction model(s). The Gistling and Brounshtein (G.B) and interface models are compared in figures 6.27a and 6.27b, respectively, by using the Baluba data for molar ratio of MS:CaO:C = 1:2:2. It is apparent from figures 6.27a and 6.27b that the Baluba data fits well into the Gistling and Brounshtein (G.B) and interface models.

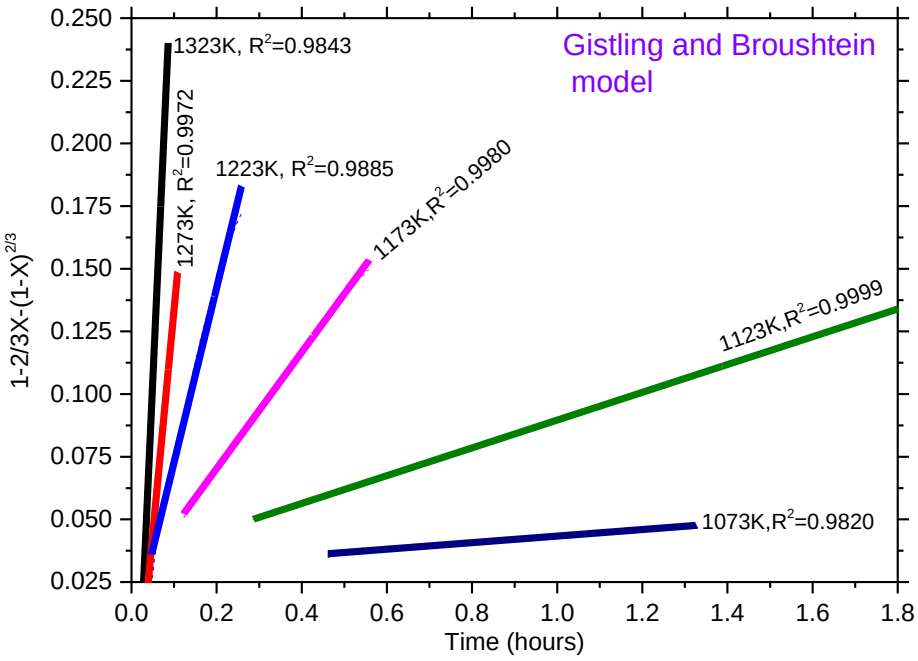

Figure 6.27a – Plots of Gistling and Brounshtein model against time for the Baluba isothermal data at various temperatures, at molar ratio of MS:CaO:C = 1:2:2

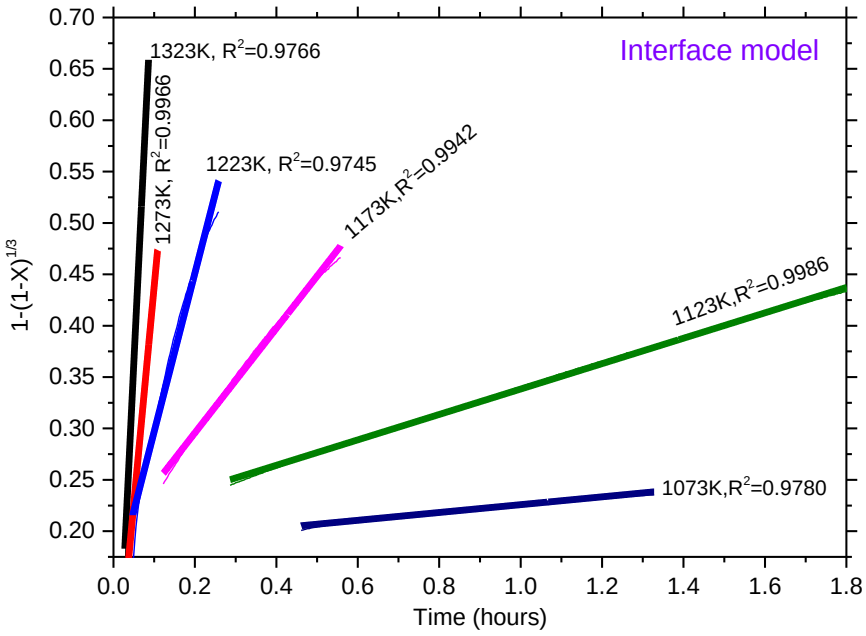

Figure 6.27b – Plots of interface model against time (hours) for the Baluba isothermal data at various temperatures, molar ratio of MS:CaO:C = 1:2:2

The summary of derived values of slope for each isotherm from the fitted models [181], for Nchanga, Nkana and Baluba at molar ratio of MS:CaO:C = 1:2:2 are presented in

table 6.2. As the experimental data fit into the diffusion and interface models (table 6.2), it can be concluded that the reduction of mineral sulphides follows the mixed reaction model. The mixed kinetic model is possible due to the fact that there are several reaction steps leading to the metallisation of Cu, Co and Fe, which may include; (i) diffusion of the Ca^{2+} and O^{2-} ions from the lime particles to the mineral sulphide particles, (ii) diffusion of the metallic and S^{2-} ions from the mineral sulphide particles and (iii) gasification of carbon.

Table 6.2 – Linear regression analysis of rate constants at different temperatures using equations 2.10a and 2.10c, molar ratio of MS:CaO:C = 1:2:2

Nchanga						
Temp. (K)	G.B model		Interface model		G.B + interface model	
	$K(hr^{-1})$	R^2	$K(hr^{-1})$	R^2	$K(hr^{-1})$	R^2
1323	3.6544	0.9915	8.9350	0.9977	12.6342	0.9986
1273	2.1759	0.9949	5.4088	0.9845	7.6516	0.9924
1223	0.3031	0.9914	0.6455	0.9864	0.9891	0.9902
1173	0.0735	0.9857	0.1009	0.9599	0.1658	0.9489
1123	0.0386	0.9971	0.0839	0.9954	0.1240	0.9946
1073	0.0130	0.9826	0.0290	0.9854	0.0414	0.9864
Nkana						
1323	5.7028	0.9909	14.1295	0.9994	19.7870	0.9989
1273	2.4563	0.9950	5.9222	0.9849	8.5180	0.9951
1223	1.2022	0.9969	2.7792	0.9655	3.5830	0.9923
1173	0.2018	0.9973	0.4465	0.9919	0.6470	0.9953
1123	0.0431	0.9992	0.0974	0.9980	0.1410	0.9978
1073	0.0075	0.9515	0.0172	0.9817	0.0220	0.9828
Baluba						
1323	3.7261	0.9843	9.6316	0.9766	13.5347	0.9977
1273	1.4393	0.9972	3.9367	0.9966	5.7500	0.9921
1223	0.6965	0.9885	1.9373	0.9745	2.2640	0.9906
1173	0.2323	0.9980	0.4980	0.9942	0.7000	0.9929
1123	0.0554	0.9999	0.1240	0.9986	0.1800	0.9990
1073	0.0131	0.9820	0.0382	0.97780	0.0520	0.9753

Where G.B. is the Ginstling and Brounstein model

The SEM results in figures 6.20a and 6.28a show the presence of metallic copper surrounding the unreacted core of Cu-S confirming that metallisation of copper occurs via outward diffusion of the S^{2-} ions from the mineral to the lime particles. Therefore, metallisation of copper might be limited by the diffusion of the S^{2-} ions through the dense outer layer of Cu. The metallisation of copper via diffusion of the S^{2-} ions from the mineral sulphide, was also confirmed when the pellets of mineral sulphide concentrates or pieces of natural $CuFeS_2$ and Cu_5FeS_4 were covered in a mixture of CaO + C powder and heated at 1273 K (see figure 6.22). Similarly, the formation of CaS takes place via counter diffusion of the S^{2-} and O^{2-} ions and/or, SO_2/S_2 gas, through the CaS rich layer because of the presence of CaS layer around the un-reacted core of CaO (figure 6.28b). However, the metallisation of Fe is controlled by the reduction reaction or chemical reaction between Fe-O and carbon because of the presence of the porous Fe-O phase in the partially reacted samples (see figures 6.9, 6.11 and 6.11). It is for this reason that the metallisation of Fe was highly sensitive to the reduction (reaction) temperature because, interface controlled reactions are very sensitive to the reaction temperature [155]. It has been shown in figure 6.9 that a layer of Fe-O surrounds the un-reacted core of Cu-S in the partially reacted $CuFeS_2$ and Cu_5FeS_4 mineral particles and hence metallisation of Cu might be limited by the diffusion of the reacting species through the outer layer of Fe-O.

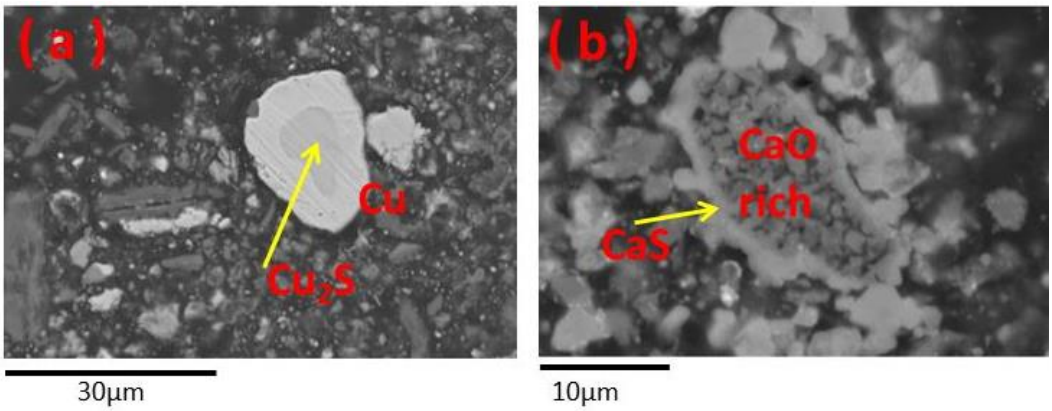

Figure 6.28 – Backscattered SEM images at molar ratio of MS:CaO:C = 1:2:2; (a) Nchanga at 1073 K and (b) Baluba at 1273 K. Argon flow rate = 0.6 litre min^{-1}

Because the experimental data fits into the diffusion and interface kinetic models, several mixed kinetic reaction models were tried but the experimental data deviated at certain mole ratios of CaO and C. Nonetheless, the experimental data fitted very well

into the sum of the diffusion (G.B) and interface (interface reaction) models (table 6.2), at all mole ratios of CaO and C. The sum of the diffusion (G.B) and interface (interface reaction) models was therefore used in analysing the reaction kinetics.

The plots of the lnK against 1/T line are shown in figure 6.29 and it is evident that a straight line cannot be fitted into the experimental data from 1073 K to 1323 K as the slope of the line changes at 1273 K for Nchanga and at 1223 K for Nkana and Baluba. The change in the slope of the line might be due to the presence of the liquid phase at high temperatures. It is interesting to note that the Nkana and Baluba samples which are rich in $CuFeS_2$ and FeS_2 minerals (see tables 3.2 and 3.3 and figure 4.1), the slope of the lnK versus 1/T line changes at the melting point of $CuFeS_2$ (1223 K). Furthermore, the reduction of FeS_2 mineral particles yields the liquid phase belonging to the Fe-O-S system, above 1173 K [182] so that it can be suggested that the liquid phase dominates above 1223 K in the Nkana and Baluba samples. On the other hand, the slope of the lnK versus 1/T line changes at higher temperature (1273 K) for Nchanga because this sample is dominated by the Cu_2S mineral, which melts at 1402 K.

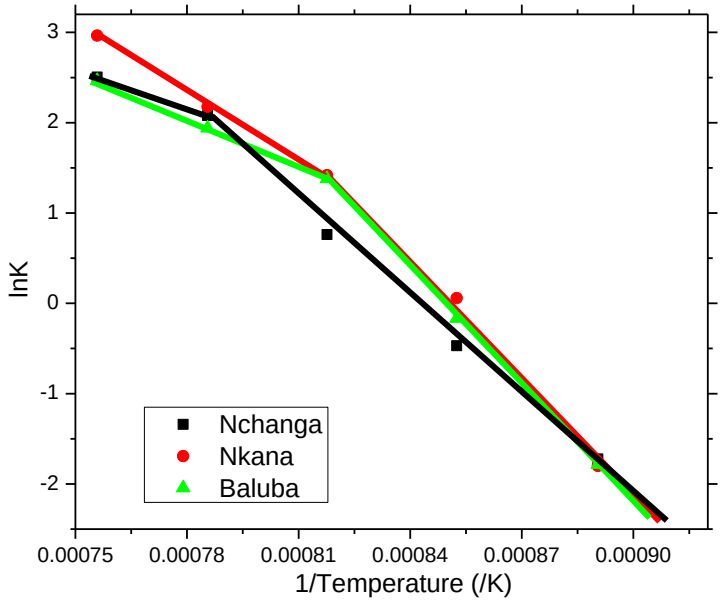

Figure 6.29 – Plots of the lnK versus 1/T, for the derivation of the activation energy (Q), the rate constants were

The plots of lnK versus 1/T were used to estimate the activation energy for the carbothermic reduction of the mineral sulphide concentrates in the presence of CaO. The activation energy was calculated by multiplying the gradient of the lnK versus 1/T

line, by the universal gas constant (R = 8.314 $Jmol^{-}K^{-1}$) as the gradient is equal to the quotient of activation energy and university gas constant. The activation energies were determined at different mole ratios of CaO and C and, the average values are given in table 6.3. The average activation energies in the high temperature regime (T ≥ 1223 K) for Nkana (220 ± 17 kJ) and Baluba (209 ± 40 kJ) are comparable to the activation energies of 200 kJ – 233 kJ, for reduction of various mineral sulphides in the presence of CaO (table 6.4) [55, 183]. The average activation energies in the high temperature regime (T ≥ 1223 K) for Nkana (220 ± 17 kJ) and Baluba (209 ± 40 kJ) are also comparable to the enthalpy change for reaction 6.8a. Since CaS and $CaSO_4$ were observed in the first 6 minutes at 1273 K, it can be suggested that the formation of CaS occurs partly via equation 6.8a. The Nkana and Baluba mineral sulphide concentrates are rich in $CuFeS_2$ and FeS_2 minerals and these mineral decompose rapidly by releasing S_2 gas in the high temperature regime and hence reaction 6.8a may take place. On the other hand, the content of FeS_2 and $CuFeS_2$ minerals are very low in the Nchanga sample such that equation 6.8a may not be the limiting factor. The average activation energy was 126 ± 17 kJ, in the high temperature regime for Nchanga and, this is comparable to the enthalpy change of 125 kJ for equation 6.8b. Note that the Nchanga mineral sulphide concentrates have about 28.3 wt. % Cu_2S (see table 3.1).

$$S_2(g) + CaSO_4 = CaS + 2SO_2(g),\ \Delta G = 219 - 0.2T\ kJ,\ T > 1223\ K \qquad 6.8a$$

$$Cu_2S + CaO + C = 2Cu + CaS + CO(g),\ \Delta G = 125 - 0.13T\ kJ,\ 1273K - 1323\ K \qquad 6.8b$$

The average activation energies of 278 kJ – 364 kJ in the low temperature regime agrees with the activation of 251 kJ – 360 kJ for the CO_2 – C reaction [184, 185]. As noted earlier, there was less metallisation but the exchange reaction occurred to a greater extent by yielding high fractions of metal oxides (Fe_3O_4 and FeO) in the low temperature regime. This confirms that the overall reaction was controlled by the CO_2 – C(carbon black) reaction. However, the average activation energies in the low temperature regime for Nchanga and Baluba are slightly lower than for Nkana, probably due to: (i) the catalytic effect [183] of copper on the Boudouard reaction [183], as copper is highest in these samples, (ii) catalytic effect of the alkaline carbonates such as potassium carbonate [186, 187] and (iii) the presence of H_2O from the gangue minerals

and moisture as the Nchanga and Baluba concentrates have high H_2O (see figure 4.6). Note that the activation energy for the H_2O – C reaction is 250 kJ - 334 kJ [188].

Table 6.3 - Summary of the average activation energies for the different samples

	High temperature regime		Low temperature regime	
	Average (kJ)	Std dev (kJ)	Average (kJ)	Std dev (kJ)
Nchanga	126	17	289	6
Nkana	220	17	364	3
Baluba	209	40	278	3

Where the higher temperature regime is T ≥ 1273 K for Nchanga and T ≥ 1223K for Nkana and Baluba and, Std dev is the standard deviation

Table 6.4 – Activation energy for the reduction of mineral sulphides reported in the literature

Reaction	Temperature (K)	Activation energy (kJ)	Reference
Sb_2S_3+CaO+C	973 – 1123	233	[184]
Cu_2S+CaO+CO(g)	1123 – 1273	164	[50]
MoS_2+CaO+C	1173 -1473	219	[55]
ZnS+CaO+C	1323 - 1473	200	[183]
FeS+CaO + C(activated	1223 - 1323	299 ± 27	[53]
FeS+CaO+C(coal)	1073 – 1273	270 ± 14	[34]
FeS+CaO+C(graphite)	1073 – 1273	308 ± 45	[34]

6.1.10.1 Effect of mole ratio of carbon

The summary of the activation energies at different molar ratios of carbon are presented in table 6.5 from which the following observations were made:

i. The activation energies are lowest in the high temperature regime but highest in the low temperature regime at molar ratio of MS:CaO:C = 1:2:1. This could be because of the presence of Ca_2CuFeO_3S in the high temperature regime at molar ratio of MS:CaO:C = 1:2:1. However, the lower temperature regime is controlled by the CO_2 – C reaction and hence the activation energy is highest at the lower molar ratio of carbon (MS:CaO:C = 1:2:1).

ii. The activation energy was generally lower in the low temperature regime at higher molar ratio of carbon (MS:CaO:C = 1:2:4) because of the increased reduction reaction or gasification of carbon at higher mole ratio of carbon.

iii. The activation energies were nearly the same in the high and low temperature regimes for Baluba at molar ratio of MS:CaO:C = 1:2:4. This suggests that the exchange reaction is slower in the upper region at high mole ratio of carbon as a result of limited contact between mineral sulphide and lime particles.

Table 6.5 – Calculated activation energies from the lnK vs. 1/T plots at various mole ratio of C for molar ratio of MS:CaO = 1:2

Nchanga	High temperature regime		Low temperature regime	
	Q (kJ)	R^2	Q (kJ)	R^2
MS:CaO:C = 1:2:1	110	-	298	0.9534
MS:CaO:C = 1:2:2	140	-	281	0.8802
MS:CaO:C = 1:2:3	135	-	294	0.9984
MS:CaO:C = 1:2:4	136	-	287	0.9606
Nkana				
MS:CaO:C = 1:2:1	220	0.9704	418	0.9859
MS:CaO:C = 1:2:2	220	0.9894	365	0.9937
MS:CaO:C = 1:2:3	230	0.8482	338	0.9942
MS:CaO:C = 1:2:4	212	0.9752	388	0.9972
Baluba				
MS:CaO:C = 1:2:1	168	0.9510	332	0.9916
MS:CaO:C = 1:2:2	232	0.9877	292	0.9764
MS:CaO:C = 1:2:3	180		276	0.9976
MS:CaO:C = 1:2:4	244	0.9984	260	0.9523

Where the higher temperature regime is $T \geq 1273$ K for Nchanga and $T \geq 1223$ K for Nkana and Baluba and, Q is the activation enrgy

6.10.1.2 Effect of CaO mole ratio

The summary for activation energies at different mole ratio of CaO are presented in table 6.6 and the following observations were made:

i. The activation energy was generally high at the lowest molar ratio of CaO (MS:CaO:C = 1:1.5:4) in the high temperature regime. The higher activation

energy at low mole ratio of CaO can be suggested as follows; (a) smaller volume of the liquid phase in the sample, caused by the rapid rate of the reduction of the metal oxides and (b) decreased contact between CaO and MS (exchange reaction).

ii. The activation energy was increasing with increase in the mole ratio of CaO for Baluba in the low temperature regime due to the formation of solid layer of Fe-O around the un-reacted core of Cu-S, at the high mole ratio of CaO. However, the solid layer of Fe-O decreases as the mole ratio of CaO decreases.

iii. The activation energy was nearly the same in the low temperature regime ($T \leq 1273$ K) for Nchanga.

iv. The activation energy is the same for molar ratios of MS:CaO:C = 1:1.5:4, 1:2:4 and 1:3:4 but lowest at molar ratio of MS:CaO:C = 1:4:4 in the high temperature regime for Baluba, probably due to the larger volume of the liquid phase at the molar ratio of MS:CaO:C = 1:4:4.

Table 6.6 – Calculated activation energies from lnK versus 1/T plots at various mole ratio of CaO for molar ratio of MS:C = 1:4

	High temperature regime		Low temperature regime	
Nchanga	Q (kJ)	R^2	Q (kJ)	R^2
MS:CaO:C = 1:1.5:4	143	-	286	0.9894
MS:CaO:C = 1:2:4	136	-	287	0.9606
MS:CaO:C = 1:3:4	95	-	294	0.9918
MS:CaO:C = 1:4:4	119	-	286	0.9955
Nkana				
MS:CaO:C = 1:1.5:4	251	0.9939	323	0.9888
MS:CaO:C = 1:2:4	210	0.9752	388	0.9972
MS:CaO:C = 1:3:4	219	0.9617	346	0.9930
MS:CaO:C = 1:4:4	208	0.9977	371	0.9931
Baluba				
MS:CaO:C =1:1.5:4	244	0.9843	226	0.9141
MS:CaO:C = 1:2:4	244	0.9984	259	0.9523
MS:CaO:C = 1:3:4	250	0.9918	271	0.9517
MS:CaO:C = 1:4:4	146	0.9999	291	0.9648

Where the higher temperature regime is $T \geq 1273$ K for Nchanga and $T \geq 1223$ K for Nkana and Baluba, and, Q is the activation energy

6.2 Higher temperature carbothermic reduction at 1573 K

The high temperature carbothermic reduction experiments were carried out in the elevating hearth furnace at 1573 K. The X-ray diffraction patterns for the samples which were held for 1 hour at 1573 K are given in figure 6.30. There are no peaks for SiO_2 and excess CaO in the XRD patterns for Nchanga and Nkana samples at twice the stoichiometric molar ratio of CaO (MS:CaO = 1:2). The absence of SiO_2 and CaO in the Nchanga and Nkana diffraction patterns is due to the formation of calcium silicate ($CaSiO_3$ and $Ca_2Al_2SiO_7$). Based on the XRD patterns in figure 6.30, it can be concluded that excess CaO was consumed by the gangue minerals in the Nchanga and Nkana samples at 1573 K. However, the excess CaO is present in the Baluba sample because this sample has the lowest gangue mineral content. In other words, not all of the excess CaO was consumed by the gangue minerals in the Baluba sample.

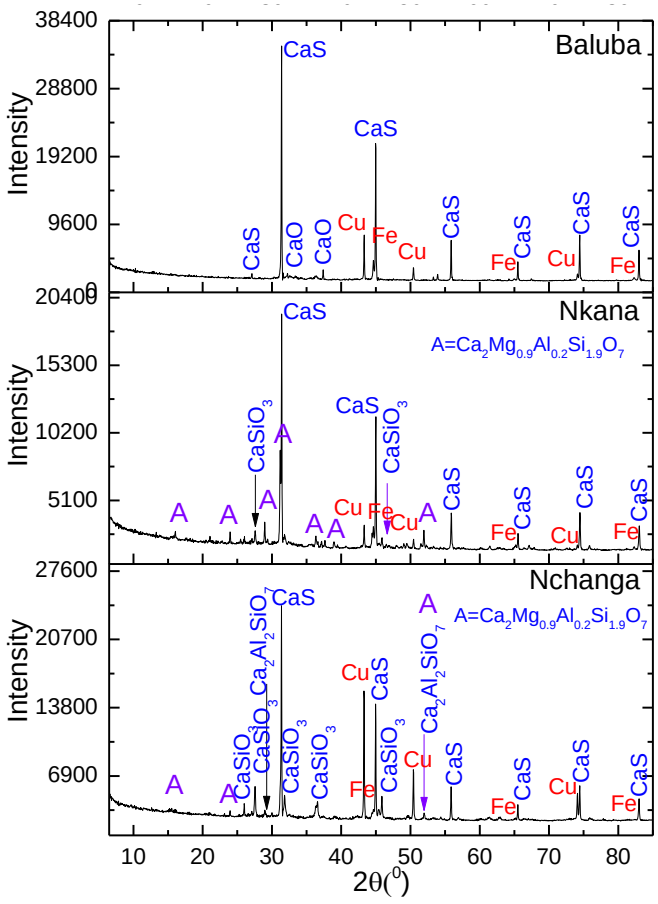

Figure 6.30 – XRD patterns after reduction of the mineral sulphide concentrates at molar ratio of MS:CaO:C = 1:2:2.2, the sample was heated from 1273 K to 1573 K and held for 1 hour at 1573 K. Argon flow rate = 2000 litres min^{-1}

6.2.1 Microstructure examination

Microscopic examination of the reacted samples revealed that most of the metallic particles were spherical even though the original mineral sulphides had various shapes, which is an indication of partial or complete melting [175]. The metallic particles can be partially or completely molten by considering the fact that the mineral sulphides, Cu and Cu-rich alloys are molten at 1573 K. Some metallic iron and cobalt spheres were embedded in the copper matrix and these types of phases might have resulted from the reduction of the $CuFeS_2$, Cu_5FeS_4 and $CuCo_2S_4$ mineral particles. The presence of Fe and Co spheres in the copper matrix is due to the de-mixing tendency between Cu and Fe or Co [126, 189, 190] and the non-wettable Cu-Fe interface [190]. The copper rich phase is on the outer surface or surrounds the Fe and Co spheres because it has low surface energy [189]. The embedded spheres were of varying sizes, as a result of coagulating of the smaller particles in order to decrease the interface energy [189] with the Cu-rich phase. It can be observed from the elemental mapping in figure 6.31 that coagulation of the particles was incomplete confirming that the time was not enough and, this was also observed by Curiotto [189]. The outer copper rich phase had about 94 wt. % Cu whereas the embedded spheres had nearly 94 wt. % Fe or 75 wt. % Fe + 22 wt. % Co as a result of low solubility between Cu and Fe/Co. On the other hand, Cu and Fe spheres were also observed in the reacted samples due to the reduction of Cu_2S and FeS_2 mineral particles, respectively. By comparison, the Cu spheres were more common in the Nchanga sample because the Nchanga concentrates are rich in the Cu_2S mineral.

Metallisation process was unaffected by the MS/C ratio as the reactions were complete even at molar ratio of MS:CaO:C = 1:2:4, which was not possible below 1323 K. This is because the mineral sulphides ($CuFeS_2$, Cu_5FeS_4 and CuS) are completely molten at 1573 K. As earlier observed, the reduction of the Cu_2S mineral particles was the slowest at $T \leq 1323$ K due to the presence of thick layer of metallic copper around the un-reacted sulphide core at the higher mole ratio of C than CaO (see figure 6.20a).

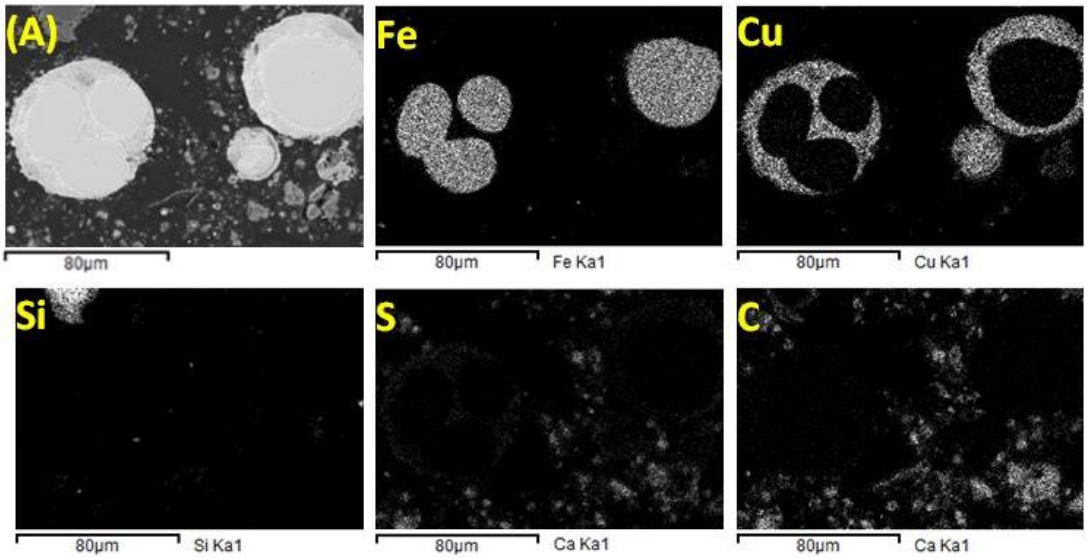

Figure 6.31 - Elemental mapping for Baluba at molar ratio of MS:CaO:C = 1:2:4, the sample was heated in the elevating hearth furnace from 1273 K to 1573 K and held for 1 hour at 1573 K (A) is the sample area analysed. Argon flow rate = 2 litres min^{-1}

6.2.2 Isothermal reduction

Isothermal experiments were carried out at 1573 K particularly, for understanding the reactions between CaO and mineral sulphides or gangue minerals. This is because there was no excess CaO in the Nchanga and Nkana samples which were reduced by continuous heating from 1323 K to 1573 K. It is possible that metallisation/reduction occurs as the samples are heated from 1323 K to 1573 K, so that the calcium silicates are formed after metallisation/reduction. As a result, the high temperature isothermal studies were important. It is worth noting that there is a competition for CaO, between the MS - CaO exchange reaction and formation of calcium silicate compounds, in the presence of carbon. Metallisation would be incomplete if the driving force for the formation of calcium silicate is higher than for the MS - CaO exchange reaction, in the presence of carbon. However, the Gibbs energy changes for the MS - CaO exchange reaction, in the presence of carbon and the formation of $CaSiO_3$ and $CaAl_2SiO_6$ are very comparable at 1573 K as shown in equations 6.12a – 6.12d, per mole of CaO.

$$Cu_2S(l) + CaO + C = 2Cu(l) + CaS + CO(g), \quad \Delta G_{1573K} = -87.7kJ \qquad 6.12a$$

$$FeS(l) + CaO + C = Fe + CaS + CO(g), \quad \Delta G_{1573K} = -99.8kJ \qquad 6.12b$$

$$SiO_2 + CaO = CaSiO_3, \Delta G_{1573K} = -90.8kJ \quad 6.12c$$

$$SiO_2 + CaO + Al_2O_3 = CaAl_2SiO_6, \Delta G_{1573K} = -96.2kJ \quad 6.12d$$

In order to understand the reaction mechanism taking place at high reduction temperature, the isothermal reduction experiments were carried out at 1573 K for 1 and 2 hours. It was found that metallisation was complete in either case. Since metallisation was complete under isothermal reduction at 1573 K, it can be suggested that the formation of calcium silicates occurs after the reduction of the mineral sulphides.

Even though the Gibbs energy changes for the carbothermic reduction of mineral sulphides in the presence of CaO and for the formation of calcium silicates, are very comparable in equations 6.11a – 6.11d, carbothermic reduction of mineral sulphides may take place before formation of calcium silicates as a result of high thermal decomposition of S_2 gas from the mineral sulphides at high temperature (1573 K). The decomposed S_2 gas from the mineral sulphide leads to the CaO(s) – S_2(g) reaction and, this reaction is more favourable than the CaO(s) – SiO_2(s) reaction. Furthermore, the formation of solid calcium silicate compounds may retard the kinetics of the CaO - SiO_2 reaction. Based on the experimental results, it can be concluded that the formation of calcium silicate is slower than the reduction of mineral sulphides.

6.3 Carbothermic reduction of mineral concentrates enriched with CoO

As shown in tables 3.1 - 3.3, the content of cobalt is very low (< 2 wt. %) in the mineral sulphide concentrates and hence the peaks for Co were not observed from the XRD diffraction patterns. Therefore, some experiments were designed, whereby the mineral sulphide concentrates were enriched with 10 wt. % CoO and mixed with CaO and C before reduction. The XRD patterns for the mineral sulphide concentrates which were enriched with 10 wt. % CoO and carbothermically reduced in the presence of CaO at 1273 K and 1573 K are presented in figure 6.32 and the following observations were made.

(i) The XRD peak intensities for Co are highest and lowest in the Nchanga and Baluba samples, respectively, at 1273 K. This is because Baluba sample has the

highest content of Fe and hence more Co was consumed by formation of Co-Fe alloys.

(ii) There were no XRD peaks for the excess CaO in the Nchanga and Nkana samples as a result of formation of complex silicate compounds at 1573 K.

(iii) The Co peaks have shifted to the lower angles at 1573 K and this has been observed by Curiotto [189].

(iv) The Fe peaks have shifted to the higher angle at 1573 K.

The XRD analysis showed that the cobalt at 1273 K and 1573 K had compositions of $Co_{0.82}Fe_{0.18}$ and $Co_{0.74}Fe_{0.26}$ respectively, and it is for this reason that the peaks for Co have shifted to the lower angles at 1573 K, since the lattice parameter for Co expands with increase in the content of Fe [129]. Fe formed mainly $Fe_{15}Co$, Fe_3Co and FeCo alloys at 1573 K and the XRD peaks have shifted to the high angle because the addition of Co decreases the lattice parameter of Fe [191, 192].

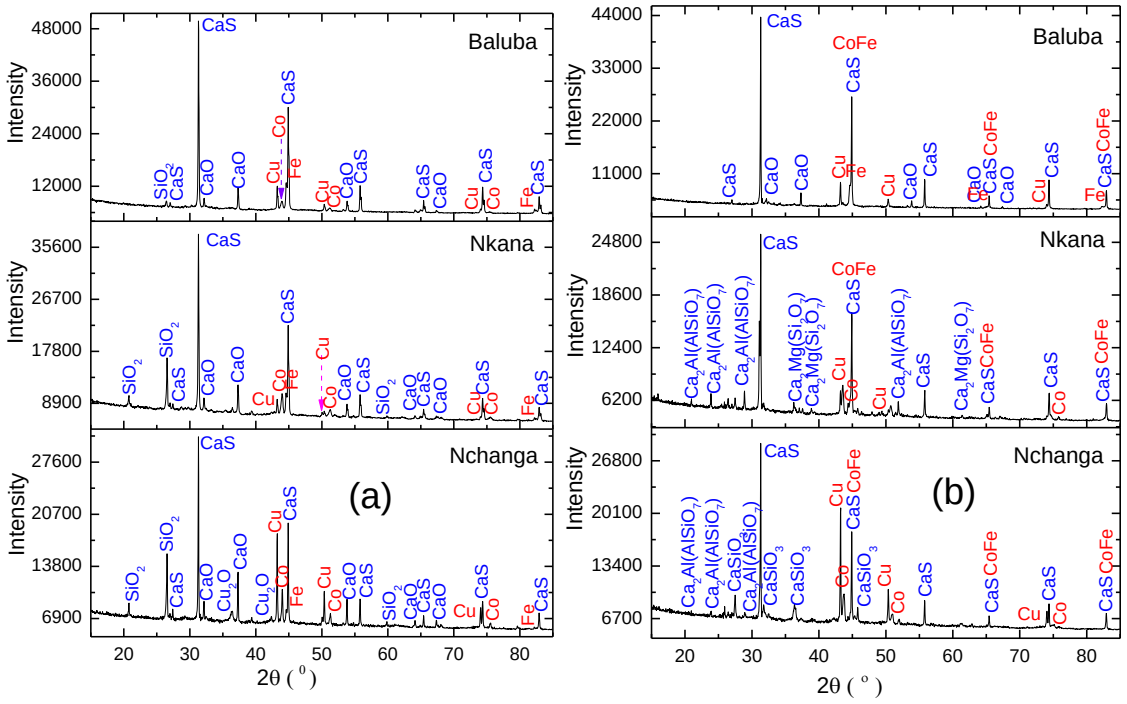

Figure 6.32 - XRD patterns for the samples enriched with 10 wt. % CoO and reduced at molar ratio of MS:CaO:C = 1:2:3 in the elevating hearth furnace; (a) 2 hours at 1273 K and (b) held for 1 hour at 1573 K. Argon flow rate = 2 litres min^{-1}

6.4 Sulphur analysis of the reduced samples at 1273 K and 1573 K

The analysis of sulphur was carried out in order to determine the amount of sulphur that can be lost during the carbothermic reduction of the mineral sulphide concentrates in the presence of CaO. The mineral sulphide concentrates were isothermally reduced in the elevating hearth furnace for 2.5 hours at 1273 K and for 1 hour 1573 K and the XRF results are presented in table 6.6. The mass balance for sulphur in table 6.7 shows that there was no loss of sulphur during the carbothermic reduction of the mineral sulphide concentrates in the presence of CaO at 1273 K. However, the sulphur content is slightly lower at 1573 K than at 1273 K in the Nchanga sample, which may be due to: (i) thermal decomposition of the mineral sulphides such that part of the S_2 gas is lost out at the start of the experiments and (ii) evolution of SO_2 gas as a result of reaction between the metal sulphides and, H_2O and CO_2 in the first few minutes of the experiment at 1573 K. Since the sulphur contents are nearly the same at 1273 K and 1573 K in the Baluba concentrates which are rich in the $CuFeS_2$ and FeS_2 minerals, it can be concluded that the slight loss of sulphur in the Nchanga sample at 1573 K, is not because of the thermal decomposition of the mineral sulphides but due to decomposition of the volatile components (H_2O and CO_2). This is because the Nchanga concentrates has the highest volatile species (see figure 4.6). Based on the XRF results in table 6.7, it can be concluded that carbothermic reduction of mineral sulphides in the presence of CaO is a clean process as there very less or no emission of the sulphurous gas.

Table 6.7 – XRF semi-quantitative analysis (wt. %) for the samples, after isothermal reduction of mineral sulphide concentrates in the presence of CaO, in the elevating hearth furnace. Argon flow rate = 2 litres min^{-1}

	Cu	Fe	Co	S	Ca	Si	Na	Al	Mg	K
Nchanga-1573K	27.2	7.1	0.3	11.1	34.4	11.1	1.4	2.7	1.3	1.1
Nchanga-1273K	26.5	6.0	0.6	13.5	34.4	11.6	1.3	2.3	2.0	1.6
Nkana-1573K	9.7	13.6	1.0	12.9	37.3	14.9	1.2	3.9	2.5	2.7
Nkana-1273K	8.4	13.2	0.8	13.6	36.4	14.7	1.2	4.4	3.7	3.2
Baluba-1573K	12.2	15.1	0.4	24.2	42.2	2.9	1.1	0.5	1.0	0.4
Baluba-1273K	11.6	15.7	0.5	24.7	41.5	2.5	1.3	0.6	1.2	0.3
Error = ±2 wt. %										

6.5 Separation of metallic phase from the reduced products

As discussed in chapter 2, CaS and CaO are soluble in acetic or hydrochloric acid. Therefore, the carbothermically reduced samples were leached in 5 % acetic acid at room temperature and selective dissolution of CaS and excess CaO was achieved. However, alumina, silica, complex alumina silicates did not dissolve in acid, remained with the metallic phases. It was therefore concluded that selective dissolution of the unwanted phases in either 5 % acetic acid or 5 % hydrochloric acid is ineffective method for obtaining the metallic phases from the reaction products because of the acid insoluble non-metallic phases.

6.5.1 Magnetic separation

The X-ray diffraction results for the mineral sulphide concentrates carbothermically reduced in the presence of CaO at 1273 K and subjected to magnetic separation are shown in figures 6.33a and 6.33b. The magnetic fractions contain high XRD peak intensities for the metallic phases (Cu and Fe). CaS is the main impurity in the magnetic fractions (figure 6.33a) although present in smaller quantity. There are no XRD peaks for the metallic phases (Cu, Fe, Co) in the non-magnetic fractions (figure 6.33b) for Nkana and Baluba. However, Cu is the only metallic phase in the non-magnetic fraction for Nchanga and this is because, Cu is a non-magnetic phase, unless it dissolves a small amount of Fe and Co [8]. By comparison, the Cu from the Nkana and Baluba samples was magnetically separated due to the fact that it originated from the $CuFeS_2$, Cu_5FeS_4 and $CuCo_2S_4$ mineral particles. As showed in the SEM microstructures in figures 6.18, 6.25 and 6.31 the cobalt and iron originating from Cu-Fe-S or Cu-Co-S type of mineral particles, were embedded in the copper matrix such that all the metallic phases were magnetic in the Nkana and Baluba samples. On the other hand, Cu_2S is the main copper sulphide mineral in the Nchanga concentrate and the reduced Cu from the Cu_2S mineral particles did not react with Co or Fe at 1273 K. Consequently, the copper originating from the Cu_2S mineral particles was non-magnetic. It is more likely that the copper that is in the Nchanga magnetic fraction originated from the $CuFeS_2$, Cu_5FeS_4 and $CuCo_2S_4$ minerals because these minerals are present in the as-received mineral concentrates (see table 3.1).

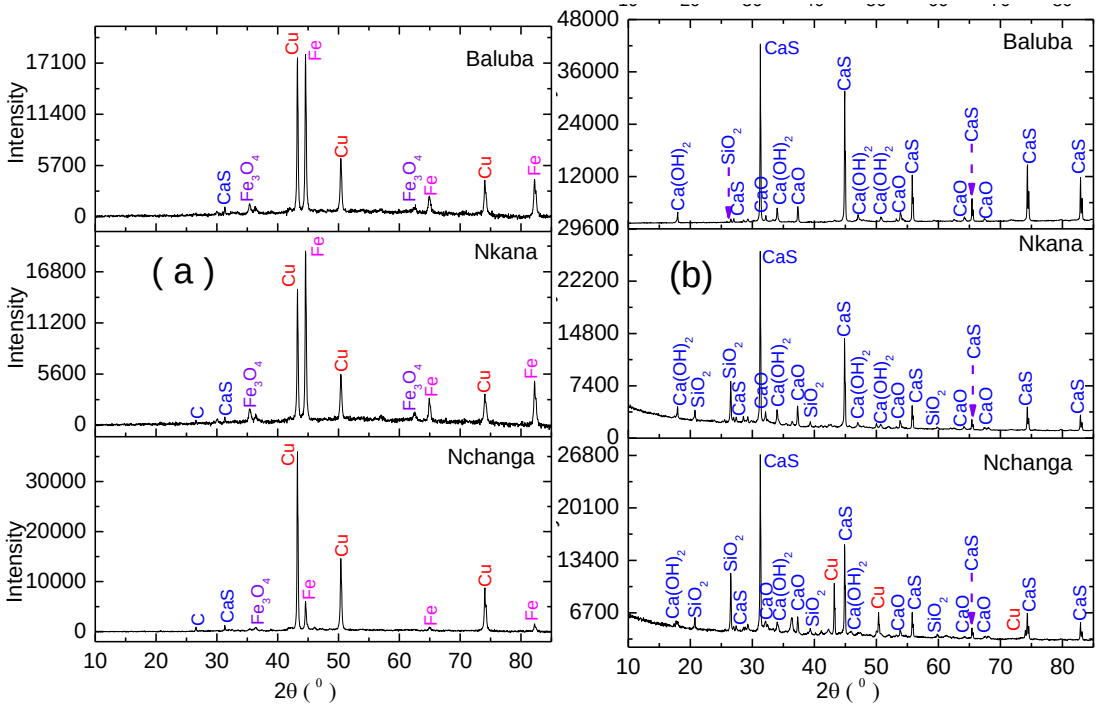

Figure 6.33 – XRD patterns after magnetic seperation of the reduced mineral sulphide concentrates at 1273 K, molar ratio of MS:CaO:C = 1:2:3, with carbon black; (a) magnetic fraction and (b) non-magnetic fraction

Mass balances for the samples which were reduced at 1273 K and magnetically separated are presented in table 6.8. The weights of the magnetic and non-magnetic fractions do not add up to the initial weight of the reduced sample before magnetic separation process. This is due to the dissolution of water soluble compounds during the wet magnetic separation. The weight of the magnetic fraction was much smaller than the weight of the metallic phases (Cu, Co and Fe) in the Nchanga concentrates (before reduction) as part of copper was collected in the non-magnetic fraction (figure 6.33b).

The XRF analysis results of the magnetic and non-magnetic fractions obtained after magnetic separation of the reduced samples are given in table 6.9. It can be deduced from the XRF results in table 6.9 that the magnetic fractions had about 90 wt. % metallic phases. The major phase impurities in the magnetic fractions were Ca and S and where identified as CaS, in the XRD patterns (figure 6.33a). The non-magnetic fractions for Nkana and Baluba had only about 8 % metallic phases which shows that magnetic separation was more effective than in the Nchanga sample. SEM analysis of the non-magnetic fractions showed that metallic phases in the non-magnetic fractions for Nkana and Baluba were mainly in the sulphide form, as a result of the incomplete reduction. This shows that more metallic phases can be recovered in the

magnetic fraction by ensuring complete reduction of the samples, prior to magnetic separation.

Table 6.8 - Mass balance showing the weights (g) of the reduced samples before and after magnetic separation, the samples were reduced for 2.2 hours at 1273 K, molar ratio of MS:CaO:C = 1:2:3

	Weight of concentrate	Weights of Cu+Fe+Co in concentrate	Weight of reduced sample before separation (with CaO and C)	Magnetic Fraction	Non-magnetic fraction
Nchanga	10.0	4.2	12.4	1.8	9.0
Nkana	10.0	2.0	13.0	2.2	9.2
Baluba	10.0	4.4	15.5	4.3	10.0

Table 6.9 – XRF semi-quantitative analysis (wt. %) of the magnetic (mag) and non-magnetic (non-mag) fractions, the samples were reduced at 1273 K, molar ratio of MS:CaO:C(carbon black) = 1:2:3

	Cu	Fe	Co	S	Ca	Si	Al	Mg	Ti
Nchanga Mag	65.2	21.4	0.7	4.3	4.7	1.9	1.1	0.3	0.4
Nkana Mag	29.5	58.1	3.9	3.2	2.8	1.0	1.2	0.2	0.1
Baluba Mag	33.9	55.5	2.1	3.7	3.1	0.8	0.3	0.4	0.2
Nchanga non-mag	21.5	3.7	0.1	14.1	40.8	12.3	4.7	2.1	0.6
Nkana non-mag	3.9	4.2	0.1	17.3	47.2	17.3	4.6	4.8	0.5
Baluba non-mag	3.8	3.9	0.1	29.4	57.4	2.6	0.7	1.9	0.5
Error = ±2 wt. %									

6.5.2 Gravity separation of copper

As observed in the XRD pattern in figure 6.33a and XRF results in table 6.9, the Nchanga non-magnetic fraction had the highest amount of copper and hence a second process is required for separating out the remaining copper from the non-magnetic fraction. Therefore, an experiment was carried out, where magnetic separation was

followed by the gravity separation [79] of copper from the non-magnetic fraction. The non-magnetic samples were placed in the beaker and water was added. The contents were gently shaken for about 1 minute and the lighter phases such as CaS and gangue minerals were taken into suspension or floated in what is known as sink-float process [79, 193]. The sink-float process appears to be assisted by the presence of residual carbon and the finer gangue minerals [79]. The beaker was tilted and, the floated sample was quickly poured out into another beaker. The sediments or the particles that sunk to the bottom of the first beaker had both reddish and large white (SiO_2) particles. On the other hand, the large white SiO_2 particles were nearly removed after repeating the gravity separation process for 2 - 3 times. The major disadvantage is that, some finer copper particles were lost out, by repeating the gravity separation process. This is because the smaller copper particles were floated with the larger SiO_2 particles. The XRD analysis of copper separated by the gravity method after 3 cycles is shown in figure 7.34 and it is evident that copper was the main phase.

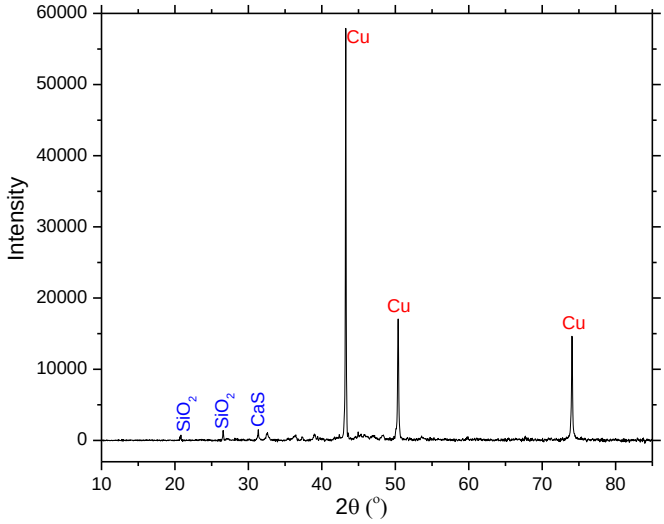

Figure 6.34 – XRD patterns for the copper fraction obtained from the gravity (sink-float) separation of the non-magnetic residue from Nchanga, the sample was reduced at 1273 K at molar ratio of MS:CaO:C = 1:2:3, with carbon black

However, it is possible that the remaining copper can be completely separated out, using the sink-float process by changing the density of the liquid medium. The liquid medium should have density between that of copper and SiO_2 so that even the finer copper particles can be separated from the larger SiO_2 particles without any problem.

6.5.3 Effect of reduction temperature

The metallic phases, metal sulphides (Cu_2S, Cu_5FeS_4) and magnetite (Fe_3O_4) were all present in the magnetic fraction because of incomplete metallisation of the samples which were reduced at lower temperature, such as 1173 K as shown in figure 6.35a. Magnetite (Fe_3O_4) which is a highly magnetic iron oxide phase was found at the surface of the particles, surrounding the core of Cu_2S, for the partially reacted $CuFeS_2$ and Cu_5FeS_4 mineral particles. The mechanism leading to the formation of Fe_3O_4 at the periphery of the mineral particles has been discussed in detail, in section 6.3.

The effect of reduction temperature on magnetic separation of the metallic phases was further investigated by reducing the mineral sulphide concentrates at 1373 K and 1573 K. The XRD pattern for the Nchanga sample which was reduced at 1373 K and subjected to the magnetic separation is shown in figure 6.35b and it can be observed that Cu and Fe are the major phases in the magnetic fraction. By comparison, complete magnetic separation was easier for the samples which were reduced at 1573 K or 1373 K than those at 1273 K. The reason is that larger particles (metallic, CaS and gangue minerals) were obtained when the mineral sulphide concentrates were reduced at temperatures above 1273 K. Figure 6.36a is the SEM image of the sample after carbothermic reduction at 1573 K and it is evident that the metallic phases were growing by coalescence. Magnetic separation of the coarse particles was easier than for fine particles because, very fine non-magnetic particles tend to get trapped or stick to the magnetic powders.

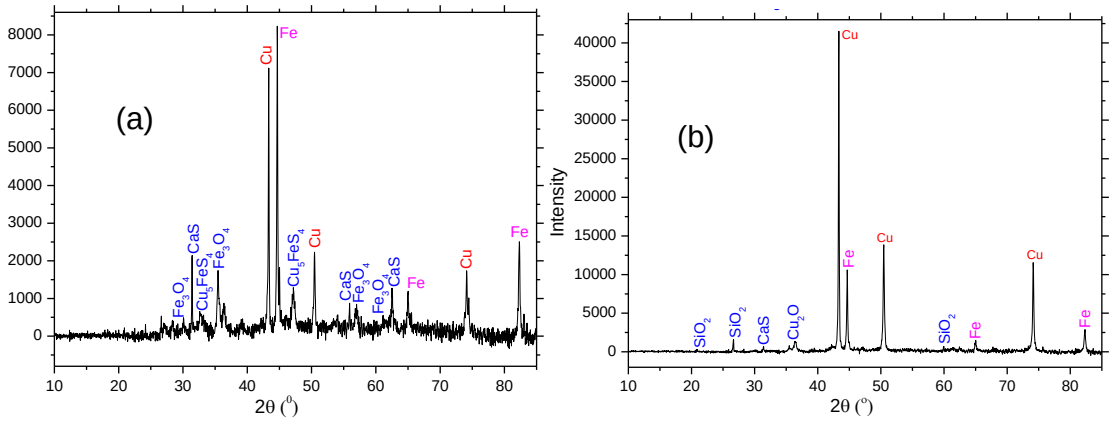

Figure 6.35 - XRD patterns of the magnetic fractions; (a) Baluba reduced at 1173 K, MS:CaO:C = 1:2:3 and (b) Nchanga reduced at 1373 K, MS:CaO:C = 1:2:4, reduced with carbon black

On the other hand, magnetic separation was more effective at higher mole ratio of C than CaO such as MS:CaO:C = 1:2:4, for the samples reduced above 1273 K. This is due to sintering between CaS and the metallic phases at slightly higher molar ratio of C than CaO as shown in figure 6.36b. The sintering between CaS and the metallic phases, increases the fraction of the CaS phase in the magnetic fraction [53].

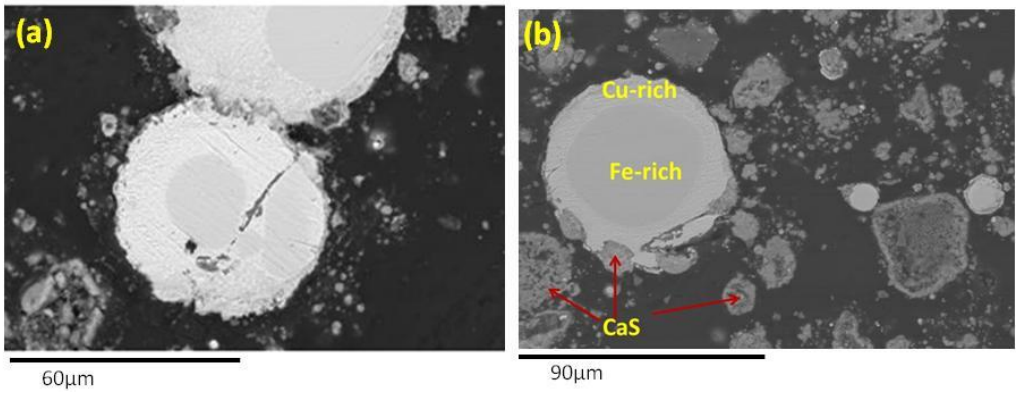

Figure 6.36 – Backscattered SEM images for the Baluba sample reduced for 1 hour at 1573 K, molar ratio of MS:CaO:C = 1:2:2.2 (a) coalescence of metallic phases and (b) sintering between CaS and metallic phases

6.5.4 Effect of using graphite as a reductant

Magnetic separation was not possible for the samples which were reduced with graphite, due to excessive sintering of the samples, regardless of the CaO/C mole ratio. Excessive sintering occurred during reduction with graphite, because metallisation occurred via reduction of the Ca_2CuFeO_3S intermediate liquid phase.

6.5.5 Magnetic separation of the samples enriched with 10 wt. % CoO

The reduced samples which were enriched with 10 wt. % CoO before reduction were highly magnetic due to the presence of cobalt metal/alloy phases. Moreover, the proportion of the magnetic phase increases as CoO is added into the samples before reduction and hence the sample becomes more magnetic. The XRD patterns for the magnetic and non-magnetic fractions are given in figure 6.37a and 6.37b. It is evident from figure 6.37a, that the main phases in the magnetic fraction were Cu, Co and Fe. As

observed earlier in figure 6.33b, there are no XRD peak intensities for metallic phases (Cu, Co and Fe) in the non-magnetic fractions for Nkana and Baluba.

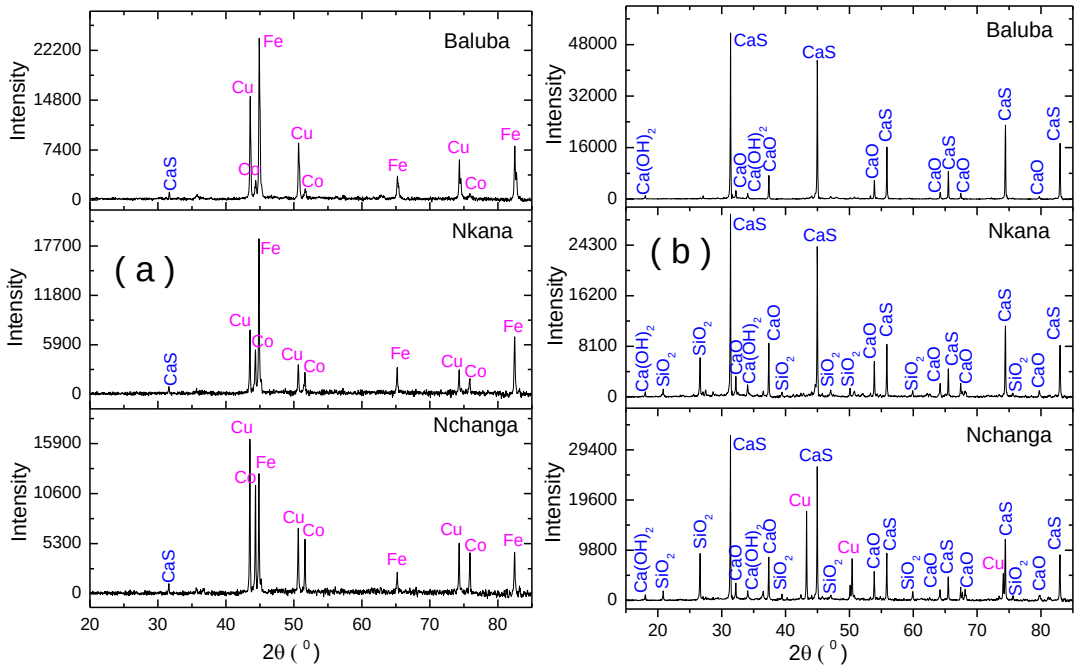

Figure 6.37 – XRD patterns for; (a) magnetic fraction and (b) non-magnetic fraction. The mineral sulphide concentrates were enriched with 10 wt. % CoO and reduced at 1273 K, MS:CaO:C = 1:2:3, with carbon black. Argon flow rate = 2 litres min^{-1}

6.5.5.1 Melting of the magnetic fraction samples

The magnetic fractions were melted for 2 hours, under argon atmosphere at 1823 K. The melted alloys were silvery due to the presence of cobalt and iron and, a very thin black layer was observed on the inner surface of the crucibles suggesting that molten slag was expelled from the melt. The presence of slag is evident because the magnetic fraction contains small concentrations of Al_2O_3, MgO and SiO_2 (see table 6.9). However, the volume of the expelled slag was too small to be collected for analysis and hence it was not characterised. The EDX semi-quantitative analyses for the melted alloys are given in table 6.10 and it can be observed that sulphur and silicon are the main impurity in the melted alloys. The presence of sulphur in the melted alloys is because the magnetic fractions had residual CaS (see figure 6.37a). Nonetheless, the purity of the melted alloys are much higher than the copper-cobalt-iron alloy produced in the slag cleaning electric furnace at Nchanga smelter, in Zambia.

The elemental distribution for the Baluba alloy is shown in figure 6.39 and it can be observed that there are three phases in the melted magnetic alloys and they are the Cu rich, Cu-S rich and Co-Fe rich phases. The magnetic fractions did not contain any Cu-S phase and CaS was the only source of sulphur in the melted alloys. However, detailed analysis of the melted alloys showed no evidence of CaS phase or any calcium compound (calcium oxide, calcium sulphide, calcium oxy-sulphide) suggesting that the residual CaS reacted with Cu. The reaction between CaS and Cu can occur via formation of the stable compound such as Ca silicate as shown in the overall reaction 6.13. Based on equation 6.13, it is understood as to why the Co-Fe rich alloy had about 3 wt. % Si.

$$3SiO_2 + CaS + 2Cu + 6Fe + 3C = CaSiO_3 + 2Fe_3Si + Cu_2S + 3CO(g), \qquad 6.13$$

$$\Delta G_{1823K} = -78\,kJ$$

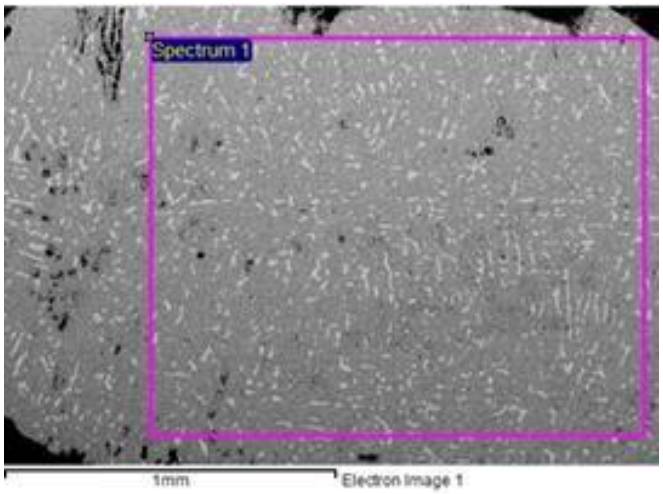

Figure 6.38 – Backscattered SEM image for Nkana at low magnification showing the area analysed, the semi-quantitative EDX analysis in table 6.10

Table 6.10 – SEM-EDX semi-quantitative analysis (wt. %) of the alloys after melting the magnetic fractions at 1823 K, the mineral sulphide concentrates were enriched with 10 wt. % before reduction at 1273 K

	Cu	Co	Fe	Ca	S	O	Si
Nchanga	19.2	28.0	45.8		2.2	2.8	2.0
Nkana	26.0	36.0	33.0	-	2.3	2.0	2.4
Baluba	32.0	12.0	49.5	-	4.7	3.0	1.8

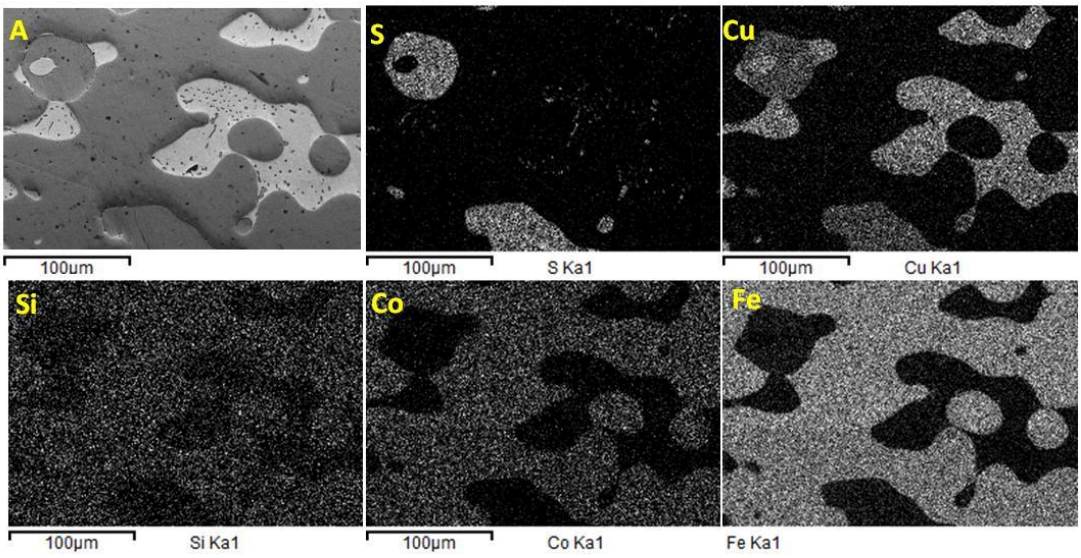

Figure 6.39 – Elemental mapping for the Baluba magnetic fraction, melted at 1823 K, A is the sample area analysed under backscattered electron imaging

6.5.5.2 Regeneration of lime from CaS

The non-magnetic fractions containing CaS were heated in the presence of calcium sulphate for the regeneration of CaO [84, 85]. Calcium sulphate was added to the non-magnetic fraction according to equation 6.14 and heated under argon atmosphere at 1373 K. The X-ray diffraction results are given in figure 6.40 and it is evident that $CaSO_4$ reacted with CaS by yielding CaO according to equation 6.14. The results in figure 6.40 suggest that there was insufficient $CaSO_4$ in the Nchanga and Baluba samples due to the presence of CaS. However, the presence of CaS can be as a result of

calcination of part of $CaSO_4$ to CaS since the non-magnetic fractions had residual carbon.

$$3CaSO_4 + CaS = 4CaO + 4SO_2(g) \qquad 6.14$$

Part of the regenerated CaO, reacted with SiO_2 in the Nchanga and Nkana samples to give di-calcium silicate ($2CaO \bullet SiO_2$). The formation of calcium silicates decreases the amount of lime regenerated. Metallic copper from the Nchanga non-magnetic fractions was converted to copper sulphide, identified as $Cu_{1.8}S$ from the X-ray diffraction pattern. The formation of copper sulphide can be represented by equation 6.15.

$$2Cu + SO_2 + C = Cu_2S + 2CO(g) \qquad 6.15$$

It can be observed from equation 6.14 that the off-gas will be nearly pure SO_2 gas and can thus be converted to sulphuric acid or elemental sulphur without polluting the environment with the sulphurous gas. The CaO can be re-used for the carbothermic reduction. The regeneration of CaO from CaS in the presence of $CaSO_4$ lowers the amount of waste generation during metal production unlike in conventional copper smelting where iron, gangue minerals and flux are discarded.

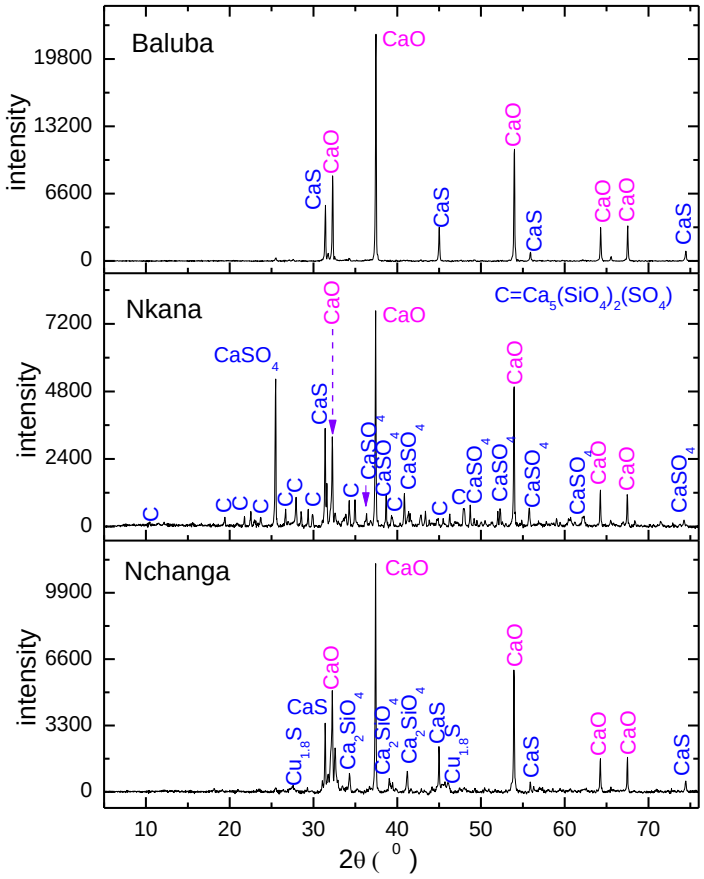

Figure 6.40 – XRD patterns for the non-magnetic fractions after heated in the presence of $CaSO_4$ at 1373 K for the regeneration of CaO

6.6 Estimation of energy requirement

Energy is required in the metallurgical processes for: (i) heating up the material to the required or processing temperature [10, 28], which can be given as $MC_p\Delta T$, where M is mass, C_p is specific heat capacity and ΔT is the temperature change, (ii) supplying latent heat for melting and evaporating [10, 28] and, (iii) for endothermic reactions [10, 28]. Even though the carbothermic reduction of copper, cobalt and iron sulphides in the presence of CaO are endothermic reactions, the process offers advantages for treating of copper-cobalt-iron sulphide concentrates, compared with the conventional smelting of mineral sulphide concentrates. This is because cobalt and iron, as elements are lost into the slag during conventional smelting, thereby requiring further treatment of the slag via smelting at 1923 K, for recovering metallic constituents. This is an energy intensive process when compared with carbothermic reduction at lower temperatures. Moreover, the white alloy produced by smelting of slag, is further processed by pressure leaching

in autoclave at high temperatures for taking copper and cobalt into solution before eletro-winning [22]. The consumption of furnace refractory lining is undoubtedly much lower for the proposed carbothermic reduction method, compared to the conventional smelting of concentrates above 1473 K, as a first step of pyrometallurgical beneficiation of complex sulphide concentrates.

The theoretical energy requirement for the process was calculated using the HSC 5.1 software [39]. The following assumptions were made for calculating the energy requirement for the carbothermic reduction of mineral sulphide concentrates in the presence of CaO:

i. The reduction reaction 1.5a completes to 100 % by forming metallic (Cu, Co and Fe), CaS and CO gas phases.
ii. There is no reaction between CaO and the gangue minerals
iii. The reactants (mineral sulphide concentrates + CaO + C) and the reaction products (metallic phases, CaS, gangue minerals and CO gas) enter and leave the reaction chamber at 298 K and 1273 K, respectively.
iv. The moisture (H_2O) and CO_2 from the carbonates in the mineral concentrates react with carbon to form H_2 and CO gases, according to equations 6.16a and 6.16b.

$$H_2O(g) + C(s) = H_2(g) + CO(g) \qquad 6.16a$$

$$CaMg(CO_3)_2 + 2C = CaO \bullet MgO + 4CO(g) \qquad 6.16b$$

v. The off-gas only contains CO and H_2 gases.
vi. All Co is contained in the carrollite mineral ($CuCo_2S_4$) due to lack of thermodynamic data in the HSC software for the cobaltian pyrite mineral ((Fe,Co)S) [9].
vii. The carrollite mineral ($CuCo_2S_4$) exist as Cu and CoS_2 mineral via equation 6.17, due to lack of thermodynamic data for the $CuCo_2S_4$.

$$CuCo_2S_4 = Cu + 2CoS_2 \qquad 6.17$$

The analysis of the theoretical energy requirement for the carbothermic reduction of the mineral sulphide concentrates are presented in table 6.11. The analysis in table 6.11

includes the total energy requirement for the carbothermic reduction, the weights of the metallic phases (Cu, Co and Fe) produced from the carbothermic reduction and the heat requirement (kWh) per Kg of the metallic phases (Cu + Co + Fe). The theoretical energy requirement for Nkana and Baluba are about double that of Nchanga, probably due to the reduction calcination of the dolomite mineral ($CaMg(CO_3)_2$) (see equation 6.16b). By comparison, the theoretical energy requirement for smelting of Cu-Co-Fe slag at 1923 K is about 2.8 kWh per kg of the metallic phases (Cu + Co + Fe) [194] whereas it is 0.4 kWh – 0.6 kWh per kg of Cu, for conventional copper smelting (table 6.12) [12]. The above analysis clearly shows that the theoretical energy requirement for the carbothermic reduction of minerals sulphides in the presence of CaO, is lower than that required for the combination of copper smelting and slag smelting processes.

Table 6.11 – Analysis of heat requirement for carbothermic reduction of mineral sulphides concentrates in the presence of CaO, computed using HSC software 5.1 [39], the details for mass balance are given in table A.6.2 – A.6.4

	Heat requirement (kWh) for carbothermic reduction of concentrates	Weight of Cu + Co + Fe (Kg) produced from carbothermic reduction	Heat requirement (kWh) per kg of metallic phases (Cu+Co+Fe)
Nchanga	45.6	39.9	1.10
Nkana	60.3	21.1	2.90
Baluba	92.4	47.8	1.90

Table 6.12 – Theoretical energy requirement (kWh/per kg of metal) for extraction of metals [12]

metal	*Theoretical energy*	*Extraction mode*
Cu	0.4 – 0.6	smelting
Fe	1.8 - 2.4	blast furnace smelting

Moreover, the CO gas from equation 1.5a can be used to meet part of the energy requirement for the carbothermic reduction of the mineral sulphides in the presence of CaO. The CO gas can be burnt in O_2 gas to give CO_2 gas (see equation 2.15). The total

heat produced from burning of CO gas in O_2 gas is given in table 6.13. It can be observed in table 6.13 that the heat produced from burning of CO gas in O_2 gas is actually higher than for the carbothermic reduction of the Baluba mineral sulphide concentrates. The net heat requirement for the carbothermic reduction of mineral sulphide concentrates in the presence of CaO and for burning of CO gas in O_2 was calculated from tables 6.12 and 6.13 and, is given in table 6.14. It can be observed from table 6.14 that: (i) no heat is required for Baluba and (ii) less than 0.3 kWh of heat per kg of Cu + Co + Fe, is required for Nchanga and Nkana.

Since carbothermic reduction of the mineral sulphides in the presence of CaO does not require O_2 gas, the CO gas can be burnt externally as shown in figure 6.41. The CO_2 gas produced from the oxidation of CO gas can be used for the carbonation of CaS, after magnetic separation (see figure 2.6)

Table 6.13 – Energy analysis for burning of CO gas in O_2 gas, the CO gas is produced from the reduction of mineral concentrates, estimated using HSC software 5.1 [39]

	Weight of Cu + Co + Fe (Kg) produced from carbothermic reduction	Heat (kWh) produced in burning CO gas in O_2 gas
Nchanga	39.9	-39.5
Nkana	21.1	-54.3
Baluba	47.8	-121.1

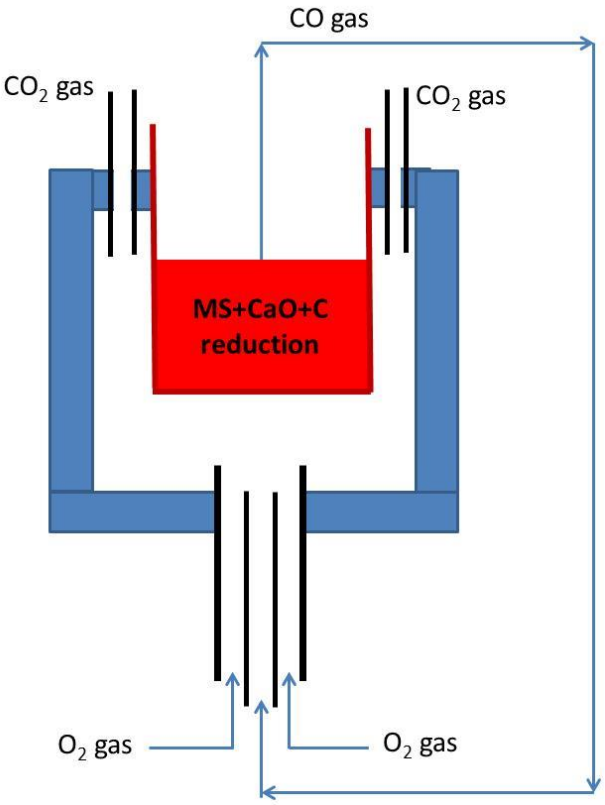

Figure 6.41 – Schematic arrangement for utilization of heat from burning of CO gas in O_2 gas

Table 6.14 – Overall heat (kWh) required for the carbothernic reduction of mineral sulphide concentrates in the presence of CaO and burning of CO gas with O_2 gas, estimated using HSC software 5.1 [39]

	Net heat required based on tables 6.11 and 6.13	Net heat requirement per kg of metallic phases (Cu+Co+Fe)
Nchanga	6.1	0.1
Nkana	6.0	0.3
Baluba	-28.7	-0.6

7.0 Lime roast - reduction of mineral sulphide concentrates

As discussed in chapter 6, carbothermic reduction of the mineral sulphides occurs via reduction of the intermediate metal oxide (MO) phases. However, the low temperature carbothermic reduction of the Cu-S mineral phase was limited by the ion exchange reaction i.e., formation of Cu-O, at T < 1173 K. Nevertheless, mineral sulphides are easily oxidised in the presence of O_2 gas, meaning that it is possible to attain low temperature carbothermic reduction of the mineral sulphide concentrates via lime roast - reduction process. Lime roasting of mineral sulphides has been carried out by many authors [28, 41, 195-198] and the major reaction is shown in equation 7.1. In essence, metal oxides/sulphates/oxysulphates may be produced depending on the partial pressure of O_2 gas and roasting temperature. Even though lime roasting of the mineral sulphide concentrates has been carried out by a number of authors, the lime roast calcine has been treated through the hydrometallurgical route (leaching). The lime roast calcines were leached in acid with the purpose of selectively dissolving the metal oxides but the challenge is that, excess CaO and basic gangue minerals (e.g. MgO, K_2O) are soluble in acid and hence they increase the consumption of acid. In short, acid leaching of the lime roast calcine is undesirable because of the acid soluble components (CaO and MgO, K_2O).

$$MS + 2O_2 + CaO = MO + CaSO_4 \qquad 7.1$$

The aim of this chapter is to investigate the low temperature reduction (< 1173 K) of the mineral sulphide concentrates via lime roast - reduction process. The reaction chemistry and kinetics for the lime roast process have been discussed. Unless stated, the weight of the sample in each lime roast experiment is 3 g. The carbothermic reduction of the lime roast calcine is discussed in two parts: (i) reduction with carbon black for the selective metallisation of Cu and (ii) reduction with activated charcoal for metallisation of Cu, Co and Fe.

7.1 Lime roasting of the mineral sulphide concentrates

The % oxidation at time‘t’ was calculated according to equation 7.2.

$$\%\ oxidaton\ = \frac{actual\ \ or\ \exp erimental\ \ weight\ \ gain}{Theoretical\ weight\ \ gain} \times 100\% \qquad 7.2$$

Where the theoretical weight gain is the weight of O_2 gas required for formation of $CaSO_4$ and most stable metal oxides (CuO, CoO and Fe_2O_3) via equation 7.1

The plots of % oxidation versus time curves for the lime roast of the mineral sulphide concentrates in air at different temperatures are presented in figure 7.1. Two main observations can be made from figure 7.1: (i) the extent of oxidation and the reaction time was lower and shorter, respectively, for Nchanga and (ii) the reaction time was longer for Baluba. The decreased or low % oxidation for Nchanga can be due to formation of the Cu_2O and $CuSO_4$ phases from part of Cu_2S via equations 7.3a and 7.3b. It can be observed from equations 7.3a and 7.3b that 2 moles of O_2 gas are required for oxidation of 1 mole of Cu_2S to either Cu_2O or $CuSO_4$. However, 2.5 moles of O_2 gas are required for the oxidation of 1 mole of Cu_2S to CuO and $CaSO_4$ in the presence of CaO (equation 7.3c).

$$Cu_2S + 2O_2 + CaO = Cu_2O + CaSO_4 \qquad 7.3a$$

$$Cu_2S + 2O_2 = CuSO_4 \qquad 7.3b$$

$$Cu_2S + 2.5O_2 + CaO = 2CuO + CaSO_4 \qquad 7.3c$$

The low % oxidation in the Nchanga can also be due to internal oxidation, because the sample had the highest amount of H_2O, in the form of moisture and hydrated compounds. The reaction between H_2O and Cu_2S is shown in equation 7.4 and it can be observed that 2 moles of O_2 gas are required for complete oxidation of Cu_2S to CuO, compared to 2.5 moles in the absence of H_2O (see equation 7.3c). The Gibbs energy change for reaction 7.4 is highly negative at all roasting temperatures.

$$Cu_2S + H_2O(g) + CaO + 2O_2(g) = 2CuO + CaSO_4 + H_2(g) \qquad 7.4$$

The Nkana and Baluba reacted samples were both sintered but sintering was more severe in the later sample and this could be the reason for the longer roasting time (figure 7.1). It is worth noting that both Nkana and Baluba samples have similar types of mineral sulphides (FeS_2, $CuFeS_2$ and Cu_5FeS_4), the only difference is that Nkana has the highest gangue content (about 70 wt. %). The presence of gangue minerals appears to have decreased sintering in the Nkana sample. On the other hand, there was no sintering in the Nchanga sample which is dominated by the Cu_2S and this could be one of the reasons for the shorter reaction time.

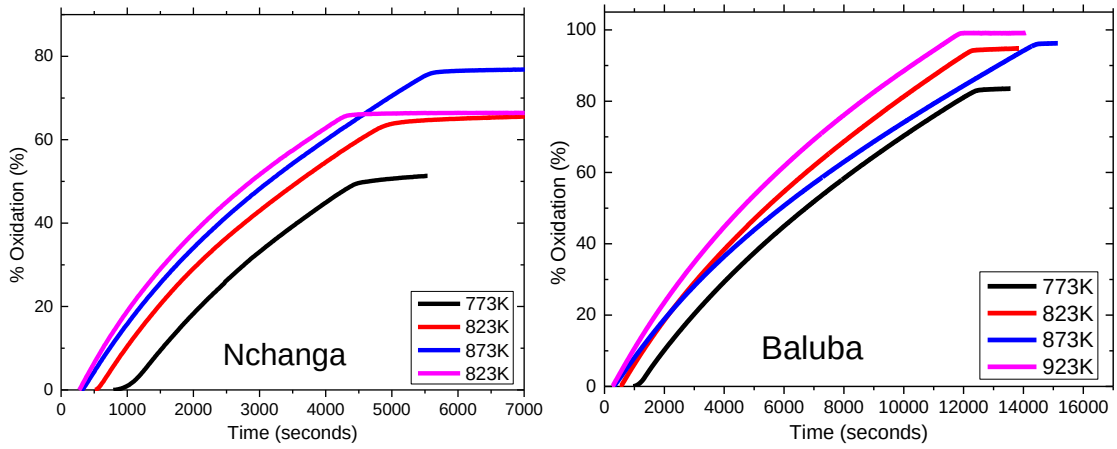

Figure 7.1 - Plots of % conversion against time curves for Nchanga and Baluba, lime roasted in air (21% O_2) at molar ratio of MS:CaO = 1:1.5

XRD analysis of the lime roast samples showed that the main phases were metal oxides (CuO, Fe_2O_3) and $CaSO_4$. The XRD peak intensities for CuO were highest in the Nchanga sample because the Nchanga mineral concentrates have high copper content (34 wt. % Cu), mainly in the form of Cu_2S/Cu_8S_5 ($Cu_{1.6}S$) minerals. On the other hand, the XRD peak intensities for Fe_2O_3 were highest in the Nkana and Baluba samples as these samples contain more Fe than Cu.

7.1.1 Effect of reaction temperature and mole ratio of MS:CaO

The effect of reaction temperature and molar ratio of MS:CaO was studied at MS:CaO = 1:1, 1:1.5 and 1:2 and, the major findings are discussed below:

MS:CaO = 1:1 – Residual CaO was present in the samples which were roasted at T ≤ 923 K but absent in the samples which were roasted at 973 K (figure 7.2a). Residual

CaO was found with $CuSO_4$ at T ≤ 923 K, owing to the stability of the later phase below 923 K [15]. Since $CuSO_4$ was absent at 973 K, it can be concluded that SO_2 gas from the oxidation of Cu_2S reacted with CaO to form $CaSO_4$, so that the general reactions can be represented by equations 7.5a and 7.5b.

$$MS + 1.5O_2(g) = MO + SO_2(g) \qquad 7.5a$$

$$CaO + SO_2(g) + O_2(g) = CaSO_4(g) \qquad 7.5b$$

The Cu_8S_5 phase is present in the XRD patterns in figure 7.2. The presence of Cu_8S_5 can be due to incomplete oxidation at the bottom of the sample because the bottom sample had a greyish colour whereas the rest of the sample was dark for Nchanga and, brownish for Nkana and Baluba. It appears that the oxidation reactions ceased before the bottom sample was fully oxidised. The effects of sample size and height are discussed later in section 7.1.2.

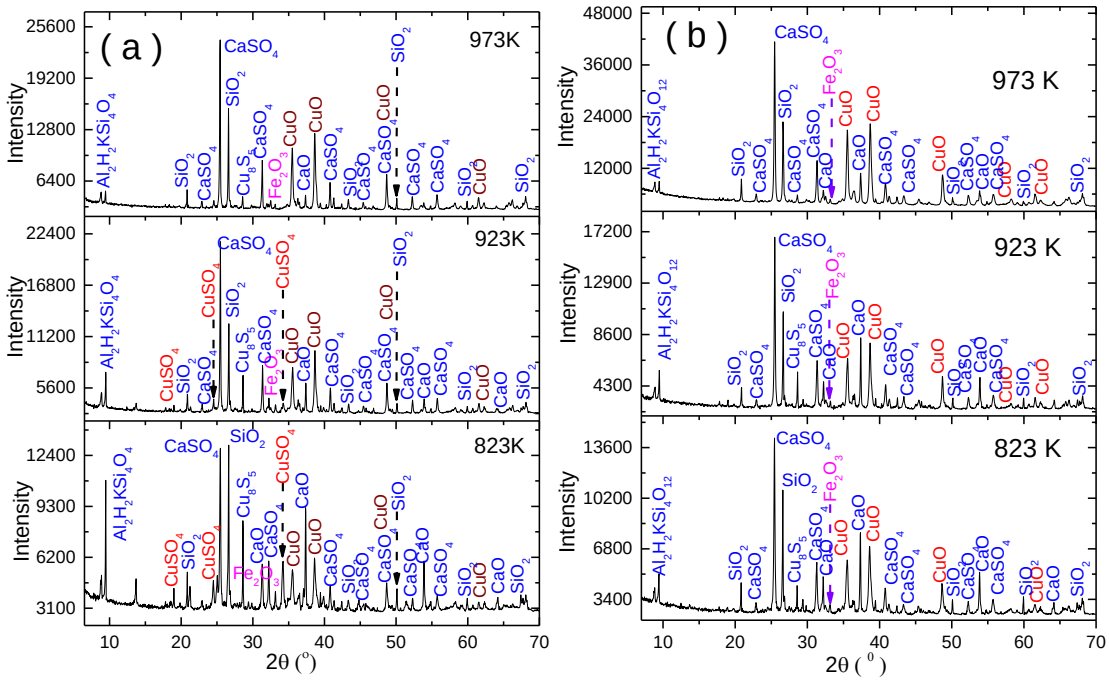

Figure 7.2 – The XRD pattern showing the effect of temperature for lime roasting of Nchanga concentrates, in air (21% O_2) at molar ratio of; (a) MS:CaO = 1:1 and (b) MS:CaO = 1:1.5

MS:CaO = 1:1.5 – The $CuSO_4$ phase was absent in the Nchanga sample even at temperature as low as 823 K (figure 7.2b) which suggests that the SO_2 gas from the oxidation reaction, reacted with CaO in the presence of O_2 gas to form $CaSO_4$. It is for this reason that the XRD peak intensities for $CaSO_4$ are higher at the molar ratio of MS:CaO =1:1.5, at 823 K (figure 7.2b). The concentration of CaO increases with increase in its mole ratio and hence the $CuSO_4$ phase is not expected to be present, as a result of equation 7.6. Based on the XRD results in figures 7.2a and 7.2b and the thermodynamic prediction in equation 7.6, it is necessary to add CaO above its stoichiometric mole ratio, for yielding metal oxide (CuO, Fe_2O_3) and $CaSO_4$ in the Nchanga lime roast calcine.

$$CuSO_4 + CaO = CaSO_4 + CuO; \quad \Delta G_{873K} = -189324 - 0.968T(joules) \qquad 7.6$$

On the other hand, $CuSO_4$ was present in the Nkana and Baluba samples but the XRD peak intensities for $CuSO_4$ were high in the later sample. The presence of the $CuSO_4$ phase in the Nkana and Baluba samples can be due to: (i) sintering because these samples were sintered as discussed above and (ii) mineralogical composition since these samples have more Fe than Cu and have $CuFeS_2$ as the major copper bearing mineral phase (see tables 3.1 – 3.3 and figure 4.1).

MS:CaO = 1:2 – The $CuSO_4$ phase was absent in all the samples at 773 K – 923 K (figure 7.4b). It can be concluded that all SO_2 gas from oxidation of metal sulphides reacted with CaO. However, the % oxidation was low at 823 K (between 35 % and 45 % conversion) than at 773 K or 873 K (figure 7.3). The decreased % oxidation at 823 K shows that the extent of oxidation was lower. The X-ray diffraction results for the samples roasted at 823 K are given in figure 7.4b. It is evident from the XRD patterns in figure 7.4b that CaS, $CuFeS_2$ and Cu_8S_5 are present in the samples roasted at 823 K and this is why the % oxidation was lower (figure 7.3). CaS was only observed in the Nkana and Baluba samples and, these samples are richer in the $CuFeS_2$ and FeS_2 minerals.

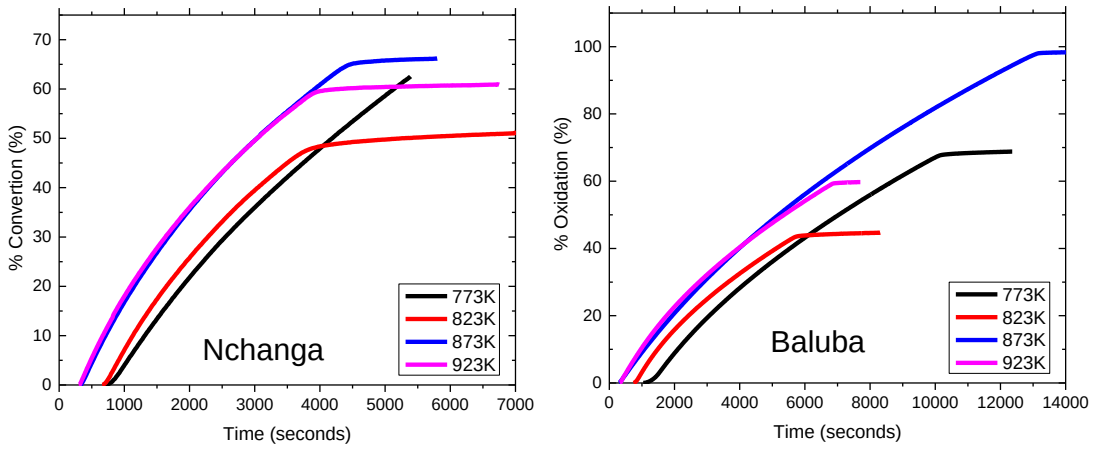

Figure 7.3 – Plot of % Oxidation against time curves for Nchanga and Baluba, lime roasted in air (21% O_2) at molar ratio of MS:CaO = 1:2

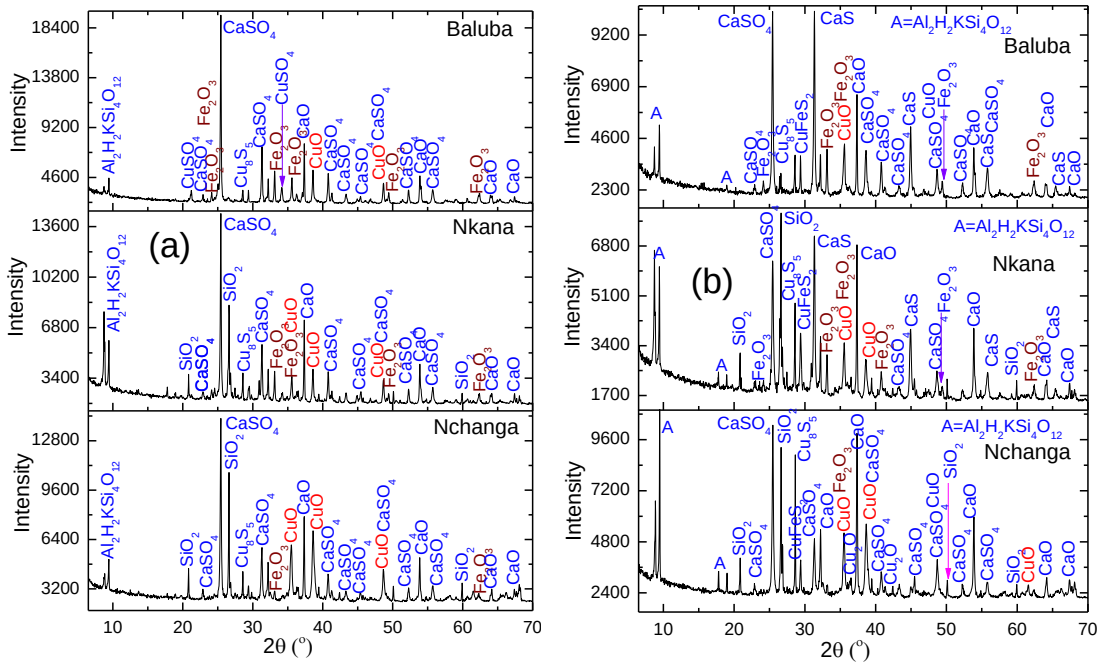

Figure 7.4 – The XRD patterns for the samples lime roasted in air (21% O_2) at 823 K, at molar ratio of; (a) MS:CaO = 1:1.5 and (b) MS:CaO = 1:2

$CaSO_4$ and CaS were also observed by Terry et al. [196] during lime roasting of copper-iron sulphide minerals. However, Terry et al. [196] found that the CaS phase was absent and present in the lime roasted copper sulphides (CuS and $Cu_{1.8}S$) and FeS_2 minerals, respectively. Terry et al. [196] proposed that the existence of CaS and $CaSO_4$, was due to reaction 7.7a [196]. It was suggested that CaS might be partially oxidised to $CaSO_4$, according to equation 7.7b [196]. Although reaction 7.7a is thermodynamically feasible,

it may not be the only mechanism leading to the formation of CaS. This is because, the proportion of CaS is expected to be one third or less, to that of $CaSO_4$ (equation 7.7a) but this is not the case from the XRD patterns in figure 7.4b, because of the high XRD peaks intensities for both $CaSO_4$ and CaS.

$$CaO + SO_2 = 0.75CaSO_4 + 0.25CaS,\ \Delta G^0 = 233340 - 16T\ J\ mol^{-1} \quad 7.7a$$

$$0.5CaS + O_2 = 0.5CaSO_4,\ \Delta G^0 = -455300 + 158T\ J\ mol^{-1} \quad 7.7b$$

The formation of CaS may occur under two conditions: (i) via ion exchange reaction between mineral sulphide and CaO (equation 7.8a) and (ii) under low and high partial pressure of O_2 gas and S_2 gas, respectively.

$$FeS + CaO = FeO + CaS \qquad \Delta G_{823K} = -12.5\ kJ \quad 7.8a$$

$$Cu_2S + CaO = Cu_2O + CaS \qquad \Delta G_{823K} = +87.8\ kJ \quad 7.8b$$

The Gibbs energy change for reaction 7.8a is negative and hence the ion exchange reaction between FeS and CaO can take place. However, the Gibbs energy change for equation 7.8b is positive and this is consistent with the computed Ca-Cu-O-S system by Rosenqvist [41] where it was shown that it is only Cu and Cu_2S that can co-exist with CaS. Based on the thermodynamic prediction in equation 7.8b, it is impossible to produce CaS during lime roasting of Cu_2S without metallisation of copper and this is the reason why Terry et al. [196] did not observed CaS after lime roasting of the Cu-S mineral.

Thermodynamically, CaS is stable under high partial pressure of S_2 gas and a low partial pressure of O_2 gas [28, 41]. The partial pressure of S_2 gas can be high during lime roasting, owing to the thermal decomposition of the S_2 gas from the FeS_2 and $CuFeS_2$ minerals when heated above 773 K [78]. The partial pressure of O_2 gas can be lowered by the rapid oxidation of FeS, since iron oxide is more stable than iron sulphide [14]. With a view of analysing the phases that form in the absence of O_2 gas, the mineral sulphide concentrates were mixed with CaO at molar ratio of MS:CaO = 1:2 and heated under argon atmosphere at 823 K (figure 7.5). It is evident from the XRD results in figure 7.5 that Fe_3O_4, CaS and $CaSO_4$ phases were formed during heating of

the mineral sulphide concentrates in the presence of CaO, under inert (argon) atmosphere. The XRD peak intensities for the Fe_3O_4 and CaS phases were high in the Nkana and Baluba samples because these samples have the highest Fe content in the form of $CuFeS_2$ and FeS_2 minerals. From the results in figure 7.5, it can be concluded that the exchange reaction between FeS and CaO occurs in the absence of O_2 gas at 823 K by yielding Fe_3O_4, CaS and $CaSO_4$ phases.

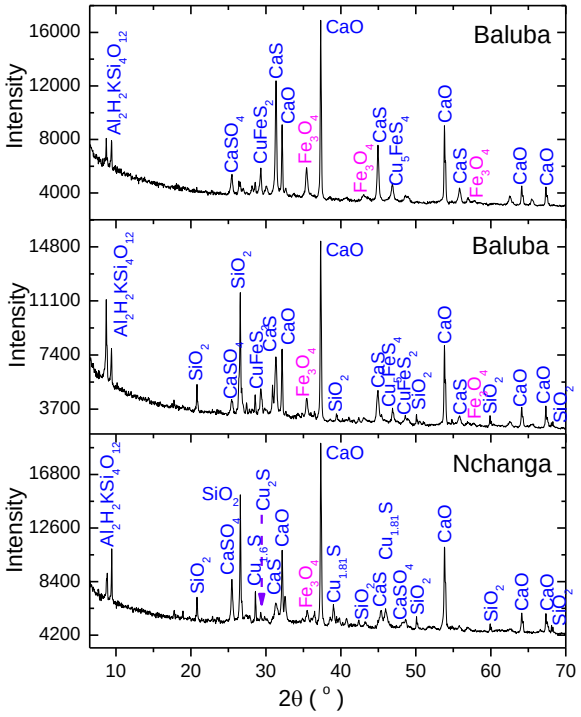

Figure 7.5 - XRD patterns for the mineral sulphide concentrates heated under argon atmosphere at 823 K, molar ratio of MS:CaO = 1:2. Argon flow rate = 0.6 litre min^{-1}

The formation of CaS and $CaSO_4$ can take place when the rate of thermal decomposition of S_2 gas from the mineral sulphides is equal to, or higher than the rate of oxidation reaction as shown in equation 7.9a, where the decomposed S_2 gas can react with O_2 and CaO. In addition, the formation of CaS can occur at low concentration of O_2 gas as shown in equation 7.9b, where 6 moles of CaS are produced from 6 moles of FeS, per mole of O_2 gas. As shown in equations 7.9a and 7.9b, the formation of CaS under O_2 gas atmosphere is favoured by the high concentration of CaO, which is why it was observed at the molar ratio of MS:CaO = 1:2. Based on the thermodynamic prediction in equations 7.8b, 7.9a and 7.9b, it is unsurprising that the XRD peak intensities for CaS are very low in the Nchanga sample, which has low Fe-S minerals.

$$S_2(g) + 2CaO + O_2(g) = CaS + CaSO_4, \quad \Delta G_{823K} = -489kJ \qquad 7.9a$$

$$6FeS + 6CaO + O_2(g) = 2Fe_3O_4 + 6CaS, \quad \Delta G_{823K} = -502kJ \qquad 7.9b$$

From the experimental results in figure 7.5 and the thermodynamic predictions in equations 7.8a, 7.9a and 7.9b, it can be concluded that the presence of CaS is due to the ion exchange reaction between CaO and Fe-S (see equation 7.8a) and/or reaction between CaO and S_2/O_2 gases (see equations 7.7a and 7.9a).

The decreased % oxidation and hence the presence of metal sulphides (Cu_8S_5 and $CuFeS_2$) in all samples at 823 K, shows that the oxidation reactions were incomplete. It can be suggested that the incomplete oxidation of the metal sulphides is as a result of formation of the metal oxysulphate liquid phase in the samples which decreases the transport of O_2 gas. However, the metal oxysulphate liquid phase may disappear at high temperature due to loss of SO_2 [41] and this could be the reason for the increased % oxidation at 873 K (figure 7.3). A molten phase containing CuO and $CuO{\cdot}CuSO_4$ has been reported during roasting of chalcocite (Cu_2S), above 773 K [199].

7.1.2 Effect of sample size and height

As discussed above, the samples were not fully reacted at the bottom due to presence of the Cu_8S_5 phase. It was therefore important to analysis the effect of sample size and height. Residual copper sulphide (Cu_8S_5) was present for the 3 g roasted samples (figure 7.6a) but there was no evidence of mineral sulphide at sample size of 2 g (figures 7.6b), in a 1.5 mm diameter cylindrical crucible. The heights of the 2 g and 3 g samples were about 13 mm and 20 mm, respectively. The roasted 2 g samples had uniform colour because the reaction was complete whereas the 3 g sample had a greyish colour at the bottom as a result of incomplete oxidation. The 3 g sample did not fully react at the bottom since the sample height increases with increase in the sample size. The increase in sample height decreases the diffusion of O_2 gas to the bottom of sample because of the sintering of the reacted top sample. Nevertheless, complete oxidation was achieved when 8.5 g samples were packed to a height of 5 mm in the rectangular alumina crucibles. Oxygen gas was able to diffuse to the bottom of the crucible when the

samples were packed to heights of 5 mm, in the rectangular alumina crucibles and oxidation was thus complete.

In summary, the size of the sample is not necessary for achieving complete oxidation. What matters is the height of sample. The height of the sample should not be too high in order to allow diffusion of the O_2 gas to the bottom of the sample.

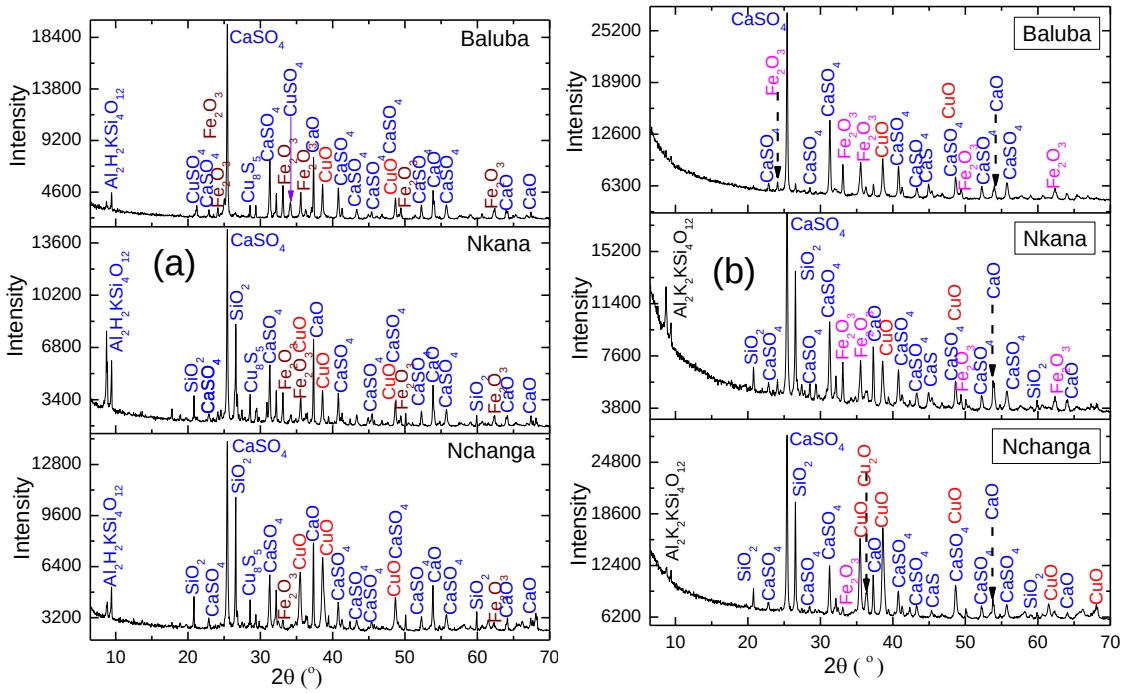

Figure 7.6 – The XRD patterns for the lime roasted samples in air (21% O_2) at 873 K, molar ratio of MS:CaO = 1:1.5, showing the effect of sample size; (a) 3 g sample and (b) 2 g sample

7.1.3 SEM analysis

Elemental maps for the roasted Nchanga sample are shown in figure 7.7. A rim of iron oxide (Fe_2O_3) surrounds CuO and this might have resulted from the roasting of $CuFeS_2$ mineral particle. This is because $CuFeS_2$ and Cu_5FeS_4 are the only Cu-Fe mineral sulphides but the former has the same atomic % of Cu and Fe, which appears to be the case from the maps of Fe and Cu in figure 7.7. The presence of Fe_2O_3 on the periphery is due to counter diffusion of the ions of iron and copper to the periphery and centre, respectively. The counter diffusion of iron and copper ions is as a result of the higher stability of iron oxide than copper oxide, known as kernel roasting [85]. SEM analysis of the partially reacted samples showed a Cu-S rich core and Fe-O on the periphery

(figure 7.7) indicating that there was preferential oxidation of FeS at the start of the reaction. Although not shown, a rim of Fe-O was found on the periphery, surrounding the core of Co-O for the reduced Co-Fe-S mineral particles, due to the higher stability of Fe-O than CoO.

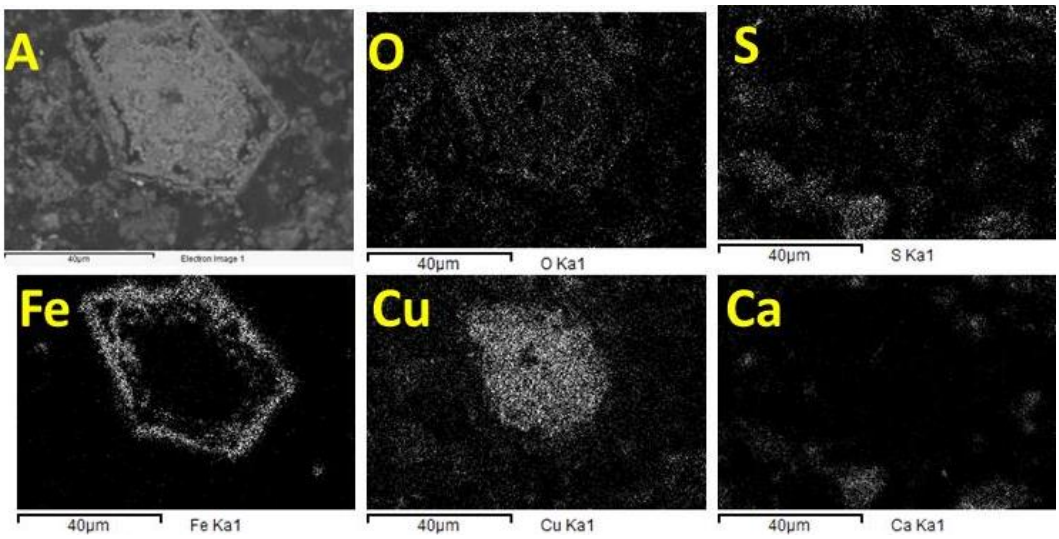

Figure 7.7- SEM elemental mapping for Nchanga, the sample was lime-roasted in air (21% O_2) at 873 K, molar ratio of MS:CaO = 1:1.5, A is the analysed sample area

The initial mineral sulphide particles had uniform textures but two textures [200] of Fe_2O_3 were observed in the roasted FeS_2 particles as shown in figure 7.8. The SEM-EDX semi-quantitative point analysis showed similar compositions in both areas (A and B). Therefore, the difference in textures between area A and B is because of the change in oxidation/reaction mechanisms between the periphery and core of the particle. Since the oxidation of metal sulphides starts from the surface of the particles where the concentration of oxygen gas is high, a dense layer of Fe_2O_3 can form at the surface of the partially reacted samples [28]. However, the layer of Fe-O on the periphery may retard the diffusion of O_2 gas and thus leading the thermal decomposition of the inner FeS_2 (at the core), similar to thermal decomposition of FeS_2 under inert atmosphere (equation 7.10a) [78, 88]. The decomposed S_2 gas reacts with O_2 gas, as the former diffuses through the metal oxide layer, to form SO_2 (equation 7.10b). The O_2 gas will be able to reach the surface of FeS, in the absence of S_2 gas or when thermal decomposition is complete and, oxidation of FeS is expected to occur via equation 7.10c.

$$FeS_2 = FeS + 0.5S_2(g) \quad 7.10a$$

$$S_2(g) + 2O_2(g) = 2SO_2(g) \quad 7.10b$$

$$FeS + 1.75O_2(g) = 0.5Fe_2O_3 + SO_2(g) \quad 7.10c$$

The SEM image in figure 7.8 is similar to the one obtained by Dunn and De [201], after heating FeS_2 in air from 303 K to 969 K [201] and it was also proposed that the two different textures can be formed via formation of metal sulphate, followed by decomposition of metal sulphate to metal oxide [200, 202]. Nonetheless, this mechanism may not occur under isothermal reaction at 873 K because the Gibbs energy change is more negative for equation 7.11a than for equations 7.11b and 7.11c, per mole of O_2 gas.

$$\frac{4}{11}FeS_2 + O_2(g) = \frac{2}{11}Fe_2O_3 + \frac{8}{11}SO_2(g), \quad \Delta G_{873K} = -278kJ \quad 7.11a$$

$$\frac{2}{7}FeS_2 + O_2(g) = \frac{1}{7}Fe_2(SO_4)_3 + \frac{1}{7}SO_2(g), \quad \Delta G_{873K} = -240kJ \quad 7.11b$$

$$\frac{1}{3}FeS_2 + O_2(g) = \frac{1}{3}FeSO_4 + \frac{1}{3}SO_2(g), \quad \Delta G_{873K} = -265kJ \quad 7.11c$$

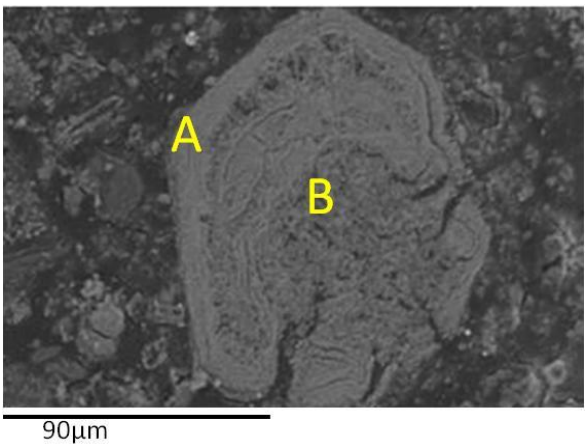

Figure 7.8 – Backscattered SEM image for Nchanga showing different texture in the roasted FeS_2 mineral particle at 873 K (MS:CaO = 1:1.5)

Because of the low % oxidation, detailed scanning electron microscopy analysis was carried out for the samples roasted at 823 K, molar ratio of MS:CaO = 1:2 and the results are presented in figure 7.9. It can be observed from figure 7.9a that some reacted particles were molten in the Baluba sample due to the presence of larger pores at the centre of the particles as observed by Hansen [200]. The pores were formed as a result of evolution of the S_2/SO_2 gases from the molten particles. Elemental mapping for figure 7.9a showed that the pores were formed from the Cu-Fe-S mineral particles. It appears that the SO_2 gas was evolved from the rich Cu-O-S liquid phase at the center, because of the presence of the Fe-O phase at the periphery of the particles.

The outer layer of Fe_2O_3 for the partially oxidised FeS_2 particles has a texture of FeS (figure 7.9b) which shows that oxidation occurred after thermal decomposition of FeS_2 to FeS [200]. The decomposition of FeS_2 to FeS confirms that the oxidation reaction was much slower at molar ratio of MS:CaO = 1:2 at 823 K which could be due to presence of liquid phase. A Cu-Ca-O-S liquid phase can also be observed from the reacted Cu-S mineral particles (images 7.9c – 7.9f), in the Nchanga sample. The Ca-Cu-O-S liquid phase might have been formed as a result of the reaction between $CuSO_4$ and CaO.

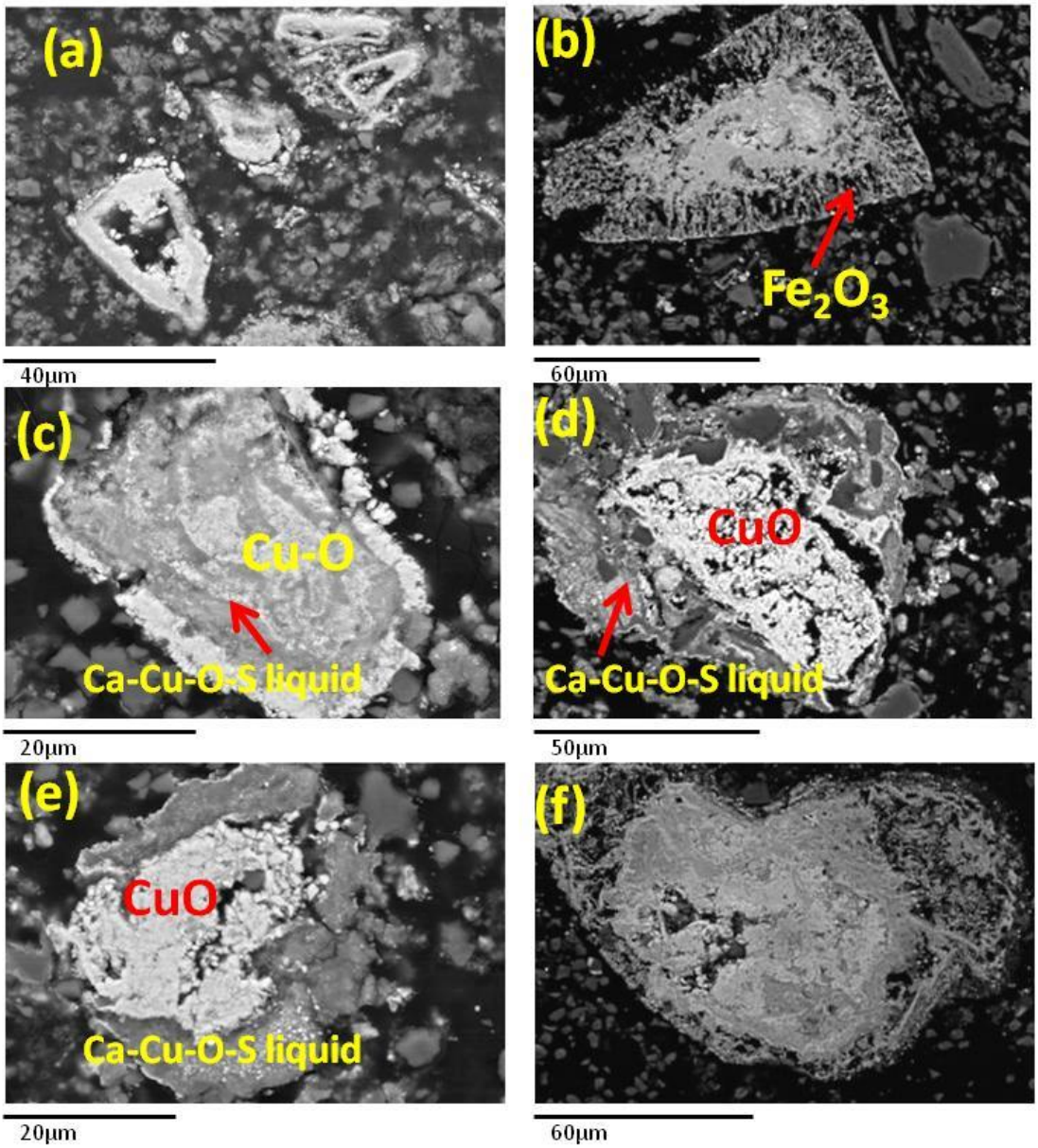

Figure 7.9 – Backscattered SEM images for the samples that were lime roasted in air (21% O_2) at 823 K, molar ratio of MS:CaO = 1:2; (a) and (b) Baluba and (c) – (f) Nchanga

7.1. 4 Reaction kinetics

The experimental data were fitted into the diffusion (G.B) and interface models as shown in figures 7.10a and 7.10b. It can be observed from figures 7.10a and 7.10b that the chemical reaction (interface reaction) is the best fitting model for the lime roasting of the mineral sulphide concentrates and, a similar analysis was made by Terry [196], based on the activation energy, although by using the linear reaction model.

Intermediate phases ($CuSO_4$, $CuO{\cdot}CuSO_4$) were obtained in the reacted samples for MS:CaO = 1:1 but the intermediate phases were not observed at higher molar ratio of CaO (MS:CaO = 1:1.5) and, this is a characteristic of chemically controlled reactions [155]. The presence of the intermediate phases ($CuSO_4$, $CuO{\cdot}CuSO_4$) suggests that the lime roast reactions were controlled by interface reaction mechanism at the CaO particles (equation 7.11) even though the reaction mechanism may be controlled by the diffusion or mixed reaction mechanims in the final stages

$$CaO + SO_2(g) + O_2(g) = CaSO_4 \qquad 7.12$$

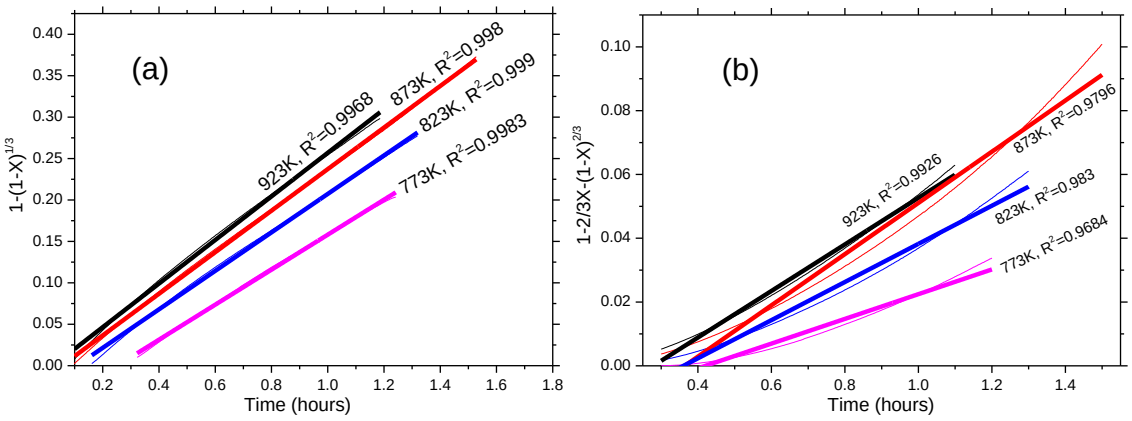

Figure 7.10 - Plot of; (a) interface model and (b) Ginstling–Brounstein, as a function time at various temperatures, molar ratio of MS:CaO = 1:1.5

The plots of lnk versus 1/T line for the three samples are shown in figure 7.11, and the calculated values of the overall activation energies have been inserted in each line. The activation energies are similar for the Nchanga and Nkana sample but slightly smaller than for Baluba sample, probably due to higher content of gangue minerals in the former samples. The apparent activation energies in figure 7.11 are in very good agreement with the activation energy of 8 - 14 kJ for the sulphation of CaO in the presence of SO_2 and O_2 gases (see equation 7.12), reported by Allen and Hayhurst [203]. The apparent activation energies in figure 7.11 are slightly higher than the activation energy of 6.2 ± 0.9 kJ, for the reaction between CaO and SO_2 under nitrogen atmosphere [173]. Therefore, the activation energy for the lime roasting of the mineral sulphide concentrates is controlled by equation 7.12.

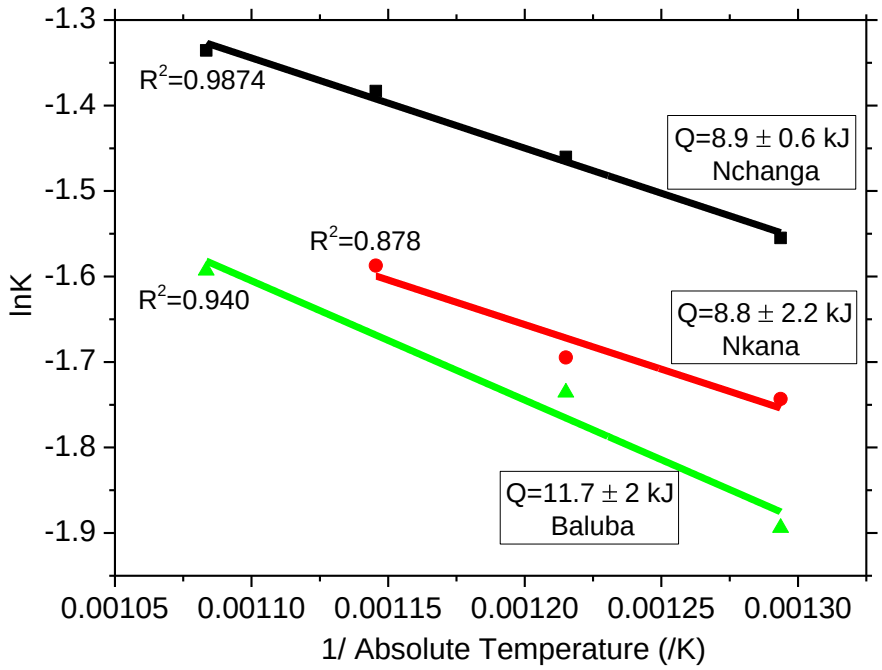

Figure 7.11 - Arrhenius plots, lnk against reciprocal of temperature (1/K) for the derivation of activation energy, using the interface model (MS:CaO = 1:1.5)

7.2 Reduction of CuO, CoO and Fe_2O_3 at 1073 K

It was important to investigate the approximate reaction time for achieving selective metallisation of Cu and Co from the reduction of metal oxides (CuO, CoO, Fe_2O_3 and FeO) at 1073 K. As a result, metal oxides were mixed with carbon black and reduced in the TGA equipment. The plots of the % reduction versus time curves for the reduction of the metal oxides are given in figure 7.12. The carbothermic reduction of CuO was extremely rapid, completing within 5 minutes at 1073 K as shown in figure 7.12. On the other hand, the carbothermic reduction of CoO was completed in about 30 minutes. It is evident from figure 7.12 that only about 25 %R was achieved for the carbothermic reduction of Fe_2O_3. XRD analysis of the samples showed no evidence of unreacted Cu_2O or CoO but Fe_3O_4 was the main phase for the carbothermic reduction of Fe_2O_3. From the TGA results in figure 7.12, it was concluded that it is possible to achieve selective metallisation of Cu and Co by stopping the reaction within an hour at 1073 K.

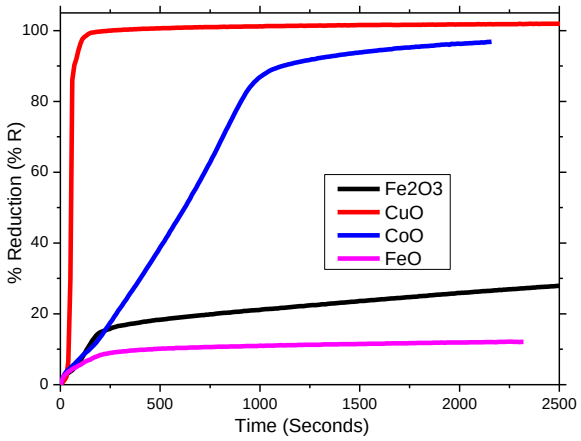

Figure 7.12 – Plots of the % reductions versus time curves for carbothermic reduction of metal oxides with carbon black at 1073 K, for molar ratio of MO:C = 1:2

7.3 Selective metallisation of Cu from the lime roast calcine

The carbothermic reduction of the lime roast calcine was carried out on the fully reacted samples (figure 7.6b), to avoid metallisation of copper via equation 7.13 [11].

$$2Cu_2O + Cu_2S = 6Cu + SO_2(g) \qquad 7.13$$

The XRD pattern for the Nchanga sample which was lime roasted in air at 873 K and carbothermically reduced for 50 minutes at 1073 K is given in figure 7.13a. The major phases in the XRD pattern for the lime roast – reduced sample, were Cu, Fe_3O_4, $CaSO_4$ and SiO_2 and CaO. The phases obtained are consistent with the thermodynamic predictions in figure 2.31 [28], where Cu, Fe_3O_4 and $CaSO_4$ co-exist at 1073 K, at $logPO_2$(atm) between – 7 and -12. In summary, the XRD pattern in figure 7.13a clearly shows that: (i) CuO was reduced to Cu, (ii) Fe_2O_3 was reduced to Fe_3O_4 and (iii) $CaSO_4$ remained stable, during the carbothermic reduction of the lime roast calcine with carbon black.

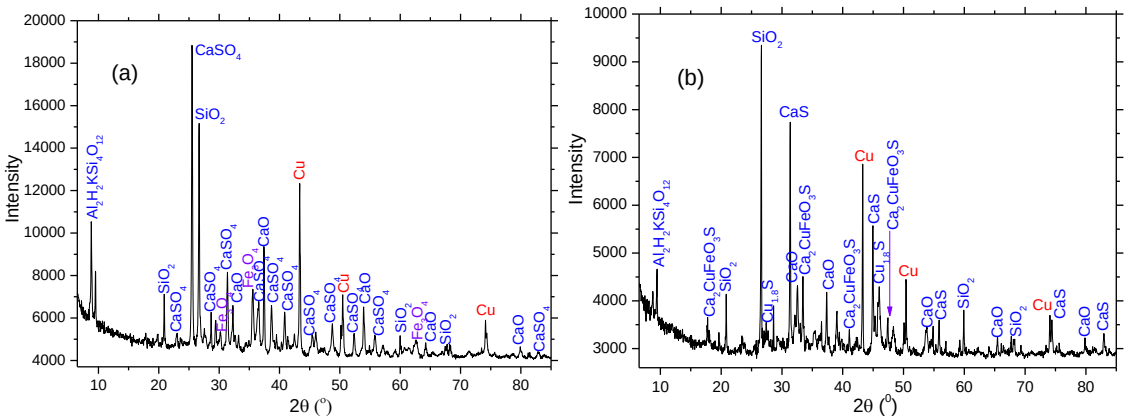

Figure 7.13 - XRD patterns for Nchanga sample, lime roasted in air (21% O_2) at 873 K, molar ratio of MS:CaO = 1:1.5 and carbothermically reduced with carbon black, for 50 minutes at; (a) 1073 K and (b) at 1093 K

SEM images of the reduced samples are shown in figure 7.14 and it can be observed that metallic copper is segregated throughout the sample. The metallic copper particles have various sizes due to the difference in the mineral sulphide particles from the as received samples. Magnetite (Fe_3O_4) can be observed from the SEM images. SEM-EDX semi-quantitative point analyses were carried out on several areas and the purity of copper phase was found to be between 97.5 and 98.2 wt. % Cu as shown in table 7.1. It is worth noting that the purity of copper produced via lime roast – carbothermic reduction process, is comparable to the blister copper (Cu ≈ 98 wt-%) produced via conventional copper smelting - converting processes at about 1473 K [8, 11].

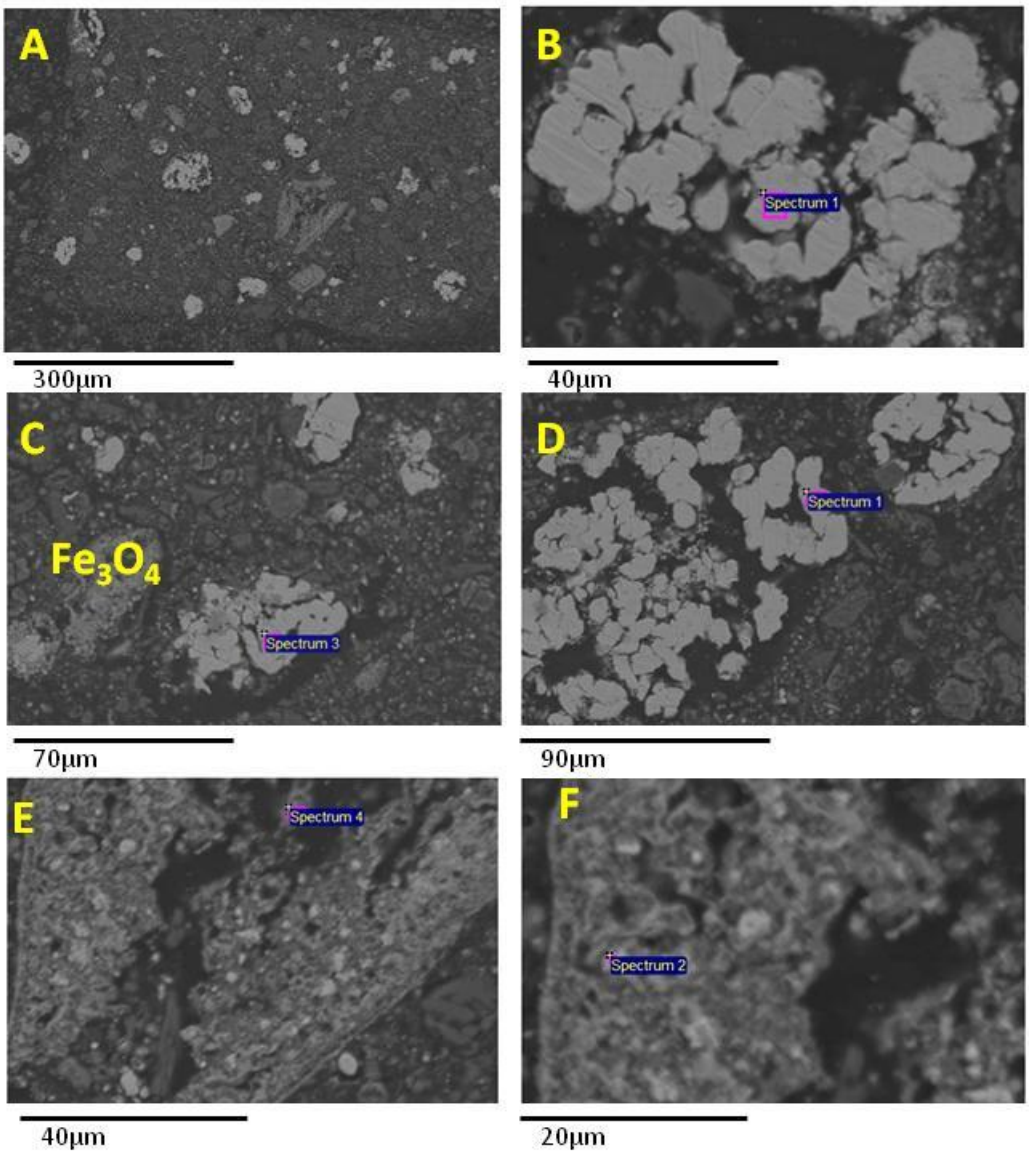

Figure 7.14 – Backscattered SEM images for Nchanga, lime roasted in air (21% O_2) at 873 K, molar ratio of MS:CaO = 1:1.5, followed by carbothermic reduction with carbon black for 50 minutes at 1073 K

Table 7.1 – EDX semi-quantitative analysis (wt. %) taken from figure 7.14

Micrograph and analysed areas	Cu	Co	O	Fe
B-Spectrum 1	98	-	2	-
C-Spectrum 3	98	-	2	-
D - Spectrum 1	97	-	3	-
E- Spectrum 4	12	49	18	18
F- Spectrum 2	53	25	16	5

7.3.1 Effect of reduction temperature

The reduction temperature was found to be a very important parameter for metallisation of copper and retaining of the $CaSO_4$ phase. Cuprous oxide (Cu_2O) and metallic copper were obtained when the lime roasted samples were carbothermically reduced for 1 hour at 1048 K. The presence of Cu_2O and Cu shows that carbothermic reduction was incomplete at 1048 K in the presence of carbon black. It can be observed from the thermodynamic prediction (Cu-Fe-Ca-O-S system) in figure 2.31 that the partial pressure of O_2 gas for the equilibrium between Cu + Cu_2O + $CaSO_4$ and Cu_2O + $CuFeO_2$ phase fields, decreases with a decrease in temperature. This means that for complete metallisation of Cu, the partial pressure of O_2 gas should decrease, significantly with decrease in the reduction temperature. However, the partial pressure of O_2 gas might increase at low reduction temperature since the reactivity of carbon decreases with a decrease in reaction temperature and, this is why the Cu_2O phase was obtained.

On the other hand, metallic copper co-exists with CaS, Cu_2S and Ca_2CuFeO_3S phases for the lime roast calcine when reduced at 1093 K (figure 7.13b). The presence of CaS is because of the reduction calcination of $CaSO_4$ as the reduction temperature was increased. The thermodynamic prediction (Cu-Fe-Ca-O-S system) in figure 2.31 shows that Cu co-exists with CaS and Fe_3O_4 and is in equilibrium with Cu_2S and CaO at very low partial pressure of O_2 gas. The partial pressure of O_2 gas is lower at higher temperature because of the increased reactivity of carbon with temperature [204]. The formation of CaS, CaO and Cu_2S can occur via equations 7.13a – 7.13c. The presence of the Ca_2CuFeO_3S phase is as a result of liquid phase formation between the CaS, Fe_3O_4, CaO and Cu_2S phases as discussed in chapters 5 and 6.

$$CaSO_4 + 4C = CaS = 4CO(g) \qquad 7.14a$$

$$CaSO_4 + C = CaO + SO_2(g) + CO(g) \qquad 7.14b$$

$$Cu_2O + SO_2(g) + C = Cu_2S + CO(g) \qquad 7.14c$$

7.3.2 Effect of metal sulphates in lime roast clacine

Metal sulphides ($CuFeS_2$, Cu_2S etc.) were present after carbothermic reduction of the samples which were lime roasted below 873 K at molar ratio of MS:CaO = 1:1, although the lime roast calcine did not contain these phases. The formation of metal sulphides was due to the presence of $CuSO_4$ in the lime roast calcine and the reactions might have occurred via equations 7.15a – 7.15c.

$$CuSO_4 + CuO + C = 5Cu_2S + 5CO, \quad \Delta G_{1073K} = -710 \text{ kJ} \qquad 7.15a$$

$$4CuSO_4 + 16C = 2Cu_2S + S_2(g) + 16CO(g), \quad \Delta G_{1073K} = -2052 \text{ kJ} \qquad 7.15b$$

$$3Cu + Fe_3O_4 + 3S_2(g) + 4CO(g) = 3CuFeS_2 + 4CO_2(g), \quad \Delta G_{1073K} = -475 \text{ kJ} \qquad 7.15$$

It was necessary to roast the samples at higher roasting temperature (T > 923 K) for molar ratio of MS:CaO = 1:1, because of the formation of metal sulphates below 923 K. In summary, the following parameters are important for avoiding formation of metal sulphides during carbothermic reduction of the lime roast calcine at 1073 K:

i. High roasting temperature (above 923 K) is required for MS:CaO = 1:1 due to formation of metal sulphates at low temperature.

ii. Low roasting temperature (at about 873 K) for MS:CaO = 1:1.5 because metal sulphates are not formed during roasting of Nchanga.

7.3.3 Effect of mineralogical composition

Carbothermic reduction of lime roast calcine yielded metallic copper for the Nchanga sample but metallic copper and copper ferrites were observed in the Nkana and Baluba samples. This is because Cu_5FeS_4 and $CuFeS_2$ are the main copper bearing minerals in the Nkana and Baluba concentrates, whereas Cu_2S/$Cu_{1.6}S$(Cu_8S_5) are major copper bearing minerals in the Nchanga concentrate. As already explained, iron oxide (Fe_2O_3) was found on the periphery, surrounding copper oxide (see figure 7.7) for the roasted Cu_5FeS_4 and $CuFeS_2$ mineral particles. The presence of iron oxide on the periphery of the roasted Cu_5FeS_4 and $CuFeS_2$ mineral particles prevents the direct reduction of Cu-O such that the reduction of Cu-O is possible mainly via diffusion of the intermediate CO

gas through the porous layer of iron oxide. The indirect reduction of the inner copper oxide by the CO gas is practically possible if the reduction of outer Fe_2O_3 to Fe_3O_4/FeO yields high concentration of CO gas. In the case that CO gas does not diffuse through the outer layer of Fe-O, the reaction between Fe-O and Cu-O becomes inevitable at 1073 K [28]. Nonetheless, CuO and Fe_2O_3 appear as separate particles in the Nchanga roasted samples since they originate from separate mineral particles of Cu_2S/$Cu_{1.6}S$ and FeS_2, respectively. The formation of copper ferrite from separate CuO and Fe_2O_3 particles may require higher temperature, above 1073 K [28] or longer reaction time. As a result, the lime roast - reduction process can be more efficient for the mineral sulphides concentrates containing mainly Cu_2S, CuS and FeS_2 minerals such as the Nchanga concentrates. These types of concentrates are common in the Democratic Republic of Congo.

7.3.4 Analysis of cobalt in the reduced lime roast calcine

As stated in chapters 3 and 6, the mineral sulphide concentrates have low cobalt content so that phase analysis of cobalt by XRD analysis was not possible. Cobalt was therefore analysed by the SEM-EDX semi-quantitative analysis. SEM-EDX analysis showed that the cobalt bearing phase had oxygen and copper/iron, as shown in table 7.1. The presence of oxygen in the cobalt bearing phase confirms that a Co-Cu/Fe-O phase was formed during the reduction process. The presence of the Co-Cu/Fe-O phase in table 7.1 agrees broadly with the thermodynamic prediction in figure 7.15 as Co does not co-exist with $CaSO_4$. It can be observed from the thermodynamic prediction in figure 7.15 that Co and Cu can only co-exist with either CaO or CaS. This means that metallisation of Co may occur only when $CaSO_4$ is calcined to CaO or CaS.

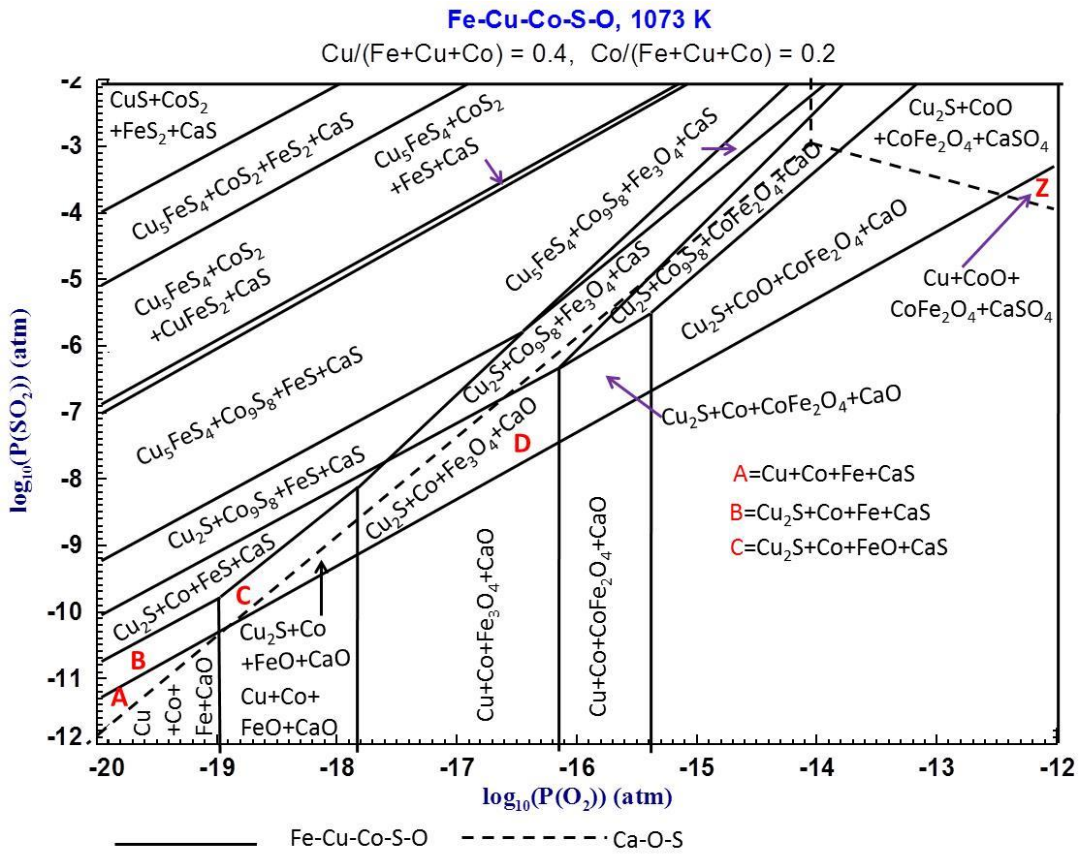

Figure 7.15 – Cu-Co-Fe-Ca-O-S predominance area diagram at 1073 K, computed using FactSage software 6.1 [24]

To investigate the complete metallisation of Cu, Co and Fe, a mixture of 0.8g-Fe_2O_3, 0.6g-CuO, 0.6g-CoO, 0.68g-$CaSO_4$ and 1.1g activated charcoal were heated for 1 hour at 1073 K and the only phases were Cu, Co, Fe and CaS, meaning that metallisation was complete. However, Fe_2O_3 was only reduced to FeO and Fe_3O_4 when the experiment was carried out in the absence of CuO, CoO and $CaSO_4$. It was therefore concluded that metallisation of Fe at 1073 K was catalysed by the reduction of CuO, CoO and $CaSO_4$. To be precise, the metallisation of Co lowers the activity of Fe via formation of Co-Fe alloy while the reduction CuO, CoO and $CaSO_4$ decreases the partial pressure of O_2 gas because of the evolution of CO gas.

7.4 Reduction of lime roast calcine with activated charcoal

For metallisation of Cu, Co, Fe, the lime roast calcine was mixed with 10 wt. % CoO and 1.5 times the stoichiometric mole ratio of activated charcoal (equation 7.16). The

samples were reduced at 1073 K and 1123 K and, the XRD results are presented in figure 7.16.

$$MO + CaSO_4 + 7.5C = M + CaS + 5CO + 2.5C \qquad 7.16$$

It can be observed from the XRD patterns in figure 7.16 that there are no metal oxides (Cu-O, Co-O and Fe-O) and $CaSO_4$ phases, confirming that the reactions occurred according to equation 7.15. In short, metal oxides were reduced to metallic/alloy state and $CaSO_4$ was calcined to CaS during reduction of the lime roast calcine, with activated charcoal. The XRD peaks for Co have shifted to the lower angle at 1123 K because of the increased dissolution of Fe in Co, with increase in temperature. Part of Co dissolved in Fe and the XRD peaks for Fe shifted to the high angle, overlapping with the CaS peaks at 1073 K and 1123 K.

Two important observations can be made from the XRD patterns in figure 7.16; (i) the XRD peak intensities for Cu are slightly higher at 1123 K than at 1073 K, and (ii) the XRD peak intensities for CaO and $Cu_{1.8}S$ are slightly higher at 1073 K than at 1123 K. It is important to note that there was no $Cu_{1.8}S$ in the lime roast calcine (before reduction) and hence this phase was formed during the reduction process. Based on the thermodynamic prediction in figure 7.15, $Cu_{1.8}S$ may only be formed at higher partial pressure of SO_2 gas and this happened, as a result of calcination of part of $CaSO_4$ to CaO and SO_2 phases. The calcination of $CaSO_4$ to CaO and SO_2 gas only occurs under low reactivity of carbon and it is for this reason that the XRD peak intensities for CaO and $Cu_{1.8}S$ are slightly higher at 1073 K than at 1123 K, considering the fact that the reactivity of carbon decreases with increase in temperature. However, it is possible to eliminate the sulphidisation of Cu or calcination of $CaSO_4$ to CaO and SO_2 by increasing the mole ratio of carbon.

As noted in chapter 6, metallisation of Cu and Fe was limited by the exchange (oxidation) and reduction reactions respectively, below 1173 K, during carbothermic reduction of the mineral sulphide concentrates in the presence of CaO. However, this has not been the case by following the lime roast - reduction process with activated charcoal. The low temperature (< 1173 K) lime roast reduction process is a major breakthrough to the carbothermic reduction of Cu-S, Co-S and Fe-S minerals in the presence of CaO. It is necessary to further investigate the separation of the metallic phases (Cu, Co and Fe) from the reduced samples.

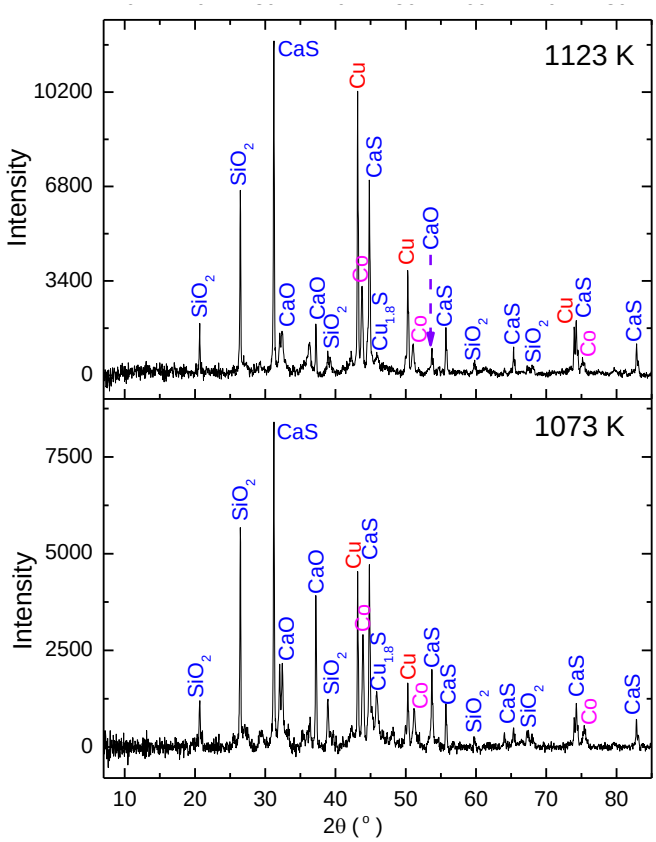

Figure 7.16 – XRD patterns of Nchanga, lime roasted in air at 873 K, enriched with 10 wt. % CoO and reduced with activated charcoal at 50 % excess C.

The SEM images for the samples, lime roasted at 873 K, enriched with 10 wt. % CoO and reduced with activated charcoal at 1073 K and 1123 K are presented in figure 7.17. The metallic phases are segregated throughout the sample and the EDX semi-quantitative compositions are presented in table 7.2. As shown in table 7.2, the purity of the metallic / alloy phases is about 98 wt. %.

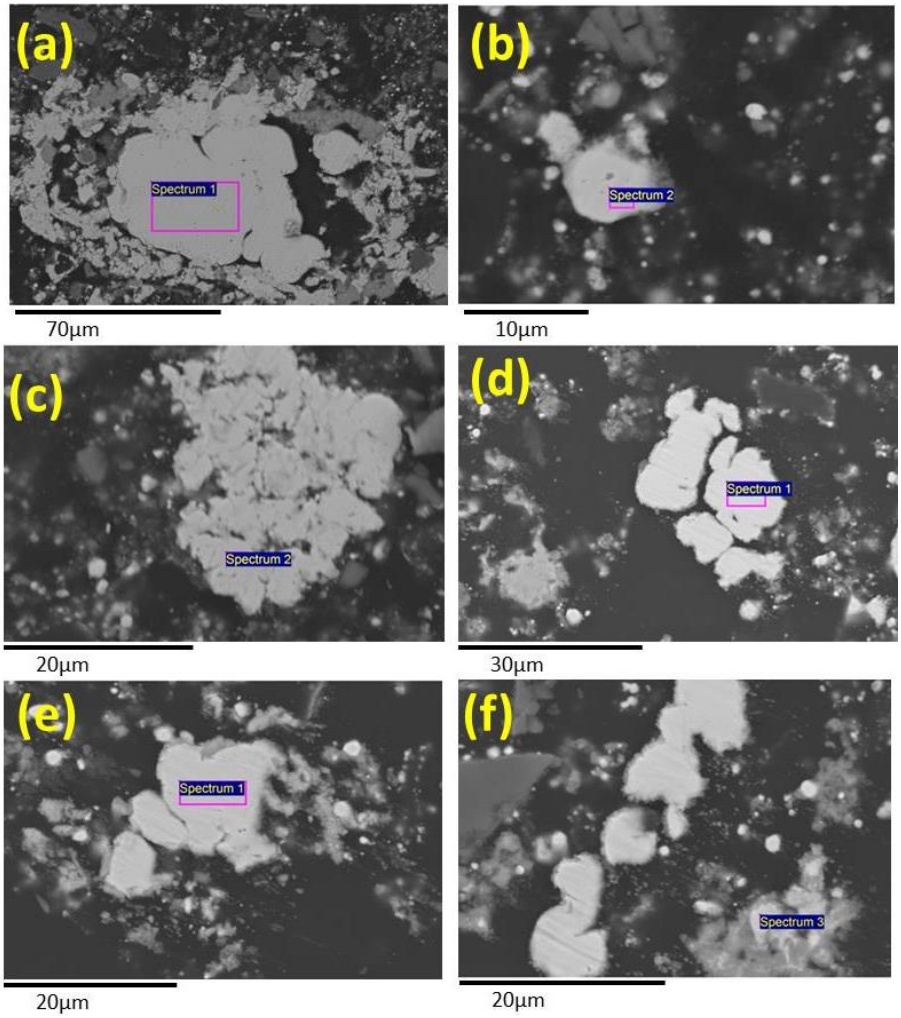

Figure 7.17 – Backscattered SEM images for Nchanga, lime roasted at 873 K, enriched with 10 wt. % CoO and carbothermically reduced with activated charcoal in the TGA equipment; (a) and (b) Nchanga at 1123 K, (c) Nchanga at 1073 K and, (d) – (f) Baluba at 1123 K, the SEM-EDX semi-quantitative analysis are given in table 7.2

Table 7.2 – EDX semi-quantitative analysis (wt. %) taken from figure 7.17

Micrograph and analysed areas	Cu	Co	O	Fe
(a) - Spectrum 1	97.0	0.4	1.3	1.2
(b) - Spectrum 2	9.0	87.5	1.4	2.0
(c) - Spectrum 2	1.8	95.8	1.3	0.7
(d) - Spectrum 1	-	98.3	-	1.7
(e) - Spectrum 1	1.7	15.4	1.2	81.7
(f) - Spectrum 3	1.6	28.7	1.3	62.7

7.5 Sulphur analysis for the reduction with carbon black

The lime roasted calcine and the reduced lime calcine were analysed by the XRF semi-quantitative elemental analysis in order to track the loss of sulphur and, the results are given in table 7.3. The results in table 7.3 show that there was no loss of sulphur during lime roasting of samples at 873 K. On the other hand, there was only about 4 wt. % of sulphur lost during carbothermic reduction of the Nchanga lime roast calcine. It can further be observed from table 7.3 that the loss of sulphur was higher during carbothermic reduction of Nkana and Baluba samples. Nonetheless, it is the Nchanga sample that yielded higher metallic phases than Nkana and Baluba samples, for the carbothermic reduction with carbon black.

Table 7.3 – XRF semi-quantitative elemental analysis (wt. %) of the lime-roasted samples in air (21% O_2) at 873 K and, followed by carbothermic reduction at 1073 K

	Cu	Fe	Co	S	Ca	Si	Al	Na	Mg	K
Nch-roasted	29.9	7.2	0.3	13.8	33.0	9.6	2.4	0.6	1.8	1.5
Nch-roasted and reduced	31.0	7.5	0.3	13.2	31.0	10.3	3.1	0.3	2.0	1.5
Nka-roasted	9.1	14.8	1.0	15.7	34.2	14.0	4.5	0.6	3.2	3.0
Nka-roasted and reduced	10.3	15.2	1.1	13.8	32.9	14.7	4.6	0.5	3.8	3.0
Bal-roasted	15.4	20.2	0.6	20.5	38.2	2.2	0.5	0.7	1.5	0.2
Bal-roasted and reduced	16.9	22.2	0.7	16.4	37.6	2.9	0.7	0.7	1.7	0.3
Error = ±2 wt. %										

7.6 Energy analysis

The theoretical energy requirement for the lime roast process at 873 K, preferential metallisation of copper via carbothermic reduction of the lime roast calcine at 1073 K and complete metallisation of Cu, Co and Fe via carbothermic reduction of the lime roast calcine at 1073 K were estimated using HSC software [39].

7.6.1 Lime-roast process

The following assumptions were made in estimating the theoretical energy requirement for the lime roasting of mineral sulphide concentrates:

- The gangue minerals (SiO_2, Al_2O_3 and MgO) do not react with CaO or form any compounds.
- Complete oxidation of metal sulphides into stable metal oxides i.e. Cu_2S to CuO, FeS_2/ FeS to Fe_2O_3 and CoS to CoO.
- The reactants enter the reaction chamber at 298 K and the products leave the reaction chamber at 873 K.
- Dolomite ($CaMg(CO_3)_2$ remains stable during roasting.
- Moisture is evaporated as H_2O gas.

The energy requirement for the lime roasting of the mineral sulphide concentrates are presented in table 7.4. The total energy in table 7.4 has a negative sign due to the exothermic nature of the lime roast reactions.

Table 7.4 – Energy analysis for the lime roasting of mineral sulphide concentrates, the details for mass balance are given in table A.7.1 – A.7.3

	Heat requirement (kWh) for lime roast of concentrates	Weight of concentrates (kg)	Heat requirement (kWh) per kg of concentrates
Nchanga	-91.2	119.2	-0.8
Nkana	-86.9	114.9	-0.8
Baluba	-214.6	156.2	-1.4

7.6.2 Selective metallisation of Cu from the lime roast calcine

The assumptions made in estimating the theoretical energy requirement for preferential reduction of lime roast calcine at 1073 K were:

- The reactants enter the reaction chamber at 298 K and the products leave the reaction chamber at 1073 K.
- $CaSO_4$ remains stable and Fe_2O_3 is converted to the Fe_3O_4 phase and, Co remains as CoO.
- Complete metallisation of copper.
- The product gas is 100 % CO gas.

- The CO_2 from the carbonates reacts with carbon to form CO gas (equations 7.17).

$$CaMg(CO_3)_2 + 2C = CaO \bullet MgO + 4CO(g) \qquad 7.17$$

The computed energy requirement for the preferential reduction of Cu in the Nchanga sample was calculated as 1.1 kWh per kg of Cu (see table A.7.4 for details). The theoretical energy requirement decreased to 0.47 kWh per kg of Cu if the lime roast calcine enters the reaction chamber at 873 K, assuming that the lime roast calcine is not cooled down to room temperature, after roasting. The theoretical energy of 0.47 kWh per kg of Cu is very comparable to that of conventional copper smelting, which is 0.4 – 0.6 kWh per kg of Cu [12]. Furthermore, the theoretical energy can be decreased by burning off the CO gas from the reduction reaction. The combustion of CO gas from the reduction reaction yields 1.1 kWh per kg of Cu. In summary, the theoretical energy requirement for the preferential metallisation of Cu via lime roast reduction process is comparable or lesser than for the conventional copper smelting. Other than that, the production of copper via lime roast reduction process at 1073 K does not require expensive furnace linings compared to the conventional smelting, above 1473 K.

7.6.3 Complete metallisation of Cu, Co and Fe from the lime roast calcine

The assumptions were similar to section 7.6.2 except that the metallisation of Cu, Co, and Fe was complete and that $CaSO_4$ is reduced to CaS. The theoretical energy requirement for the metallisation of Cu, Co and Fe via lime roast reduction process is presented in table 7.5. The theoretical energy requirement is slightly higher for Nkana and Baluba due to the reduction of dolomoite ($CaMg(CO_3)_2$) as the content of this mineral is highest in these samples. The theoretical energy requirement for Nchanga (2.7 kWh per kg of Cu + Co + Fe) is comparable to the value of 2.8 kWh per kg of Cu + Co + Fe, for smelting of slag at 1923 K [194]. As stated above, it is highly advantageous to recover copper and cobalt from the mineral sulphide concentrates via lime roast reduction process at 1073 K because there is less wearing of refractory material, compared to conventional copper smelting at about 1473 K and smelting of slag at 1923 K. In short, the operational costs are much lower for the lime roast – reduction process. The energy given off by burning the CO gas from the reduction of the lime roast calcine is given in table 7.6. It can be observed from table 7.6 that the

energy given off from burning of CO gas is 1.4 – 1.8 times higher than that, needed for the reduction of the lime roast calcine. The net heat required for the carbothermic reduction of the lime roast calcine and burning of the CO gas in O_2 gas are given in table 7.7. The net heat requirement in table 7.7 shows that no heat is required by utilizing the heat from burning of the CO gas.

Table 7.5 – Analysis of heat requirement for carbothermic reduction of lime roast calcine at 1073 K, using HSC software 5.1 [39], the details for mass balance are given in table A.7.5 – A.7.7

	Heat requirement (kWh) for carbothermic reduction of concentrates	Weight of Cu + Co + Fe (Kg) produced from carbothermic reduction	Heat requirement (kWh) per kg of metallic phases (Cu + Co + Fe)
Nchanga	108.8	39.9	2.7
Nkana	119.8	21.1	5.7
Baluba	234.6	47.8	4.9

Table 7.6 – Heat (kWh) given out for burning of CO gas from carbothermic reduction of lime roast calcine, with O_2 gas, estimated using HSC software 5.1 [39]

Nchanga	-180.0
Nkana	-170.5
Baluba	-373.6

Table 7.7 – Overall heat (kWh) required for the carbothernic reduction of lime roast calcine and burning of CO gas with O_2 gas, estimated using HSC software 5.1 [39]

	Net heat required based on tables 7.5 and 7.6	Net heat requirement per kg of metallic phases (Cu+Co+Fe)
Nchanga	-71.2	-1.8
Nkana	-50.7	-2.4
Baluba	-139.0	-2.9

8.0 Treatment of Cu-Co slag

8.1 Introduction

As discussed in chapters 1 and 2, copper smelting and converting slag are the major source of Cu and Co and hence it was necessary to investigate the recovery of metallic values (Cu, Co and Fe) from slag. The Cu–Co slag synthesised in the laboratory by melting up the mixture of metal oxides (CuO, CoO and Fe_2O_3), CaO, Al_2O_3 and SiO_2 (see chapter 3). The recovery of Cu, Co and Fe from slag was carried out via: (i) carbothermic reduction with carbon black and activated charcoal in order to obtain metallic/alloy phases, (ii) sulphidisation in the presence of $CaSO_4$ and graphite or activated charcoal so as to recover Cu, Co and Fe in the sulphide or matte form and, (iii) sulphidisation in the presence of CaS in order to obtain matte phase and calcium silicates ($CaSiO_3$ and Ca_2SiO_4). The reaction kinetics and thermodynamics for the carbothermic reduction of slag and sulphidisation of slag in the presence of $CaSO_4$ are discussed in this chapter.

8.2 Phase analysis of Cu-Co synthetic slag

The X-ray powder diffraction pattern for the synthetic slag is shown in figure 8.1 and it is evident that the only crystalline phases are $Co_{0.62}Fe_{2.38}O_4$ and SiO_2. There are no peaks for Ca and Al containing phase(s) in the XRD pattern and this can be due to formation of amorphous glassy phase [205]. The presence of amorphous phase is evident as there is a broad hump for 2θ between 20 º and 34º [206].

The backscattered SEM images of the synthetic slag are shown in figures 8.2a and 8.2b and it can be observed that there are three phases in the synthetic slag. The three phases in figures 8.2a and 8.2b were analysed by SEM-EDX semi-quantitative analysis and the results are given in table 8.1. As shown in table 8.1 the $Co_{0.68}Fe_{2.38}O_4$ crystals contain up to 3.6 wt. % Cu, which might be as a result of ionic substitution between the Cu^{2+} (0.73 Å) and Co^{2+} (0.74 Å) ions [107]. The $Co_{0.68}Fe_{2.38}O_4$ phase occurs as smaller euhedral to subheudral crystals and this texture suggests that, the phase was crystallised earlier, during slow cooling of the melt [205, 207, 208]. The glassy phase contains almost all the elements Si, Ca, Cu, Fe, Al and Co in the decreasing order. Ideally, the glassy phase should contain mainly silicon, calcium, iron

and aluminium [205] but it also hosts all elements that fail to enter or form crystalline phases [205, 208].

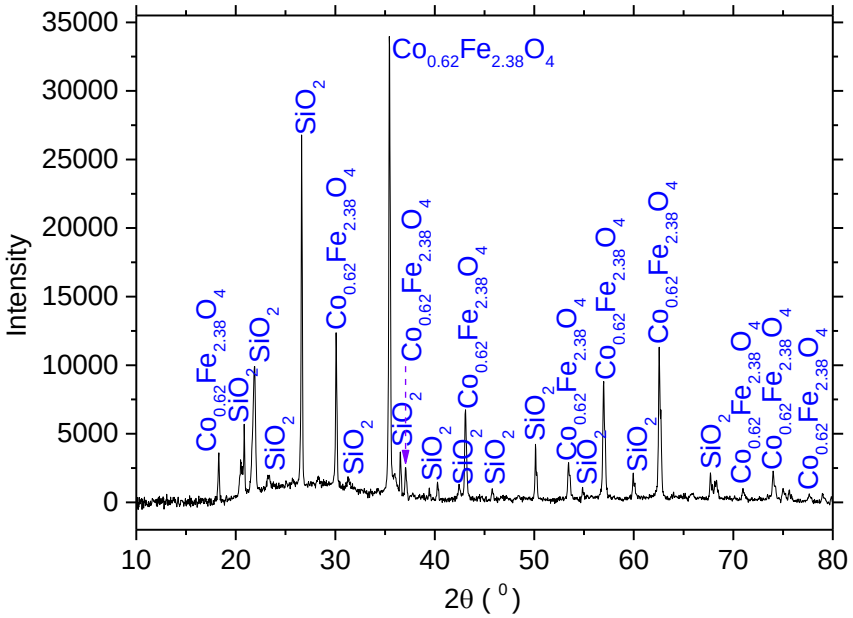

Figure 8.1 – XRD pattern for slag, synthesised in air (21 % O_2) at 1523 K

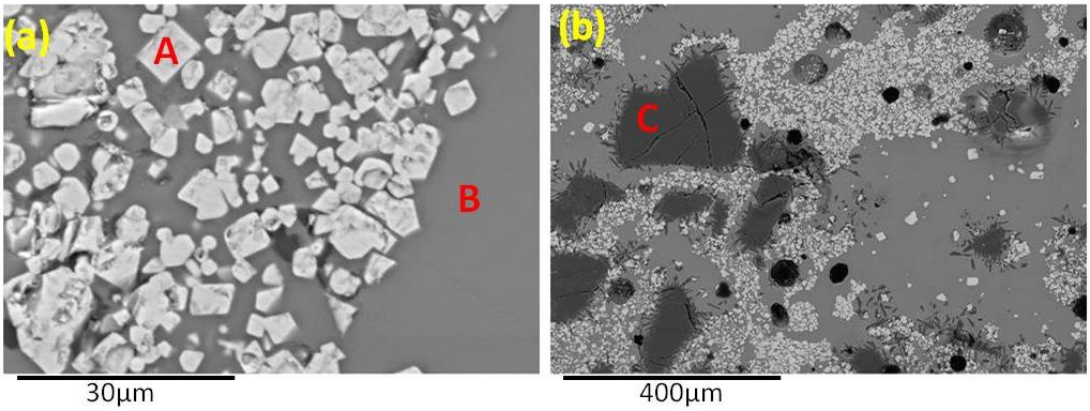

Figure 8.2 – Backscattered SEM images for the slag, synthesised in air (21 % O_2) at 1523 K, the composition of areas A, B and C are given in table 8.1

Table 8.1 - EDX semi-quantitative analysis (wt. %) of areas A, B and C from figures 8.2a and 8.2b

Area	Cu	Fe	Co	Si	Ca	Al	O
A	3.6	52.8	13.8	-	-	0.8	28.7
B	10.3	6.4	1.9	23.1	11.6	4.2	42.5
C	-	-	-	46.4	-	-	53.6

8.3 Carbothermic reduction of slag

Metal oxides are commonly reduced to metallic state via carbothermic reduction [10, 15, 28] and since a majority of Cu and Co in the copper smelting and converting slag, are in the oxide form [3, 20], it was necessary to carry out carbothermic reduction of the slag. The carbothermic reduction of the slag was carried out in the temperature range of 1173 K – 1323 K, considering the fact that the reduction of Fe-O is extremely slow below 1173 K [15].

The plots of % reduction versus time curves for the carbothermic reduction of slag with carbon black and activated charcoal are shown in figures 8.3a and 8.3b, respectively. It is evident from figure 8.3a (with carbon black) that the extent of reduction/metallisation is less sensitive to the reduction temperature, between 1173 K and 1273 K. For example, the increase in % reduction was only about 5 %R, from 1173 K to 1223 K, after 1.5 hours. However, the % reduction increased by about 35 %R in 1.5 hours as the reduction temperature was increased from 1273 K to 1323 K. Even though the % reduction increased as the reduction temperature was raised to 1323 K, metallisation was incomplete (figure 8.3a) and hence it can be concluded that the carbothermic reduction of slag with carbon black requires higher temperature (T > 1323 K).

The extent of reduction/metallisation was higher for the carbothermic reduction of slag with activated charcoal as shown in figure 8.3b. Furthermore, from this figure, it is apparent that the carbothermic reduction of slag with activated charcoal is more sensitive to the reduction temperature than that observed with carbon black. The apparent sensitivity to the reduction temperature may be deduced from the apparent 93 %R (figure 8.3b) achieved in 1.5 hours at 1323 K. This comparative observation in figures 8.3a and 8.3b between carbon black and activated charcoal, respectively, suggests that activated charcoal is a better reducing agent than carbon black.

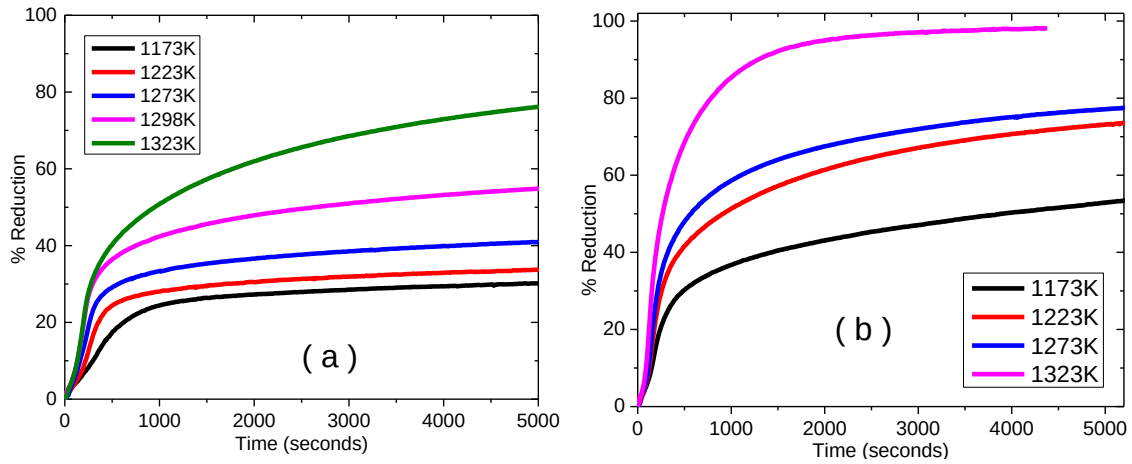

Figure 8.3 – Reduction of slag in the TGA equipment at molar ratio of MO:C = 1:3; (a) with carbon black and (b) with activated charcoal, argon flow rate = 0.6 litre min^{-1}

The XRD patterns for the slag samples that were reduced with carbon black and activated charcoal are shown in figures 8.4a and 8.4b, respectively. Similar phases were obtained at 1173 K and 1223 K in figure 8.4a (with carbon black) and this is in good agreement with the TGA results in figure 8.3a, as the %reduction only increased by about 5 %R when the reduction temperature was increased from 1173 K to 1223 K. The XRD results in figure 8.4a show that the reduction of Cu-O was higher than that of Co-O and Fe-O at 1173 K. In other ways, there was preferential reduction of Cu-oxide at 1173 K with carbon black and this is due to the fact the reduction of Cu-O oxide occurs at relatively higher partial pressure of O_2 gas than the reduction of Fe-O [24, 39].

As discussed above and shown from the TGA results in figure 8.3b, the extent of reduction was higher for the carbothermic reduction of slag with activated charcoal and this is why the XRD peak intensities for the metallic/alloy phases (Cu and Co-Fe) are high in figure 8.4b. There are no peaks for Co in the XRD patterns in figure 8.4b due to the dissolution of Co in Fe [209, 210].

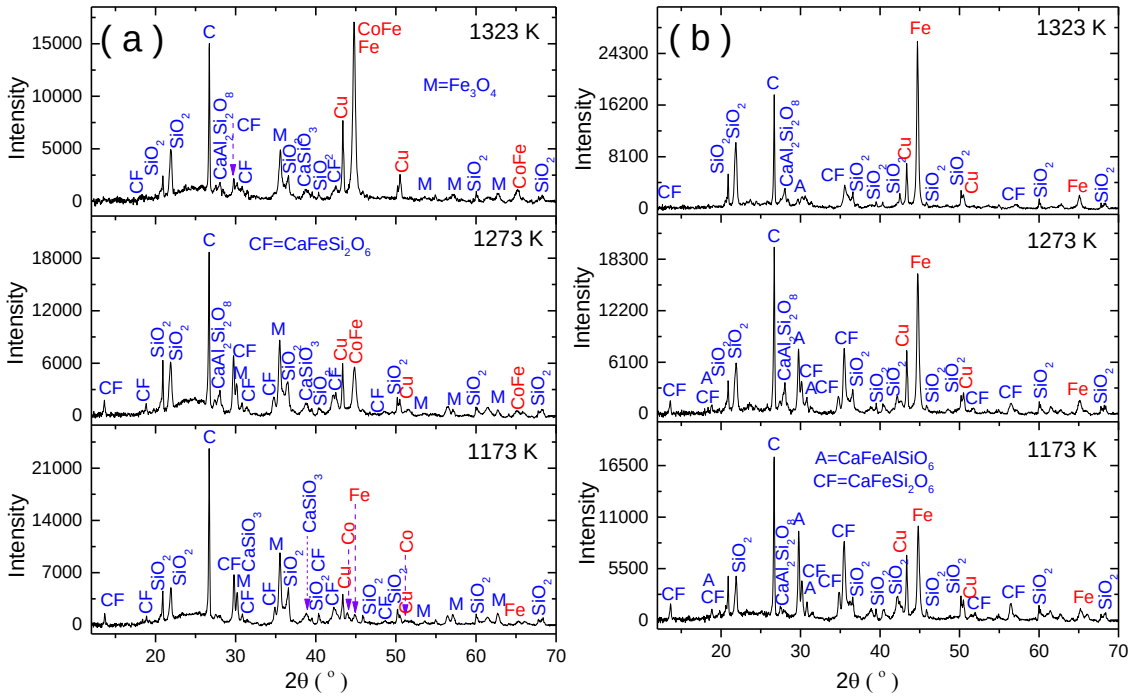

Figure 8.4 – XRD patterns after reduction of slag at molar ratio of MO:C = 1:3, with; (a) carbon black and (b) activated charcoal. Argon flow rate = 0.6 litre min^{-1}

8.3.1 Reaction mechanism for the carbothermic reduction of slag

As shown from the SEM images in figure 8.2, the $Co_{0.62}Fe_{2.38}O_4$ crystals are enclosed in the glassy phase and hence the reduction of metal oxides may occur via diffusion of cations, anions and gases (CO and CO_2 gas), due to lack of contact between the metal oxides in the slag and solid carbon. The reduction reactions may involve the following mechanisms:

(i) Diffusion of the oxygen (O^{2-}) and metal (M^{2+}) ions from the metal oxide (MO) in the slag, to the slag/carbon interface, followed by adsorption of the O^{2-} ions on the carbon surface. The overall rate of reaction may be controlled by the diffusion of the O^{2-} and metal (M^{2+}) ions through the slag matrix and/or gasification of carbon.

(ii) Diffusion of carbon or the intermediate CO gas through the slag matrix so that the metallic phase is formed within the slag phase.

The SEM images for the slag samples which were reduced with carbon black and activated charcoal are shown in figures 8.5a - 8.5d. The metallic phases are mainly found at the periphery of the particles and partly within the slag phase. The metallic phases at the periphery of the particles were formed via diffusion of the metallic ions

(cations) and oxygen ions (anions) from the slag phase. As a result, the overall reactions leading to the formation of metallic phase at the slag particle periphery may be represented by equations 8.1a – 8.1c. The CO gas from equation 8.1b may diffuse into the slag phase via cracks, react with the O^{2-} ions (equation 8.1d) and cause metallisation in the slag phase via equation 8.1c. The diffusion of the CO and CO_2 gases might have occurred through the cracks since the partially reacted samples had several cracks.

$$MO = M^{2+} + O^{2-} \text{ in the slag phase} \qquad 8.1a$$

$$C + O^{2-} = CO(g) + 2e \text{, at slag/carbon interface} \qquad 8.1b$$

$$M^{2+} + 2e = M \text{, at the slag particle periphery or cracks} \qquad 8.1c$$

$$CO(g) + O^{2-} = CO_2(g) + 2e \text{, at the slag particle surface or cracks} \qquad 8.1d$$

The $Co_{0.62}Fe_{2.38}O_4$ crystals [208] are still present after carbothermic reduction at 1173 K, with carbon black or activated charcoal due to incomplete reduction. In addition to the $Co_{0.62}Fe_{2.38}O_4$ phase, the Fe rich (≈10 - 13 wt. % Fe) slag phase in the form of laths and dendrites and, the amorphous glass phase (≈ 3 wt.% Fe) are present at 1173 K.

A significant proportion of Fe is still dissolved in the slag phase at 1323 K, for the reduction with carbon black (figure 8.5b) as a result of incomplete metallisation. The content of Fe in the slag phase in figure 8.5b is between 7 wt.% Fe and 22 wt.% Fe. On the other hand, there is high fraction of the metallic phases at 1323 K with activated charcoal (figure 6d) and hence the content of Fe in the slag phase is lower (< 5 wt. % Fe). It is evident from the SEM images in figures 8.5b and 8.5d that Co and Cu are absent in the slag phase at 1323 K, for reduction with carbon black and activated charcoal. In short, Fe was the only metallic phase that was dissolved in the slag phase at 1323 K and this is due to the fact that metallisation of Fe requires lower partial pressure of O_2 than Cu and Co [24, 39]. Furthermore, the activity of Fe in silicate slag is lower than that of Cu and Co [24].

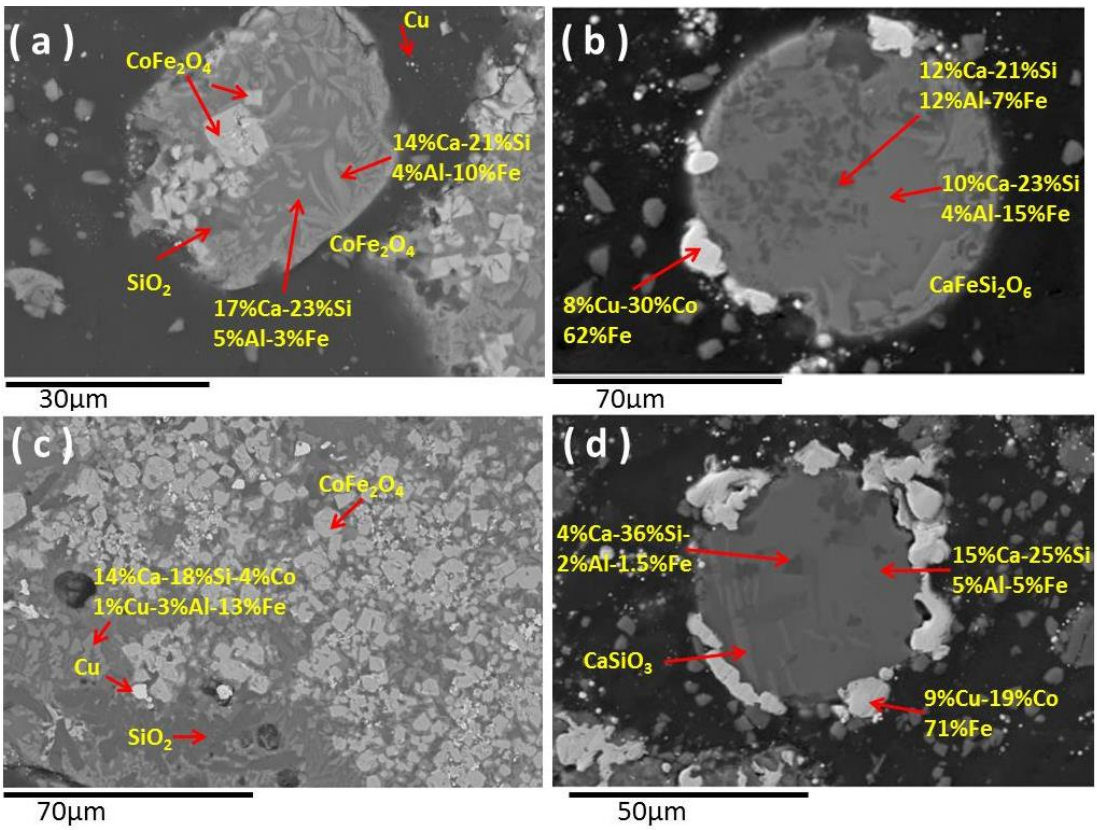

Figure 8.5 – Backscattered SEM images of the slag samples, after reduction at molar ratio of MO:C = 1:3, with; (a) carbon black at 1173 K, (b) carbon black at 1323 K, (c) activated charcoal at 1173 K, (d) activated charcoal at 1323 K

8.3.2 Thermodynamic analysis

Two major observations can be made from the XRD results in figure 8.4 and SEM results in figures 8.5a – 8.5d:

i. Metallic phases (Cu, Co and Fe) co-exist with SiO_2, $CoFe_2O_4$, Fe_3O_4 and complex silicates (e.g. $CaSiO_3$, $CaFeSi_2O_6$) at 1173 K.

ii. Metallic phases (Cu, Co and Fe) co-exist with SiO_2 and complex silicates (e.g. $CaSiO_3$, $CaFeSi_2O_6$) at 1323 K.

The phases obtained at 1323 K agree broadly with the thermodynamic prediction in figure 8.6 as there is an equilibrium between Co + Fe + $CaSiO_3$ and Co + Fe + $CaFeSi_2O_6$ phase fields at $\log_{10}(P(O_2))(atm) < -16.4$. By comparing the phases obtained at 1173 K and 1323 K and, thermodynamic prediction in figure 8.6, it can be concluded that the partial pressure of O_2 gas increases with increase in reduction temperature and this is due to increase in the reactivity of carbon. Note that the analysis in figure 8.6

does not include alloy phases and hence metallisation of Fe and Co might occur at slightly lower partial pressure of O_2 gas, due to the formation of Co-Fe alloy phase(s).

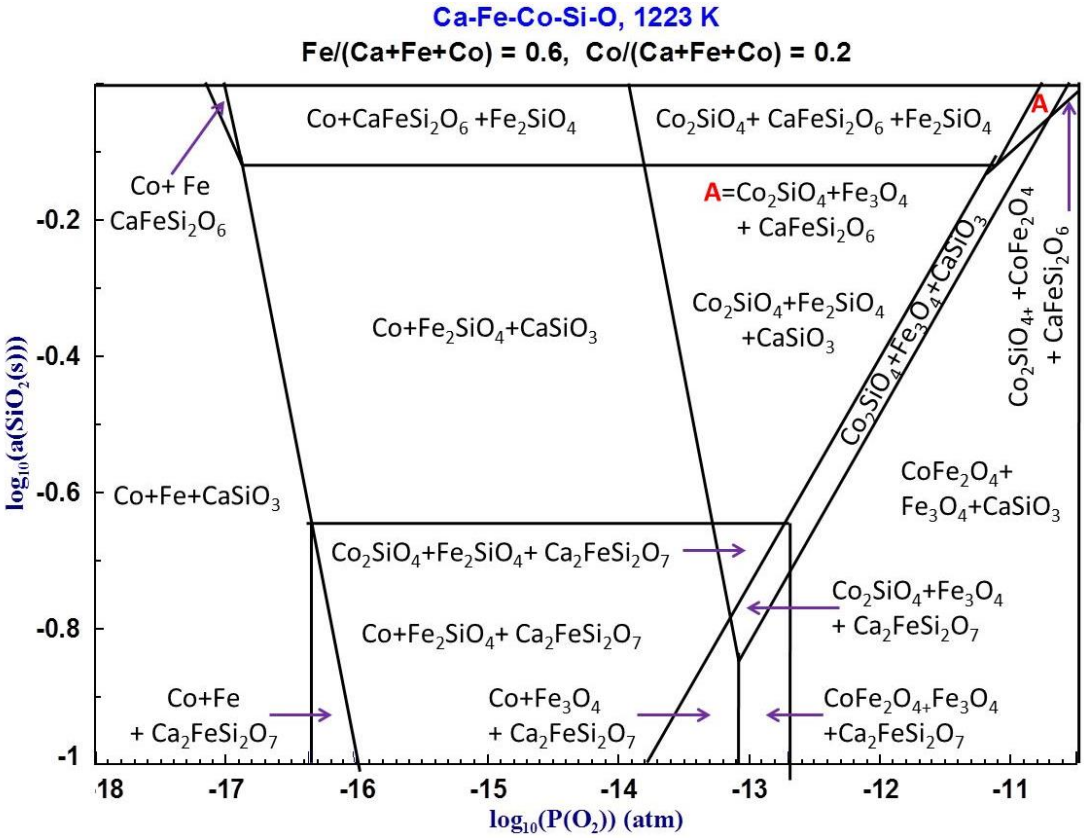

Figure 8.6 – Ca-Fe-O-S-Si predominace area diagram at 1223 K, computed using FactSage software 6.1 [24]. The analysis does not include alloy phases

8.3.3 Effect of additional CaO

Several studies have showed that the solubility of Cu and Co in the molten silicate slag, decreases with increase in basicity of slag [211, 212] and this may increase the extent and rate of reduction. Moreover, the equilibrium partial pressure of O_2 gas required for complete metallisation of Co and Fe, increases with decrease in the activity of SiO_2 (figure 8.6). For example, complete metallisation of Co and Fe occurs at $\log_{10}(P(O_2))(atm) < -16.4$ for $\log_{10}(a(SiO_2))(atm) \approx -0.75$ but at $\log_{10}(P(O_2))(atm) < -17$ for $\log_{10}(a(SiO_2))(atm) \approx 0$. This means that metallisation may easily be achieved by lowering the activity of SiO_2, which is possible by forming calcium silicates. To understand the effect of CaO during low temperature (< 1323 K) carbothermic reduction, the slag sample was mixed with 25 wt. % CaO before reduction. The plots of

the % reduction versus time curves for the reduction of slag with additional 25 wt. % CaO, are shown in figure 8.7a and it is evident that the extent of metallisation was greatly increased. The % reduction reached about 90 %R even at low temperature (1173 K), compared to about 55 % without the additional CaO (both with activated charcoal).

The addition of CaO breaks down the silicate tetrahedral network in the silicate phase [212, 213], thereby decreasing the solubility of the dissolved metal oxides. As a result, the activity of the metal oxides (Cu-O, Co-O and Fe-O) increases [3, 214, 215], leading to high reduction. The carbothermic reduction of FeO-SiO_2-CaO-Al_2O_3 slag has been studied by Li and Ratchev between 1673 K and 1873 K [216], the rate of reduction of Fe-O increased as the ratio of CaO/SiO_2 was increased between 1 and 1.3. The effect of additional CaO during reduction of molten Cu-Co slag has been studied by Banda et al. [214] and the recoveries of Cu, Co and Fe increased when CaO was increased between 2 wt.% and 8 wt. %. However, the metal recoveries decreased as CaO was added above 8 wt. %, which might have been due to increase in the viscosity of the molten slag.

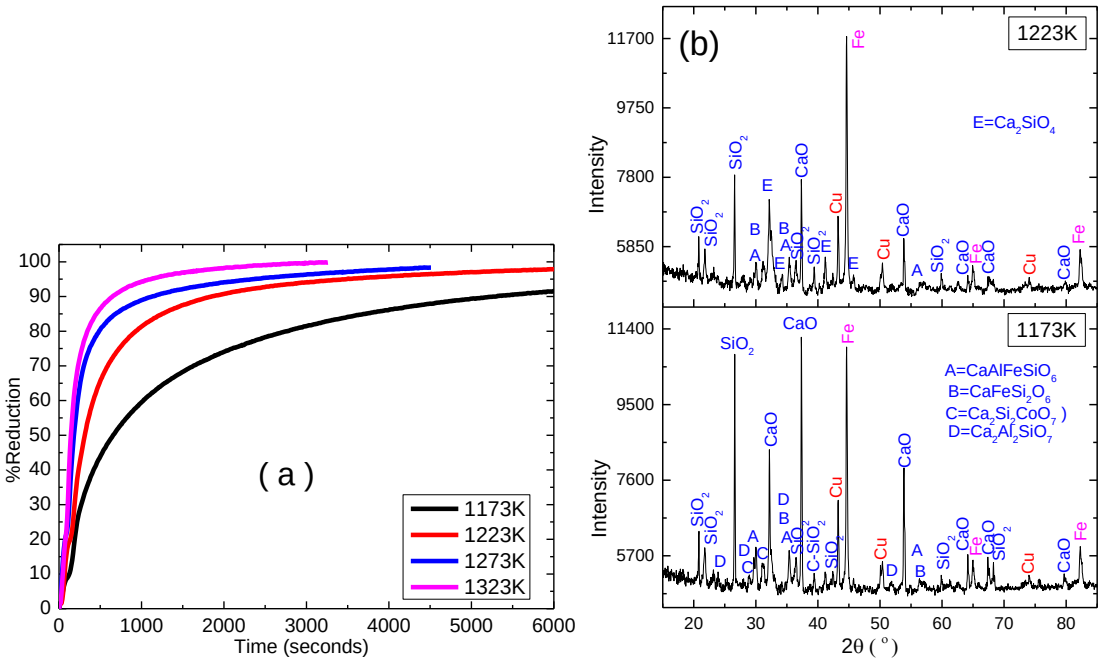

Figure 8.7 – Carbothermic reduction of slag in the presence of additional 25 wt. % CaO, with activated charcoal at molar ratio of MO:C = 1:3; (a) plot of % reduction versus time curves (b) XRD patterns. Argon flow rate = 0.6 litre min^{-1}

The Gibbs energy changes for the formation of calcium silicates (CaO-SiO_2) and iron silicates (FeO-SiO_2) are compared in figure 8.8a, per mole of SiO_2 and, it can be

observed that the Gibbs energy changes are more negative for the formation of calcium silicates ($CaO\text{-}SiO_2$) than for iron silicates ($FeO\text{-}SiO_2$) [10]. Based on the thermodynamic prediction in figure 8.8a, the iron silicate ($FeO\text{-}SiO_2$) phase will be less stable in the presence of excess CaO thereby leading to the increased rate of reduction of Fe from slag due to formation of the stable calcium silicate ($CaO\text{-}SiO_2$) phase(s). The reduction of FeO, $FeSiO_3$ and $CaFeSiO_4$ are compared in figure 8.8b, the Gibbs energy change is more negative and less negative for the carbothermic reduction of $CaFeSiO_4$ and $FeSiO_3$, respectively. This suggests that the reduction of $FeSiO_3$ will be higher in the presence of CaO, due to the formation of the stable calcium silicate ($CaO\text{-}SiO_2$) phase(s).

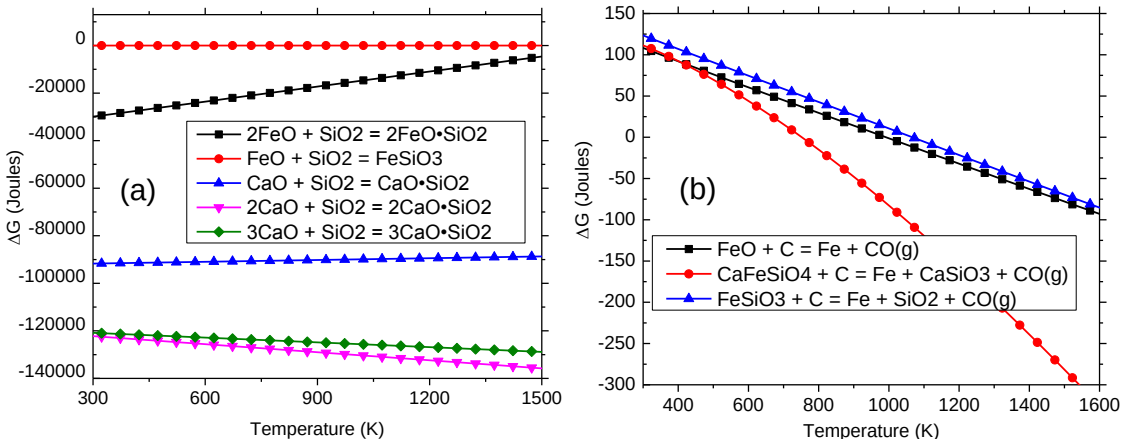

Figure 8.8 – Computed Gibbs energy against absolute temperature; (a) for the formation of $CaO\text{-}SiO_2$ and $FeO\text{-}SiO_2$ per mole of SiO_2 and (b) carbothermic reduction of FeO, $CaFeSiO_4$ and $FeSiO_3$ per mole of C, computed using HSC 5.1 software [39]

The XRD patterns for the samples that were mixed with 25 wt.% CaO and reduced with activated charcoal, at 1173 K and 1223 K are shown in figure 8.7b and it can be observed that the XRD peak intensities for metallic/alloy phases (Cu, Fe and Co-Fe) are higher at 1173 K. The metallic/alloy phases co-exist with Ca_2SiO_4, $Ca_2Al_2SiO_8$ and $CaFeSi_2O_6$ because, part of CaO reacted with or dissolved in the glassy phase.

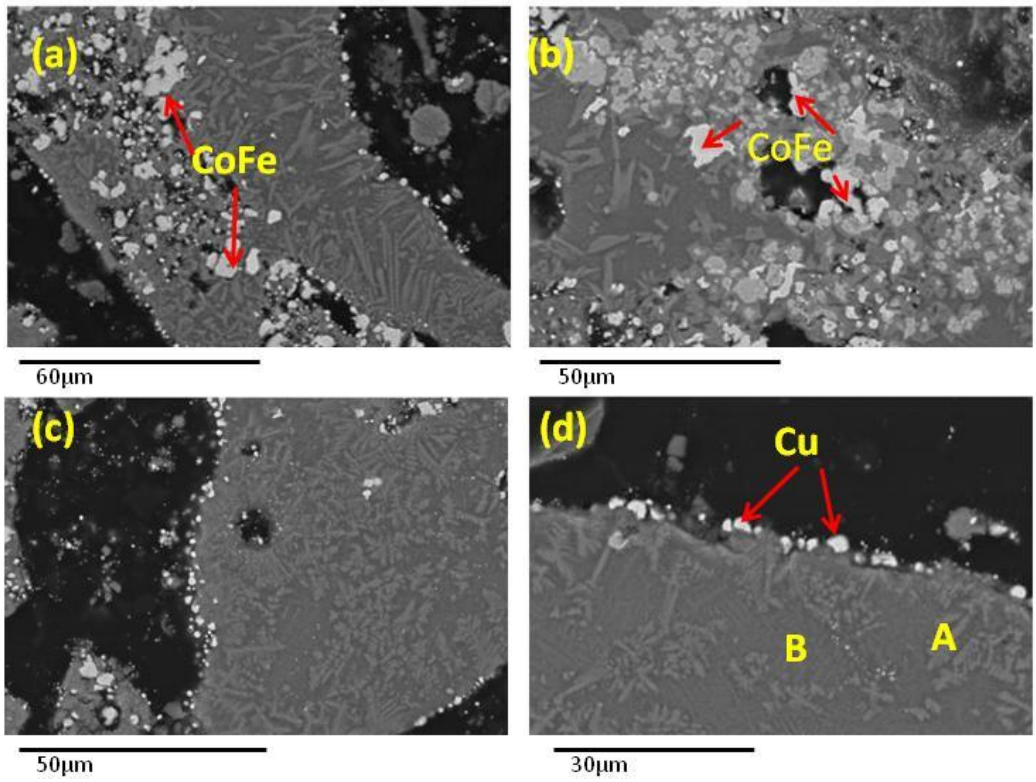

Figure 8.9 – Backscattered SEM images of the reduced slag at 1223 K, the sample was enriched with 25 wt. % CaO before reduction, the composition of areas A and B from image (d) are given in table 8.2

Table 8.2 – SEM-EDX semi-quantitative analysis (wt. %) of areas A and B from image (d) of figure 8.9

Area	Cu	Co	Fe	Ca	Si	Al	O
A	0.3	2.3	9.7	12.5	21.5	3.8	49.4
B	0.4	0.8	4.7	15.0	22.5	4.4	51.4

The SEM images of the sample which was reduced in the presence of additional 25 wt. % CaO at 1223 K are shown in figure 8.8b from which the following observations were made:

i. Metallic copper is found at the periphery of the slag particles, in the form of beads.
ii. CaO rich phases are observed within the particles.
iii. Metallic and alloy phases of Fe and Co are found within the sample particles but near the cracked zones.

Observations (i) and (ii) suggests that the Ca^{2+} ions substitute the Cu^{2+} ions in the glassy phase via diffusion of the Ca^{2+} and Cu^{2+} ions from the lime particles and glassy phase, respectively. The ionic substitution between the Cu^{2+} ions and the Ca^{2+} ions is very favourable because of the ionic radius for Cu^{2+} ion (0.96 Å) is comparable to the Ca^{2+} ion (0.99 Å) [211]. The dissolution or diffusion of the Ca^{2+} ions into the glassy phase appears to have caused cracking, as a result of structural changes, such that the CO gas from the metallisation of Cu diffused and reacted with the $Co_{0.62}Fe_{2.38}O_4$ crystals. The unreacted $Co_{0.62}Fe_{2.38}O_4$ crystals appear to have dissolved into the Ca-Si-Al-O phase. The metal containing Ca-Si-Al-O phase was in the form of lath and dendrites [207]. The SEM-EDX semi-quantitative analysis of areas A and B from image 8.8d are given in table 8.2 and it is evident that Cu was nearly absent from the slag particles, as a result of counter diffusion between the Cu^{2+} and Ca^{2+} ions. It can also be noticed from table 8.2 that the concentration of Fe and Co decreases with increase in the concentration of Ca in the glassy phase.

8.3.4 Reaction kinetics for carbothermic reduction of slag

The rate of reduction, derived from %R versus time plots in figures 8.4a and 8.4b,were fitted into the interface model (see equation 2.10a), diffusion model (see equations 2.10b and 2.10c) and mixed reaction model (equation 8.2 [217]) in order to establish the reaction mechanism which might be governing the overall rate. The experimental data fitted well with the mixed reaction model in equation 8.2. The cross-sectional SEM analysis of the reduced samples, showed the presence of metallic phases at the periphery of the slag particles (figures 8.5 and 8.9) thereby confirming that there was diffusion of the metallic (M^{2+}) and oxygen (O^{2-}) ions. The extent of metallisation was sensitive to the reduction temperature and type of carbon and, this is a characteristic of a chemically controlled reaction. In summary, the presence of metallic phases at the periphery and the high sensitivity of the reduction reaction to the type of carbon and reduction temperature, confirms that the carbothermic reduction of slag is controlled by the mixed reaction.

$$1 - 2(1 - X)^{\frac{1}{3}} + (1 - X)^{\frac{2}{3}} = Kt \qquad 8.2$$

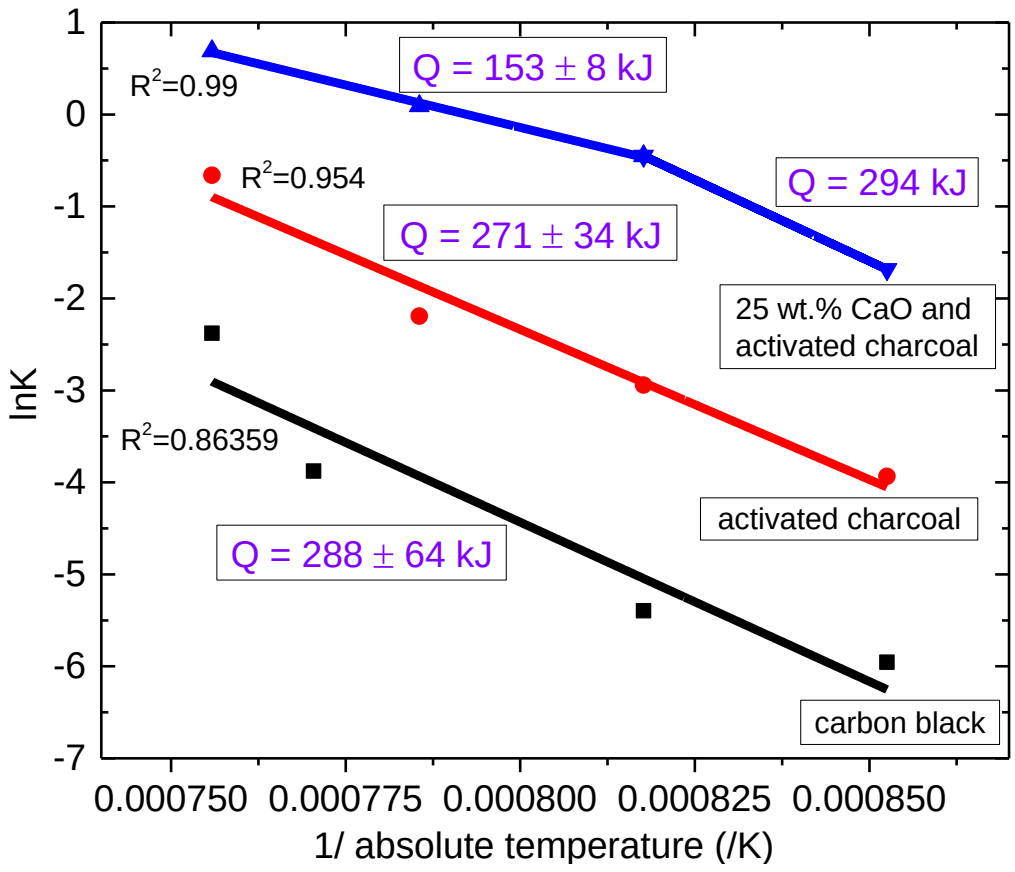

Figure 8.10 - Arrhenius plots (lnK against reciprocal of temperature) for the carbothermic reduction of slag, the rate constant k was calculated using the G.B + interface model. The activation energy is inserted in each line

The plots of the lnK versus 1/T lines are shown in figure 8.10 and the calculated value of overall activation energy is inserted on each fitted line. For carbon black in figure 8.10, the derived value of activation energy is 288 ± 64 kJ mol^{-1} and this agrees with the activation energy of 333 ± 21 kJ for the $CO_2(g)$ – C(carbon black) reaction, determined by Rao and Jalan [185]. The value of apparent activation energy is 271 ± 34 kJ with activated charcoal and it is in a reasonable agreement with the values of 252 - 268 kJ mol^{-1} reported by various authors for the CO_2 – C (activated charcoal) reaction [218, 219]. The activation energies for the reduction of slag with carbon black and activated charcoal are also comparable to the activation energy of 300 ± 37 kJ for the diffusion of oxygen in $Ca_2Al_2SiO_7$ in a temperature range of 1273 K – 1573 K [220, 221]. It can be observed in figure 8.10 that the natural logarithmic values of the rate constant (lnK) are higher for the reduction of slag with activated charcoal than with carbon black implying that the rate of reductions are higher with the former (activated charcoal) than with later (carbon black). Note that the reduction of the slag was incomplete with carbon black or

activated charcoal (see figures 8.4a and 8.4b) such that the activation energies are for less than 75 % reduction.

The values of lnK are highest for the carbothermic reduction of slag with activated charcoal in the presence of additional 25 wt. % CaO, meaning that the rate of reduction was highest. On the other hand, the slope of the lnK versus 1/T line changes at 1223 K for the carbothermic reduction of slag with activated charcoal in the presence of additional 25 wt. % CaO. The change in the slope of the line might be due to the presence of the liquid phase above 1223 K. The activation energies were 153 ± 8 kJ and 294 kJ for the high ($T \geq 1223$ K) and low ($T \leq 1223$ K) temperature regimes, respectively. The activation energy in the lower temperature regime (294 kJ) is close to the activation energy of 271 ± 34 kJ in the absence of additional 25 wt. % CaO (with activated charcoal) and for reduction with carbon black (288 ± 64 kJ).

8.3.5 General discussion for the carbothermic reduction of slag

Although carbothermic reduction of slag with activated charcoal yielded a larger volume fraction of metallic phase at 1323 K, the magnetic separation of the metallic phases was not successful. This was due to two problems: (i) sintering between the metallic and slag particles (see figure 8.5 and 8.8) and (ii) the metallic particles were smaller (less than 10 µm). The above problems may be overcome by grinding the reduced samples to fine particle of less than 10 µm, so as to liberate the metallic particles. However, fine grinding consumes a lot of energy and hence carbothermic reduction of slag in the temperature range herein (1173 K – 1323 K) may not be followed by magnetic separation. It is therefore necessary to carbothermically reduce the slag above 1323 K for obtaining larger metallic particles that may easily be magnetically separated.

8.4 Sulphidisation of slag in the presence of $CaSO_4$

As stated in chapter 2, metal oxides may be converted into metal sulphides in the presence of $CaSO_4$ and carbon [15, 85], in what is known as sulphidisation. Turkdogan [85] has found out that the sulphidisation of metal oxides in the presence of $CaSO_4$ and C can be affected by the type of carbon and the molar ratio of $CaSO_4$:C. This is due to the fact that $CaSO_4$ can be calcined to CaO and SO_2 gas and/or, CaS and CO/CO_2 gas, depending on the type of carbon and the molar ratio of $CaSO_4$:C [85]. In particular,

Turkdogan has suggested that maximum sulphidisation occurs at the molar ratio of $CaSO_4$:C = 2:1 [85] and with a less reactive carbon such as graphite, because:

i. There is no formation of CaS. The formation of CaS decreases the amount of sulphur that reacts with the metal oxide phase as CaS is a stable phase in the presence of carbon [85].

ii. All sulphur is calcined as SO_2 gas which then reacts with the metal oxides [85].

However, Turkdogan did not point out the effect of SiO_2 on the $CaSO_4$ – C reaction. The presence of SiO_2 may promote the evolution of SO_2 gas even at higher mole ratio of carbon due to the formation of $CaSiO_3$. With a view of finding the best sulphidisation conditions, slag was sulphidised in the presence of $CaSO_4$ and less reactive carbon (graphite) or more reactive carbon (activated charcoal), in a temperature range of 1173 K – 1323 K. The experiments were carried out in the TGA equipment and in the elevating hearth furnace.

8.4.1 Sulphidisation of slag in the TGA equipment

The experiments were carried out in the TGA equipment in order to determine the extent of reaction as a function of time at each isothermal temperature. The fraction of the experimental weight loss over the theoretical weight loss in equation 2.41b was multiplied by 100 % to obtain the % conversion.

8.4.1.1 Sulphidisation of slag in the presence of $CaSO_4$ and graphite

The effect of reaction temperature was studied at the molar ratio of MO:$CaSO_4$:C = 1:1.3:1.5 and the plots of % conversion versus time curves are shown in figure 8.11a. It is evident from figure 8.11a that the sulphidisation of slag is quite sensitive to the reaction temperature. For example, the reaction was incomplete after 2 hours at 1173 K but completed within 15 minutes at 1323 K, based on the results in figure 811a. The results in figure 8.11a shows that the extent of % conversion was slightly higher at 1273 K than at 1323 K but this may be due to evolution of CO + CO_2 gases, rather than CO_2 gas.

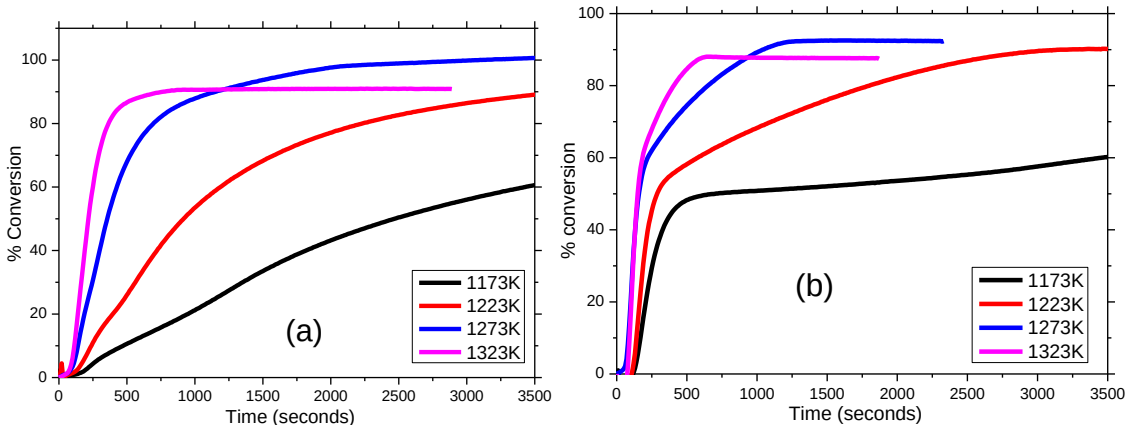

Figure 8.11 – Plots of % conversion versus time curves for the sulphidisation of slag at molar ratio of MO:$CaSO_4$:C = 1:1.3:1.5, with; (a) graphite and (b) activated charcoal. Argon flow rate = 0.6 litre min^{-1}

The XRD patterns of the slag samples which were reacted in the presence of $CaSO_4$ and graphite, are shown in figure 8.12 from which the following observations were made: (i) the reduction calcination of $CaSO_4$ was incomplete even after holding the samples for 2.5 hours at 1173 K and 1223 K and, (ii) part of $CaSO_4$ was calcined to CaS at 1173 K and 1223 K. It is worth noting that the phases obtained at 1173 K and 1223 K agree broadly with the Ca-Fe-O-S system [24] as there is an equilibrium between CaS + Fe_3O_4 and $CaSO_4$ + $Ca_2Fe_2O_5$ phase fields.

The sulphidisation of slag in the presence of $CaSO_4$ and carbon can occur, only when: (i) sulphur is calcined from $CaSO_4$ and, (ii) metal oxide is reduced to metallic state. Nonetheless, the metal oxides may not be reduced to metallic state when the reactivity of carbon is low and hence sulphidisation does not take place. The Gibbs energy change for reduction calcination of $CaSO_4$ to CaS and carbothermic reduction of Fe_3O_4 are compared in equations 8.3a and 8.3b, respectively, and it can be observed that the Gibbs energy change is more negative for equation 8.3a than 8.3b. Therefore, equation 8.3a may occur preferentially, when the reactivity of carbon (graphite) is low. Based on the thermodynamic prediction in equations 8.3a and 8.3b and the presence of CaS and Fe_3O_4 phases in the XRD patterns at 1173 K and 1223 K (figure 8.12), it can be concluded that the sulphidisation of Fe in the presence of $CaSO_4$ and graphite was limited by the reduction of Fe_3O_4. Fe_3O_4 co-exists with $Ca_2Fe_2O_5$ and the formation of the later can be represented by equation 8.3c.

$$CaSO_4 + 2C = CaS + 2CO_2(g), \quad \Delta G_{1173K} = -244 \text{ kJ} \qquad 8.3a$$

$$Fe_3O_4 + 2C = 3Fe + 2CO_2(g), \quad \Delta G_{1173\,K} = -51\ kJ \qquad 8.3b$$

$$Fe_3O_4 + 3CaSO_4 + \frac{5}{4}C = \frac{3}{2}Ca_2Fe_2O_5 + 3SO_2 + \frac{5}{4}CO_2,$$

$$\Delta G_{1173\,K} = -94.5\ kJ \qquad 8.3c$$

The Gibbs energy change for the carbothermic reduction of FeO, CoO and Cu_2O are compared in equations 8.4a, 8.4b and 8.4c, respectively, per mole of C. The Gibbs energy change is more negative for equation 8.4c and hence metallisation of Cu occurred, which then led to its sulphidisation at 1173 K and 1223 K. The above analysis shows that there is broad agreement between the thermodynamic prediction in equations 8.3a – 8.4c and the experimental results in figure 8.12, at 1173 K and 1223 K.

$$2FeO + C = 2Fe + CO_2(g), \quad \Delta G_{1173\,K} = -21\ kJ \qquad 8.4a$$

$$2CoO + C = 2Co + CO_2(g), \quad \Delta G_{1173\,K} = -93\ kJ \qquad 8.4b$$

$$2Cu_2O + C = 4Cu + CO_2(g), \quad \Delta G_{1173\,K} = -230\ kJ \qquad 8.4c$$

The reactivity of graphite increases with an increase in temperature such that Fe_3O_4 is reduced to Fe and hence sulphidisation of Fe takes place. It is for this reason that the XRD peak intensities for the metal sulphides ($CuFeS_2$ and Cu_2S) are higher above 1223 K. The metal sulphides co-exist with the Ca_2SiO_4 and $Ca_2Al_2SiO_7$ phases at $T \geq 1223$ K because, CaO from the reduction calcination of $CaSO_4$ reacted with SiO_2 and glassy phase.

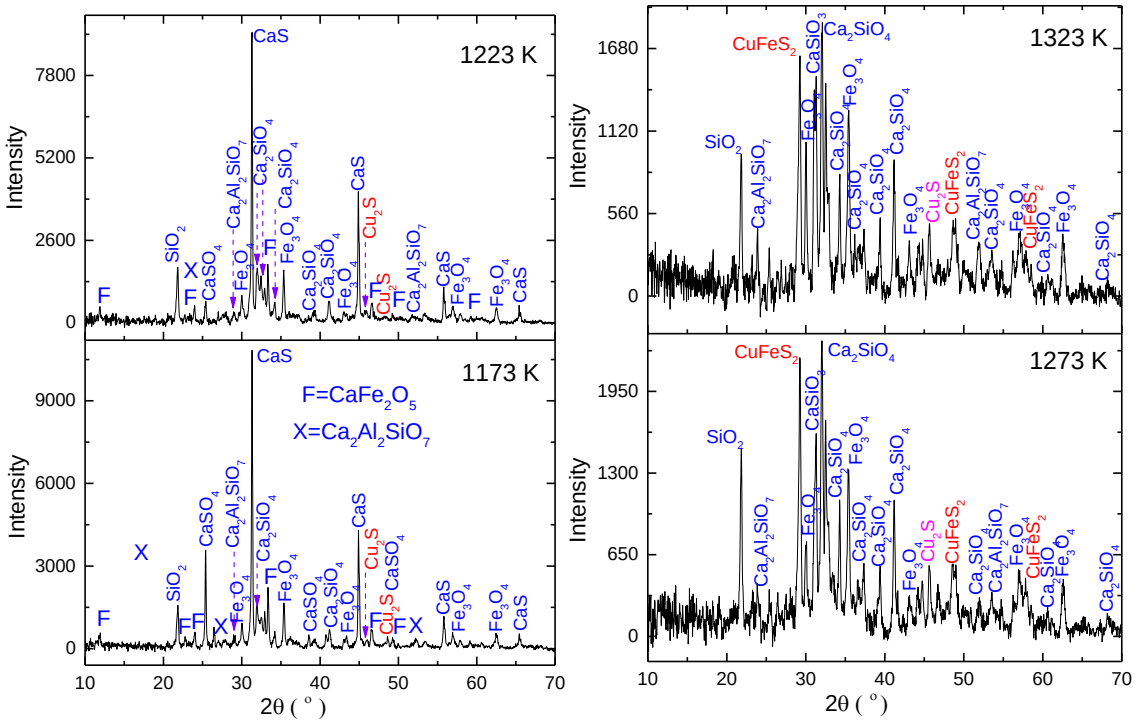

Figure 8.12 - XRD patterns of the slag samples, sulphidised in the presence of $CaSO_4$ and graphite in the TGA equipment at molar ratio of MO:$CaSO_4$:C = 1:1.3:1.5. Argon flow rate = 0.6 litre min^{-1}

8.4.1.2 Sulphidisation of slag in the presence of $CaSO_4$ and activated charcoal

As stated above, the sulphidisation of Fe in the presence of $CaSO_4$ and graphite was limited by the reduction of Fe_3O_4 at 1173 K and 1223 K. As a result, slag was sulphidised in the presence of $CaSO_4$ and activated charcoal, since activated charcoal is more reactive than graphite. The plots of the % conversion versus time curves for the sulphidisation of slag in the presence of $CaSO_4$ and activated charcoal are given in figure 8.11b. It is evident from figure 8.11b that the plots of % conversion versus time curves are characterised by two regimes: (i) the first regime with a steep slope which terminates at about 50 % conversion and (ii) the second regime with a gradual gradient. The steep slope in the first regime in figure 8.11b confirms that activated charcoal is quite reactive [204].

The XRD patterns of the slag samples which were sulphidised in the presence of $CaSO_4$ and activated charcoal are shown in figure 8.13. The main phases at 1173 K are metal sulphides ($CuFeS_2$ and Cu_5FeS_4), $Ca_2Fe_2O_5$, $CaSO_4$, CaS, SiO_2 and Fe_3O_4. The presence of metal sulphides ($CuFeS_2$ and Cu_5FeS_4) shows that sulphidisation was higher with activated charcoal than with graphite at 1173 K. There is no residual $CaSO_4$ for

the sulphidisation with activated charcoal at T ≥ 1223 K and, the XRD peak intensities for the metal sulphides are high.

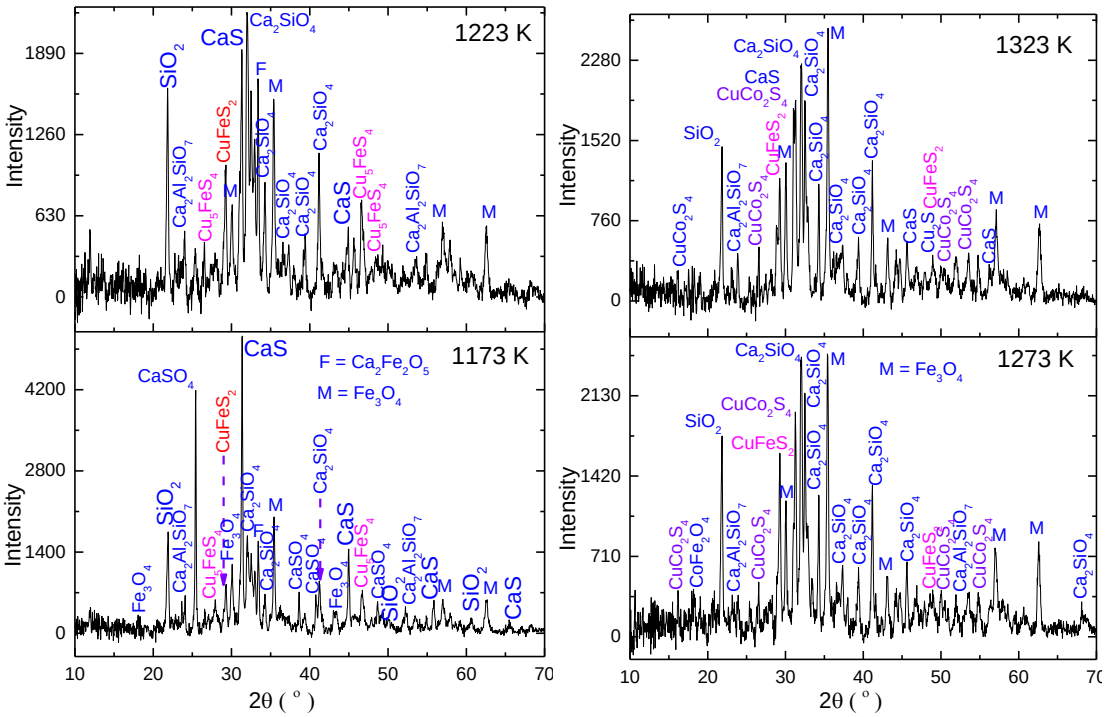

Figure 8.13 - XRD patterns of the slag samples, sulphidised in the presence of $CaSO_4$ and activated charcoal in the TGA equipment at molar ratio of MO:$CaSO_4$:C = 1:1.3:1.5. Argon flow rate = 0.6 litre min^{-1}

The backscattered SEM images of the sulphidised slag samples are shown in figures 8.14a - 8.14d. Copper sulphide (Cu_2S) is found at the periphery of the particles at 1173 K (figures 8.14a and 8.14c), due to diffusion of copper from slag. As already mentioned, sulphidisation occurs when the metal oxide phase is reduced to metallic state. However, some of the $Co_{0.62}Fe_{2.38}O_4$ crystals were neither reduced nor sulphidised and therefore remained in the slag phase at 1173 K (figures 8.14a and 8.14c). The volume of the matte phase is high at 1323 K than at 1173 K as shown in figures 8.14b and 8.14d. The matte phases were bordered with the rich CaO slag at 1323 K. The rich CaO slag was formed as a result of reaction between CaO from the reduction calcination of $CaSO_4$ and the rich SiO_2 slag phase. Cu-Co-Fe sulphide (matte) can be observed from figure 8.14d although this type of phase was not characterised by the XRD technique probably, due to low concentration or lack of reference patterns from the HighScore plus software.

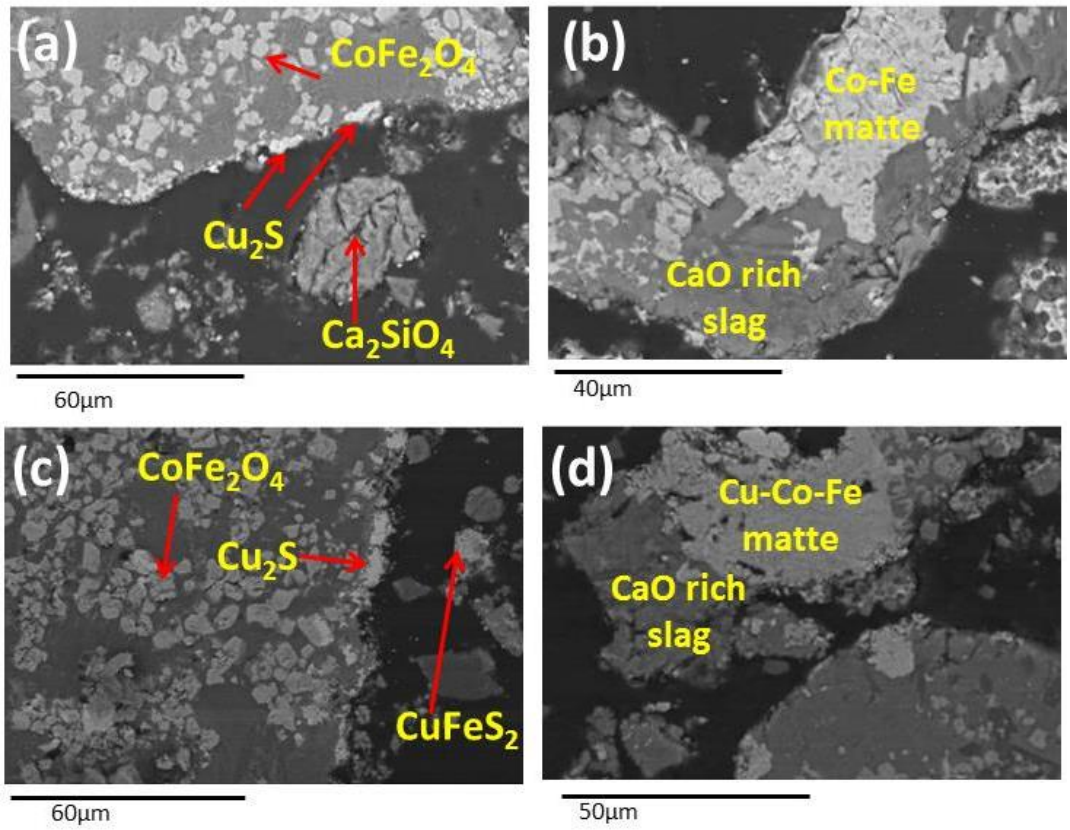

Figure 8.14 – Backscattered SEM images of the slag samples which were sulphidised at molar ratio of MO:$CaSO_4$:C = 1:1.3:1.5 at; (a) 1173 K with graphite, (b) 1323 K with graphite, (c) 1173 K with activated charcoal and (d) 1323 K with activated charcoal. Argon flow rate = 0.6 litre min^{-1}

8.4.1.3 Activation energy for the sulphidisation of slag

The experimental data for the sulphidisation of slag fitted well with the mixed reaction model, discussed in chapter 6 (sum of the interface and diffusion reaction models). The plots of the lnK versus 1/T lines are shown in figures 8.15a and 8.15b and it is evident that the slope of the line changes at 1273 K for the sulphidisation of slag in the presence of $CaSO_4$ and graphite. The change in the slope of the line agrees very well with the XRD results in figure 8.12, as similar phases were obtained at 1173 K/1223 K and 1273 K/1323 K. The activation energy of 311 ± 6 kJ in the low temperature regime (between 1173 K and 1273 K) is comparable to: (i) activation energy of 305 kJ – 340 kJ for the CO_2 gas – C (graphite) reaction, determined by various authors [222-224], in the temperature range of 1123 K – 1373 K and, (ii) enthalpy change of 303 kJ for reaction

8.3b. Note that the carbothermic reduction of Fe_3O_4 is directly related to the speed of the CO_2 – C reaction [28]. Therefore it can be concluded that the sulphidisation reaction was controlled by the reduction of Fe_3O_4 in the low temperature regime (T < 1273 K).

On the other hand, the activation energy of 215 kJ in the upper temperature regime (T ≥ 1273 K) is comparable to the activation energy of 239 ± 18 kJ, for the reaction between CaS and $CaSO_4$ (equation 8.5c) [53] and this is because, the reduction calcination of $CaSO_4$ to CaO and SO_2 occurs via equations 8.5a - 8.5c [85]. The SO_2 gas from equation 8.5c may react with the metal oxides according to equation 8.5d. The enthalpy change for reaction 8.5c is 234 kJ $mole^{-1}$ SO_2 gas [85]. By comparing the enthalpy change of 234 kJ and the activation energy of 239 ± 18 kJ for reaction 8.5c with the activation energy of 215 kJ in the upper temperature regime (figure 8.15a), it can be concluded that sulphidisation of slag in the presence of $CaSO_4$ and graphite, was limited by equation 8.5c.

$$CaSO_4 + C = CaS + 2CO_2(g) \qquad 8.5a$$

$$CO_2(g) + C = 2CO(g) \qquad 8.5b$$

$$CaS + 3CaSO_4 = 4CaO + 4SO_2(g) \qquad 8.5c$$

$$MO + 3CO(g) + SO_2 = MS + 3CO_2(g) \qquad 8.5d$$

As observed in figure 8.11b, the slope of the % conversion versus time curves for the sulphidisation of slag with activated charcoal, changes at about 50 % conversion. As such, the activation energies were calculated in the first (≤ 50 % conversion) and second (≥ 50 % conversion) regimes. The activation energy of 111 ± 26 kJ in the first regime (≤ 50 % conversion) is comparable to the activation energy of 103 K for the diffusion of Fe^{2+} ions in FeO [107]. The slope of the lnK vs. 1/T line in the second regime (≥ 50 % conversion) changes at 1223 K and this is in very good agreement with the XRD results in figure 8.13, as similar phases were obtained at T ≥ 1223 K. The high temperature regime (T ≥ 1223 K) has the activation energy of 213 kJ, similar to the activation energy of 215 kJ for the sulphidisation with graphite (figure 8.15a).

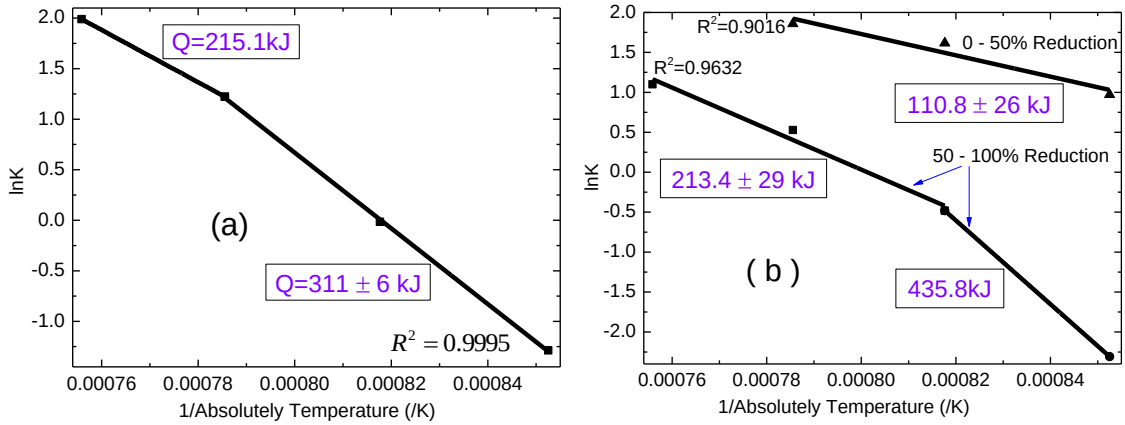

Figure 8.15 - Arrhenius plot of lnK versus 1/T (a) with graphite and (b) with activated charcoal

8.4.2 Sulphidisation of slag in the elavating hearth furnace

Even though metal sulphides were obtained after sulphidisation of slag in the presence of $CaSO_4$ and graphite or activated charcoal in the TGA equipment, residual Fe_3O_4/$CoFe_2O_4$ were present in the reacted samples (see figures 8.10b, 8.12 and 8.13). Nonetheless, the presence of Fe_3O_4/$CoFe_2O_4$ might be due to increase in the partial pressure of O_2 gas as carbon (graphite/activated charcoal) is consumed.

The Ca-Fe-Si-O-S predominace area diagram is shown in figure 8.16 and it can be observed that the partial pressure of O_2 gas should be kept lower throughout the experiment, if the $CaSiO_3$ and FeS phases are to remain stable. Any increase in the partial pressure of O_2 gas will result in the oxidation of the FeS phase as shown in figure 8.15. It is evident from figure 8.15 that starting with $CaSiO_3$ and FeS phases and then increasing the partial pressure of O_2 gas to $\log_{10}(P(O_2)) > -10.4$, the $CaSiO_3$ + Fe_3O_4 phase field is obtained. In practice, the partial pressure of O_2 gas might increase when carbon (graphite or activated charcoal) has been consumed. Therefore, the presence of the Fe_3O_4 phase might have been caused by the increase in partial pressure of O_2 gas. Even though the partial pressure of O_2 gas, can be kept lower (in the stability region of metal sulphides) by using excess carbon, sulphidisation does not occur because of the metallisation and calcination of $CaSO_4$ to CaS. In short, metallic phases and CaS are obtained at higher molar ratio of carbon (graphite/activated charcoal). With a view of maintaining lower partial pressure of O_2 gas, sulphidisation was carried out in the elevating hearth furnace, where the alumina crucible containing the sample was placed in the graphite clay crucible and covered with a graphite lid (see figure 3.2).

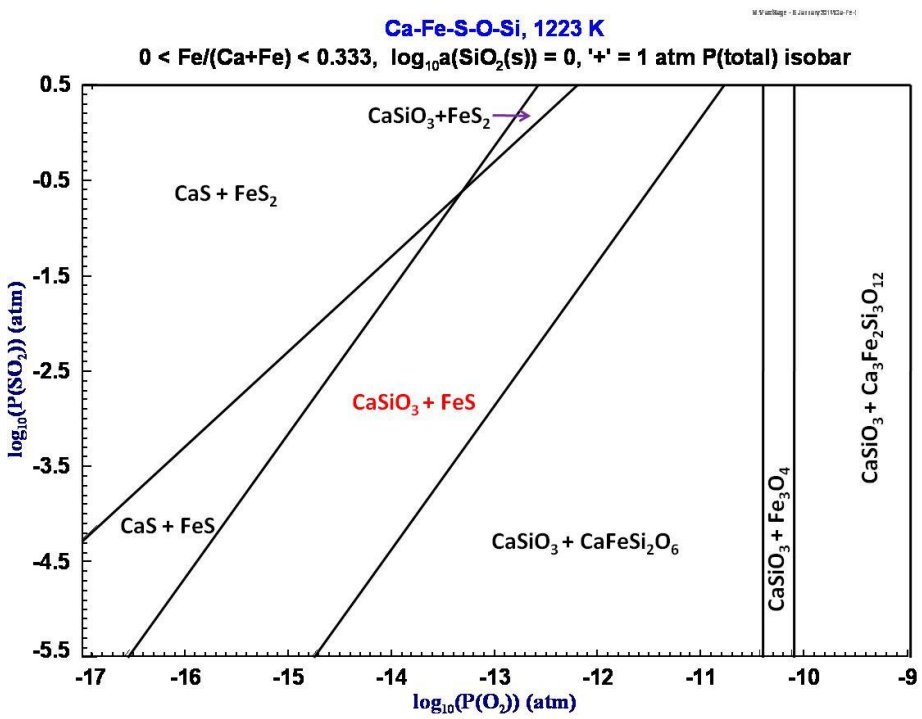

Figure 8.16 – Ca-Fe-Si-O-S predominance area diagram at 1223 K, computed using FactSage software 6.1 [24]

The XRD patterns for the samples which were sulphidised in the elevating hearth furnace are shown in figure 8.17. Sulphidisation was complete at the molar ratio of MO:$CaSO_4$:C = 1:1.3:0.65 as there are no metal oxides in the sample, after 2 hours at 1323 K. The XRD peak intensities for the FeS phase were very high, which was not the case for the sulphidisation of the samples in the TGA equipment (without placing the alumina crucible inside the graphite clay crucible). The higher sulphidisation of the slag in the elevating hearth furnace is due to:

i. Slow rate of reaction, since the exit gases do not easily escape out when the alumina crucible containing the sample is placed inside the graphite clay crucible. The extent of sulphidisation increases with decrease in the rate of reaction as nearly all sulphur from $CaSO_4$ is consumed by the metallic phases.

ii. Low partial pressure of O_2 gas because of the presence of graphite blocks and graphite clay surrounding the alumina crucible. The graphite blocks and clay graphite crucible burns externally and hence they do not cause metallisation or formation of CaS but, helps in maintaining low partial pressure of O_2 gas which is needed for the stability of the matte phase.

FeS co-exists with $CuFeS_2$ and Cu_5FeS_4 and this is consistent with Cu_2S-FeS pseudo binary phase diagram [15], towards the rich FeS region. The metal sulphides co-exist with the calcium silicates (Ca_2SiO_4, $CaSiO_3$, $CaAl_2Si_2O_8$) as CaO from the reduction calcination of $CaSO_4$, reacted with SiO_2 and Al_2O_3. On the other hand, the XRD peak intensities for CaS and metal sulphides ($CuFeS_2$, FeS and Cu_5FeS_4) were extremely high and low, respectively, at high molar ratio of $CaSO_4$, (MO:$CaSO_4$:C = 1:1.8:0.9). This was due to partial reduction of the metal sulphide phases (matte). Not all of the CaO from the reduction calcination of $CaSO_4$, reacts with SiO_2 and Al_2O_3 at high mole ratio of $CaSO_4$ and hence metallisation occurs via FeS – CaO (exchange) and MO – CO (reduction) reactions.

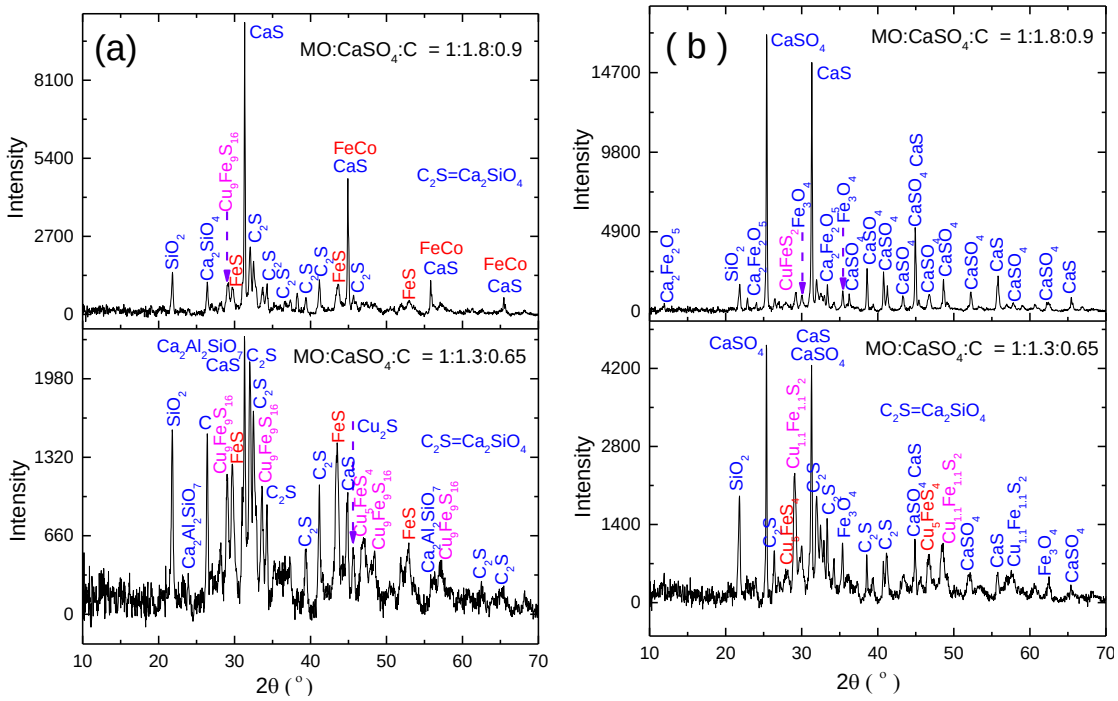

Figure 8.17 - XRD patterns of the slag samples which were sulphidised in the presence of $CaSO_4$ and graphite at 1323 K in the elevating hearth furnace; (a) 2 hours and (b) 1.3 hours. Argon flow rate = 2 litres min^{-1}

8.4.2.1 Effect of holding time

To study the effect of reaction time in the elevating hearth furnace, some experiments were stopped after 1.3 hours at 1323 K. The XRD patterns of the samples that were reacted for 2 hours and 1.3 hours are compared in figures 8.17a and 8.17b, respectively, from which the following observations were made:

i. $CaSO_4$ is present in the samples that were reacted for 1.3 hours (figure 8.17b).

ii. The XRD peak intensities for the metal sulphides ($CuFeS_2$,$Cu_{1.1}Fe_{1.1}S_2$, Cu_5FeS_4) are high in the samples which were reacted for 1.3 hours at molar ratio of MO:$CaSO_4$:C = 1:1.3:0.65 The metal sulphides co-exist with Fe_3O_4 as a result of incomplete sulphidisation.

The presence of $CaSO_4$ after 1.3 hours at 1323 K confirms that sulphidisation was much slower when the alumina crucible containing the sample was placed inside the graphite clay crucible and this is expected, because the product gas(es) do not easily escape out from the sample. However, slow reactions promote higher sulphidisation because nearly all S_2/SO_2 gas reacts with the metallic phases, as discussed above.

8.4.2.2 Effect of reaction temperature

The XRD pattern for the slag sample which was sulphidised in the presence of $CaSO_4$ at 1173 K is shown in figure 8.18. It can be observed from figure 8.18 that sulphidisation was high as a result of high and low XRD peak intensities of the metal sulphides ($CuFeS_2$, Cu_5FeS_4, $Cu_{1.8}S$) and Fe_3O_4, respectively. Note that sulphidisation was very low in the TGA equipment (without placing the alumina crucble inside the graphite clay crucible) at 1173 K but this is not the case in figure 8.18.

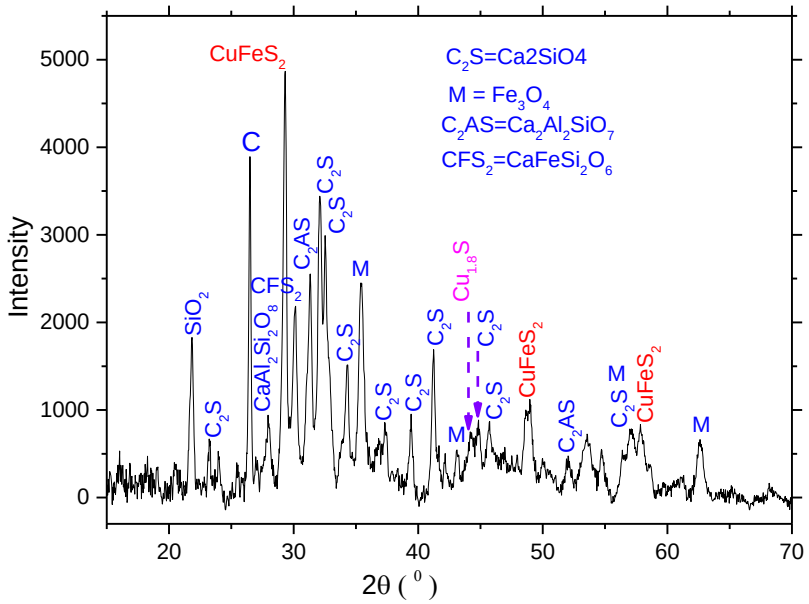

Figure 8.18 - XRD pattern of the slag sample, sulphidised in the presence of $CaSO_4$ and graphite for 2.5 hours at 1173 K in the elevating hearth furnace, molar ratio of MO: $CaSO_4$:C = 1:1:2. Argon flow rate = 2 litres min^{-1}

8.4.3 SEM analysis for the sulphidised samples

Elemental maps of the slag sample which was sulphidised for 2 hours at 1323 K, in the elevating hearth furnace, at molar ratio of MO:$CaSO_4$:C = 1:1.3:0.65, are shown in figure 8.19. The SEM results in figure 8.19 agree with the XRD results in figure 8.17a as there are no metal oxides in the sample. The elemental maps further show that iron sulphide reacted with cobalt sulphide to form cobalt-iron sulphide phases. The Fe-Co-S phases were not identified from the XRD patterns, probably due to overlap in peaks between the Fe-S and Co-Fe-S phases.

The SEM image of the slag sample which was sulphidised at 1323 K and molar ratio of MO:$CaSO_4$:C = 1:1.8:0.9 is shown in figure 8.19. Metallic phases can be observed in figure 8.19 and detailed analysis of the sample showed that, only Co and Fe were partially metallised at molar ratio of MO:$CaSO_4$:C = 1:1.8:0.9. By comparison, the metallisation of Co was higher than for Fe and this agrees well with the thermodynamic prediction in figure 2.3b as the Gibbs energy change is more negative for the carbothermic reduction of CoS in the presence of CaO (see figure 2.3b).

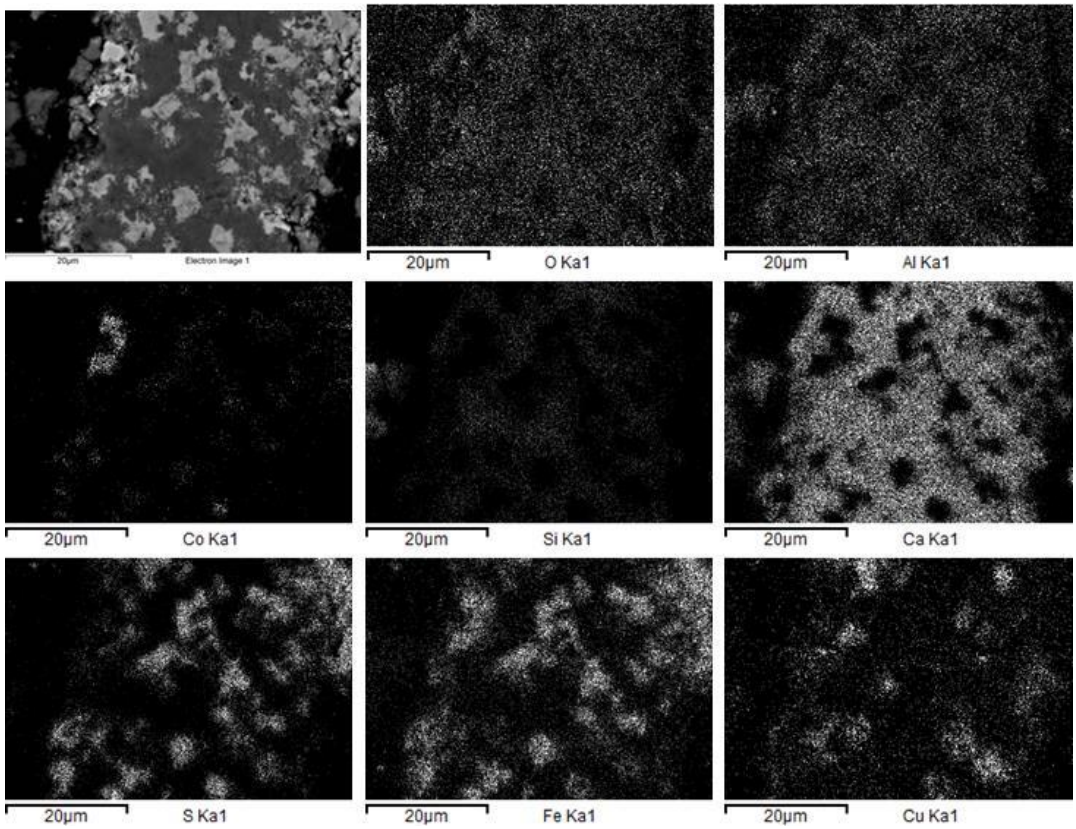

Figure 8.19 - Elemental mapping of the slag sample, sulphidised for 2 hours at 1323 K in the elevating hearth furnace, molar ratio of MO:$CaSO_4$:C = 1:1.3:0.65. Argon flow rate = 2 litres min^{-1}

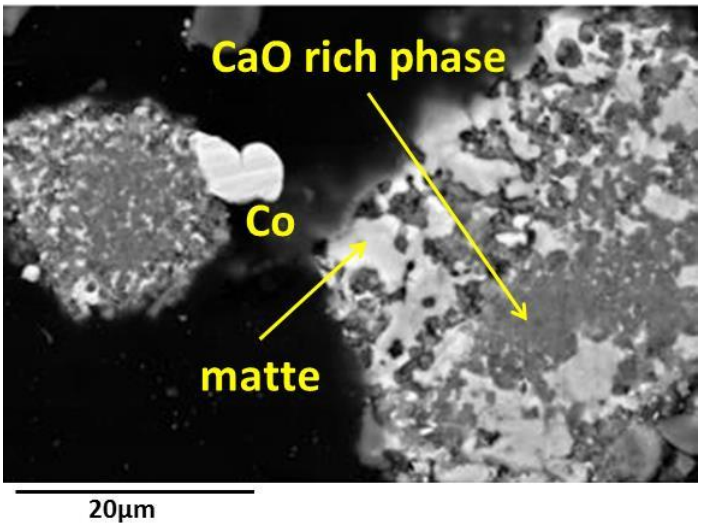

Figure 8.20 - SEM image of the slag sample, sulphidised for 2 hours at 1323 K in the elevating hearth furnace, molar ratio of MO:$CaSO_4$:C = 1:1.8:0.9. Argon flow rate = 2 litres min^{-1}

8.4.2.4 Carbothermic reduction of matte

The sulphidised slag was mixed with CaO and activated charcoal at molar ratio of MS:CaO:C = 1:2:2 and, heated/reduced between 1173 K and 1323 K. The plots of the % reduction against time curves are given in figure 8.21a. It can be observed from the plots of the % reduction versus time curves in figure 8.21a that the carbothermic reduction of sulphidised slag (matte) was extremely fast, completing in an hour, at temperature as low as 1173 K, which was not possible without sulphidising the slag (see figures 8.3a and 8.3b). The XRD pattern of the reduced sulphidised slag sample at 1173 K is shown in figure 8.21b and, there is no evidence of metal sulphides or metal oxides.

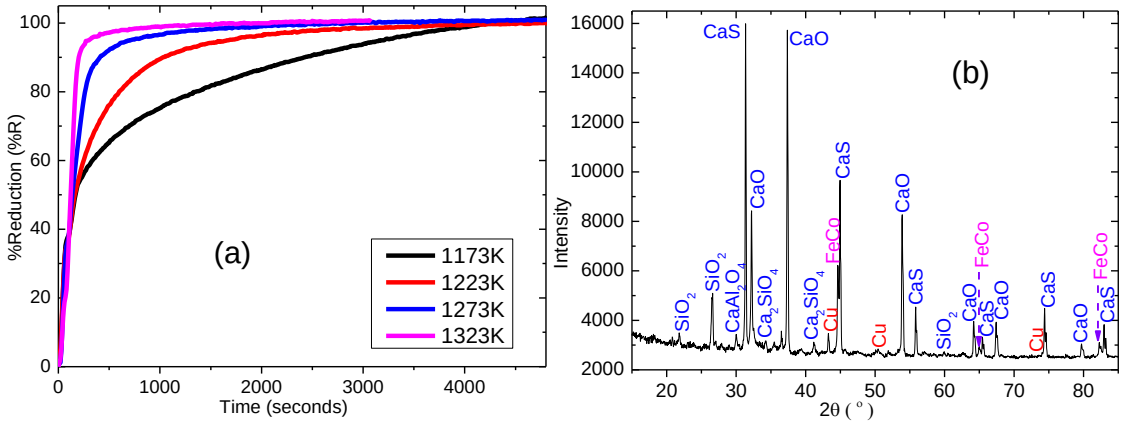

Figure 8.21 – Reduction of the sulphidised slag, in the presence of CaO and activated charcoal in the TGA equipment, molar ratio of MS:CaO = 1:2:2; (a) plots of % reduction versus time curves and (b) XRD pattern at 1173 K. Argon flow rate = 0.6 litres min^{-1}

The backscattered SEM images of the sample that was produced by carbothermic reduction of the sulphidised slag at 1323 K are presented in figure 8.22. A very rich CaO slag was produced due to presence of excess CaO from the carbothermic reduction. By comparison, the metallic phases produced via sulphidisation - carbothermic reduction processes are larger than those produced via direct reduction of the slag with carbon (see figures 8.5 and 8.9), which can be due to the difference in the volume of the liquid phases. The volume of the liquid phases is expected to be larger for the carbothermic reduction of the sulphidised slag due to presence of matte phase and this promotes rapid growth of the metallic phases during the reduction provcess.

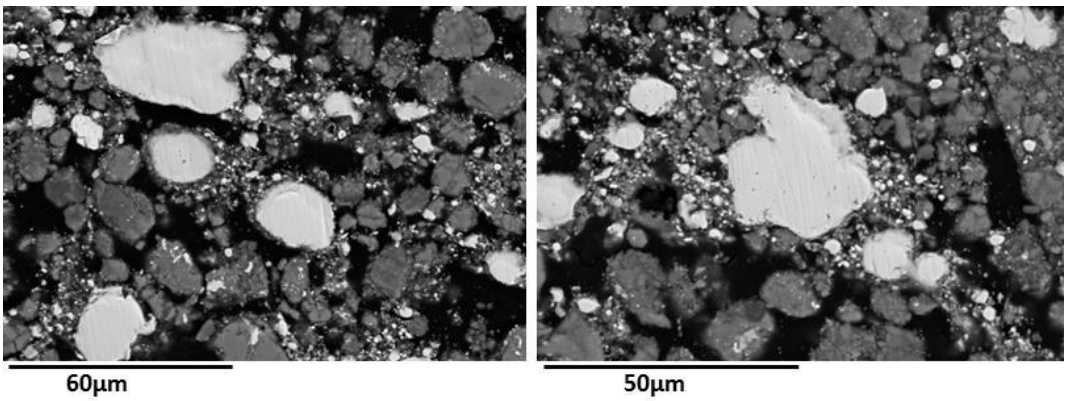

Figure 8.22 – Backscattered SEM images of the slag sample, sulphidised at 1323 K with $CaSO_4$ and reduced in the presence of CaO and activated charcoal at 1323 K, molar ratio of MS:CaO:C = 1:2:2. The bright phases are the metallic phases. Argon flow rate = 2 litres min^{-1}

8.4.2.5 General discussion

Calcium silicates and calcium aluminium silicates compounds were produced during sulphidisation of slag in the presence of $CaSO_4$. The formation of calcium silicates and calcium aluminium silicates enhances the calcination of $CaSO_4$ via reaction 8.6a as the Gibbs energy change for reaction 8.6a is more negative than for reaction 8.6b, per mole of $CaSO_4$.

$$CaSO_4 + SiO_2 + 3C = CaSiO_3 + 3CO(g) + 0.5S_2(g),\ \Delta G_{1173K} = -276kJ \qquad 8.6a$$

$$CaSO_4 + 3C = CaO + 3CO(g) + 0.5S_2(g),\ \Delta G_{1173K} = -185kJ \qquad 8.6b$$

There was significant metallisation of Co and Fe at high molar ratio of $CaSO_4$ (MO:$CaSO_4$:C = 1:1.8:9) such that high matte grade was produced during sulphidisation. The main disadvantage of high matte grade is that they have high melting point and, would therefore require higher operating temperature, if matte/slag phase separation is to be employed. Furthermore, metallisation of Fe-S and Co-S via exchange reaction with CaO yields CaS which has low solubility in either matte or slag phase and this would make the matte/slag phase separation very difficult to achieve.

The experimental results in figures 8.17a, 8.17b and 8.18 have showed that high sulphidisation of slag can be achieved by placing the alumina crucible inside the

graphite clay crucible. As a result, it would be essential to sulphidise slag in a graphite lined furnace for the industrial application. Alternatively, sulphidisation should be carried out in a controlled CO gas atmosphere.

8.4.2.6 Achieviments in sulphidisation of slag in the presence of $CaSO_4$

The experimental results have showed that nearly all Cu, Co and Fe oxide phases convert into metal sulphide phases ($CuFeS_2$, Cu_5FeS_4, Cu_2S, $CuCo_2S_4$ etc.) via sulphidisation of the slag in the presence of $CaSO_4$, in the temperature range of 1173 K – 1323 K. The sulphidisation of slag in this temperature range (1173 K – 1323 K) has never been studied and may offer several advantages to the extractive metallurgy industry as:

i. There is no production of sulphurous gas during sulphdisation.
ii. Unused $CaSO_4$ from the thermal power plant [225, 226] and from hydrometallurgical processes (see figure 1.4), may be utilised in treating the slag
iii. Corrosion is expected to be less during sulphidisation of slag in a temperature of 1173 K – 1323 K and hence cheaper furnaces may be used.

8.4.2.7 Discussion on separation techniques of the sulphidised slag

The experimental results have showed that metal oxides in the slag phase convert to metal sulphides ($CuFeS_2$, Cu_5FeS_4, $CuCo_2S_4$, FeS etc.) during sulphidisation in the presence of $CaSO_4$ and C and that the carbothermic reduction of the sulphidised slag in the presence of CaO yield metallic and alloy phases of Cu, Co and Fe (see figures 8.21b and 8.22). As noted from the SEM images in figure 8.22, the metallic phases produced via sulphidisation – carbothermic reduction of the slag are not dissolved in the slag phase and hence they may be leached in weak sulphuric acid. The dissolution of calcium silicates is not expected to occur during leaching of the metallic phases in weak acid. The CaS is expected to dissolve to yield H_2S gas which may be used for manufacturing sulphuric acid (H_2SO_4) and the proposed summary for the flow sheet is given in figure 8.23. The calcium silicate slag may be used for construction.

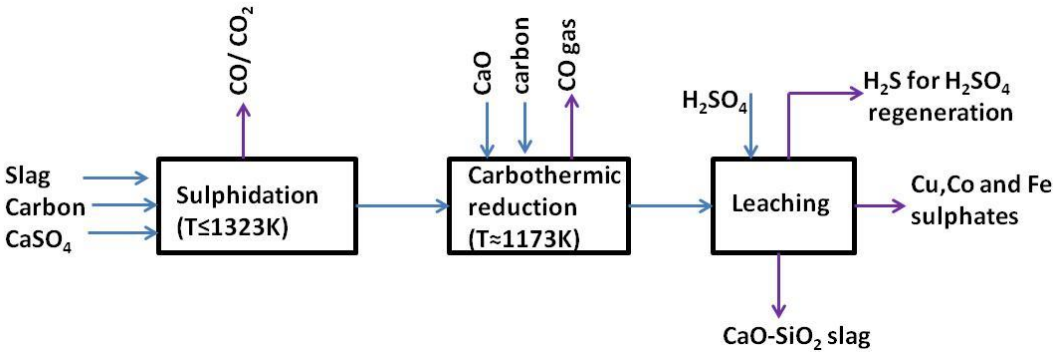

Figure 8.23 - Proposed process flow sheet for the recovery of Cu and Co from slag via sulphidisation, carbothermic reduction and leaching route

Alternatively, the sulphidised slag may be sulphate roasted below 873 K to yield Cu and Co sulphates and Fe_2O_3, under controlled partial pressures of O_2 and SO_2 gases [227]. The calcine from sulphate roasting may be leached in water or weak sulphuric acid to selectively solubilise or leach the Cu and Co sulphates as presented in the flow sheet in figure 8.24. The Nkana Cu-Co mineral sulphide concentrates are treated via sulphate roasting and water/acid leach process.

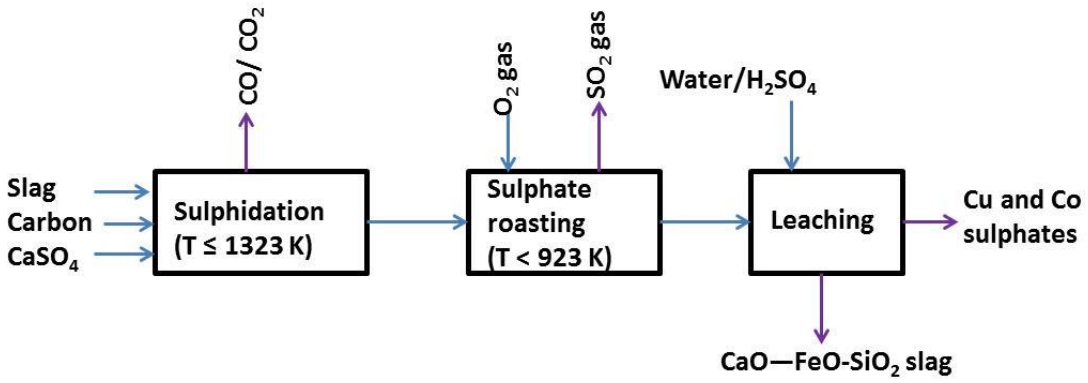

Figure 8.24 – Proposed process flow sheet for the recovery of Cu and Co from slag via sulphidisation, roasting and leaching route

8.5 Sulphidisation of slag in the presence of calcium sulphide (CaS)

Sulphidisation of slag in the presence calcium sulphide (CaS) was carried out considering that the non-magnetic fractions from the separation of the reduced mineral sulphide concentrates, contain significant amount of CaS. In addition, the regeneration

of CaO from CaS yields SO_2 and H_2S gases which needs to be captured to avoid pollution of the environment. However, CaS may be used for sulphidisation of slag in the presence and absence of carbon, as shown in figures 8.25 and 8.26, respectively. Based on the thermodynamic predictions in figures 8.25 and 8.26, slag was intimately mixed with CaS. Calcium sulphide was obtained by calcining $CaSO_4$ with activated charcoal at 1323 K via equation 8.3a.

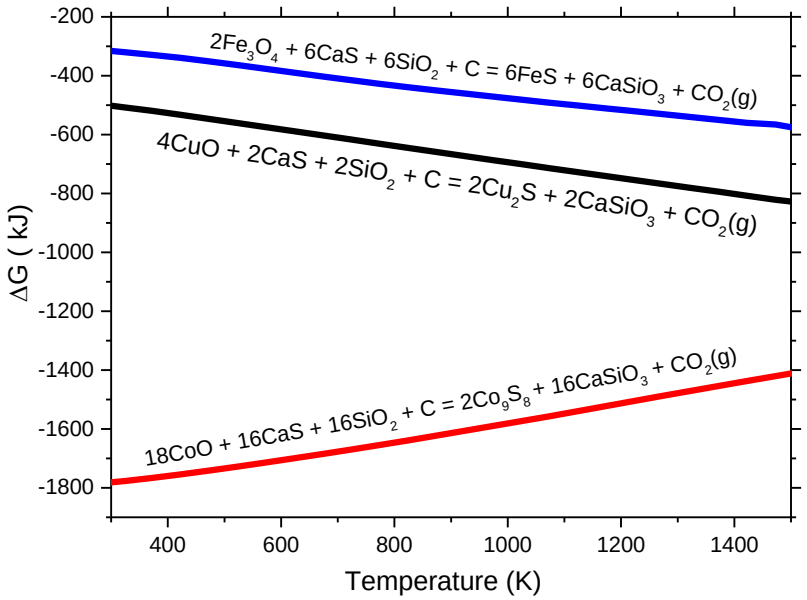

Figure 8.25 – Computed Gibbs energy change for the sulphidisation of metal oxides in the presence of CaS, SiO_2 and C,from HSC software 5.1 databse [39]

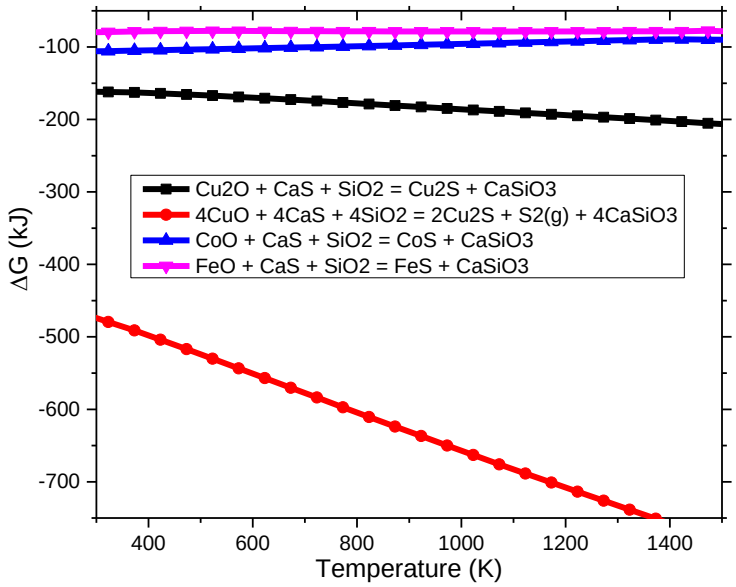

Figure 8.26 – Computed Gibbs energy change for the sulphidisation of metal oxides in the presence of CaS, and SiO_2, from the HSC software 5.1 database [39]

Sulphidisation of slag in the presence of CaS was carried out at 1173 K and 1323 K, in the elevating hearth furnace. The experiments were carried out at different mole ratios of CaS and graphite and the XRD patterns are shown in figures 8.27a, 8.27b, 8.28a and 8.28b. It can be observed from the XRD patterns in figures 8.27a, 8.27b, 8.28a and 8.28b that the sulphidisation of the slag in the presence of CaS was high, as the XRD peak intensities for the metal sulphides ($CuFeS_2$, Cu_5FeS_4, FeS) are very high. The XRD results in figures 8.27a, 8.27b, 8.28a and 8.28b further shows that sulphidisation occurred in the absence of carbon, as predicted from figure 8.26. The metal sulphides co-exist with calcium silicates ($CaSiO_3$, Ca_2SiO_4 and $Ca_2Al_2SiO_7$). By comparison, sulphidisation was higher at 1323 K than at 1173 K due to residual Fe_3O_4 in the samples at 1173 K. Similarly, residual Fe_3O_4 was present when the mole ratio of CaS was decreased to 0.8 and this is expected because there is less sulphur to react with all the metal oxides.

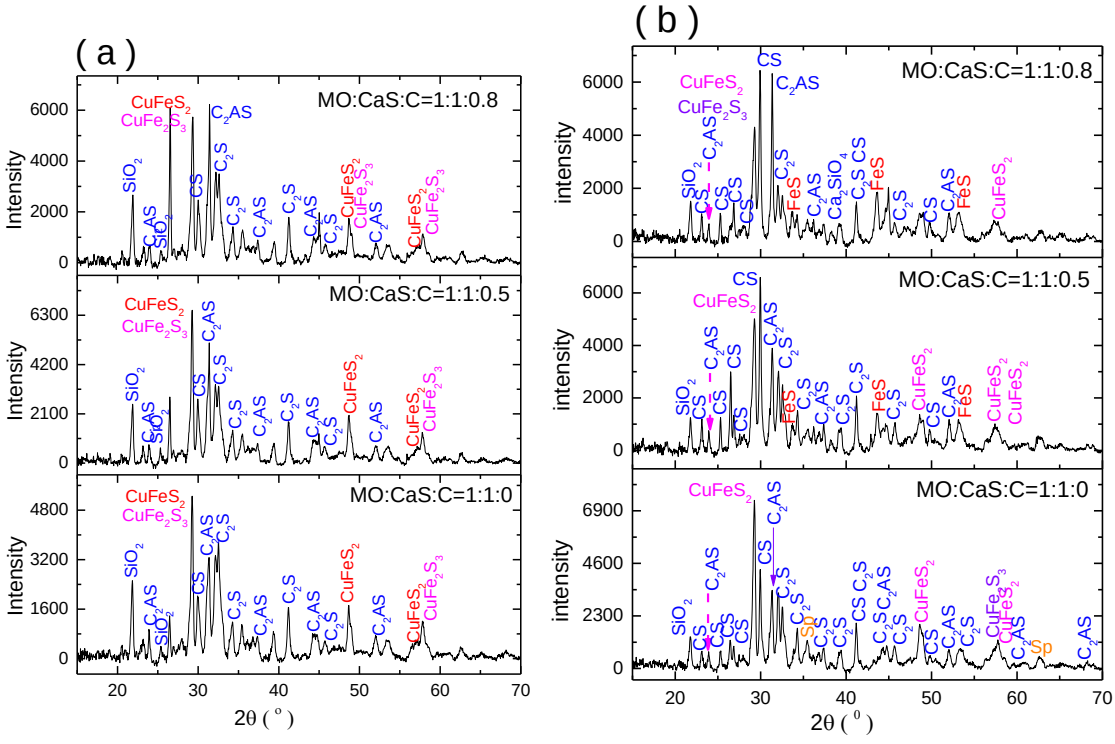

Figure 8.27 – XRD patterns of slag samples which were sulphidised for 2.5 hours in the presence of CaS and various mole ratios of graphite, in the elevating hearth furnace; (a) 1173 K and (b) 1323 K. Argon flow rate = 2 litres min^{-1}

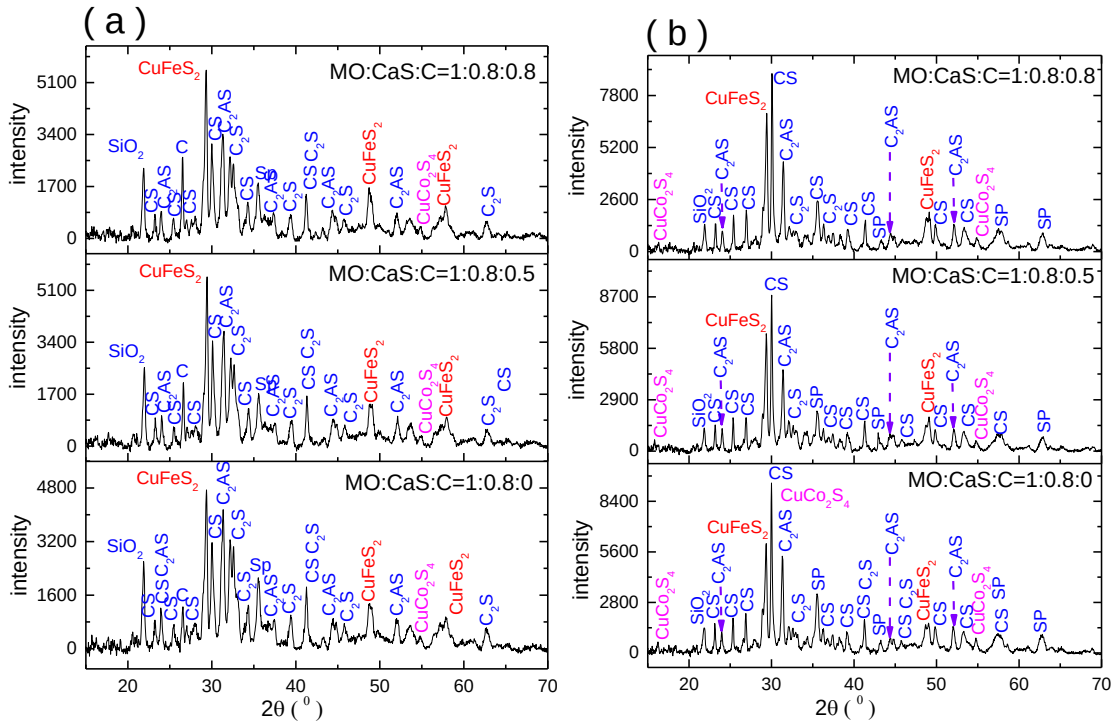

Figure 8.28 – XRD patterns of slag samples which were sulphidised for 2.5 hours in the presence of CaS and various mole ratios of graphite, in the elevating hearth furnace; (a) 1173 K and (b) 1323 K. Argon flow rate = 2 litres min^{-1}

The SEM elemental mapping of the slag samples which were sulphidised in the presence of CaS and graphite at 1173 K and 1323 K are presented in figures 8.29 and 8.30, respectively. The metal sulphide or matte phase is at, or nearer the periphery of the particles. The metallic values may be recovered by roasting the sulphidised slag at low temperatures (below 923 K) to obtain water soluble $CuSO_4$ and $CoSO_4$ as described in figure 8.24. As result, the overall process may be limited to a maximum temperature of 1323 K.

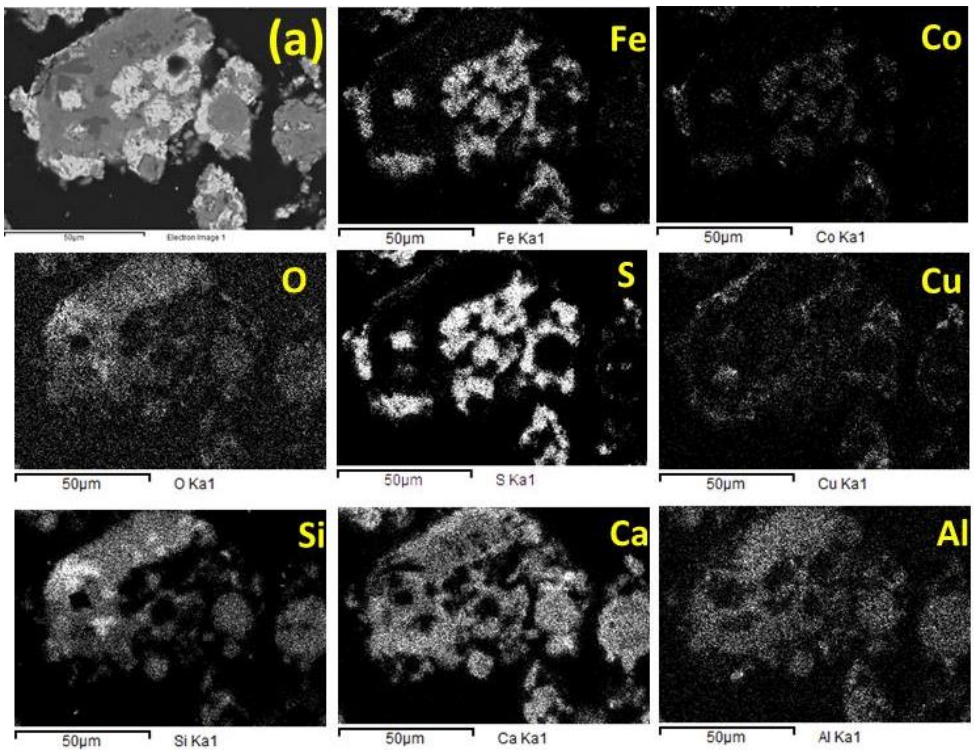

Figure 8.29 – Elemental mapping of the slag sample which was sulphidised in the presence of CaS and graphite,for 2.5 hours at 1173 K in the elevating hearth furnace, molar ratio of MO:CaS:C = 1:1:0.5

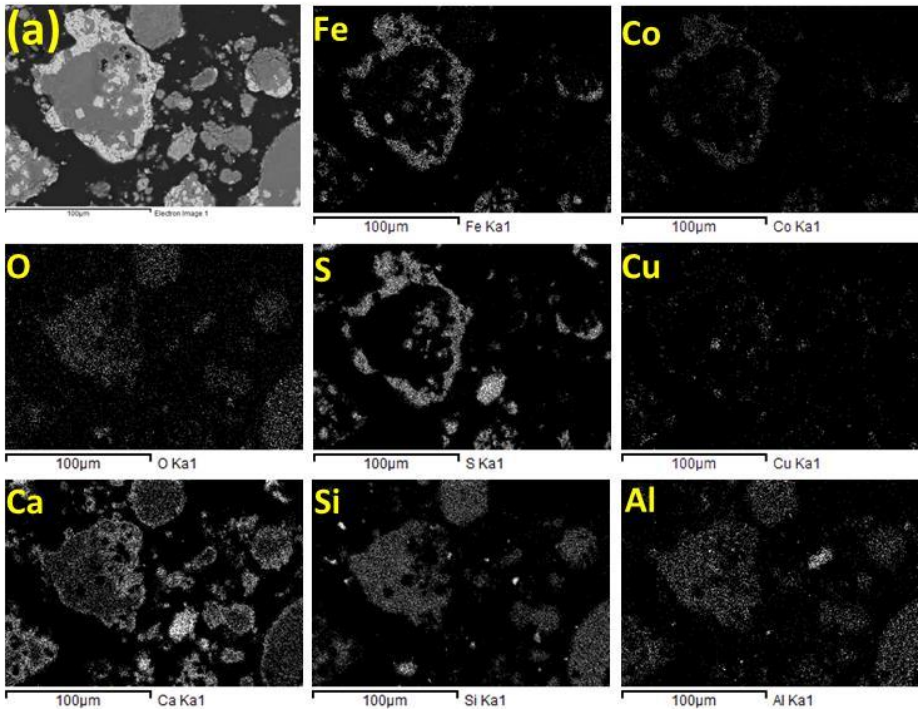

Figure 8.30 – Elemental mapping of the slag sample which was sulphidised in the presence of CaS and graphite,for 2.5 hours at 1323 K in the elevating hearth furnace, molar ratio of MO:CaS:C = 1:1:0.5

8.5.1 Summary for the sulphidisation of the slag in the presence of CaS

The sulphidisation of the slag in the presence of CaS has never been studied but it has been achieved in the present investigation (see figures 8.26 – 8.30). The major benefits of this process are:

1. The non-magnetic fractions containing CaS and SiO_2 from the reduction of Nkana and Nchanga mineral concentrates, can be used for treating slag since SiO_2 is required for the sulphidisation of metal oxide in the presence of CaS
2. There is no need to convert CaS to stable forms ($CaSO_4$, $CaCO_3$ and CaO). Note that the conversion of CaS to $CaCO_3$ and CaO releases H_2S or SO_2 poisonous gases but, this is not the case when CaS is used for treating slag
3. Production of rich calcium silicates slag which can be sold to the construction industry.

9.0 Conclusions and future work

9.1 Heat treatment of mineral concentrates in the absence and absence of CaO

1. There is a broad agreement between the experimental results in figure 5.1b and the thermodynamic predictions in figures 2.20, 5.2a, and 5.2b. For example, the main mineral sulphide phase after heating the Nchanga mineral concentrates at 1273 K, was Cu_5FeS_4, because the as-received Nchanga concentrates are rich in the Cu_2S mineral. On the other hand, the major mineral sulphide phases after heating the Nkana and Baluba mineral concentrates at 1273 K, were $CuFeS_2$ and FeS, because the as-received Nkana and Baluba concentrates are rich in the FeS_2 mineral.
2. The ion exchange reaction between iron sulphide (FeS_2 or FeS) and CaO readily takes place to yield Fe_3O_4 and $Ca_2Fe_2O_5$ phases as shown in figures 5.7a, and 5.7b. However, the ion exchange reaction between Cu_2S and CaO was very slow because residual Cu_2S was present at all temperatures. The experimental results agree with the thermodynamic prediction in figure 2.3 as the Gibbs energy change is more negative for the FeS – CaO exchange reaction.
3. The Ca_2CuFeO_3S liquid phase was formed during heat treatment of the Nchanga and Baluba mineral sulphide concentrates in the presence of CaO. This liquid phase has never been reported before.
4. The driving force for the CaO – MS exchange reaction is higher than for the CaO – SiO_2 reactions because, CaO reacted with MS to give metal oxides and CaS in the first 3 minutes at 1273 K in the Nkana sample (see figure 5.8), which has the highest SiO_2 content (40 wt. % SiO_2)
5. The metal oxides from the exchange reaction were re-sulphidised in the Nkana sample at $T \leq 1173$ K (see figures 5.7b and 5.8), because of the reactions involving CaS, metal oxides and SiO_2/Al_2O_3.

9.2 Carbothermic reduction of mineral sulphides in the presence of CaO

1. Copper, cobalt and iron metallic/alloy phases were obtained after carbothermic reduction of the mineral sulphide concentrates in the presence of CaO, with carbon black. The phase and microstructural analyses of the reacted samples using XRD and SEM-EDX, showed no evidence of mineral sulphides ($CuFeS_2$, Cu_2S, $CuCo_2S_4$, FeS), when the reduction reaction was complete. SEM-EDX semi-quantitative analysis of the metallic/alloy phases confirmed that their purity were over 96 wt. % (see table 6.1).
2. The carbothermic reduction of the mineral sulphides in the presence of CaO, with carbon black is quite sensitive to the reduction temperature as shown from; (i) the plots of % reduction versus time curves (see figure 6.1), (ii) XRD patterns (see figure 6.2a and 6.2b) and (iii) SEM images (see figure 6.9, 6.11, 6.13 – 6.15). Reduction was incomplete at 1073 K, irrespective of the holding time, but completed within 2 hours at $T \geq 1223$ K.
3. The extent of metallisation increases with increase in the mole ratio of CaO as shown in figure 6.3. However, the effect of changing the mole ratio of CaO is not important below 60 % reduction at 1273 K as the exchange reaction appear to occur mainly via CaO - S_2 gas reaction.
4. The mole ratio of carbon black should be equal to or higher than that of CaO as metallisation was incomplete at the molar ratio of MS:CaO:C = 1:2:1. The metallic/alloy phases of Cu, Co and Fe co-exist with; (i) Cu_2S and calcium silicates ($CaSiO_3$, Ca_2SiO_4, $CaAl_2Si_2O_7$ etc.) in the Nchanga and Nkana samples and (ii) $Ca_2Fe_2O_5$ in the Baluba sample at the molar ratio of MS:CaO:C = 1:2:1 (see figure 6.5a). On the other hand, the mole ratio of CaO should not be too high as metallisation is incomplete at the molar ratio of MS:CaO:C = 1:2:4 at $T \geq 1223$ K. The exchange reaction is suppressed with increase in the mole ratio of CaO, because of the increasing distance between the CaO and MS particles.
5. CaO does not react with the gangue minerals (SiO_2 and Al_2O_3) at molar ratio of $C/CaO \geq 1$ and $T \leq 1323$ K. This is because the metallic phases co-exist with CaS, SiO_2 and excess CaO (see figure 6.5b). The volume of the liquid phase is smaller in the sample at the molar ratio of $C/CaO \geq 1$ and hence the CaO – SiO_2 solid state reaction does not take place.

6. The extent and rate of metallisation increases with increase in the mole ratio of graphite as shown in figure 6.6. It seems that the overall reduction is governed by the reduction of the intermediate Ca_2CuFeO_3S liquid phase.

9.2.1 Reaction mechanisms and kinetics

1. The rate of reduction of the mineral sulphide concentrates in the presence of CaO and carbon black is faster at molar ratio of MS:CaO:C = 1:2:1, (see figures 6.4) at T ≥ 1223 K because of the presence of the Ca_2CuFeO_3S liquid phase (see figures 6.26a and 6.26b). However, the metallic phases are surrounded by the CaS rich phase when metallisation takes place via reduction of the Ca_2CuFeO_3S liquid phase (see figure 6.25b and 6.25d).
2. The metallisation of Fe occurs via reduction of the intermediate phase of Fe-O (FeO and Fe_3O_4). This is because Fe-O (FeO and Fe_3O_4) and CaS were obtained in the first 2 minutes at 1273 K and molar ratio of C/CaO ≥ 1, with carbon black (see figures 6.16 and 6.18).
3. The formation of CaS and hence metallisation of Cu, Co and Fe require that there is good contact between the CaO and C particles. CaS was hardly formed when the pellet consisting of the mixture of mineral sulphide concentrates + C was covered by CaO powder (see the arrangement in figure 6.21b).
4. The metallisation of Cu may take place via diffusion of sulphur from the mineral sulphide to the CaO particles in the presence of carbon black (see figures 6.20a, 6.22a and 6.22b).
5. The carbothernic reduction of the mineral sulphide concentrates in the presence of CaO is controlled by the mixed reaction model as analysed in figures 6.27a and 6.27b and, table 6.2.
6. The average activation energies in the lower temperature regime (T ≤ 1223 K) (278 kJ – 364 kJ) for the reduction of mineral sulphides with carbon black agrees with the activation of 251 kJ – 360 kJ for the CO_2 – C reaction [184, 185]. Phase analysis of the partially reacted samples in the lower temperature regime, e.g. at 1073 K showed the presence of Fe_3O_4 (see figure 6.2a, 6.9 and 6.11) and the reduction of this phase is controlled by the CO_2 – C reaction [28].
7. The average activation energies in the high temperature regime (T ≥ 1223 K) for Nkana (220 ± 17 kJ) and Baluba (209 ± 40 kJ) are comparable to the enthalpy change for reaction 6.8a. CaS and $CaSO_4$ were observed in the first 6 minutes at

1273 K suggesting that reaction 6.8a might be the determining factor to the overall metallisation. The average activation energy was 126 ± 17 kJ in the high temperature regime (T ≥ 1273 K) for Nchanga and this is comparable to the enthalpy change of 125 kJ for the carbothermic reduction of the Cu_2S mineral (reaction 6.8b).

8. The activation energies were lowest and highest in the high temperature regime and low temperature regime, respectively, at the molar ratio of MS:CaO:C = 1:2:1 (see table 6.5). This is because there is a larger volume of the liquid phase (Ca_2CuFeO_3S) in the high temperature regime.

9.2.2 High temperature carbothermic reduction at 1573 K

1. Excess CaO reacted with the gangue minerals to form complex calcium silicate compounds at twice the stoichiometric molar ratio of CaO (MS:CaO = 1:2), irrespective of the mole ratio of C at 1573 K (see figures 6.30 and 6.32b). The samples are nearly molten at 1573 K and, the presence of the liquid phase favours the reactions between CaO and gangue minerals (SiO_2, Al_2O_3). The metallic phases did not dissolve in the slag phase as shown in figure 6.31.
2. The reduction of the mineral sulphides were completed within an hour at 1573 K, even at very high molar ratio of C (MS:CaO:C = 1:2:4), which was not possible at T ≤ 1323 K.
3. The metallic and CaS particles were larger for the carbothermic reduction at 1573 K than at T ≤ 1323 K, as the samples are complete molten at 1573 K.

9.2.3 Separation of metallic phases

1. Nearly all the metallic/alloy constituents of Cu, Co and Fe were magnetically separated from the reduced Nkana and Baluba samples. The high separation of the metallic/alloy phases in these samples is because, the Co and Fe spheres were embedded in the Cu matrix (see figures 6.18, 6.25 and 6.31). The Co and Fe spheres were embedded in the Cu matrix as Cu mainly originates from the $CuFeS_2$, Cu_5FeS_4 and $CuCo_2S_4$ mineral phases, in the Nkana and Baluba samples. However, the embedment of Co and Fe spheres in Cu matrix prevents further separation of Co and Fe from Cu.

2. Part of Cu was not separated out or recovered in the magnetic fraction, from the reduced Nchanga sample. Microscopic examination showed that the unseparated Cu originated from the reduction of the Cu_2S.
3. Magnetic separation is greatly affected by the reduction temperature. The magnetic fraction had Fe_3O_4 and Cu_5FeS_4 when the samples were reduced at 1173 K, due to incomplete reduction (see figures 6.35). Reduction was complete within 2 hours at T $\geq$ 1223 K, but separation required fewer cycles when the samples were reduced at 1573 K than at 1273 K since the metallic particles are larger at 1573 K.
4. The mole ratio of CaO and C is important for the effective separation of the metallic phases. The mole ratio of C should be higher than for CaO to avoid sintering between the metallic and CaS phases. Part of CaS reports to the magnetic fraction when there is sintering between CaS and metallic phases.
5. The gravity method may be applied to separate out copper from the non-magnetic fraction.
6. Magnetic separation is not possible for the samples reduced with graphite due to sintering between CaS and metallic phases, as metallisation takes place via reduction of the intermediate Ca_2CuFeO_3S liquid phase.

9.2.4 Energy analysis

The theoretical energy requirement for the carborthermic reduction of mineral sulphides in the presence of CaO was estimated by the HSC software. The theoretical energy was 1.1 kWh – 2.9 kWh per kg of metallic phase (Cu + Co + Fe) as shown in table 6.11. The theoretical energy requirement compares well with the theoretical energy of 1.8 kWh – 2.4 kWh, for the production of Fe in the blast furnace, per ton of metal (see table 6.12). The theoretical energy for the carbothernic reduction of mineral sulphides may decrease to less than 0.3 kWh per kg of Cu + Co + Fe, if the CO gas from the reduction reaction is utilised in the reduction process (see figure 6.41).

9.3 Lime roast – reduction of the mineral sulphides

1. Metal oxides (CuO and Fe_2O_3) and $CaSO_4$ were produced during roasting of the mineral sulphide concentrates in the presence of CaO, in air (21 % O_2), at 773 K

– 973 K. However, the molar ratio of MS:CaO = 1:1.5 is necessary for obtaining metal oxides and $CaSO_4$ phases in the lime roast calcine at T ≤ 923 K because; (i) metal sulphates are produced at molar ratio of MS:CaO = 1:1 and (ii) CaS is produced at molar ratio of MS:CaO = 1:2 (see figures 7.2a, 7.2b, 7.4a and 7.4b).

2. The formation of CaS during roasting of the mineral sulphide concentrates in the presence of CaO, at molar ratio of MS:CaO = 1:2, is caused by; (i) the ion exchange reaction between CaO and Fe-S or S_2 gas (see figure 7.5) and (ii) the reactions involving FeS / S_2 gas, CaO and O_2 gas (see equations 7.9a and 7.8b).
3. The sample height should not be too high during roasting of the mineral sulphides concentrates in the presence of CaO, as discussed in section 7.1.2. This is because O_2 gas does not easily diffuse to the bottom of the sample when the height of the sample is too high. Therefore, the roasting reactions should be carried out in the rotary kiln, to allow uniform exposure of the sample to the O_2 gas.
4. The roasting of the mineral sulphides in the presence of CaO, in air, follows the interface model (see figure 7.10a) with activation energy in the range of 8.8 kJ – 11.7 kJ (see figure 7.11). The activation energy is comparable to the activation energy of 8 kJ - 14 kJ for the sulphation of CaO in the presence of SO_2 and O_2 gases, reported by Allen and Hayhurst [203].
5. Metallic Cu with a purity of about 98 wt.% was produced after carbothermic reduction of the lime roast calcine at 1073 K, with carbon black (see table 7.1). Metallisation of Cu was incomplete below 1073 K but, Cu, Cu_2S and CaS were obtained above 1073 K.
6. The loss of sulphur was very minimal during lime roast - carbothermic reduction process of the Nchanga sample, with carbon black (table 7.3). XRD analysed in figure 7.13a showed that sulphur was fixed as $CaSO_4$.
7. Mineralogical composition is very important for achieving preferential metallisation of copper at 1073 K with carbon black. Copper ferrite ($CuFeO_2$) was also formed during reduction of CuO which originated from the roasted Cu_5FeS_4 and $CuFeS_2$ mineral particles. For example, metallisation of Cu was low in the Nkana and Baluba samples because most of the copper is found in the chalcopyrite ($CuFeS_2$) mineral. It has been proposed that the preferential reduction of Cu via lime roast - carbothermic reduction with carbon black would be more suitable for mineral sulphide concentrates containing Cu_2S or CuS mineral phases, such as the Nchanga concentrates.

8. Complete metallisation of Cu, Co and Fe was achieved when the lime roast calcines were reduced with activated charcoal at 1073 K and 1123 K. The metallic phases co-exist with CaS (see figure 7.17) because $CaSO_4$ was calcined to CaS in the presence of activated charcoal. The metallisation of Cu, Co and Fe was very low at 1073 K and 1123 K, without lime roasting of the mineral sulphide concentrates. Therefore, the lime roast - reduction route is a major breakthrough to the carbothermic reduction of mineral sulphides.
9. The theoretical energy for the preferential reduction of copper from the lime-roast calcine at 1073 K is very comparable to the theoretical energy for producing copper via conventional smelting at about 1473 K, per ton of metal.
10. The theoretical energy requirement for the complete metallisation of Cu, Co and Fe from the Nchanga lime roast calcine at 1073 K, is equal to the theoretical energy for smelting of the Cu-Co slag at 1923 K. However, considering the energy involved in conventional copper smelting at 1473 K and for recovering the Cu and Co via smelting of slag at 1923 K and the theoretical energy requirement for producing Cu, Co and Fe via lime roast – reduction process at 1073 K is lower.

9.4 Treatment of copper-cobalt slag

1. Complete solid state reduction of metal oxides from slag via carbothermic reduction requires higher reduction temperature ($T \geq 1323$ K) and a very reactive carbon such as activated charcoal as shown in figures 8.3a, 8.3b, 8.4a, 8.4b and 8.5. The addition of 25 wt.% CaO increased the extent of metalilisation as shown in figures 8.7a and 8.7b. However,the metallic phases were too small (< 15 µm) in the samples reduced, with and without additional 25 wt. % CaO (see figures 8.5 and 8.9) such that magnetic separation was not possible.
2. The rate of reduction was higher with activated charcoal than with carbon black as shown in figure 8.10. However, the rate of reduction was highest for the carbothermic reduction of slag with activated charcoal, in the presence of addition 25 wt. % CaO. The activation energies were 288 ± 64 kJ and 271 ± 34 kJ for the carbothermic reduction of slag with carbon black and activated charcoal, respectively, suggesting that the rate determining step is the CO_2 – C reaction, which has the activation energy in the range of 250 kJ – 360 kJ [218, 219].

3. The metal oxides in the slag were converted to metal sulphides ($CuFeS_2$, Cu_2S, Cu_5FeS_4) when slag was sulphidised in the presence of $CaSO_4$ and C (graphite and activated charcoal), in the temperature range of 1173 K - 1323 K.
4. The sulphidisation of Fe in the TGA equipment appear to be controlled by the reduction of the Fe_3O_4 phase. It is for this reason that the overall sulphidisation was slightly higher with activated charcoal than with carbon black, at 1173 K and 1223 K (see figures 8.12 and 8.13).
5. The XRD results in figures 8.12 and 8.13 and the reaction kinetics analysis in figure 8.13, shows that there is a change in the reaction mechanism for the sulphidisation of slag at 1273 K and 1223 K with carbon black and activated charcoal, respectively. The activation energies were about 215 kJ in the high temperature regimes (i.e. $T \geq 1273$ K with graphite and $T \geq 1223$ K with activated charcoal) and hence sulphidisation was controlled by the $CaSO_4 - CaS$ reaction (equation 8.5c), based on the experimental data and analysis from the previous authors [85]. On the other hand, the low temperature regimes appear to be controlled by the $CO_2 - C$ reaction based on the activation energy values and phase analysis.
6. The highest sulphidisation of the slag in the presence of $CaSO_4$ and graphite occurred when the experiments were carried out in the elevating hearth furnace, where the alumina crucible containing the sample was placed inside the graphite clay crucible (figures 8.17 and 8.18). Therefore, it is important to maintain a lower partial pressure of O_2 gas, throughout the experiment so as to maintain the stability of the metal sulphide (see figure 8.16).
7. The use of excess $CaSO_4$ promote metallisation during sulphidisation of slag as shown in figures 8.17a and 8.20.
8. There is a broad agreement between the thermodynamic prediction in figure 2.16 and the experimental results in figure 8.17a as $CuFeS_2$ and Cu_5FeS_4 co-exist with FeS.
9. Complete metallisation was achieved via sulphidisation of the slag, followed by carbothermic reduction of sulphidised slag (matte) at 1173 K (figure 8.21a, 8.21b and 8.22). The metallic phase particles produced via sulphidisation and carbothermic reduction of the sulphidised slag, were larger than those produced via carbothermic reduction of the slag.

10. The metal oxides (Cu-O, Co-O and Fe-O) in the slag transforms into a mixture of metal sulphide ($CuFeS_2$, Cu_5FeS_4, Cu_2S and FeS) via sulphidisation reaction in the presence of CaS, at 1173 K and 1323 K as shown in figures 8.27 – 8.30.

9.5 Major achievements of the project

1. The mineral sulphides were reduced to metallic/alloy phases after carbothermic reduction of the mineral sulphide concentrates in the presence of CaO, above 1223 K. Sulphur was tied up as CaS during reduction. The metallic/alloy phases were separated from the reduced samples by magnetic separation. The proposed method looks to be economical and environmentally friendly for treating the Cu-Co mineral sulphide concentrates as:
    (i) Co and part of Cu are lost into the slag phase during the conventional copper smelting process. The recovery of Cu and Co from slag is such a complex and energy intensive process. Moreover, Cu and Co are recovered from slag as a Cu-Co-Fe alloy which requires further processing.
    (ii) A dilute SO_2 gas is generated when the mineral sulphides concentrates are roasted below 973 K. In addition, the production of Cu and Co from the leach solution has many stages and part of cobalt is lost in to the solution [29].
2. The optimum conditions for the carbothermic reduction of the mineral sulphide concentrate in the presence of CaO have been determined. The reduction temperature should be above 1173 K for the complete reduction of the mineral sulphides and the mole ratio of carbon should be slightly higher than that of CaO to avoid sintering between CaS and metallic phases.
3. Calcium sulphide (CaS) from the reduction of mineral sulphides may be utilised in the slag treatment or sulphidisation of the Cu-Co slag as shown from the experimental results in figures 8.27 – 8.30.
4. The low temperature ($\leq$ 1123 K) recovery of metallic/alloy phases of Cu, Co and Fe has been investigated. It can be achieved by employing the lime roast - reduction process.
5. Sulphidisation of the slag in the presence of $CaSO_4$ or CaS and carbon has been achieved by controlling the mole ratio of $CaSO_4$ or C and carbon, reaction

temperature and reaction vessel atmosphere. The sulphidised slag samples were reduced in the presence of CaO and carbon.

9.6 Future work

1. The metallic/alloy phases of Cu, Co and Fe were separated from the reduced mineral sulphide concentrates, via magnetic separation. However, it was not possible to obtain the pure phases of Cu, Cu, Fe and Co-Fe alloy because, the Co and Fe metallic/alloy phases were embedded in the Cu matrix. As such, further work is required to obtain pure phases of Cu, Co and Fe from the magnetic fraction as the pure phases of Cu, Co and Fe have more economic value. Hydrometallurgical treatment (leaching of the magnetic fraction and electrowinning) might be be the easiet route for obtaining pure Cu and Co.
2. The CaO – Cu_2S eutectic melt requires further investigation as it was difficult to analyse it in detail, due to the formation of the Ca_2CuFeO_3S liquid phase.
3. The separation of metallic/alloy phases produced via lime roast – reduction process, should be investigated.
4. The experimental results in figure 8.22 have showed that the metallic phases produced via sulphidisation and carbothermic reduction of the slag are larger than those produced without sulphidisation of slag (figures 8.5 and 8.9) and hence magnetic separation should be investigated for separating Cu, Co and Fe from the reduced samples.

9.0 Appendices

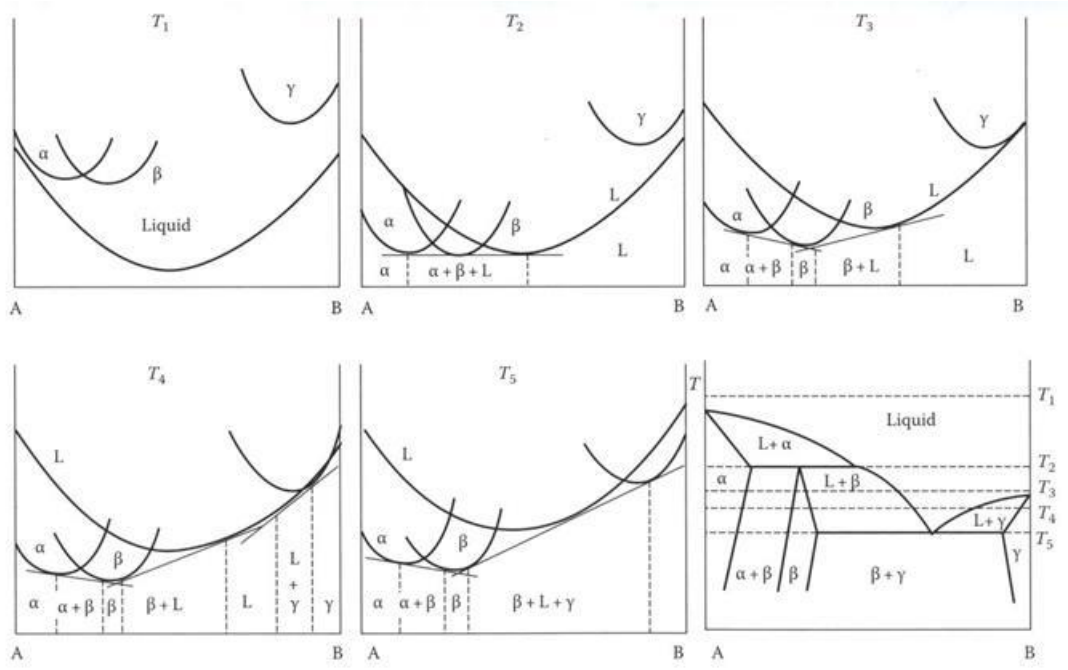

Figure A.2.1 – Derivation of the complex binary phase diagram from the free energy curves at T_1, T_2, T_3, T_4 and T_5 [100]

A.6.1. Carbothermic reduction of samples pre-heated with CaO at 1273 K

The mineral sulphide concentrates pre-heated with CaO (after mineral sulphide-lime exchange reactions) at 1273 K for MS:CaO = 1:2, were mixed with carbon equivalent to MS:CaO:C = 1:2:2 and reduced at 1273 K. The reactions were very faster for Nchanga and Baluba as shown in figure A.6.1 due to presence of the Ca_2CuFeO_3S liquid phase that was formed during mineral sulphide-lime exchange reactions (see figures 6.2b and 6.5). The plots of % reduction versus time curves show that the reduction was slow for Nkana and this is because of the absence of the Ca_2CuFeO_3S liquid phase and the presence of the metal sulphide phase ($CuFeS_2$).The SEM analysis for Baluba is shown in figure A.6.2 and the EDX semi quantitative analysis for selected areas are given in table A.6.1. It can be noted from the SEM analysis in figure A.6.2 and table A.6.1 that the metallic phases were surrounded by the CaS rich phase, owing to the fact that the

Ca_2CuFeO_3S liquid phase was the intermediate phase during reduction. The reduction reaction for the Ca_2CuFeO_3S liquid phase can be represented by equation A.6.1.

$$Ca_2CuFeO_3S + 2C = Cu + Fe + CaS + CaO + 2CO(g) \qquad \text{A.7.1}$$

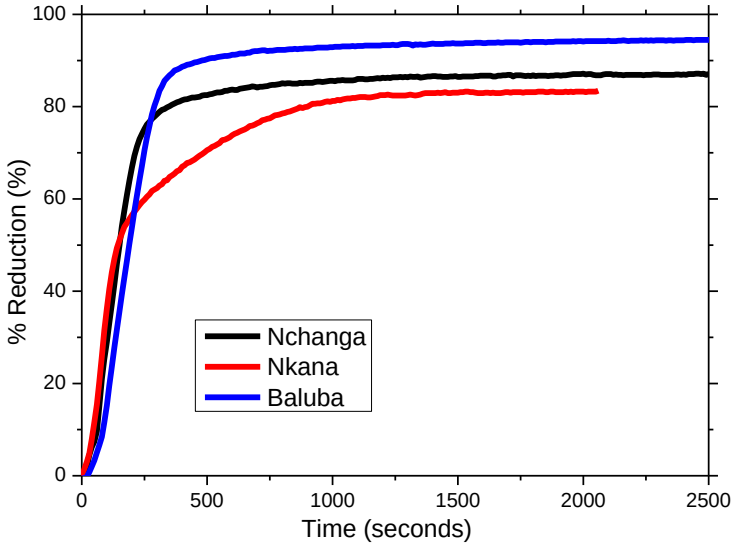

Figure A.6.1. – Plot of the % reduction versus time for the carbothermic reduction at 1273 K for MS:C = 1:2 with carbon black , the mineral sulphide concentrates was preheated in the presence of CaO at 1273 K, for MS:CaO = 1:2

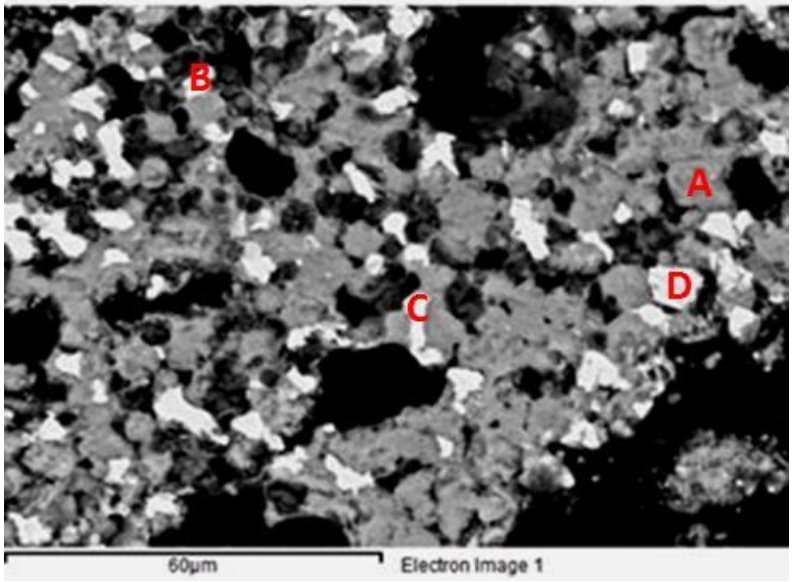

Figure A.6.2 – SEM image for Baluba sample, after carbothermic reduction at 1273 K for MS:C = 1:2 with carbon black , the mineral sulphide concentrates was preheated in the presence of CaO at 1273 K, molar ratio of MS:CaO = 1:2. The compositions of areas A – D are given in table A.61. Argin flow rate = 0.6 litres min^{-1}

Table A.6.1 SEM-EDX semi-quantitative analysis (wt.%) for the sample in figure A.6.2

Area	Cu	Fe	Co	Ca	S	O
A	4.2	1.6	-	41	37.8	15
B	71.6	16.9	-	-	-	8.9
C	76.2	23.6	-	-	-	-
D	11.4	82.6	3.8	1.35	0.8	-

Table A.6.2 – Energy analysis and mass balance for the carbothermic reduction of Nchanga in the presence of CaO

Feed	T(°C)	Kmoles	Wt(kg)
$CuFeS_2$	25	0.032	5.872
Cu_5FeS_4	25	0.022	11.04
Cu_2S	25	0.178	28.329
Cu	25	0.005	0.318
CoS_2	25	0.002	0.246
FeS_2	25	0.041	4.919
$CuCO_3$	25	0.023	2.842
Cu_2O	25	0.008	1.145
$CaMg(CO_3)_2$	25	0.007	1.291
SiO_2	25	0.574	34.488
Al_2O_3	25	0.005	0.51
CaO	25	0.414	23.217
C	25	0.749	9
Output			
Cu	1000	0.543	34.505
Fe	1000	0.095	5.305
Co	1000	0.002	0.118
CaS	1000	0.413	29.794
CO(g)	1000	0.785	22
CaO*MgO	1000	0.007	0.675
Al_2O_3	1000	0.005	0.51
$H_2(g)$	1000	0.276	0.556

	kMol	amount	Heat (kwh)
IN1	2.338	128.225	-261.33
OUT1	2.7	127.952	-197.68
BALANCE	0.362	-0.273	63.65

Table A.6.3 – Energy analysis and mass balance for the carbothermic reduction of Nkana in the presence of CaO

Feed	T(°C)	Kmoles	Wt(kg)
$CuFeS_2$	25	0.069	12.6
Cu_5FeS_4	25	0.002	1
Cu_2S	25	0.02	3.2
Cu	25	0.006	0.4
CoS_2	25	0.02	2.5
FeS_2	25	0.11	13.2
$CuCO_3$	25	0.006	0.7
$CaMg(CO_3)_2$	25	0.054	10
SiO_2	25	0.656	39.4
Al_2O_3	25	0.08	8.2
CaO	25	0.404	22.67
C	25	0.579	6.96
H_2O	25	0.056	1
Output			
Cu	1000	0.131	8.3
Fe	1000	0.208	11.64
Co	1000	0.02	1.2
CaS	1000	0.404	29.14
CO(g)	1000	0.694	19.433
CaO*MgO	1000	0.054	5.222
Al_2O_3	1000	0.08	8.2
$H_2(g)$	1000	0.055	0.111
SiO_2	1000	0.656	39.4

	kMol	amount	Heat (kwh)
IN1	2.063	121.83	-325.39
OUT1	2.303	122.646	-265.04
BALANCE	0.24	0.816	60.34

Table A.6.4 - Energy analysis and mass balance for the carbothermic reduction of Baluba in the presence of CaO

Feed	T(°C)	Kmoles	Wt(kg)
$CuFeS_2$	25	0.281	51.6
Cu_5FeS_4	25	0.007	3.5
Cu_2S	25	0.018	2.8
Cu	25	0.009	0.6
CoS_2	25	0.019	2.3
FeS_2	25	0.138	16.5
$CaMg(CO_3)_2$	25	0.072	13.2
SiO_2	25	0.163	9.8
Al_2O_3	25	0.023	2.3
CaO	25	0.921	51.625
C	25	1.175	14.114
H_2O	25	0.111	2
Output			
Cu	1000	0.361	22.923
Fe	1000	0.426	23.77
Co	1000	0.019	1.1
CaS	1000	0.92	66.375
CO(g)	1000	1.319	36.942
CaO*MgO	1000	0.072	6.9
Al_2O_3	1000	0.023	2.3
$H_2(g)$	1000	0.11	0.222
SiO_2	1000	0.163	9.8

	kMol	amount	Heat (kWh)
IN1	2.935	170.339	-292.49
OUT1	3.411	170.332	-200.11
BALANCE	0.476	-0.007	92.38

Table A.7.1 – Energy analysis and mass balance for the lime roast of Nchanga concentrates

Feed	T(°C)	Kmoles	Wt(kg)
$CuFeS_2$	25	0.032	5.872
Cu_5FeS_4	25	0.022	11.04
Cu_2S	25	0.178	28.329
Cu	25	0.005	0.318
CoS_2	25	0.002	0.246
FeS_2	25	0.041	4.919
$CuCO_3$	25	0.023	2.842
Cu_2O	25	0.008	1.145
$CaMg(CO_3)_2$	25	0.007	1.291
SiO_2	25	0.574	34.488
Al_2O_3	25	0.005	0.51
CaO	25	0.414	23.217
$O_2(g)$	25	0.943	30.18
H_2O	25	0.278	5
Output			
CuO	600	0.503	40
Fe_2O_3	600	0.047	7.58
CoO	600	0.002	0.15
$CaSO_4$	600	0.413	56.28
$CaMg(CO_3)_2$	600	0.007	1.291
Al_2O_3	600	0.005	0.51
SiO_2	600	0.574	34.488
$CuCO_3$	600	0.023	2.842
Cu_2O	600	0.008	1.145
$H_2O(g)$	25	0.278	5

	kMol	amount	Heat (kwh)
IN1	2.532	149.396	-261.29
OUT1	1.86	149.286	-352.49
BALANCE	-0.671	-0.11	-91.2

Table A.7.2 - Energy analysis and mass balance for the lime roast of Nkana in the presence of CaO

Feed	T(°C)	Kmoles	Wt(kg)
$CuFeS_2$	25	0.069	12.6
Cu_5FeS_4	25	0.002	1
Cu_2S	25	0.02	3.2
Cu	25	0.006	0.4
CoS_2	25	0.02	2.5
FeS_2	25	0.11	13.2
CuCO3	25	0.006	0.7
$CaMg(CO_3)_2$	25	0.054	10
SiO_2	25	0.656	39.4
Al_2O_3	25	0.08	8.2
CaO	25	0.404	22.67
$O_2(g)$	25	0.835	26.73
H2O	25	0.056	1
Output			
CuO	600	0.125	9.925
$Fe2O_3$	600	0.104	16.629
CoO	600	0.02	1.525
$CaSO_4$	600	0.404	55.06
$CaMg(CO_3)_2$	600	0.054	10
Al_2O_3	600	0.08	8.2
$H_2O(g)$	600	0.056	1
SiO_2	600	0.656	39.4

	kMol	amount	Heat (kwh)
IN1	2.319	141.6	-325.39
OUT1	1.5	141.739	-412.27
BALANCE	-0.819	0.139	-86.88

Table A.7.3 - Energy analysis and mass balance for the lime roast of Baluba

Feed	T(°C)	Kmoles	Wt(kg)
$CuFeS_2$	25	0.281	51.6
Cu_5FeS_4	25	0.007	3.5
Cu_2S	25	0.018	2.8
Cu	25	0.009	0.6
CoS_2	25	0.019	2.3
FeS_2	25	0.138	16.5
$CaMg(CO_3)_2$	25	0.072	13.2
SiO_2	25	0.163	9.8
Al_2O_3	25	0.023	2.3
CaO	25	0.921	51.625
$O_2(g)$	25	1.89	60.466
H_2O	25	0.111	2
Output			
CuO	600	0.361	28.716
Fe_2O_3	600	0.213	33.957
CoO	600	0.019	1.398
$CaSO_4$	600	0.921	125.375
$CaMg(CO_3)_2$	600	0.072	13.2
Al_2O_3	600	0.023	2.3
H_2O	600	0.111	2
SiO_2	600	0.163	9.8

	kMol	amount	Heat (kwh)
IN1	3.65	216.691	-292.49
OUT1	1.882	216.746	-507.06
BALANCE	-1.768	0.055	-214.57

Table A.7.4 - Energy analysis and mass balance for the selective reduction Cu from the Nchanga lime roast calcine

Feed	T(°C)	Kmoles	Wt(kg)
CuO	25	0.503	40
Fe_2O_3	25	0.047	7.58
CoO	25	0.002	0.15
$CaSO_4$	25	0.413	56.28
$CaMg(CO_3)_2$	25	0.007	1.291
Al_2O_3	25	0.005	0.51
SiO_2	25	0.574	34.488
$CuCO_3$	25	0.023	2.842
Cu_2O	25	0.008	1.145
C	25	0.569	6.836
Output			
Cu	800	0.543	34.505
Fe_3O_4	800	0.032	7.311
CoO	800	0.002	0.15
$CaSO_4$	800	0.413	56.28
CO(g)	800	0.586	16.418
$CaMg(CO_3)_2$	800	0.007	1.291
Al_2O_3	800	0.005	0.51
SiO_2	800	0.574	34.488

			Heat (kWh)
IN1	2.152	151.121	-354.11
OUT1	2.162	150.954	-316.08
BALANCE	0.01	-0.168	38.02

Table A.7.5 - Energy analysis and mass balance for the carbothermic reduction of the Nchanga lime roast calcine

Feed	T(°C)	Kmoles	Wt(kg)
CuO	25	0.503	40
Fe_2O_3	25	0.047	7.58
CoO	25	0.002	0.15
$CaSO_4$	25	0.413	56.28
$CaMg(CO_3)_2$	25	0.007	1.291
Al_2O_3	25	0.005	0.51
SiO_2	25	0.574	34.488
$CuCO_3$	25	0.023	2.842
Cu_2O	25	0.008	1.145
C	25	2.365	28.41
Output			
Cu	800	0.543	34.505
Fe	800	0.095	5.305
Co	800	0.002	0.118
CaS	800	0.413	29.794
CO(g)	800	2.402	67.272
CaO*MgO	800	0.007	0.675
Al_2O_3	800	0.005	0.51
SiO_2	800	0.574	34.488

	kMol	amount	Heat (kwh)
IN1	3.948	172.696	-354.11
OUT1	4.041	172.668	-245.29
BALANCE	0.093	-0.028	108.81

Table A.7.6 - Energy analysis and mass balance for the carbothermic reduction of the Nkana lime roast calcine

Feed	T(°C)	Kmoles	Wt(kg)
CuO	25	0.125	9.925
Fe_2O_3	25	0.104	16.629
CoO	25	0.02	1.525
$CaSO_4$	25	0.404	55.06
$CaMg(CO_3)_2$	25	0.054	10
Al_2O_3	25	0.08	8.2
SiO_2	25	0.656	39.4
C	25	2.182	26.212
Cu	800	0.131	8.3
Fe	800	0.208	11.64
Co	800	0.02	1.2
CaS	800	0.404	29.14
CO(g)	800	2.275	63.727
CaO*MgO	800	0.054	5.222
Al_2O_3	800	0.08	8.2
SiO_2	800	0.656	39.4

	kMol	amount	Heat (kwh)
IN1	3.626	166.951	-430.45
OUT1	3.829	166.829	-310.65
BALANCE	0.202	-0.122	119.8

Table A.7.7 - Energy analysis and mass balance for the carbothermic reduction of the Baluba lime roast calcine

Feed	T(°C)	Kmoles	Wt(kg)
CuO	25	0.36	28.654
Fe_2O_3	25	0.213	33.957
CoO	25	0.019	1.4
$CaSO_4$	25	0.921	125.375
$CaMg(CO_3)_2$	25	0.072	13.2
Al_2O_3	25	0.023	2.3
SiO_2	25	0.163	9.8
C	25	4.84	58.133
Output			
Cu	800	0.361	22.923
Fe	800	0.426	23.77
Co	800	0.019	1.1
CaS	800	0.92	66.375
CO(g)	800	4.986	139.668
$CaMg(CO_3)_2$	800	0.037	6.887
Al_2O_3	800	0.023	2.3
SiO_2	800	0.163	9.8

	kMol	amount	Heat (kwh)
IN1	6.61	272.819	-531.23
OUT1	6.934	272.823	-296.65
BALANCE	0.325	0.004	234.58

10.0 References

1. Malfliet, A., et al., *Degradation mechanisms and use of refractory linings in copper production processes: A critical review.* Journal of the European Ceramic Society, 2014. **34**(3): p. 849-876.
2. Fleitman, A.H., R.B. Herchenroeder, and J.G.Y. Chow, *Cobalt-base alloys for use in nuclear reactors.* Nuclear Engineering and Design, 1971. **15**(0): p. 345-362.
3. Zhai, X.-j., et al., *Recovery of cobalt from converter slag of Chambishi Copper Smelter using reduction smelting process.* Transactions of Nonferrous Metals Society of China, 2011. **21**(9): p. 2117-2121.
4. Hawkins, M.J., *Recovering cobalt from primary and secondary sources.* JOM, 1998. **50**(10): p. 44-45.
5. Anon, *Cobalt monograph*. Cobalt Monograph. 1960, Brussels, Belgium: Centre d'Information du Cobalt. 515.
6. Betteridge, W., *Cobalt and its alloys*. 1 ed. Industrial metals 1982, Chichester: Ellis Horwood Limited
7. Davis, J.R. and A.S.M. International, *Copper and copper alloys*. ASM specialty handbook. 2001, Materials Park, OH: ASM International. vii, 652 p.
8. West, E.G., *Copper and its alloys*. 1982, Chichester: Ellis Horwood.
9. Claig, J.R. and D.J. Vaughan, *Cobalt-bearing sulfide assemblages from the Shinkolobwe deposit, Katanga, Zaire.* American Mineralogist, 1979. **64**: p. 136-139.
10. Bodsworth, C., *The extraction and refining of metals*. Materials Science and Technology, ed. B. Ralph. 1994, Boca Raton: Fla. : CRC Press. 346.
11. Davenport, W.G.L., et al., *Extractive Metallurgy of Copper (4th Edition)*. Chemical, Petrochemical & Process. 2002: Elsevier. 1-452.
12. Norgate, T. and S. Jahanshahi, *Low grade ores – Smelt, leach or concentrate?* Minerals Engineering, 2010. **23**(2): p. 65-73.
13. Whyte, R., N. Schoeman, and K. Bowes, *Processing of Konkola copper concentrates and Chingola refractory ore in a fully integrated hydrometallurgical pilot plant circuit.* Journal of the South African Institute of Mining and Metallurgy(South Africa), 2001. **101**(8): p. 427-436.
14. Alcock, C.B., *Principles of pyrometallurgy (2nd edition)*. 1976, London: Academic Press.

15. Habashi, F., *Principles of Extractive Metallurgy*. 1969, London: Gordon and Breach. 194 - 196.
16. Maweja, K., T. Mukongo, and I. Mutombo, *Cleaning of a copper matte smelting slag from a water-jacket furnace by direct reduction of heavy metals.* Journal of Hazardous Materials, 2009. **164**(2–3): p. 856-862.
17. Lahtinen, E.J.P.a.M. *Outokumpu blister flash smelting processes*. in *Sohn International Symposium advanced processing metals and materials* 2006.
18. Schlesinger, M.E., et al., *Chapter 10 - Direct-To-Copper Flash Smelting*, in *Extractive Metallurgy of Copper (Fifth Edition)*, M.E. Schlesinger, et al., Editors. 2011, Elsevier: Oxford. p. 179-190.
19. Ruddle, R.W., *The physical chemistry of copper smelting*. 1953, London: Institution of Mining and Metallurgy.
20. Imris, I., *Cobalt distribution in Rokana smelter.* Transactions of the Institution of Mining and Metallurgy, Section C: Mineral Processing and Extractive Metallurgy, 1982. **91**: p. C153-C161.
21. Sinha, S.N. and M. Nagamori, *Activities of CoS and FeS in copper mattes and the behavior of cobalt in copper smelting.* Journal of Electronic Materials, 1991. **20**(12): p. 461-470.
22. Jones, R.T., et al., *Recovery of cobalt from slag in a DC arc furnace at Chambishi, Zambia.* Journal of The South African Institute of Mining and Metallurgy, 2002. **102**(Compendex): p. 5-9.
23. Banda, W., *High Temperature Phase Equilibria in the Fe-Co-Cu-Si system Pertaining to slag cleaning*, in *Department of Process Engineering*2006, Stellenbosch: Stellenbosch.
24. Bale, C.W., et al., *FactSage thermochemical software and databases.* Calphad: Computer Coupling of Phase Diagrams and Thermochemistry, 2002. **26**(2): p. 189-228.
25. Yang, Z., et al., *Selective leaching of base metals from copper smelter slag.* Hydrometallurgy, 2010. **103**(1–4): p. 25-29.
26. Banza, A.N., E. Gock, and K. Kongolo, *Base metals recovery from copper smelter slag by oxidising leaching and solvent extraction.* Hydrometallurgy, 2002. **67**(1–3): p. 63-69.
27. Barnes, A.R. and R.T. Jones. *Cobalt from slag-lessons in transition from laboratory to industry*. in *Conference of Metallurgists*. 2011. Montreal.

28. Rosenqvist, T., *Principles of Extractive Metallurgy (2nd edition)*. 1983, Japan: McGraw.Hill. 460-500.
29. Mututubanya, A., *Cobalt recovery from old Nkana Copper Slag via solid state carbothermic reduction and sulphation*, in *Metallurgy*2013, University of Zambia: Lusaka.
30. Jha, A., S.H. Tang, and A. Chrysanthou, *Phase equilibria in the metal-sulfur-oxygen system and selective reduction of metal oxides and sulfides .1. The carbothermic reduction and calcination of complex mineral sulfides.* Metallurgical and Materials Transactions B-Process Metallurgy and Materials Processing Science, 1996. **27**(5): p. 829-840.
31. Igiehon, U.O., *Carbothermic reduction of complex sulphides*, in *Department of materials*1990, Imperial College of Science: London.
32. Jha, A. and P. Grieveson, *Carbothermic reduction of chalcopyrite in the presence of lime. Part III. Production of iron and copper.* Scandinavian Journal of Metallurgy, 1992. **21**: p. 127-137.
33. Bronson, M.C. and H.Y. Sohn, *Carbothermic Reduction of Nickel Sulfide in the Presence of Lime.* Metallurgical transactions. B, Process metallurgy, 1983. **14 B**: p. 605-615.
34. Jha, A. and P. Grieveson, *Carbothermic reduction of pyrrhotite in the presence of lime for the production of metallic iron.* Scandinavian Journal of Metallurgy, 1992. **21**(2): p. 50-62.
35. Jha, A., P. Grieveson, and J.H.E. Jeffes, *An investigation on the carbothermic reduction of copper sulfide minerals: Kinetics and thermodynamic considerations.* Scandinavian Journal of Metallurgy, 1989. **18**: p. 31-45.
36. Ford, J. and M. Fahim, *Kinetics of cobalt sulfide reduction in the presence of calcium oxide.* Metall. Mater. Trans. B, 1975. **6**(3): p. 461-464.
37. Rankin, W.J. and T.P. Hall, *Lime - Enhanced Carbothermic reduction of Chalcopyrite*, in *Epd Congress 2009, Proceedings*, S.M. Howard, Editor. 2009. p. 817-827.
38. Machingawuta, N., A. Jha, and P. Grieveson, *Mechanism of Carbothermic Reduction of Nickel Sulfide Minerals in the Presence of Lime.* Scandinavian Journal of Metallurgy, 1989. **18**(2): p. 81-88.
39. Roine, A., *HSC Chemistry 5.1*, 2002, Outokumpu Research Oy: Finland.
40. Popil'skii, R.Y., *Superduty ceramics based on calcium oxide.* Refractories, 1976. **17**(11-12): p. 692-699.

41. Rosenqvist, T., *Phase equilibria in the pyrometallurgy of sulfide ores.* Metallurgical Transactions B (Process Metallurgy), 1978. **9B**(3): p. 337.
42. Huang, C.H., C.I. Lin, and H.K. Chen, *Carbothermic reduction of zinc sulfide in the presence of calcium oxide.* Journal of Materials Science, 2005. **40**(16): p. 4299-4306.
43. Prasad, P.M., T.R. Mankhand, and P.S. Rao, *Lime-scavenged reduction of molybdenite.* Minerals Engineering, 1993. **6**(8–10): p. 857-871.
44. Igiehon, U.O., B.S. Terry, and P. Grieveson, *Carbothermic Reduction of Antimony Sulphide.* Transactions of the Institution of Mining and Metallurgy, Section C(UK), 1992. **101**: p. 144-154.
45. Igiehon, U.O., et al., *Carbothermic reduction of lead sulphide in the presence of lime.* Transactions of the Institution of Mining and Metallurgy Section C-Mineral Processing and Extractive Metallurgy, 1992. **101**: p. C159-C164.
46. Weast, R.C., *CRC handbook of chemistry and physics : a ready-reference book of chemical and physical data*. 1983, Florida: CRC Press, Inc.
47. Payne, N., *Selective separation of metallic phases from chalcopyrite* in *Department of Materials*2000, University of Leeds: Leeds.
48. M.M, K.J.V.S.S.H.a.N., *Direct reduction of sarcheshme copper sulfide concentrate with carbon in the presence of lime.* Iranian Journal of Materials Science & Engineering, 2007. **4**: p. 23-30.
49. Charkin, D.O., et al., *Synthesis, crystal structure, and properties of novel perovskite oxychalcogenides, Ca2CuFeO3Ch (Ch=S or Se).* Materials Research Bulletin, 2010. **45**(12): p. 2012-2016.
50. Mohan, M.K., T.R. Mankhand, and P.M. Prasad, *Lime-enhanced carbon monoxide reduction of cuprous sulfide.* Metallurgical Transactions B, 1987. **18**(4): p. 719-725.
51. Bunkholt, I. and R.A. Kleiv, *The colouring effect of pyrrhotite and pyrite on micronised calcium carbonate slurries for the paper industry.* Minerals Engineering, 2013. **52**(0): p. 104-110.
52. Arvidson, B., et al., *Flotation of pyrrhotite to produce magnetite concentrates with a sulphur level below 0.05% w/w.* Minerals Engineering, 2013. **50–51**(0): p. 4-12.
53. Kutsovskaya, M.L., M.T. Hepworth, and J.R. McGaa, *Recovery of Lime, Sulfur, and Iron from Gypsum and Pyrite Wastes.* Ind. Eng. Chem. Res., 1996. **35**(5): p. 1736-1746.

54. Habashi, F. and R. Dugdale, *The reduction of sulfide minerals by hydrogen in the presence of lime.* Metall. Mater. Trans. B, 1973. **4**(8): p. 1865-1871.
55. Padilla, R., M.C. Ruiz, and H.Y. Sohn, *Reduction of molybdenite with carbon in the presence of lime.* Metallurgical and Materials Transactions B, 1997. **28**(2): p. 265-274.
56. Rao, Y.K. and S.K. El-Rahaiby, *Direct reduction of lead sulfide with carbon and lime; Effect of catalysts:Part i. experimental.* Metallurgical Transactions B, 1985. **16**(3): p. 465-475.
57. Igiehon, U.O., B.S. Terry, and P. Grieveson, *Carbothermic reduction of complex sulphides containing arsenic and antimony - part 2: carbothermic reduction of copper-arsenic sulphides.* Transactions of the Institution of Mining and Metallurgy, Section C: Mineral Processing and Extractive Metallurgy, 1994. **103**(Compendex): p. C48-C53.
58. Jha, A., U.O. Igiehon, and P. Grieveson, *Carbothermic reduction of pyrrhotite in the presence of lime for production of metallic iron. Part I. Phase equilibria in the Fe-Ca-S-O system.* Scandinavian Journal of Metallurgy, 1991. **20**(Compendex): p. 270-278.
59. Rao, Y.K., A. Adjorlolo, and J.H. Haberman, *On the mechanism of catalysis of the Boudouard reaction by alkali-metal compounds.* Carbon, 1982. **20**(3): p. 207-212.
60. Marsh, H. and D.W. Taylor, *Carbon gasification in the Boudouard reaction.* Fuel, 1975. **54**(3): p. 218-220.
61. Chien, A.C. and S.S.C. Chuang, *Effect of gas flow rates and Boudouard reactions on the performance of Ni/YSZ anode supported solid oxide fuel cells with solid carbon fuels.* Journal of Power Sources, 2011. **196**(10): p. 4719-4723.
62. Cheng, H., D.B. Reiser, and S. Dean Jr, *On the mechanism and energetics of Boudouard reaction at FeO (1 0 0) surface: 2CO→C+CO2.* Catalysis Today, 1999. **50**(3–4): p. 579-588.
63. Tang, Y. and J. Liu, *Effect of anode and Boudouard reaction catalysts on the performance of direct carbon solid oxide fuel cells.* International Journal of Hydrogen Energy, 2010. **35**(20): p. 11188-11193.
64. Habash, F., *Kinetics of metallurgical processes* 1999, Canada: Métallurgie Extractive

65. Lahiri, A. and A. Jha, *Kinetics and Reaction Mechanism of Soda Ash Roasting of Ilmenite Ore for the Extraction of Titanium Dioxide.* Metallurgical and Materials Transactions B, 2007. **38**(6): p. 939-948.
66. Khawam, A. and D.R. Flanagan, *Solid-State Kinetic Models: Basics and Mathematical Fundamentals.* The Journal of Physical Chemistry B, 2006. **110**(35): p. 17315-17328.
67. Qifeng, S., et al., *Phase formation mechanism and kinetics in solid-state synthesis of undoped and calcium-doped lanthanum manganite.* Materials Research Bulletin, 2009. **44**(3): p. 649-53.
68. Levenspiel, O., *Chemical reaction engineering*. 3 ed. 1999, New york: Wiley.
69. Viness, A., *Extractive metallurgy 1 Basic thermodynamics and kinetics*. Vol. 1. 2011, London: Wiley.
70. Xue, T., et al., *Decomposition kinetics of titanium slag in sodium hydroxide system.* Hydrometallurgy, 2009. **95**(1–2): p. 22-27.
71. Liddell, K.C., *Shrinking core models in hydrometallurgy: What students are not being told about the pseudo-steady approximation.* Hydrometallurgy, 2005. **79**(1–2): p. 62-68.
72. Rodríguez-Aragón, L.J. and J. López-Fidalgo, *Optimal designs for the Arrhenius equation.* Chemometrics and Intelligent Laboratory Systems, 2005. **77**(1–2): p. 131-138.
73. Rodríguez-Díaz, J.M. and M.T. Santos-Martín, *Study of the best designs for modifications of the Arrhenius equation.* Chemometrics and Intelligent Laboratory Systems, 2009. **95**(2): p. 199-208.
74. Kura, H., et al., *Effect of induced uniaxial magnetic anisotropy on ferromagnetic resonance frequency of Fe–Co alloy nanoparticle/polystyrene nanocomposite.* Scripta Materialia, 2014. **76**(0): p. 65-68.
75. Shah, I.D. and P.L. Ruzzi, *Pentlandite: Preparation, hydrogen reduction in the presence of lime to yield an iron-nickel alloy.* Metallurgical Transactions B, 1978. **9**(2): p. 247-253.
76. Habash, F. and B.I. Yostos, *Copper from chalcopyrite by direct reduction.* Journal of Metals, 1977. **29** (7): p. 11-16
77. Mankhand, T.R. and P.M. Prasad, *Lime-enhanced hydrogen reduction of molybdenite.* Metallurgical Transactions B, 1982. **13**(2): p. 275-282.
78. Habashi, F., *Chalcopyrite its Chemistry and Metallurgy*. 1978: MsGraw Hill.

79. Hata, M.F.M., *Gravity separation method using iron powder*, 1992, Kyusyumetal Industry Co., Ltd. Kitakyushu: United states.
80. Terekhov, D.S. and N.V. Emmanuel, *Direct extraction of nickel and iron from laterite ores using the carbonyl process.* Minerals Engineering, 2013. **54**(0): p. 124-130.
81. Tannenbaum, R., *Thermal decomposition of cobalt carbonyl complexes in viscous media.* Inorganica Chimica Acta, 1994. **227**(2): p. 233-240.
82. Terekhov, D.S., *Cobalt recovery process*, 2010, Google Patents: United States.
83. Tsao, U. and J. Kettell, *Multistage carbonation of calcium oxide and calcium sulfide*, 1987, Google Patents.
84. Jha, A. and P. Grieveson, *Calcination of calcium sulphate in the presence of carbon and calcium sulphide.* Scandinavian Journal of Metallurgy, 1990. **19**(1): p. 39-48.
85. Turkdogan, E.T., *Physical chemistry of high temperature technology* 1980: Academic Press.
86. Dong, Z.-B., et al., *Oxidation Reaction of Calcium Sulfide in an Advanced PFBC Condition (II) - Sulfation Reaction and Grain Model Application.* Journal of the Japan Institute of Energy, 1999. **78**(9): p. 750-759.
87. Dong, Z.-B., et al., *Oxidation Reaction of Calcium Sulfide in an Advanced PFBC Condition (I). Effects of O2 concentration, type of limestone and particle size.* Journal of the Japan Institute of Energy, 1999. **78**(2): p. 99-109.
88. Balaz, P., *Extractive Metallurgy of Activated Minerals*. Chemical, Petrochemical & Process. 2000: Elsevier. 1-290.
89. Winkel, L., et al., *Decomposition of copper concentrates at high-temperatures: An efficient method to remove volatile impurities.* Minerals Engineering, 2008. **21**(10): p. 731-742.
90. Winkel, L., I. Alxneit, and M. Sturzenegger, *Thermal decomposition of copper concentrates under concentrated radiation — Mechanistic aspects of the separation of copper from iron sulfide phases.* International Journal of Mineral Processing, 2008. **88**(1–2): p. 24-30.
91. Raghavan, V., *Cu−Fe−S (Copper-Iron-Sulfur).* Journal of Phase Equilibria and Diffusion, 2006. **27**(3): p. 290-291.
92. Pelovski, Y. and V. Petkova, *Investigation on Thermal Decomposition of Pyrite Part I.* Journal of Thermal Analysis and Calorimetry, 1999. **56**(1): p. 95-99.

93. Boyabat, N., et al., *Thermal decomposition of pyrite in the nitrogen atmosphere.* Fuel Processing Technology, 2004. **85**(2–3): p. 179-188.
94. Shah, I.D. and S.E. Khalafalla, *Thermal decomposition of CuS to Cu1.8S.* Metallurgical Transactions, 1971. **2**(2): p. 605-606.
95. Shah, I.D. and S.E. Khalafalla, *Kinetics and mechanism of the conversion of covellite (CuS) to digenite (Cu1.8S).* Metallurgical Transactions, 1971. **2**(9): p. 2637-2643.
96. Richardson, F.D., *Physical chemistry of melts in metallurgy*. Vol. 1. 1974, London: Academic Press.
97. Ray, H.S., *Introduction to Melts: Molten Salts, Slags and Glasses*. 2006, Mumbai: Allied Publishers.
98. Rahaman, M.N., *Ceramic processing and sintering* 1995, New York: M. Dekker.
99. Gaskel, D.R., *Introduction to the thermodynamics of materials* 5ed. 2008, New York ; London Taylor & Francis.
100. David A. Porter, K.E.E.a.M.Y.S., ed. *Phase transformations in metals and alloys*. 3 ed. 2009, CRC Press: London.
101. Darken, L.S., *Application of the Gibbs-Duhem Equation to Ternary and Multicomponent Systems.* Journal of the American Chemical Society, 1950. **72**(7): p. 2909-2914.
102. Schuhmann Jr, R., *Application of Gibbs-Duhem equations to ternary systems.* Acta Metallurgica, 1955. **3**(3): p. 219-226.
103. IbI, N.V. and B.F. Dodge, *Note on the Duhem equation.* Chemical Engineering Science, 1953. **2**(3): p. 120-126.
104. Pehlke, R.D., *Unit processes of extractive metallurgy* 1973, New York: Elsevier.
105. Gilchrist, J.D., ed. *Extraction metallurgy*. 3 ed. 1989, Pergamon: Oyford.
106. Tarby, S.K. and F.P. Stein, *Thermodynamics of binary metallic solutions: Application of the wilson equation.* Metallurgical Transactions, 1970. **1**(8): p. 2354-2356.
107. W.D, K., B. H.K, and U. D.R., *Introduction to ceramics* 2ed. 1976, New York ; Chichester John Wiley.
108. R, N.S.W.-K.L.P.V., ed. *Advanced physical chemistry for process metallurgy* 1997, Academic Press: San Diego, California.
109. Kubaschewski, O., C.B. Alcock, and P.J. Spencer, *Materials Thermochemistry*. 6 ed. 1993, Oxford ; New York Pergamon Press.

110. Moore, J.J., et al., *Chemical metallurgy*. 2 ed. 1990, London: Butterworths.
111. Richardson, F.D., *Physical chemistry of melts in metallurgy*. Vol. 2. 1974, London Academic Press.
112. Mills, K. *The estimation of slag properties*. in *International Conference of Southern African Pyrometallurgy, Cradle of Humankind, South Africa*. 2011. Cradle of Humankind, South Africa.
113. Matusewicz, R. and E. Mounsey, *Using ausmelt technology for the recovery of cobalt from smelter slags.* JOM, 1998. **50**(10): p. 51-52.
114. Hughes, S., *Applying ausmelt technology to recover Cu, Ni, and Co from slags.* JOM, 2000. **52**(8): p. 30-33.
115. Tumen, F. and N.T. Bailey, *Recovery of metal values from copper smelter slags by roasting with pyrite.* Hydrometallurgy, 1990. **25**(3): p. 317-328.
116. Chakrabarti, D.J. and D.E. Laughlin, *The Cu-S (Copper-Sulfur) system.* Bulletin of Alloy Phase Diagrams, 1983. **4**(3): p. 254-271.
117. Wang, L.-W., *High chalcocite Cu 2 S: a solid-liquid hybrid phase.* Physical review letters, 2012. **108**(8): p. 085703.
118. Blachnik, R. and A. Müller, *The formation of Cu2S from the elements: I. Copper used in form of powders.* Thermochimica Acta, 2000. **361**(1–2): p. 31-52.
119. Sharma, R.C. and Y.A. Chang, *A thermodynamic analysis of the copper-sulfur system.* Metallurgical Transactions B, 1980. **11**(4): p. 575-583.
120. Raghavan, V., *Phase diagrams of ternary iron alloys / V. Raghavan. Part 2, Ternary systems containing iron and sulphur*. 1988, Calcutta: Indian Institute of Metals.
121. Craig, J.R., D.J. Vaughan, and J.B. Higgins, *Phase equilibria in the copper-cobalt-sulfur system.* Materials Research Bulletin, 1979. **14**(2): p. 149-154.
122. Craig, J.R., D.J. Vaughan, and J.B. Higgins, *Phase relations in the Cu-Co-S system and mineral associations of the carrollite (CuCo 2 S 4)-linnaeite (Co 3 S 4) series.* Economic Geology, 1979. **74**(3): p. 657-671.
123. Chen, Y.O. and Y.A. Chang, *Thermodynamics and phase relationships of transition metal-sulfur systems: I. The cobalt-sulfur system.* Metallurgical Transactions B, 1978. **9**(1): p. 61-67.
124. Durand-Charre, M., *Microstructure of Steels and Cast Irons*. 2004, Verlag Berlin Springer.

125. Banda, W., et al., *Liquidus temperature determination of the Fe–Co–Cu system in the Fe-rich corner by thermal analysis.* Journal of Alloys and Compounds, 2008. **461**(1–2): p. 178-182.
126. Liu, N., et al., *Liquid-phase Separation in Rapid Solidification of Undercooled Fe–Co–Cu Melts.* Journal of Materials Science & Technology, 2012. **28**(7): p. 622-625.
127. Bein, S., C. Colinet, and M. Durand-Charre, *CVM calculation of the ternary system Co-Cu-Fe.* Journal of Alloys and Compounds, 2000. **313**(Copyright 2001, IEE): p. 133-43.
128. Hultgren, R., *Selected values of the thermodynamic properties of the elements*. 1973, Metals Park, Ohio: American Society for Metals.
129. Nishizawa, T. and K. Ishida, *The Co−Fe (Cobalt−Iron) system.* Bulletin of Alloy Phase Diagrams, 1984. **5**(3): p. 250-259.
130. Nishizawa, T. and K. Ishida, *The Co−Cu (Cobalt-Copper) system.* Journal of Phase Equilibria, 1984. **5**(2): p. 161-165.
131. Nikolaenko, I.V. and M.A. Turchanin, *Enthalpies of formation of liquid binary (copper + iron, cobalt, and nickel) alloys.* Metallurgical and Materials Transactions B, 1997. **28**(6): p. 1119-1130.
132. Fang, T., et al., *Liquid immiscibility in an Fe–Cu alloy by molecular dynamics simulation.* Journal of Physics: Condensed Matter, 2012. **24**(50).
133. Bachmaier, A., et al., *The formation of supersaturated solid solutions in Fe–Cu alloys deformed by high-pressure torsion.* Acta Materialia, 2012. **60**(3): p. 860-871.
134. Hasebe, M. and T. Nishizawa, *Calculation of phase diagrams of the iron-copper and cobalt-copper systems.* CALPHAD: Computer Coupling of Phase Diagrams and Thermochemistry, 1980. **4**(2): p. 83.
135. Chen, Q. and Z. Jin, *The Fe-Cu system: A thermodynamic evaluation.* Metallurgical and Materials Transactions A, 1995. **26**(2): p. 417-426.
136. Massalski, T.B., et al., *Binary alloy phase diagrams* ed. L.H.B. Joanne L. Murray, Hugh Baker. 1986, Metals Park, Ohio: American Society for Metals.
137. Raghavan, V., *Co-Cu-Fe (Cobalt-Copper-Iron).* Journal of Phase Equilibria, 2002. **23**(3): p. 253-256.
138. Cullity, B.D., *Introduction to Magnetic Materials*. 1972, London Addison-Wesley.

139. MacLean, W.H., *Liquidus Phase Relations in the FeS - FeO - Fe304 -Si02 System, and their Application in Geology,* in *Department of Geological Sciences*1968, McGillUniversity: Montreal, Quebec.
140. Zhong, S. and M.T. Hepworth, *Thermodynamic studies of iron oxysulfide as a sulfur sorbent.* Energy & Fuels, 1993. **7**(6): p. 1073-1078.
141. Jha, A. and K. Abraham, *Dephosphorisation of Iron–Chrome Alloy with Ca–CaF2 Melt during Electro Slag Refining.* ISIJ International, 1989. **29**(4): p. 300-308.
142. Morris, A.E. and H. Flynn, *Discussion of "lime-enhanced reduction of sulfide concentrates: A thermodynamic discussion".* Metallurgical Transactions B, 1986. **17**(4): p. 914-917.
143. Wriedt, H.A., *The Fe-O (Iron-Oxygen) System.* Journal of Phase Equilibria, 1991. **12**(2): p. 170-200.
144. Ghosh, A., *Textbook of materials and metallurgical thermodynamics* 2003, Connaught, Delhi: Meenakshi.
145. Muan, A. and E.F. Osborn, *Phase equilibria among oxides in steelmaking* 1965, Pergamon Addison-Wesley.
146. Yazawa, A.E., Motonori. *Equilibrium Studies on Copper Slags Used In Continuous Converting*. in *International Symposium on Copper Extraction & Refining* 1976 Las Vegas, Nevada: Port City Press.
147. Neumann, J., T. Zhong, and Y. Chang, *The Cu−O (Copper-Oxygen) system.* Journal of Phase Equilibria, 1984. **5**(2): p. 136-140.
148. Roberts, H.S. and F.H. Smyth, *The system copper: Cupric oxide: Oxygen.* Journal of the American Chemical Society, 1921. **43**(5): p. 1061-1079.
149. Predel, B., *Cu-O (Copper-Oxygen),* O. Madelung, Editor.
150. Schmid, R., *A thermodynamic analysis of the Cu-O system with an associated solution model.* Metallurgical Transactions B, 1983. **14**(3): p. 473-481.
151. Clavaguera-Mora, M.T., et al., *Thermodynamic description of the Cu□O system.* Journal of Alloys and Compounds, 2004. **377**(1–2): p. 8-16.
152. Weisweiler, W., et al., *Kinetic studies in the CaO-SiO2 — System Part I Mechanism and kinetic data of the reactions between CaO- and SiO2- powder compacts.* Cement and Concrete Research, 1986. **16**(3): p. 283-295.
153. Lee, Y.E., *Thermodynamics of the cao-si02 system.* Calphad, 1982. **6**(4): p. 283-291.

154. Mihailova, I. and D. Mehandjiev, *Characterization of fayalite from copper slags.* Journal of the University of Chemical Technology and Metallurgy, 2010. **45**(3): p. 317-326.
155. Habashi, F., *Kinetics of metallurgical processes*. 1999, Quebec: Metallurgie Extractive.
156. Vyazovkin, S., *Thermogravimetric Analysis*, in *Characterization of Materials*. 2002, John Wiley & Sons, Inc.
157. Bagheri, H., Y.K. Rao, and P. Pichestapong, *Reduction of copper(I) sulphide with H2-He mixtures and intrinsic rates.* Transactions of the Institutions of Mining and Metallurgy, Section C: Mineral Processing and Extractive Metallurgy, 1997. **106**(SEPT/DEC): p. C105-C114.
158. Georg, W., *Powder diffraction : The Rietveld method and the two stage method to determine and refine crystal structures from powder diffraction data*. 2006, Berlin ; New York Springer.
159. Reed, J.S., *Principles of ceramics processing* 1995, New York ; Chichester Wiley & Sons.
160. Cullity, B.D. and S.R. Stock, *Elements of X-ray diffraction*. 3 ed. 2001, Upper Saddle River: Prentice-Hall International.
161. Brandon, D. and W.D. Kaplan, *Microstructural characterization of materials* 1999, Chichester ; New York Wiley.
162. Voutou, B. and E. Stefanaki. *Electron Microscopy: The Basics*. 2008.
163. Goldstein, J., et al., *2003 Scanning Electron Microscopy and X-ray Microanalysis*. 3 ed. 2003, New york: Kluwer Academic/ Plenum Publishers.
164. Belzile, N., et al., *A review on pyrrhotite oxidation.* Journal of Geochemical Exploration, 2004. **84**(2): p. 65-76.
165. Morimoto, N. and K. Koto, *Phase relations of the cu-s system at low temperatures - stability of anilite.* American Mineralogist, 1970. **55**(1-2): p. 106-117.
166. Goble, R.J., *The relationship between crystal structure, bonding and cell dimensions in the copper sulfides* Canadian mineralogist, 1985. **23**: p. 61 - 76.
167. Vaisburd, S., et al., *Slags and mattes in vanyukov's process for the extraction of copper.* Metallurgical and Materials Transactions B, 2002. **33**(4): p. 551-559.
168. Pagliari, L., et al., *A kinetic study of the quartz–cristobalite phase transition.* Journal of the European Ceramic Society, 2013. **33**(15–16): p. 3403-3410.

169. Muszer, A., et al., *Covellinisation of copper sulphide minerals under pressure leaching conditions.* Hydrometallurgy, 2013. **137**(0): p. 1-7.
170. Santisteban, J., et al., *Loss on ignition: a qualitative or quantitative method for organic matter and carbonate mineral content in sediments?* Journal of Paleolimnology, 2004. **32**(3): p. 287-299.
171. Dutrizac, J.E., *Reactions in cubanite and chalcopyrite.* Can. Mineral., 1976. **14**(2): p. 172-181.
172. Jha, A., *Carbothermic reduction of sulphide minerals*, in *Department of Metallurgy and Materials Science*1984, Imperial College London.
173. Allen, D. and A.N. Hayhurst, *Kinetics of the reaction between gaseous sulfur trioxide and solid calcium oxide.* Journal of the Chemical Society, Faraday Transactions, 1996. **92**(7): p. 1239-1242.
174. Alcock, C.B., *The Thermodynamics of Roasting Processes*, in *Principles of pyrometallurgy*. 1976, Academic Press: London. p. 1-20.
175. Munro, N. and N. Themelis. *Rate phenomena in a laboratory flash smelting reactor*. in *Copper 91(Cobre 91)*. 1991. Otawa, Ontario, Canada: Pergamon.
176. Mankhand, T.R., V.V.P. Kutumba Rao, and P.M. Prasad, *The formation of copper fibers during the lime-enhanced hydrogen reduction of cuprous sulfide.* Metallography, 1981. **14**(4): p. 335-345.
177. Jha, A. and P. Grieveson, *Carbothermic reduction of pyrrhotite in the presence of lime for the production of metallic iron.* Scandinavian Journal of Metallurgy, 1992. **21**(Compendex): p. 50-62.
178. Jha, A., B.S. Terry, and P. Grieveson, *Physical chemistry of carbothermic reduction of sulphide minerals: 'a novel metal production route,* in *Proceedings of the International Conference on Extractive Metallurgy of Gold and Base Metals*1992, Publ by Australasian Inst of Mining & Metallurgy: Kalgoorlie, Aust. p. 433-440.
179. Li, Y. and H. Wu, *Ash Cenosphere from Solid Fuels Combustion. Part 1: An Investigation into Its Formation Mechanism Using Pyrite as a Model Fuel.* Energy & Fuels, 2011. **26**(1): p. 130-137.
180. Tathavadkar, V.D., A. Jha, and M.P. Antony, *The soda-ash roasting of chromite minerals: Kinetics considerations.* Metallurgical and Materials Transactions B, 2001. **32**(4): p. 593-602.

181. Tathavadkar, V.D., *The process physical chemistry of extraction of sodium chromates from chromite ores,* in *Department of materials school of process, environmental* 2001, Leeds.

182. NALDRETT, A.J., *A Portion of the System Fe–S–O between 900 and 1080 °C and its Application to Sulfide Ore Magmas.* Journal of Petrology, 1969. **10**(2): p. 171-201.

183. Osamu, Z.C.-f.S.R.A.I.O., *The Rate-Controlling Step for the Reduction of Zinc Sulfide Concentrate Briquetted by Utilizing Coking Coal as a Binder and a Reducing Agent, Studies on the rate-controlling step for the reduction of zinciferous coked briquettes. (2nd report).* Shigen-to-Sozai, 1989. **105**(6): p. 475 - 489.

184. M.C., P.R.C.L.C.R., *Antimony production by carbothermic reduction of stibnite in the presence of lime.* Journal of Mining and Metallurgy, Section B: Metallurgy, 2014.

185. Rao, Y.K. and B.P. Jalan, *A study of the rates of carbon-carbon dioxide reaction in the temperature range 839 to 1050 C.* Metallurgical Transactions, 1972. **3**(9): p. 2465-2477.

186. Shin-ya Yokoyama; Koshiro Miyaharat, K.-i.T.l.T.o.T., *Catalytic reduction of carbon dioxide. 1. Reduction of carbon dioxide with carbon carrying potassium carbonate.* Fuel, 1979. **58**(7): p. 510–514.

187. Halmann, M.M., *Chemical Fixation of Carbon Dioxide Methods for Recycling CO2 in to useful products*. 1993, Florida: CRC press. Inc.

188. Walker, P.L.J., F. Rusinko, Jr.; and L. G. Austin, , *Gas Reactions of Carbon.* Advance in Catalysis, 1959. **XI**: p. 133.

189. Curiotto, S., *Undercooling and phase transformations in Cu-based alloys*, in *Dipartimento di Chimica I.F.M.*2006, UNIVERSIT`A DEGLI STUDI DI TORINO.

190. Jha, A. and S. Srikanth, *Measurement of non-isothermal oxygen potentials in a Cu–Fe–Ca–S–O liquid during reduction of chalcopyrite in lime and carbon mixtures.* Mineral Processing and Extractive Metallurgy, 2014. **123**(1): p. 21-28.

191. Stuart, H., *Lattice parameters and Curie-point anomalies of iron-cobalt alloys* Journal of Physics D: Applied Physics, 1969. **2**(4): p. 485.

192. te Velthuis, S.G.E., et al., *The ferrite and austenite lattice parameters of Fe–Co and Fe–Cu binary alloys as a function of temperature.* Acta Materialia, 1998. **46**(15): p. 5223-5228.

193. Pearson, A., *Concentration of ores and other minerals by the sink and float process* 1940: United States.
194. Banda, W., N.T. Beukes, and J.J. Eksteen, *Factors influencing base metal recovery from waste reverberatory furnace slags in a 50 kVA laboratory DC plasma arc furnace.* Journal of The South African Institute of Mining and Metallurgy, 2004. **104**(3): p. 201-207.
195. Riveros, G., T. Marıin, and C. Puga, *Lime-concentrate roasting studies—effect of activated limestone.* Minerals Engineering, 2004. **17**(3): p. 469-471.
196. Terry, B.S., G. Riveros, and J.H.E. Jeffes, *Lime-concentrate process for roasting of copper-bearing sulphides - Part 3: Mechanisms of roasting reactions.* Transactions of the Institution of Mining and Metallurgy, Section C: Mineral Processing and Extractive Metallurgy, 1994. **103**: p. C210-C216.
197. Terry, B.S., G. Riveros, and J.H.E. Jeffes, *Lime-concentrate process for roasting of copper-bearing sulphides - Part 2: Effect of sulphide:lime ratio, air flow rate, pellet size and porosity on reaction kinetics.* Transactions of the Institution of Mining and Metallurgy, Section C: Mineral Processing and Extractive Metallurgy, 1994. **103**: p. C201-C209.
198. Terry, B.S., et al., *Lime-concentrate process for roasting of copper-bearing sulphides - Part 1: Analysis of optimum roasting conditions.* Transactions of the Institution of Mining and Metallurgy, Section C: Mineral Processing and Extractive Metallurgy, 1994. **103**: p. C193-C200.
199. Prasad, S. and B.D. Pandey, *Alternative processes for treatment of chalcopyrite —A review.* Minerals Engineering, 1998. **11**(8): p. 763-781.
200. Hu, G., et al., *Decomposition and oxidation of pyrite.* Progress in Energy and Combustion Science, 2006. **32**(3): p. 295-314.
201. Dunn, J.G., G.C. De, and B.H. O'Connor, *The effect of experimental variables on the mechanism of the oxidation of pyrite: Part 2. Oxidation of particles of size 90–125 μm.* Thermochimica Acta, 1989. **155**(0): p. 135-149.
202. Dunn, J.G., G.C. De, and B.H. O'Connor, *The effect of experimental variables on the mechanism of the oxidation of pyrite: Part 1. Oxidation of particles less than 45 μm in size.* Thermochimica Acta, 1989. **145**(0): p. 115-130.
203. Allen, D. and A.N. Hayhurst, *Reaction between gaseous sulfur dioxide and solid calcium oxide mechanism and kinetics.* Journal of the Chemical Society, Faraday Transactions, 1996. **92**(7): p. 1227-1238.

204. Vignes, A., *Extractive metallurgy 2 Metallurgical reaction processes*. Vol. 2. 2011, London: Wiley.
205. Manasse, A. and M. Mellini, *Chemical and textural characterisation of medieval slags from the Massa Marittima smelting sites (Tuscany, Italy).* Journal of Cultural Heritage, 2002. **3**(3): p. 187-198.
206. Ward, C.R. and D. French, *Determination of glass content and estimation of glass composition in fly ash using quantitative X-ray diffractometry.* Fuel, 2006. **85**(16): p. 2268-2277.
207. Jiménez, J.C.F.-C.G.R.J.M.F., *Occurrence and speciation of copper in slags obtained during the pyrometallurgical processing of chalcopyrite concentrates at the Huelva smelter (Spain).* Journal of Mining and Metallurgy, Section B: Metallurgy 2012. **48**(2): p. 161-171.
208. Ettler, V., et al., *Mineralogy and environmental stability of slags from the Tsumeb smelter, Namibia.* Applied Geochemistry, 2009. **24**(1): p. 1-15.
209. Hara, Y.R.S. and A. Jha. *A Novel Low Energy Route for the Extraction of Copper and Cobalt Metals/Alloys from the Zambian Sulphide Concentrates*. in *Characterization of Minerals, Metals, and Materials*. 2012. John Wiley & Sons.
210. Hara, Y. and A. Jha, *Carbothermic reduction of Zambian sulphide concentrates in presence of lime.* Mineral Processing and Extractive Metallurgy, 2013. **122**(3): p. 146-156.
211. Kim, H. and H.Y. Sohn, *Effects of CaO, Al2O3, and MgO additions on the copper solubility, ferric/ferrous ratio, and minor-element behavior of iron-silicate slags.* Metallurgical and Materials Transactions B, 1998. **29**(3): p. 583-590.
212. Zivkovic, Z., et al., *The influence of the silicate slag composition on copper losses during smelting of the sulfide concentrates.* Journal of Mining and Metallurgy, Section B: Metallurgy 2009. **45**(1): p. 23-35.
213. Reddy, R., V. Prabhu, and D. Mantha, *Recovery of copper from copper blast furnace slag*, in *SME Annual Meeting and Exhibit* 2004: Denver, Colorado.
214. Banda, W., N. Morgan, and J.J. Eksteen, *The role of slag modifiers on the selective recovery of cobalt and copper from waste smelter slag.* Minerals Engineering, 2002. **15**(11, Supplement 1): p. 899-907.
215. Zhijie, Y., et al. *Research on effect of CaO/SiO2 on recovery iron from converter slag under smelting condition*. in *Mechanic Automation and Control Engineering (MACE), 2011 Second International Conference on*. 2011.

216. Li, Y. and I.P. Ratchev, *Rate of interfacial reaction between molten CaO-SiO2-Al2O3-Fe x O and CO-CO2.* Metallurgical and Materials Transactions B, 2002. **33**(5): p. 651-660.
217. Ekmekyapar, A., et al., *Investigation of Leaching Kinetics of Copper from Malachite Ore in Ammonium Nitrate Solutions.* Metallurgical and Materials Transactions B, 2012. **43**(4): p. 764-772.
218. Matsui, I., D. Kunii, and T. Furusawa, *Study of char gasification by carbon dioxide. 1. Kinetic study by thermogravimetric analysis.* Industrial & Engineering Chemistry Research, 1987. **26**(1): p. 91-95.
219. Dutta, S., C.Y. Wen, and R.J. Belt, *Reactivity of Coal and Char. 1. In Carbon Dioxide Atmosphere.* Industrial & Engineering Chemistry Process Design and Development, 1977. **16**(1): p. 20-30.
220. Brady, J.B., *Diffusion Data for Silicate Minerals, Glasses, and Liquids*, in *Mineral Physics & Crystallography: A Handbook of Physical Constants*. 2013, American Geophysical Union. p. 269-290.
221. Yurimoto, H., M. Morioka, and H. Nagasawa, *Diffusion in single crystals of melilite: I. Oxygen.* Geochimica et Cosmochimica Acta, 1989. **53**(9): p. 2387-2394.
222. Turkdogan, E.T., et al., *Rate of oxidation of graphite in carbon dioxide.* Carbon, 1968. **6**(4): p. 467-484.
223. Karata and C., *Catalysis of the graphite–CO2 reaction by iron from in-situ reduction wustite over the range 870–1100°C.* Mineral Processing and Extractive Metallurgy, 2001. **110**(1): p. 7-13.
224. Karatas, C., *Catalytic enhancement of graphite - CO2 reaction by in situ reduced chromium and nickel from their oxides Cr2O3 and NiO over the temperature range 850-1100°C* Mineral Processing and Extractive Metallurgy, 2004. **113**(1): p. 19-24.
225. Peris Mora, E., et al., *State of the art of gypsum recovery for a Spanish power plant*, in *Studies in Environmental Science*, G.J.S. J.J.J.M. Goumans and H.A.v.d. Sloot, Editors. 1997, Elsevier. p. 581-590.
226. Hansen, B.B., S. Kiil, and J.E. Johnsson, *Investigation of the gypsum quality at three full-scale wet flue gas desulphurisation plants.* Fuel, 2011. **90**(10): p. 2965-2973.

227. Prasad, S. and B.D. Pandey, *Sulphation roasting studies on synthetic copper–iron sulphides with steam and oxygen.* Canadian Metallurgical Quarterly, 1999. **38**(4): p. 237-247.

11.0 List of publications

The results from the thesis have been published and and presented in the following journals and proceedings:

1. Hara Y.R.S. and Jha A., *Carbothermic reduction of Zambian sulphide concentrates in the presence of lime* Mineral Processing and Extractive Metallurgy 122 (3), 146-156.
2. Hara Y.R.S. and Jha A., *A Novel Low-Energy Route for the Extraction of Copper and Cobalt Metals/Alloys from the Zambian Sulphide Concentrates*, Characterization of Minerals, Metals, and Materials, TMS Annual Meeting & Exhibition, 3 – 7 March, 2012, Orlando, Florida, 77-87.
3. Hara Y.R.S. and Jha A., *Kinetic and Thermodynamic Analysis of the Reduction of Oxides of Cu and Co in a SiO_2-CaO-$(Al, Fe)_2O_3$ Slag*, Celebrating the Megascale: Proceedings of the Extraction and Processing, TMS Annual Meeting & Exhibition, 16-20 February, 2014, San Diego, California, USA, 553 – 561.
4. Jha A. and Hara Y.R.S., *An Alternative Lower Temperature Route For The Recovery of Cobalt From Slag*, Carbon Dioxide Management and Other Technologies, TMS Annual Meeting & Exhibition, 3 – 7 March, 2012, Orlando, Florida, 65-72.
5. Hara Y.R.S., *Study of Reaction Mechanisms for Copper-Cobalt-Iron Sulfide Concentrates in the Presence of Lime and Carbon*, JOM 65 (11), 1597-1607.
6. Hara Y.R.S., *Thermal Decomposition of the Froth Flotation Mineral Sulphide Concentrates Under Argon Atmosphere, in the Presence and Absence of Carbon* Mineral Processing and Extractive Metallurgy Review, 2014.
7. Hara Y.R.S., *Mineral sulphide-lime reactions and effect of CaO/C mole ratio during carbothermic reduction of complex mineral sulphides,* International Journal of Minerals, Metallurgy, and Materials 21 (1), 1-11.
8. Hara Y.R.S., *A Minimum Pollution, Low Energy Process for the Recovery of Cobalt and Copper from Complex Sulphide Minerals*, Characterization of Minerals, Metals, and Materials, TMS Annual Meeting & Exhibition, 3 – 7 March, 2013, San Antonio, Texas, USA, 333-343.